Polarimetry of small bodies of the Solar System

Aaron Stinson

A dissertation submitted in partial fulfillment

of the requirements for the degree of

Doctor of Philosophy

of

University College London.

Department of Space and Climate Physics

University College London

July 7, 2016

I, Aaron Stinson, confirm that the work presented in this thesis is my own. Where information has been derived from other sources, I confirm that this has been indicated in the work.

Abstract

In this thesis I exploit polarimetric techniques for the study of small objects of the Solar System. In particular I focus my attention on very faint objects that could not be observed before the advent of the Very Large Telescope (VLT) and its FORS instrument. I have contributed to the observations, reduction and data interpretation for two transneptunian objects (TNOs), six faint Trojans asteroids, three active comets (including the target of the ROSETTA mission 67P) and two cometary nuclei.

The scope of the various analyse differed slightly from each other. My studies of active comets have focussed on coma structure, colour and polarimetric maps, enabling a detailed characterisation of the dust of comets at large heliocentric distances that tentively suggest a difference in dust properties at large heliocentric distances.

The six trojans, two TNOs and two cometary nuclei appear only as point sources so I have performed only aperture polarimetry. The analysis of the polarimetric curves (i.e., the broadband polarisation as a function of phase angle) confirms the different types of polarisation phase behaviour of the large and smaller sized TNOs, comet nuclei have very similar polarisation properties to those of F-type asteroids and that the polarisation albedo relationship for asteroids does not hold for cometary nuclei. The polarimetric phase curve of the Trojan asteroids show a similar behaviour to P-Type asteroids and perhaps hint at diversity within the Trojan population.

As a by-product of this scientific analysis, I have contributed to a better characterisation of the instruments employed for the observations, and refined the data

reduction techniques. A full understanding of some of the technical aspects were of crucial importance for the project. The polarisation of these faint bodies is very small; because of this, slightly different data reduction methods may lead to substantially different results.

Acknowledgements

First of all I would like to thank both Dr S. Bagnulo and Dr G. Jones for their support throughout my studentship. Their knowledge has been invaluable to me and without them this thesis would not have been possible.

I would like to thank my numerous collaborators Dr H. Boehnhardt for his help with the analysis of cometary tails via the Laplace filter and Finson-Probstien calculations, Dr G.P. Tozzi for helping to check the data reduction of the low signal to noise ratio SINFONI spectra, Dr S. Protopapa for her modelling of the SINFONI infrared spectra, Dr L. Kolokolova for her insights into the properties of the cometary dust from the observed polarimetric and colour properties, Prof K. Muinonen for the use of his RT-CB modelling code and assistance modelling polarimetric data of Trans-Neptunain objects and several other collaborators for their enlightening discussions on various topics throughout this work.

I would also like to thank all the staff and students at Armagh Observatory that have made my time at the Observatory enjoyable.

Finally I like to thank the Science and Technology Facilities Council for funding my studentship and the COST Action grant MP1104 “Polarization as a tool to study the Solar System and beyond” for funding my visits to collaborators institutions and to attend conferences.

Contents

List of Figures

List of Tables

Chapter 1

Introduction to Polarisation

For many centuries astronomers have used light to study galaxies, nebulae, stars, planets and all other astronomical sources. In the 18^{th} and 19^{th} centuries this was limited to visual inspection of these bodies' images and spectra with the human eye. Later, with the advent of the photographic plate in the late 1890s, it was possible to physically record images and spectra. For over 70 years photographic plates were used until the advent of the CCD detector and it was the distribution of these to many observatories in the 1970s that the modern era of astronomy that we know today was born.

The study of astronomical sources is not limited to visible light but has been expanded to use the entire electromagnetic spectrum. Many different techniques can be applied to both spectra and imaging to probe for further information. The technique on which this work is focused on is polarimetry.

Polarimetry is the study of an object's polarisation either using images or spectral information. The study of a source's polarisation spectrum, otherwise known as spectropolarimetry, is mainly used in the detection and study of stars which have magnetic fields. The ability to detect and measure the strength of the magnetic field is dependent on the size of the Zeeman splitting in the star's absorption lines. Imaging polarimetry has been extensively used for the study of planetary and minor bodies of the Solar System to probe for information about the surface and atmospheric properties of these bodies. It is this technique that this work is concerned with. I will use imaging polarimetry to study several different sources from dwarf

planets to asteroids. In this Chapter I will give a basic definition of what polarisation is and how it has been applied to study the objects of our Solar System.

1.1 What is polarisation?

Light can be described as being a electromagnetic wave. An electromagnetic wave is characterised by an electric field vector **E** and a magnetic field vector **H**. They are perpendicular to each other and to the direction of propagation of the wave. Light from most sources can be described as being unpolarised, meaning that the direction of oscillation of the electric field vector is equally probable in all directions. However, if the electric field vector has a preferred direction of oscillation it is then said to be linearly polarised. Additionally if the electric field vector rotates around the direction of propagation of the wave it is said to be circularly polarised. All three of these polarisation states are presented in the Figure below.

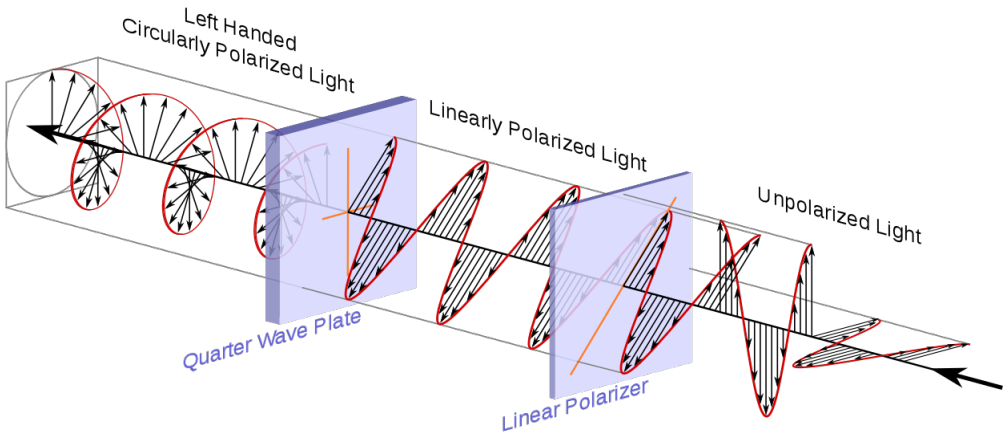

Figure 1.1: The difference between unpolarised, linear polarised and circularly polarised light. Source: wikipedia

Polarisation arises whenever there is a mechanism that breaks the symmetry in the radiative source, or between the source and the observer, for instance in the presence of a magnetic field, or scattering processes.

Polarisation occurs naturally all around us since sunlight reflected off any surface is polarised by a small amount depending on the angle of incidence and the surface material. The preferred direction of this polarisation is always parallel to

the reflecting surface. The reason for this can be visualised by the analogy of skipping a stone across the surface of a lake. If you want the stone to skip you would choose a flat, thin, circular stone and throw it at a glancing angle with the widest face parallel to the surface of the lake. We can consider the incoming unpolarised radiation and resolve it into two components parallel and perpendicular to the surface. In the same way as the stone skipping across the surface of the lake, the parallel component will be reflected whereas the perpendicular component will tend to be absorbed by a small amount, hence giving rise to polarisation.

Since the human eye can not detect polarisation the simplest way to show that the reflected light is polarised is with a polariod filter. Polariod filters are designed to only allow a certain orientation of the electric field vector to pass through. This means if we rotated the polariod filter we would see a change in the irradance of the reflected light from a maximum when the electric field vector parallel to the surface is allowed to pass through the polariod, and at a minimum when the electric field vector perpendicular is allowed to pass through. The ability to only allow certain

Figure 1.2: Photographs taken with and without a polariod filter. Image credit: Robert Atkins photograph[1]

.

orientations of the electric field vector through to the human eye has had many commercial applications. The most common application are polaroid sunglasses, which help reduce the reflections from roads, water, and glass, see Figure 1.2. Another instance where polarisation is utilized for commercial purposes is in the screening of modern 3D films. This technique uses different polarisation states to give the perception of a 3D object on a screen. This is achieved by using two different projectors

[1] http://bobatkins.com/photography/

spaced several metres apart that project light whose electric field vectors are perpendicular to each other. This alone doesn't cause the film to look 3D but we require a pair of special polaroid sunglasses which unlike the pair discussed previously, have two lenses each aligned perpendicular to each other, so that one eye sees the light from one projector the other eye sees the light from the other and this creates two unique perspectives and hence a 3D image. This method, however, proved to be problematic because if the viewer tilted their head slightly the 3D experience would be diminished. Hence, linear polarised light was replaced with circular polarised light and the glasses refitted with lenses that only transmit left and right circularly polarised light. With this method the intensity of the transmitted light is not affected by the movement of the viewer's head.

The use of polarisation is not limited to entertainment purposes. As we mentioned before the light reflected from a surface is polarised; this polarisation can be used as a diagnostic tool to infer properties about the surface the light was reflected from. This can be true if we are studying the light reflected from a surface on Earth or from a solar system body. By studying the observed fraction of linear polarisation, and the way in which it varies as a function of the phase-angle[2], strongly depends on the properties of the topmost surface layer of the object, such as the complex refractive index, particle size, packing density, and microscopic optical heterogeneity.

In 1929 Bernard Lyot discovered a strange phenomenon when observing the Moon at small phase angles. He noted that the polarisation from the surface of the Moon at small phase angles was directed along the scattering plane instead of being perpendicular to it (Lyot, 1929). This is the opposite to what is predicted by simple single Rayleigh-scattering or Fresnel-reflection model. This phenomenon has since been refereed to as "negative polarization". Negative polarisation can be difficult to understand but like many terms defined in physics the negative value gives information about direction compared to the initial definition. Typically polarisation is defined as the flux observed in the plane perpendicular to the plane

[2]The phase angle is the angle between the Sun, the object, and the observer

Sun-target-observer, minus the flux in that plane, divided by the sum of the two fluxes. Since its initial discovery, negative polarisation has been consistently found in all atmosphere-less bodies of the Solar System (when observed at small phase angles) and is currently explained in terms of a coherent back-scattering mechanism (Muinonen, 2004).

As I mentioned earlier, by studying how the polarization varies over the observed phase-angle range we can infer details on the surface properties of that body. The observable phase-angle range available from ground based observations depends on the object's distance from the Sun (see Figure 1.3(a)). For distant objects such as Trans-Neptunian Objects (TNOs), the observable phase-angle range is rather limited, and the observed polarisation is always negative. Nevertheless, as we will see in the next sections, it is still possible to extract useful information even from polarimetric curves that span a phase-angle range as small as 2 degrees.

1.1.1 Basic definition of Stokes parameters

The polarisation properties of light can be described in a variety of different ways but we rely on the definition of four independent quantities. These quantities are referred to as Stokes parameters which were introduced in 1852 by George Stokes. In modern notation they are represented by the symbols I, Q, U, and V.

To define Stokes parameters one first needs to make a preliminary choice of reference direction pertaining to the plane perpendicular to the direction of propagation of the radiation. The choice of reference direction is an arbitrary one, in different fields of astrophysics different systems are used but for the polarimetric observations of Solar System bodies the common choice is to adopt the reference direction of the great circle passing though the object itself and the Sun.

The definition of Stokes parameters can be achieved if we consider a right handed reference system (x, y, z) with the z-axis directed along the direction of propagation of the electromagnetic wave and x-axis directed along the reference direction. This means that Stokes Q will be defined by the difference between the amount of photons whose electric field oscillates along the reference direction x and the amount of photons whose electric field oscillates in the direction perpen-

dicular to it y. Stokes U would then be defined as the difference in the amount of photons whose electric field oscillates at 45 degrees to the reference direction and the number of photons whose electric field oscillates at 135 degrees with respect to the reference direction. Finally Stokes V is given by the right handed circular polarisation minus the left handed circular polarisation. These are defined such that at a fixed point in space, the tip of the electric field vector carried by a beam having right handed, or positive, circular polarization rotates clockwise as seen by an observer looking at the source radiation. Conversely the top of the electric field vector of a beam of having left handed, or negative, circular polarization rotates counter clockwise as seen by an observer looking at the source. Stokes I is simply the total intensity collected from the source. The definition of Stokes Q, U, and V are summarised in Figure 1.3(b). For a more rigorous definition see Landi Degl'Innocenti et al. (2007).

In most applications it is customary to normalise the Stokes parameters Q, U, and V to I and adopt the reduced Stokes parameters P_Q, P_U, and P_V as defined below.

$$P_Q = \frac{Q}{I} \tag{1.1}$$

$$P_U = \frac{U}{I} \tag{1.2}$$

$$P_V = \frac{V}{I} \tag{1.3}$$

These reduced Stokes parameters give us the fraction of polarised light from a source which is typically referred to as a percentage polarisation. The use of a percentage polarisation is much more convenient than using absolute photon counts especially when comparing the polarisation of different targets. Throughout this thesis I only measure linear polarised light (i.e. P_Q and P_U). In later sections I will show for symmetry reasons P_U will be zero in most circumstances and when I refer to the amount of linear polarisation or the percentage polarisation (P(%)) I am referring to the measured P_Q from a source.

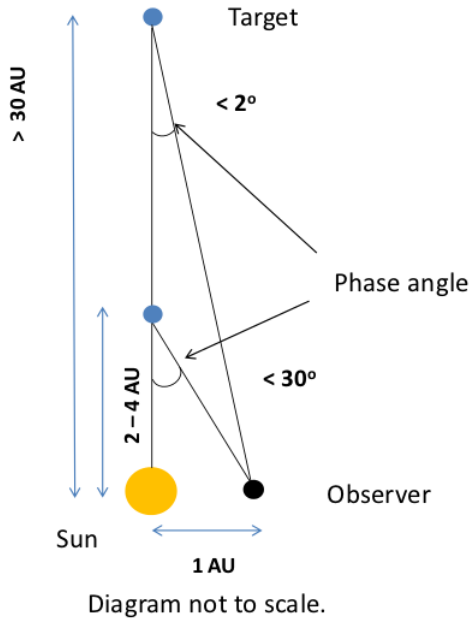

(a)

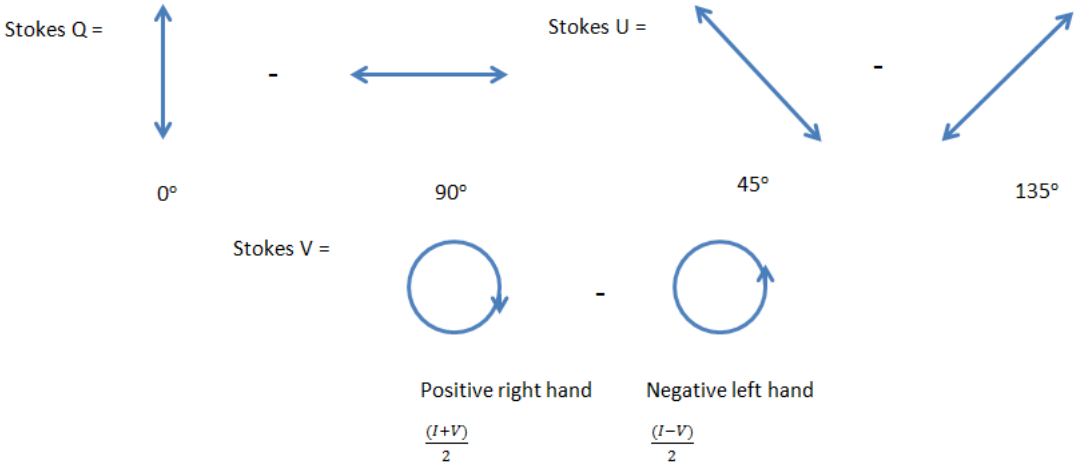

(b)

Figure 1.3: (a) How the observable phase angle changes with an object's distance from the Sun (b) Stokes parameters.

1.2 Polarimetric studies of Solar System objects

Over the past several decades polarimetric observations have been carried out on many different objects in our Solar System from planets to asteroids, in the following section we will give an overview of the results of these observations for the various bodies of our Solar System.

1.2.1 Planets

1.2.1.1 Mercury

Mercury is a unique planet due to its close proximity to the Sun, lack of substantial atmosphere and its slow rotation around its axis. It also experiences one of the largest temperature variations ($\sim 600^{\circ}C$) between its day and night side and from its equatorial region and its pole, since Mercury has nearly zero axial tilt. When passing perihelia Mercury is facing the Sun with one or the other hemisphere centred at the 0^{th} or the 180^{th} meridian often called the hot meridians. The cold 90^{th} and 270^{th} meridians face the Sun when Mercury is at aphelion. Observations of Mercury are quite difficult due to the limited observation time because of its proximity to the Sun. The observable phase angle range for Mercury is 25-150 degrees; below phase angles of 25 degrees ground based observations would have to be taken during the day.

From photometric observations of Mercury (Mallama et al., 2002) brightness variations were found depending on the central longitude of the illuminated disc. The brightness minima occurred at the hot meridian while the maxima occurred at the cold meridian, suggesting a darker and lighter surface respectively. This brightness difference could be due to the number of day and night temperature drops which could have caused countless soil baking, therefore changing the surface structure. Also at perihelion the intensity of solar radiation is 2.5 times greater than at aphelion. This variation should also be detectable via polarimetric variation where the degree of polarisation should increase and then decrease across the surface longitude.

Polarimetric observations of Mercury have been carried out by Kiselev &

Lupishko (2004). Their results showed a large scatter around approximated best fit curve which implied some form of longitudinal effect occurring over the surface of Mercurian surface. The deviation from the approximation curve is plotted as a function of longitudinal distance and can be seen in Figure 1.4. This suggests that there is a variation of surface composition or surface micro structure (e.g. albedo, packing density, etc) with longitudinal distance.

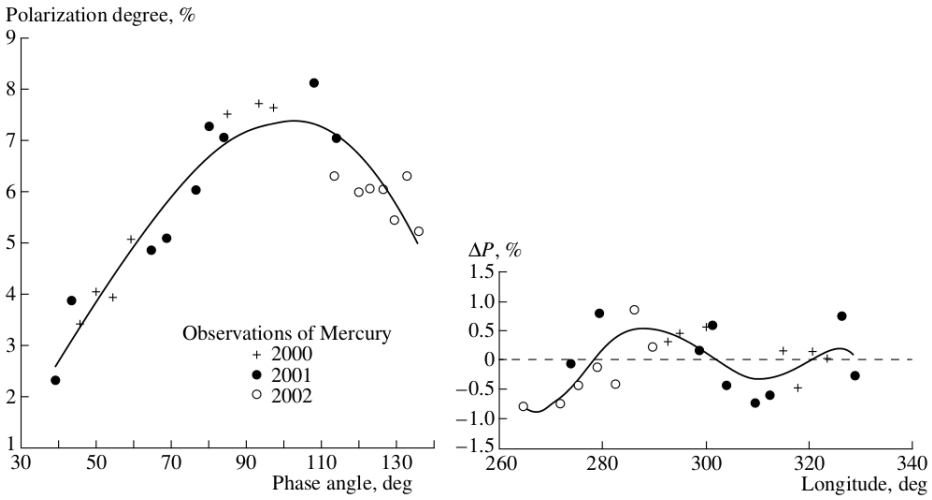

Figure 1.4: Polarisation of Mercury. Left: hand panel shows the polarisation phase curve. Right: the difference in polarisation data points from the approximation curve as a function of longitude.

1.2.1.2 Venus

Venus is one of our closest planetary neighbours, yet some 40 years ago it remained very mysterious mainly due to the planet being veiled in thick clouds. In the 1970s many possibilities for the composition of these clouds were put forward but no consensus on their composition could be reached due to spectral features being insufficient to identify specifically one compound over the others. Polarimetric observations of Venus have been carried out by many different authors over the years, Lyot (1929), Gehrels et al. (1979), Dollfus et al. (1979) to name a few. From these many observations the complete shape of Venus's polarimetric phase curve was known and resembled that of small spherical particles (see Figure 1.5).

With this information Hansen & Hovenier (1974) made the first comprehensive study of the polarimetric observations combined with multi-scattering simulations.

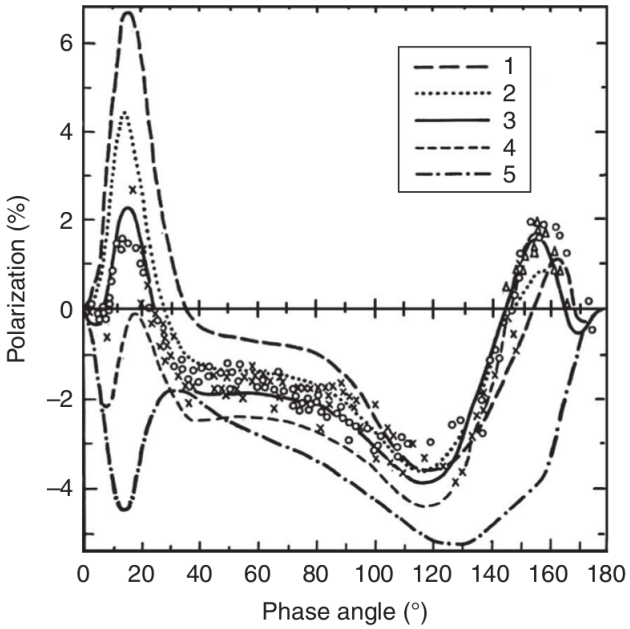

Figure 1.5: Polarimetric phase curve of Venus obtained at λ = 550nm. Open circles and crosses represent observational data and the various dashed lines represent various model particles. See Hansen & Hovenier (1974) for more details.

From this they were able to obtain constraints on the refractive index, particle shape, size distribution and composition of the clouds. They determined that the particle properties derived from their polarisation analysis eliminated all but one of the cloud compositions put forward in the literature and that was a concentrated solution of sulphuric acid.

It should also be noted that Venus has been visited by several space missions like Pioneer Venus and Venus Express. The results from these space missions and Earth-based observation came up with remarkably similar estimates on the properties for Venus's atmosphere.

1.2.1.3 Earth

Unusual as it sounds, the Earth has been polarimetrically observed by ground based observations (Dollfus, 1957). These measurements were carried out by observing the Earthshine (sunshine reflected off the Earth's surface, then reflected back to the Earth by the surface of the Moon). Dollfus reported a linear polarisation of the Earth of the order of 10% at a phase angle close to 90 degrees. Since the Moon is

not a perfect mirror, it introduces a depolarising effect on the incident light, i.e. it reduces the incident light by a factor which is thought to be approximately 3.3.
More recently, spectropolarimetric observations of the Earthshine have been carried out using the VLT by Sterzik et al. (2012). They found that their observations were consistent with models proposed by Stam (2008) for Earth-like extrasolar planets. In particular, the observations detected both O_2 and H_2O spectral lines and the so called "vegetation red edge" feature. As the name suggests, this spectral feature is caused by the vegetation on the Earth's surface. The size of this feature depends on the amount of vegetation exposed on the Earth's surface and by the amount of clouds obscuring it. Although a more realistic cloud cover and surface treatment is required to account for the differences observed between the model and the observations, spectropolarimetric observations of the Earthshine may help to constrain the Earth's surface properties, atmospheric composition and bio-signatures. This gives us a reference with which we can compare future observations of Earth-like exoplanets.

1.2.1.4 Mars

Mars has been polarimetrically observed many times in the past 40 years,Dollfus & Focas (1969), Dollfus et al. (1983, 1984, 1996), Ebisawa & Dollfus (1993). It is important to note that Mars has a thin atmosphere so all polarimetric measurements consist of a contribution from the surface and from the atmosphere. The polarimetric phase curve of Mars shows large diversity depending on whether the atmosphere is clear, if there are ice clouds, if there are dust storms, different terrain features visible and whether it is Martian winter and the polar ice caps are visible. On average the polarisation minimum has a value of $\approx 1\%$ and occurs at a phase angle of 12° and has an inversion angle from negative to positive polarisation at a phase angle of 25°. Some of the different variations in Martian polarimetric phase curves are presented in Figure 1.6.

Polarimetric measurements have also been carried out for Mars using the Hubble Space Telescope during the 2003 great opposition (Shkuratov et al., 2005). These observations took advantage of the closest Earth-Mars encounter as Mars passed within 0.372 AU of the Earth. These observations (Figure 1.7) show the

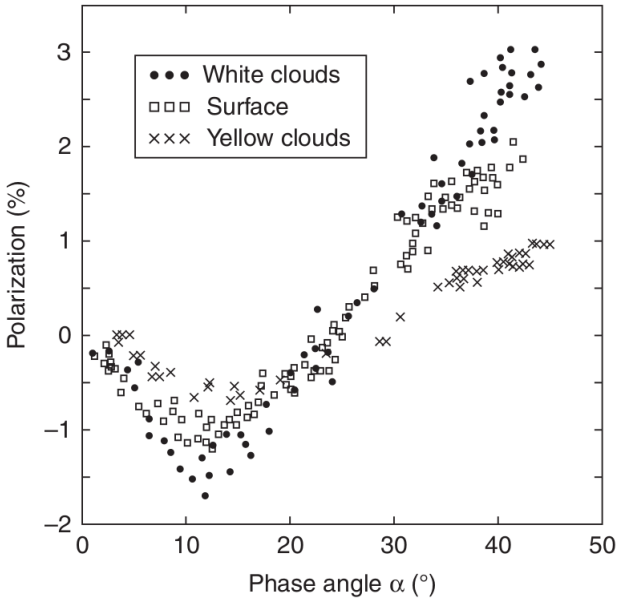

Figure 1.6: Various polarimetric behaviours shown by the Martian surface. From (Kolokolova et al., 2015)

intensity I and the normalised Stokes parameters P_Q and P_U. It was found over that all the observations carried out that P_U was almost zero. The most interesting aspect of these observations was the high negative polarisation features, marked with the white arrows in Figure 1.7, that exhibit a polarisation value of up to -2%. These clouds are semi transparent as surface features can still be seen through them suggesting they are optically thin yet strongly polarising. Theoretical modelling using these observation showed that these polarising clouds was the beginning of nucleation of H_2O ice crystals on sub micron dust particles.

1.2.1.5 The Gas Giants

The gas giants are the four largest planets in our Solar System. For Jupiter and Saturn the maximum phase angle accessible from ground based observations is 11.7° and 6.4° respectively. For the so called Ice giants, Uranus and Neptune, the maximum phase angle accessible is 3.2° and 2.0°. Jupiter and Saturn have been polarimetrically observed by several different authors: Lyot (1929), Gehrels et al. (1969), Hall & Riley (1969), and Schmid et al. (2006). Both planets show a similar trend in polarisation with latitude, with the poles showing positive polarisation while the

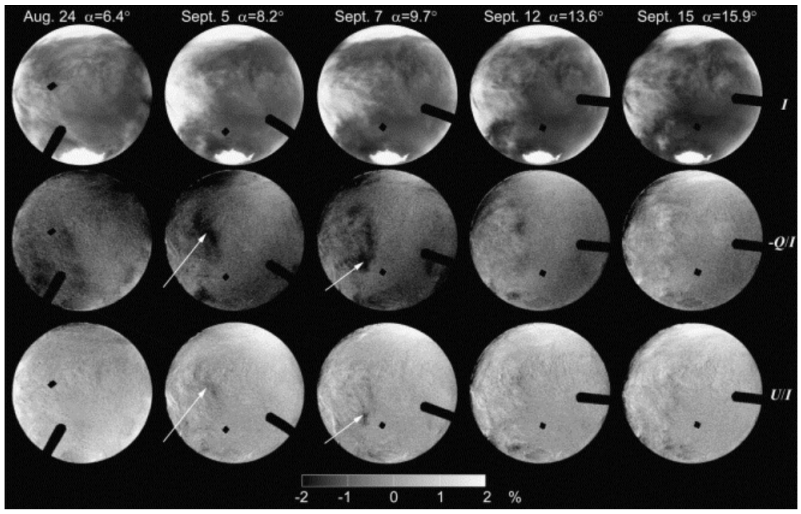

Figure 1.7: Hubble Space Telescope observations of Mars during 2003 apparition. Intensity I is shown on the top row of images, the normalised Stokes parameters -Q/I (P_Q) in the middle row and U/I (P_U) for Mars over 5 different observation dates. The black coronographic finger and spot are shadowed areas of the detector. The white arrows point to highly polarised semi-transparent clouds. Figure taken from Shkuratov et al. (2005)

mid and low latitudes show negative polarisation. Models have been put forward to explain the polarimetric properties of Jupiter (Dlugach & Mishchenko, 2004, 2005, 2008). In these papers they try to interpret the polarisation of the central disc as a collection of spherical particles but later suggest that they are likely to be non spherical in nature. They also assess what can and can not be achieved with low phase angle information. However, even though the particle shapes from the central disc have not been fully understood via models no one has been able to explain the high levels of polarisation at higher latitudes.

Currently, the polarimetric study of these objects is of particular interest as they provide guidance to how much polarisation we can expect to measure from extrasolar gas giant planets. The most favourable phase-angle range to observe is between 60-120 degrees where the polarisation is likely to be at its highest. However, this phase-angle range cannot be accessed by ground based observations due to the planet's distance from Earth. However, both Jupiter and Saturn have had their linear polarisation measured by space missions. Pioneer 10 and 11 measured the degree of linear polarisation of these two planets at a phase angle of approximately 90 degrees

(Smith & Tomasko, 1984; Tomasko & Doose, 1984). They found that for Jupiter, the amount of polarisation varied between 15-20% depending on the line of sight the planet is seen from. From a pole on perspective, one can measure in Jupiter up to 25% of polarisation due to Rayleigh scattering. For Saturn, the observed polarisation over the surface at high phase angles is much smaller, approximately 5% at the same phase angle as Jupiter. For Uranus and Neptune, no polarimetric observations are available from space missions. Ground based observations have been carried out by Schmid et al. (2006) on the limb polarisation of both Uranus and Neptune. This can be used to calculate the linear polarisation at large phase angles with aid from Monte Carlo simulations. From these simulations, Schmid et al. (2006) found that the observed maximum polarisation from both Uranus and Neptune was of the order of 25% at around 90° phase angle. This suggests that exoplanets with atmospheric properties similar to these gas giants are well suited for being searched and investigated in the future with polarimetric instruments such as SPHERE (Beuzit et al., 2008).

1.2.2 Galilean satellites

The Galilean satellites are the four best known moons of Jupiter, and were extensively observed polarimetrically during the 1970s (Veverka, 1971; Dollfus, 1975; Gradie & Zellner, 1973). Due to their distance, the phase-angle range available from ground based observations is less than 12 degrees. It was found from these observations that they have slightly different polarimetric properties, and that the polarisation depends on whether observations are carried out on the eastern or on the western elongation (since they are rotating and orbiting Jupiter synchronously, they always show the same face to Jupiter). This difference in polarimetric behaviour could mean that the leading and trailing faces of these moons could have different surface characteristics.

From polarimetric observations it was concluded that the level of polarisation present on Europa was consistent with the reflection of sunlight from a water frost covered surface. Ganymede polarisation was found to be consistent with a surface covered in frost, and parts with darker material. For Io, it was concluded that it

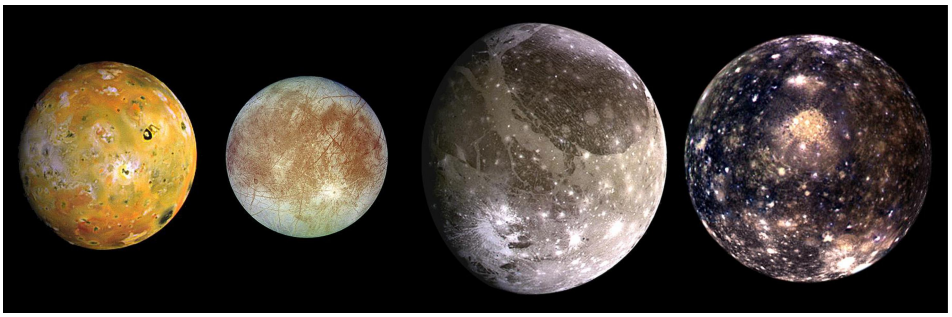

Figure 1.8: Images of the Galilean satellites taken with the Galileo Orbiter space craft. Left to right the moons are, Io, Europa, Ganymede, and Callisto. Image credit: NASA/JPL/DLR

had a surface of partially absorbing crystals thought to result from evaporates released from the mantle and damaged from radiation. The most interesting result of these observations was that Callisto exhibits very different polarimetric behaviour between its 2 hemispheres (as first noticed by Veverka (1971)). Dollfus suggested that this behaviour could be explained by having a mantle of ice containing embedded rocks, which occurred when recent evaporation left the rocks piled high on the surface in a chaotic manner. This event would have occurred after the vicinity of Jupiter had been cleared of small orbiting bodies that were able to impact Callisto. These meteorites would have entered Jupiters influence and impacted on the leading surface of Callisto, leaving the other relatively impact free. The implication is that the difference in polarisation is due to the difference in surface roughness and different materials being deposited on the surface due to these impacts. These assumptions of the surface characteristic of these bodies where made long before the first space craft missions sent back detailed images of them. Comparing the description of the surfaces above to the photos in Figure 1.8 shows that these assumptions were not far from the true surface characteristic.

1.2.3 Asteroids

The Main belt of asteroids orbits between Mars and Jupiter and have a semi-major axis between 2.1 and 3.3 AU. In recent years several authors have begun to sort and classify these objects by their reflectance spectra (Bus & Binzel, 2002; Tholen, 1989; DeMeo et al., 2009). Figure 1.9 shows a summary of asteroid reflectance

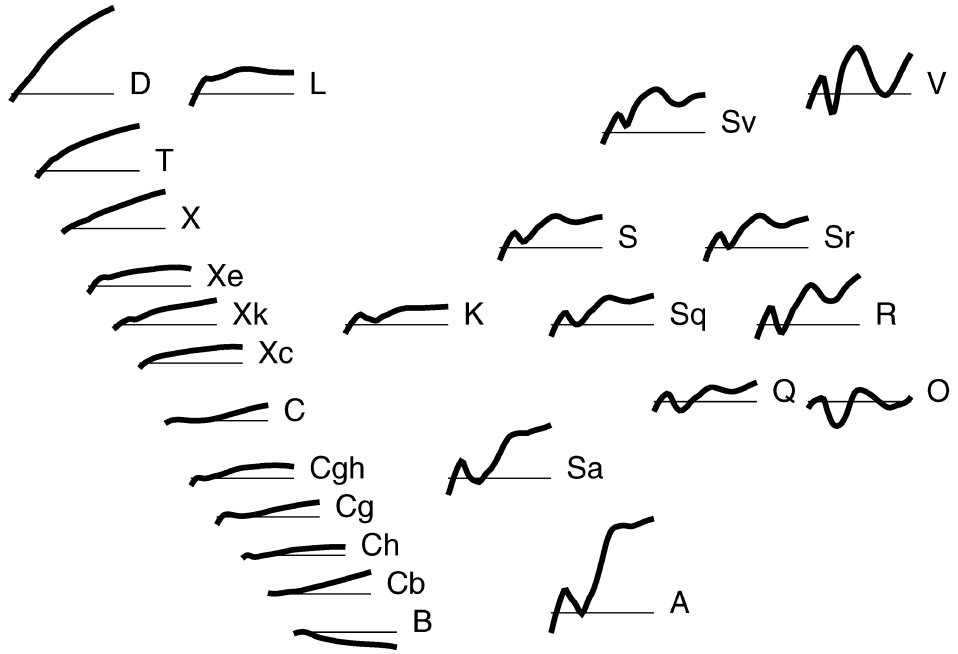

Figure 1.9: Summary of asteroid reflectance spectra as defined by the DeMeo et al. (2009) classification.

spectra of different spectra types using the DeMeo et al. (2009) class system and Table 1.1 gives an overview of the spectral features of each asteroid class (Cellino et al., 2002).

From the reflectance spectra only a few minerals are distinguishable namely; olivine, pyroxene, plagioclase, and water. The presence of metal can also be inferred from the spectral slope but can not be confirmed due to the lack of absorption features. However, the ability to link spectrally similar meteorite samples with asteroid spectra has led to a wealth of mineralogical information about asteroids. This in turn can give us clues to the conditions in the Solar nebula when these objects were formed. It should be noted that there are meteorite samples that have no asteroid analogue and vice versa. This is likely due to either space weathering changing the top most surface layer of the asteroid or the meteorite sample has undergone changes due to the large amount of heat and pressure it endures during entry into Earth's atmosphere.

Tholen Class	Bus Class	Albedo	Spectral Features
A	A	Moderate	Very steep red slope shortward of 0.75 μm; moderately deep absorption feature longward of 0.75 μm.
B, C, F, G	B, C, C_b, C_h, C_g, C_{hg}	Low	Linear, generally featureless spectra. Differences in UV absorption features and presence/absence of narrow absorption feature near 0.7 μm.
D	D	Low	Relatively featureless spectrum with very steep red slope.
E, M, P	X, X_c, X_e, X_k	From low (P) to very high (E)	Generally featureless spectrum with reddish slope; differences in subtle absorption features and/or spectral curvature and/or peak relative reflectance.
Q	Q	Moderate	Reddish slope shortward of 0.7 μm; deep, rounded absorption feature longward of 0.75 μm.
R	R	Moderate	Moderate reddish slope downward of 0.7 μm; deep absorption longward of 0.75 μm.
S	S, S_a, S_k, S_l, S_q, S_r	Moderate	Moderately steep reddish slope downward of 0.7 μm; moderate to steep absorption longward of 0.75 μm; peak of reflectance at 0.73 μm. Bus subgroups intermediate between S and A, K, L, Q, R classes.
T	T	Low	Moderately reddish shortward of 0.75 μm; flat afterward.
V	V	Moderate	Reddish shortward of 0.7 μm; extremely deep absorption longward of 0.75 μm.
—	K	Moderate	Moderately steep red slope shortward of 0.75 μm; smoothly angled maximum and flat to blueish longward of 0.75 μm, with little or no curvature.
—	L, L_d	Moderate	Very steep red slope shortward of 0.75 μm; flat longward of 0.75 μm; differences in peak level.
—	O	—	Peculiar trend, known so far only for asteroid 3628.

Table 1.1: Summary of asteroid spectral features for each taxonomic class (Cellino et al., 2002).

Polarimetry should also be able to detect differences between asteroids. The orbital parameters of the main belt asteroids yields access an observable phase-angle range of less than 30 degrees for ground based observations. Near Earth Asteroids (NEAs) by definition are bodies which have a perihelion distance ≤ 1.3 AU. Due to this closer orbital distance the observable phase angle range is much broader than for main-belt asteroids, and observations at phase angles as large as 100 degrees are feasible.

In the past 25 years approximately 200 main-belt asteroids and 15 near earth asteroids have been studied via polarimetric observations, some of the most recent have been carried by Gil-Hutton & Cañada-Assandri (2011, 2012); Cañada-Assandri et al. (2012); Belskaya et al. (2009a,b); Lupishko et al. (1995). The surface properties of asteroids are analysed by interpreting their polarisation phase curve relations. Specifically this analysis relies on the interpretation of 5 quantities:

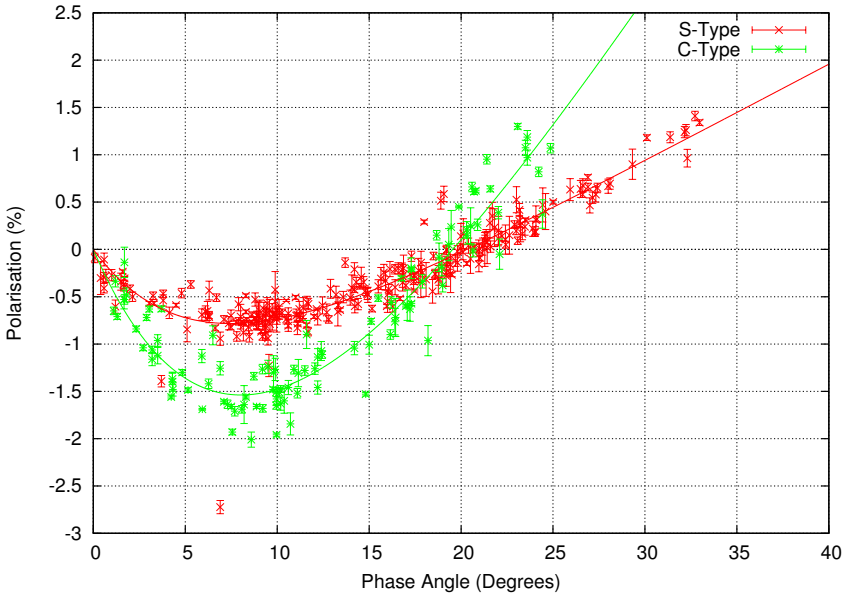

Figure 1.10: C-type and S-type asteroid phase curves.

- The value of the polarisation minimum $P_{\min}$.
- The phase angle at which the value of minimum polarisation occurs $\alpha_{\min}$.
- The phase angle at which the polarisation changes from a negative to a positive quantity α_{inv}.
- The value of the polarisation maximum $P_{\max}$.
- The phase angle when the value of maximum phase angle occurs $\alpha_{\max}$.

Since the observable phase-angle range for main belt asteroids is less than 30 degrees, we cannot determine the values of $P_{\max}$ or $\alpha_{\max}$, but it is generally possible for NEAs.

Polarimetric observations of asteroids are grouped together by their Bus & Binzel (2002) or Tholen (1989) taxonomy, for example C- and S- type asteroids as shown in Figure 1.10. These studies allow us to characterise the polarimetric curves (i.e., the fraction of linear polarisation as a function of phase angle) of different types of asteroids. Therefore, polarimetry allows us in principle to characterise asteroids,

even when no other information is available i.e. spectral information. We can do this kind of polarimetric classification by comparing the data of unclassified asteroids to polarimetric data of asteroids with an already known taxonomic class. Typically the comparison is done using a best fit of the known taxonomic class. The best fit used is a trigonometric function that was introduced by Lumme & Muinonen (1993) and outlined by Penttilä & Lumme (2005) and is defined as

$$P(\alpha) = b\,(\sin\alpha)^{c_1}\,[\cos(\alpha/2)]^{c_2}\sin(\alpha-\alpha_0) \tag{1.4}$$

where b, c_1, c_2, and α_0 are free parameters. Each of these four parameters has an affect on the shape of the fitted phase curve. The parameter b is mainly connected to the amplitude of polarisation with a physically acceptable range of values between 0 and 100. The parameter α_0 is the inversion angle where negative polarisation turns into positive polarisation. This parameter can range from between 0 and 180° but typically it will be less than 30°. The two powers c_1 and c_2 influence the shape of the phase curve. The parameter c_1 mainly affects the position of the minimum, while c_2 has an influence on the maximum and on the asymmetry of the curve. Both these parameters should have positive values. This equation can be used for extrapolation only within a phase angle range where well distributed data points are available.

The polarimetric phase curve can also be used to determine an estimate of the albedo, p_v, and hence give an estimation of its size. This is achieved by use of two empirical relations first put forward by Zellner & Gradie (1976). These empirical relations use two properties of the polarisation phase curve $P_{\min}$ and the slope h of the polarisation phase curve when the polarisation changes from negative to positive. These empirical relations have the form

$$\log p_v = C_1 \log(h) + C_2 \tag{1.5}$$

$$\log p_v = C_3 \log P_{\min} + C_4 \tag{1.6}$$

The four constants, C_1, C_2, C_3, C_4, in the above relations have been estimated by Lupishko et al. (1995), Cellino et al. (1999), Cellino et al. (2012), and Cellino

et al. (2015) by using albedo calculated from different minor planet surveys and comparing them to the polarimetric relation. Although this method of calculating the albedo can be effective, it still has a few problems. One of these problems is that the minor planet surveys used to calculate the constants in Equations 1.5 and 1.6 contain a low number of asteroids with sufficient data. This tends to make polarimetric derived albedos that are slightly higher than those calculated in the traditional way. The second relation that uses P_{min} above tends to display more scatter than the slope albedo relation when compared to the traditional methods of calculating the albedo. Another problem is that it is rather demanding in terms of the number of observations required. Since we need several observations over the course of a few months to gain access to different phase angles. However, the main problem is at low albedos the polarimetric phase relationship begins to break down. This can be clearly seen in Figure 1.11 when the best fit is constructed using asteroids with an albedo higher than 0.08. The so called "saturation" effect at low albedos is due to the reduced importance of multiple scattering between particles (Wolff, 1975).

Despite these issues, polarimetry remains a useful tool to estimate an asteroid's characteristics, in particular its classification, albedo, and size.

Polarimetric observations of NEAs not only help to characterize the surface properties of these objects, but also yield additional data on the phase curve of asteroids of the main belt at phase angles not observable from Earth. At present over 10,000 near Earth asteroids have been discovered but only 186 of these have had their taxonomic types designated. Again, observations of these objects can also help search for irregular behaviours which can be followed up with further observation to help understand their behaviour. These objects are also the subject of future sample return missions, and polarimetry can be a useful tool to help select these targets.

1.2.4 Centaurs

Centaurs are objects that exhibit behaviour similar to asteroids, and orbit the Sun between Jupiter and Neptune. These bodies have unstable orbits, in the sense that

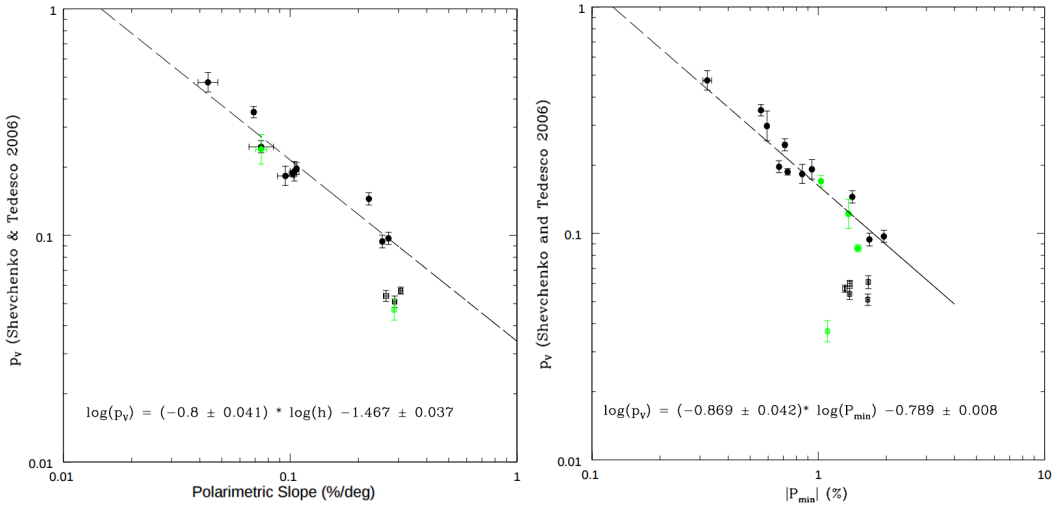

Figure 1.11: Left: The albedo-slope relation, in a log-log scale, for 15 asteroids from the list of Shevchenko & Tedesco (2006) for which the albedo is known. Right: The albedo-polarisation minimum relation, in a log-log scale, for 20 asteroids from the list of Shevchenko & Tedesco (2006) for which the albedo is known. Asteroids polarimetrically observed more than 10 times are marked with a black circles. Asteroids polarimetrically observed between 5 and 10 times are marked with green circles and are ignoring in the least-squares fitting. The best fit is constructed using asteroids whose albedo is greater than 0.08.

they are constantly under the influence of the giant planets of our Solar System and have very short dynamical life times.

For centaurs the observable phase-angle range is less than 5 degrees. This limited phase-angle range means that $\alpha_{\min}$ and $P_{\min}$ are possibly the only quantities we can use to compare them to other atmosphereless solar system bodies. However for some centaurs $\alpha_{\min}$ and $P_{\min}$ are likely to occur at phase angles higher than 5 degrees.

Chiron was the first centaur to be polarimetrically observed, by Bagnulo et al. (2006). Since then two other Centaurs, Pholus and Chariklo, have also had their polarimetric measurements investigated by Belskaya et al. (2010).

Chiron has been observed over its entire observable phase-angle range, allowing its polarisation phase curve to be fitted using the previously mentioned method, as shown in Figure 1.12(a). The study of Chiron represents a benchmark to which the other centaurs can be compared. Chirons polarisation phase curve itself differs from that of asteroids, and shows a polarisation minimum of -1.4 to -1.5 % at a

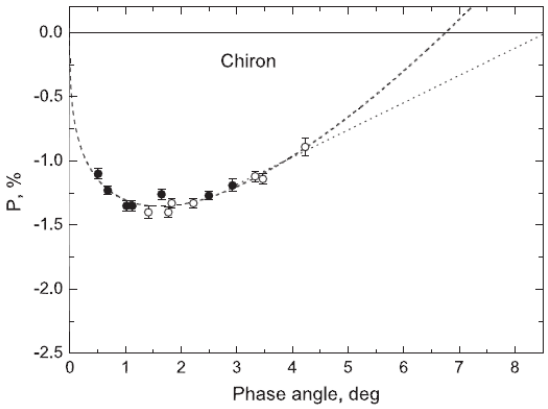

(a) Chiron

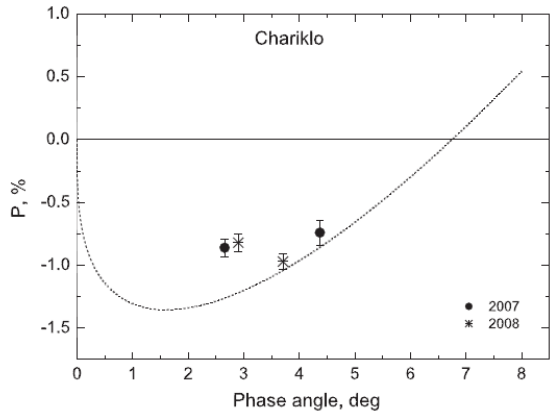

(b) Pholus

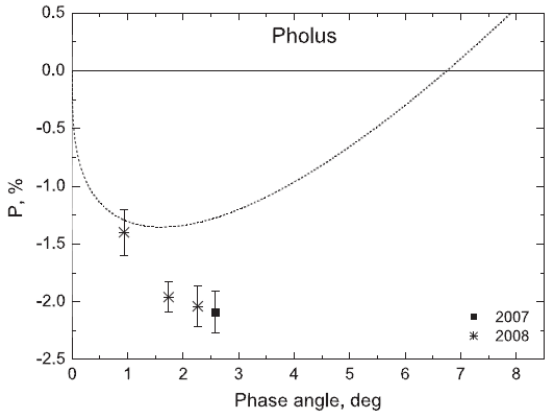

(c) Chariklo

Figure 1.12: Phase curves of the three different centaurs Chiron, Chariklo and Pholus and how they compare to Chiron. Figures taken from Belskaya et al. (2010).

phase angle less than 2 degrees.

Observations of Pholus and Chariklo both show a different behaviour, as shown in Figure 1.12(b) and 1.12(c). Pholus exhibits one of the most negative polarisation minimums of all Solar System bodies, much lower than that of Chiron, and with a much broader phase curve minimum. This suggests that Pholus has very different surface properties compared to Chiron.

Chariklo has a phase curve shallower than that of Chiron, but similar in terms of absolute polarisation, and it is comparable to an asteroid's phase curve. It is unclear what affect, if any, the recently discovered rings around Chariklo (Braga-Ribas et al., 2014) played in the amount of polarisation measured for Chariklo. The results for these three centaurs show how diverse the top most surface layer is for these objects. Also centaurs show a characteristic shift of α_{min} towards smaller angles compared to objects in the inner solar system. It has been suggested that a small amount of water frost covering a dark surface could be responsible for such behaviour.

1.2.5 Comets

Comets are icy bodies of the Solar System that can arguably sometimes be the most spectacular objects in the night sky, like Hale-Bopp's approach in 1997. These events occur when the comet gets close to the Sun and surface ices begin to sublime to form a coma and tail around the comet.

Unlike observations of many other objects of the Solar System, comets can be observed over a wide range of phase angles, typically between 0-150 degrees due to their orbital nature. This gives us a large phase angle range in which we can investigate different polarimetric behaviours. But unlike most asteroids, comets tend to become active when in close proximity to the Sun, so most polarimetric observations of comets refer to the active nucleus and the gas and dust cloud that forms around it, rather than simply from the nucleus surface itself. Only a few cometary nuclei have been studied polarimetrically, such as the Jupiter family comet 2P/Encke and the main belt comet 133P/Elst-Pizzaro (Boehnhardt et al., 2008) (Bagnulo et al., 2010).

When comets show activity, the light scattered from the cometary atmosphere

is the superposition of radiation scattered by the dust particles and that by the gaseous constituent. The scattering by dust and the resonance fluorescence from the most abundant cometary molecules CN, C_2, C_3 and NH_2 generally produce fundamentally different phase angle dependencies of their linear polarisation. Since molecular, ionic, and atomic emissions contribute to all parts of the cometary spectrum, it is often difficult to identify the uncontaminated continuum and its intrinsic polarisation. Solving this problem implies the need to perform spectropolarimetric observations with a high spectral resolution or, at least, simultaneous polarimetric and spectro-photometric observations to determine the level of gas contamination in the polarimetric results.

Over the observable phase-angle range, comets exhibit both negative and positive polarisation branches. The negative polarisation branch occurs between 0-25 degrees, and has a shape similar to that observed for asteroids. The positive branch of polarisation peaks at a phase angle of around 95 degrees. This is different to what is observed for asteroids (e.g., the polarimetric curves of S-type asteroids peak at 110 degrees, and those of E-type asteroids peak at 70 degrees). Furthermore, the degree of linear polarised light at these phase angles varies from comet to comet in such a way as to allow all comets to be placed into 2 groups:

- dust rich: these exhibit a strong continuum polarisation leading to an increase in the amount of observed linear polarisation.

- gas rich: these exhibit a strong contribution from molecular emissions and a relatively weak contribution from the continuum polarisation which leads to a much lower amount of observed linear polarisation.

The difference in these two groups is illustrated in Figure 1.13.

As previously mentioned, polarimetric observations of the nucleus of a comet are rare. For comet 2P/Encke, observations were carried out over a phase-angle range of 4-28 degrees, see Figure 1.14. From these observations, $P_{\min}$ could not be accurately determined, but the slope of the polarisation phase curve could be determined. By using the polarisation-albedo relationship for asteroids, an albedo of

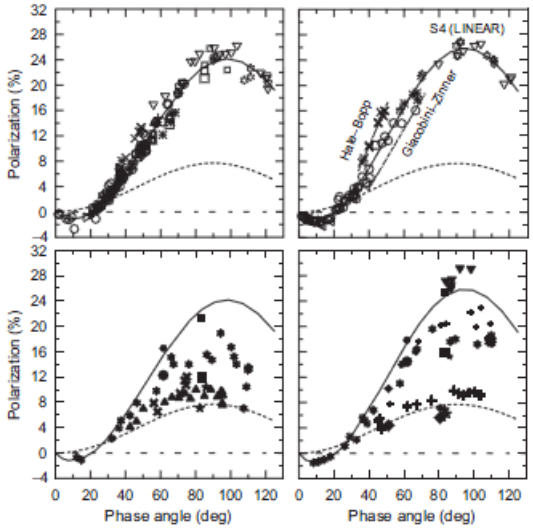

Figure 1.13: Upper panel shows dust rich comets while the lower panel shows gas rich comets. Figure taken from Mishchenko et al. (2011)

0.145 and 0.08 was calculated for 2P/Encke using the slope at polarisation inversion and the polarisation minimum respectively. These values are much higher than the albedo of 0.047 calculated from visible and thermal infra-red measurements (Lamy & Weaver, 2004). This suggests that the empirical relation for asteroids does not hold for cometary nuclei. This could be due to a different form of surface scattering involved in cometary nuclei than that found in asteroids.

The polarimetric phase curve of 2P/Encke does not fit any asteroid group well. The group with the most similar polarimetric characteristics is that of F-type asteroids, but even this differs in the fact that the angle of minimum polarisation is at least twice as large, and the polarisation slope is 3 times larger for F-type asteroids. Due to the phase-angle coverage, Encke can not easily be compared to other icy bodies such as Centaurs and TNOs (see Section 1.2.6). Centaurs would be the most appropriate objects for comparison, but even these objects do not have a polarimetric behaviour similar to that of 2P/Encke. This implies that the nucleus of 2P/Encke is unique when compared to other surface properties of objects in our Solar System. In conclusion, further polarimetric observations of cometary nuclei could yield useful results.

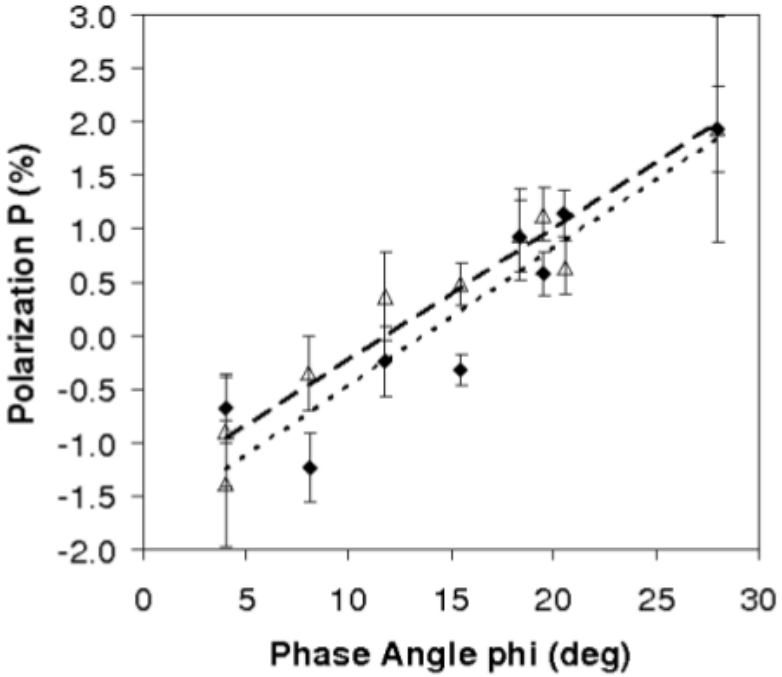

Figure 1.14: Linear polarisation of comet 2P/Encke versus phase angle. Filled triangles/squares = V/R filter measurements, long/short dash lines = linear fits to V/R filter measurements. Figure taken from Boehnhardt et al. (2008)

1.2.6 Trans-Neptunian Objects

Trans Neptunian objects (TNOs), as the name suggests are objects that orbit beyond Neptune at a heliocentric distance < 30 AU. Amongst the many thousands of TNOs there are a handful of large objects classified as dwarf planets.

Only around 10 of these large TNOs have been observed polarimetrically. Since these objects are some of the furthest known objects from the Sun, they have the smallest observable phase angle range of all Solar System bodies, typically less than 2 degrees. This prevents any albedo estimation from the observed polarimetric data due to the impossibility of being able to get enough data to see α_{min} and the slope h of the polarimetric curve. Nevertheless polarimetric observations can still provide some information on their surface properties. In fact, even with this very limited phase angle range TNOs can be separated into two distinct groups according to their polarisation-phase behaviour (Bagnulo et al., 2008). TNOs that show a large surge in polarisation with phase angle tend to have a diameter less than 1000 km. TNOs that show a small but constant negative polarisation with phase angle tend to

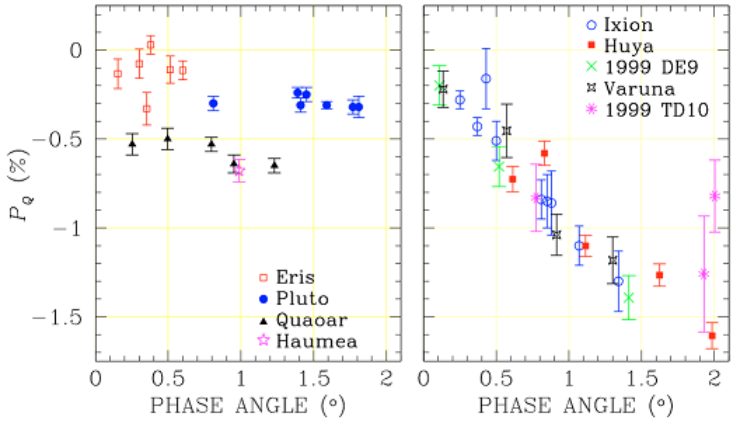

Figure 1.15: Polarimetric observations of large TNOs in the left panel and and small TNOs in the right panel. Figure taken from Bagnulo et al. (2008)

have a diameter greater than 1000 km. The difference in polarimetric behaviour of these two groups is illustrated in Figure 1.15.

Since all small TNOs show almost identical polarisation phase behaviour we can assume they all have very similar surface properties. Boehnhardt et al. (2004) completed an analysis of Ixion's surface properties which we can apply to all other small TNOs. In their analysis by taking parameters such as albedo, size, rotational variability and using a model developed by Muinonen (2004) the surface is thought to consists of a mixture of at least two non interacting compounds with different single scattering albedo and micro-porosity.

Similar modelling has been carried out for the large TNOs and they are believed to have similar surface properties yet they do not exhibit the same polarimetric behaviour. It is believed that the main difference in the polarimetric behaviour is due to large TNOs being able to retain their volatiles such as CO, N_2, CH_4 which would suppress the polarisation coming from the surface (Schaller & Brown, 2008).

To conclude, polarimetric analysis of objects can help yield useful information on the surface and atmospheric properties of a planet or small body of the Solar System. In certain cases polarimetry can provide useful information about surface characteristics of an object as in the case of NEA and TNOs. If we place all the observed polarimetric phase curves obtained for objects in our Solar System on

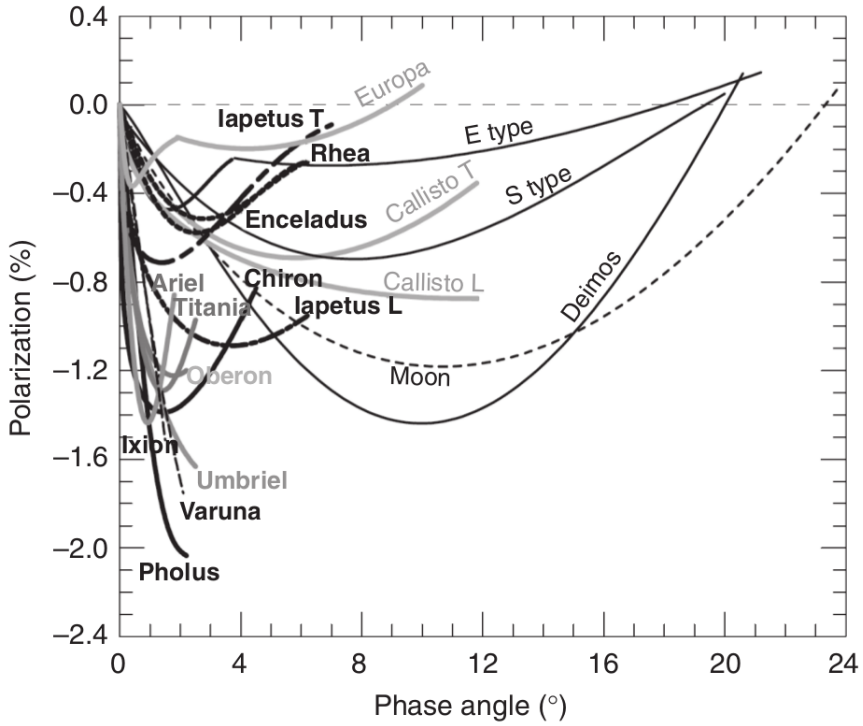

Figure 1.16: Phase curves of various Solar System bodies plotted together. Figure taken from (Kolokolova et al., 2015)

to one graph we can see how diverse and different these surfaces are (see Figure 1.16). This shows how polarimetry can help characterise these different surface properties from albedo, surface roughness and composition with the aid of computer simulations.

Even though many different types of Solar System bodies, asteroids, comets, TNOs etc, have been polarimetrically observed there are a few that have yet to be observed in great detail or have yet to have been studied polarimetrically at all.

One group of objects yet to be observed polarimetrically are the Trojan asteroids of Jupiter. These objects are of great interest in the study of Solar System dynamics as the theory of their origin within the L4 and L5 Lagrangian points is still open for debate. One theory to the origin of these objects is that they are linked to the growth and evolution of Jupiter. As Jupiter began to increase in mass from the accretion of matter, planetesimals where captured into the stable L4 and L5 Lagrangian points. This would mean that the Trojans represent material from

the middle of the Solar System nebula. Another theory to the origin of the Trojans is related to the so called "Nice model" where during planetary migration a large amount of objects from the Kuiper belt region were perturbed inward and a small portion of these were captured into the stable L4 and L5 Lagrangian points (Levison et al., 2009) (Morbidelli et al., 2005a). This would mean that the Trojans represent a repository of objects from the Kuiper belt region of our Solar System. This model of inward migration may help explain the spectral variability (Emery & Brown, 2004) caused by compositional differences shown in some Trojans and would suggest that they came from different regions of the Kuiper belt. As previously mentioned polarimetric observations are sensitive to the topmost surface structure and composition. This can help put constraints, for example, on whether the Trojans originated in the inner Solar System or were perturbed inward from the Kuiper belt region. Furthermore polarimetric observations combined with scattering models (see later) can help investigate the surface structure in a way that other techniques can't.

Another group of objects that require more study is that of comets at large heliocentric distances. Even though we have seen in Section 1.2.5 active comets have been well observed over a wide phase angle range, the main bulk of observational data at smaller phase angle ranges $\lesssim 20^{\circ}$ consists of well sampled data for comets 1P/Halley and Hale-Bopp. Very little polarimetric data is available for Jupiter Family Comets (JFCs) at small phase angles. From the database of comet polarimetry (Kiselev et al., 2006a) only comets 47P/AshbrookJackson (observations carried out by Jockers et al 1993, unpublished), 22P/Kopff (Myers, 1985), and 67P/ChuryumovGerasimenko (Myers & Nordsieck, 1984) have been observed within this phase angle range. However the measured Stokes parameters were only observed over a few values of phase angle. Almost all of these observations have been taken at heliocentric distances < 2 AU when comets become more active, and hence brighter meaning they are much easier to observe with small telescopes. Beyond this heliocentric distance they become much harder to observe and it becomes difficult to investigate the properties of the dust.

In addition to this, cometary nuclei remain unwilling to give up their secrets. Only since these objects have been observed by space telescopes, such as Spitzer space telescope and insitu measurements from flyby measurements from space craft such as, Vega 1 and 2, Giotto, Stardust, Deep Impact, Deep Space 1 and most recently Rosetta, has our understanding of these primitive bodies begun to move forward. These missions have allowed us not only to get the first resolved images of the surfaces of these bodies but also derive size, albedo, and constraints on the composition. The most interesting of these missions is the currently ongoing Rosetta mission. Not only did this mission orbit the comet through its perihelion approach but it has also deployed a lander called Philae that should give us the first insitu measurements of the surface composition, grain size and grain morphology. However Philae's acrobatic landing has left the mission's relative success in the balance. Even if Philae wakes up again and transmits information on the surface this will be the surface characteristics of one location on the surface of the nucleus on one comet. These results will not be ubiquitous to all comets but only a bench mark to compare other comets to. This brings us back to the usefulness of polarimetric observations; from these measurements we may only get global surface properties but be can directly compare these to other comets and to other objects in our Solar System.

In recent times Near Earth Asteroids have been increasingly in the news, first with the close approach of 2012 DA14 and then the completely unexpected arrival of the object close to Chelyabinsk. It is becoming increasingly more important to categorize these objects' composition and how large of a risk they pose if they were to hit Earth.

In this work I hope to help our understanding of some of these objects. In Chapter 2 I will briefly outline the mathematics of scattering and discuss some of the theoretical models used to interpret polarisation measured from Solar System bodies. In Chapter 3 I discuss the components that make up a polarimeter, instruments I have used and observing techniques employed for polarimetric observations. In Chapter 4 I discuss in detail the data reduction techniques used throughout

this thesis and the importance of accurately determining the background sky level when calculating the polarisation of a Solar System object.In the remaining chapters I discuss the observations and results obtained during my thesis. In Chapter 5 I present the results of new polarimetric observations of Barbarian asteroids, Trojan asteroids of Jupiter and Trans-neptunian objects. In Chapter 6 I present the first polarimetric observations of Jupiter family comets at large heliocentric distances and polarimetry taken at the time of the Deep Impact event. In Chapter 7 I discuss the results of two new polarimetric measurements of cometary nuclei and compare them to other bodies of the Solar System.

Chapter 2

Mathematical description and modelling of scattered light

The study of scattered light and its applications is a very important field of study. Without the theoretical interpretation of observational results it would be difficult to infer physical properties about the scattering media. In this chapter I will go through the mathematical definition of the Stokes parameters and the 4×4 Muller matrix, usually referred to as the scattering matrix, using a similar approach as in (Bohren & Huffman, 1998). The scattering matrix forms the bedrock on which all theoreticians base their models. In the final sections of this chapter I will outline how various models have been used to study the scattered light from a medium.

2.1 Mathematical description of scattering

The scattering of an electromagnetic wave by any system can be related to the heterogeneity of the system, be that on the scale of a single particle or a collection of many particles. Regardless of the heterogeneity of the system the underlying physics is the same. All matter is made up of a collection of discrete electric charges, namely electrons and protons. If an electron, atom, molecule, a solid or a liquid particle is illuminated by light, then the electric charges in that obstacle are set into oscillatory motion by the incoming electric field of the incident wave. These oscillating charges will then re-radiate electromagnetic radiation in all directions. It is this secondary radiation that is the scattered radiation light from the source.

$$\text{Scattering} = \text{excitation} + \text{re} - \text{radiation} \tag{2.1}$$

Additionally during the re-radiation of electromagnetic energy, the excited particle may transform a part of the energy into other forms, for example thermal energy. This process is known as absorption. Even though throughout this section we will only refer to scattering of light we also include absorption as well.

An electromagnetic wave is characterised by the electric field vector **E** and the magnetic field vector **H**. Both of these are perpendicular to each other and to the direction of propagation of the wave. However, when discussing polarisation we tend to only refer to the electric field vector of the incident and scattered radiation.

We consider a simple electromagnetic wave propagating in the z direction. According to Maxwell's equations the electric field vector resides in the xy plane so that we can describe it in the form of its parallel $E_{\parallel}$ and perpendicular $E_{\perp}$ components

$$E_{\parallel} = a_{\parallel}\exp\left(-i\delta_{\parallel}\right)\exp\left(-ikz + i\omega t\right) \tag{2.2}$$

$$E_{\perp} = a_{\perp}\exp\left(-i\delta_{\perp}\right)\exp\left(-ikz + i\omega t\right) \tag{2.3}$$

where $a_{\parallel}$ and $a_{\perp}$ are the amplitude of the parallel and perpendicular components respectively, $\delta_{\parallel}$ and $\delta_{\perp}$ are the positive of the parallel and perpendicular components, k is the wave constant $k = 2\pi/\lambda$, ω is the angular frequency and t is time.

If we consider only the real parts of the equation above it can be re-written in the cosine form

$$E_{\parallel} = a_{\parallel}\cos\left(\zeta + \delta_{\parallel}\right) \tag{2.4}$$

$$E_{\perp} = a_{\perp}\cos\left(\zeta + \delta_{\perp}\right) \tag{2.5}$$

where $\zeta = kz - \omega t$ and $\zeta + \delta$ is the phase of the wave.

Separating ζ and δ yields

$$\frac{E_{\parallel}}{a_{\parallel}} = \cos(\zeta)\cos\left(\delta_{\parallel}\right) - \sin(\zeta)\sin\left(\delta_{\parallel}\right) \tag{2.6}$$

$$\frac{E_{\perp}}{a_{\perp}} = \cos(\zeta)\cos(\delta_{\perp}) - \sin(\zeta)\sin(\delta_{\perp}) \tag{2.7}$$

with a little further mathematical manipulation we get

$$\left(\frac{E_{\parallel}}{a_{\parallel}}\right)^2 + \left(\frac{E_{\perp}}{a_{\perp}}\right)^2 - 2\frac{E_{\parallel}}{a_{\parallel}}\frac{E_{\perp}}{a_{\perp}}\cos(\delta) = \sin^2(\delta) \tag{2.8}$$

where $\delta = \delta_{\perp}$ - $\delta_{\parallel}$ and is the phase difference between the 2 components.

Equation 2.8 above represents an elliptically polarised wave, and can be used to specify all types of polarised light when δ meets certain criteria, for example if $\delta = m\pi$ where m =0,± 1,± 2, ... $sin(\delta) = 0$ and the equation becomes;

$$\left(\frac{E_{\parallel}}{a_{\parallel}} - \frac{E_{\perp}}{a_{\perp}}\right)^2 = 0 \Rightarrow \frac{E_{\parallel}}{a_{\parallel}} = \frac{E_{\perp}}{a_{\perp}} \tag{2.9}$$

This represents a linear polarised wave.

If δ = m $\frac{\pi}{2}$ where m= ± 1, ± 2, ... and $a_{\parallel} = a_{\perp} = a$ then the equation becomes

$$\left(\frac{E_{\parallel}}{a_{\parallel}}\right)^2 - \left(\frac{E_{\perp}}{a_{\perp}}\right)^2 = a^2 \tag{2.10}$$

and hence we have a circular polarised wave.

Even though parameters completely specify a monochromatic wave of a given frequency, they are not particularly helpful to understand the changes that light undergoes upon scattering. Also they are particularly difficult quantities to measure directly, and are not adaptable to a discussion of partially polarized light.

The parameters that are chosen for the discussion of polarised light are the so called Stokes parameters that we have briefly discussed in the previous chapter. These parameters are equivalent to the previous equations but are much more useful.

In the previous Chapter we mentioned that the polarisation state of an electromagnetic wave can be changed whenever something breaks the symmetry of the system, be it on reflection or transmission through a medium. An arbitrary

monochromatic wave may be treated as the superposition of two orthogonal components, for example horizontal and vertical or left handed and right handed etc. The splitting of terms into these components offers a way to analyse the properties of the light. We can use polarisers to allow only one of these components to be detected.

If we consider carrying out a few thought experiments on an arbitrary unpolarised monochromatic wave using suitable polarisers and a detector, we should be able to gain information about the properties of that light. We assume that the detector will respond to the irradiance of the incoming radiation independently of its polarisation state and the polarisers used are ideal and don't change the amplitude of the wave. As before we split the incoming radiation electric field vectors into two components which are orthogonal to each other $E_{\parallel}$ and $E_{\perp}$ so that

$$E = E_0 \exp(\mathrm{ikz} - \mathrm{i}\omega\mathrm{t}) \tag{2.11}$$

$$E_0 = E_{\parallel}\hat{e}_{\parallel} + E_{\perp}\hat{e}_{\perp} \tag{2.12}$$

$$E_{\parallel} = a_{\parallel}\exp\left(-\mathrm{i}\delta_{\parallel}\right) \tag{2.13}$$

$$E_{\perp} = a_{\perp}\exp(\mathrm{i}\delta_{\perp}) \tag{2.14}$$

where $\hat{e}_{\parallel}$ and $\hat{e}_{\perp}$ are the orthogonal axes in which the E-field is directed, i.e horizontally and vertically to the scattering plane.

If for the first experiment we allow the incident beam to go straight through and not interact with a polariser the detector would record the irradiance that would be simply the sum of the 2 components, $E_{\parallel}E_{\parallel}^{*} + E_{\perp}E_{\perp}^{*}$, where $E_{\parallel}^{*}$ and $E_{\perp}^{*}$ are the complex conjugates of $E_{\parallel}$ and $E_{\perp}$.

For the next experiment we allow the incident light to interact with a horizontal polariser (90°). This means the detector would only record the irradiance from the $E_{\parallel}$ component so the total detected irradiance I, would equal $E_{\parallel}E_{\parallel}^{*}$. Likewise if we used a vertical polariser the irradiance would be $E_{\perp}E_{\perp}^{*}$. So the difference between the two irridiances would be

$$I_{\parallel} - I_{\perp} = E_{\parallel}E_{\parallel}^{*} - E_{\perp}E_{\perp}^{*} \tag{2.15}$$

If the incident radiation was not polarised, both $I_{\parallel}$ and $I_{\perp}$ would be the same and hence give a zero value, however if either $I_{\parallel}$ or $I_{\perp}$ was greater than the other we could describe the incident light as being partially polarised.

For the next experiment we consider a polariser that only transmits light whose electric field vectors are aligned ± 45°. To make the mathematics more convenient we shall introduce a new set of perpendicular base vectors offset by 45° from the previous $\hat{e}_{\parallel}$ and $\hat{e}_{\perp}$ and we will call them $\hat{e}_{+}$ and $\hat{e}_{-}$ where

$$\hat{e}_{+} = \frac{1}{\sqrt{2}}\left(\hat{e}_{\parallel} + \hat{e}_{\perp}\right) \tag{2.16}$$

$$\hat{e}_{-} = \frac{1}{\sqrt{2}}\left(\hat{e}_{\parallel} - \hat{e}_{\perp}\right) \tag{2.17}$$

We may also rewrite the incident electric field E_0 defined in 2.12 as

$$E_0 = E_{+}\hat{e}_{+} + E_{-}\hat{e}_{-} \tag{2.18}$$

where

$$E_{+} = \frac{1}{\sqrt{2}}\left(E_{\parallel} + E_{\perp}\right) \tag{2.19}$$

$$E_{-} = \frac{1}{\sqrt{2}}\left(E_{\parallel} - E_{\perp}\right) \tag{2.20}$$

Now if we analyse the light which is transmitted through the polariser at +45° the irrdiance would be

$$I_{+} = \frac{\left(E_{\parallel}E_{\parallel}^{*} + E_{\parallel}E_{\perp}^{*} + E_{\perp}E_{\parallel}^{*} + E_{\perp}E_{\perp}^{*}\right)}{2} \tag{2.21}$$

Similarly for the polariser at −45°

$$I_{-} = \frac{\left(E_{\parallel}E_{\parallel}^{*} - E_{\parallel}E_{\perp}^{*} - E_{\perp}E_{\parallel}^{*} + E_{\perp}E_{\perp}^{*}\right)}{2} \tag{2.22}$$

Again the difference between these two irradiances would be

$$I_+ - I_- = E_\parallel E_\perp^* - E_\perp E_\parallel \tag{2.23}$$

As before if the indent light is unpolarised then I_+ would equal I_- and if either was greater than the other we would have partial linear polarisation.

For our final thought experiment we will use polarisers that only allow either left or right handed circularly polarized be transmitted. As in the previous experiment for convenience we introduce another set of orthogonal base vectors $\hat{e}_r$ and $\hat{e}_l$

$$\hat{e}_r = \frac{1}{\sqrt{2}}\left(\hat{e}_\parallel + i\hat{e}_\perp\right) \tag{2.24}$$

$$\hat{e}_- = \frac{1}{\sqrt{2}}\left(\hat{e}_\parallel - i\hat{e}_\perp\right) \tag{2.25}$$

These new base vectors represent right handed and left handed polarised light and are orthogonal so that

$$\hat{e}_r \bullet \hat{e}_r^* = 1,\ \hat{e}_l \bullet \hat{e}_l^* = 1,\ \hat{e}_r \bullet \hat{e}_l^* = 0 \tag{2.26}$$

The incident beam may be re-written as

$$E_R = \frac{1}{\sqrt{2}}\left(E_\parallel - iE_\perp\right) \tag{2.27}$$

$$E_L = \frac{1}{\sqrt{2}}\left(E_\parallel + iE_\perp\right) \tag{2.28}$$

If we use a polariser that only allows right handed polarised light to be transmitted, the irradiance the detector would record is

$$I_R = \frac{\left(E_\parallel E_\parallel^* - iE_\parallel^* E_\perp + iE_\parallel^* E_\perp + E_\perp E_\perp^*\right)}{2} \tag{2.29}$$

Similarly for the left handed polariser the irradiance would be

$$I_R = \frac{\left(E_\parallel E_\parallel^* + iE_\perp E_\parallel^* - iE_\parallel E_\perp^* + E_\perp E_\perp^*\right)}{2} \tag{2.30}$$

The difference between these two quantities would be

$$I_R - I_L = i\left(E_\perp^* E_\parallel - E_\parallel^* E_\perp\right) \tag{2.31}$$

Again if the light was unpolarised I_R and I_L would be equal to each other.

These four thought experiments give us four different quantities that we can use to define the polarisation of light, and these are referred to as Stokes parameters I, Q, U, and V. These parameters can be readily applied to the discussion of partially polarised light that can arise from scattering.

$$I = \left\langle E_\parallel E_\parallel^* + E_\perp E_\perp^* \right\rangle = a_\parallel^2 + a_\perp^2 \tag{2.32}$$

$$Q = \left\langle E_\parallel E_\parallel^* - E_\perp E_\perp^* \right\rangle = a_\parallel^2 - a_\perp^2 \tag{2.33}$$

$$U = \left\langle E_\parallel E_\perp^* + E_\perp E_\parallel^* \right\rangle = 2a_\parallel a_\perp \cos(\delta) \tag{2.34}$$

$$V = \left\langle i\left(E_\parallel E_\perp^* - E_\perp E_\parallel^*\right) \right\rangle = 2a_\parallel a_\perp \sin(\delta) \tag{2.35}$$

Where $\langle \cdots \rangle$ represents the time averaged irradiance collected by the detector.

2.1.1 Scattering by an arbitrary particle

In the previous section we have given a mathematical overview of how we can measure the various types of polarisation properties of light. Now we will look at the effect that an arbitrary particle has on an incident beam of radiation. If we consider an arbitrary particle, we can define the origin O, of a Cartesian co-ordinate system as any point on its surface. When the particle is illuminated by a beam of radiation we define the direction of propagation of this wave as the z-axis. As before we employ a set of orthonormal base vectors $\hat{e}_x$, $\hat{e}_y$, $\hat{e}_z$ which are the positive directions of the x, y, z axis. We also define the direction of scatter as $\hat{e}_r$. The positive direction $\hat{e}_z$ and the direction of scattering $\hat{e}_r$ define the scattering plane. The scattering plane is uniquely determined by the azimuthal angle ϕ. For a clearer

picture of the how the base vectors are aligned see Figure 2.1. As before we split the incident electric field E_i into its components parallel $E_{i\|}$ and perpendicular $E_{i\perp}$ to the scattering plane so that;

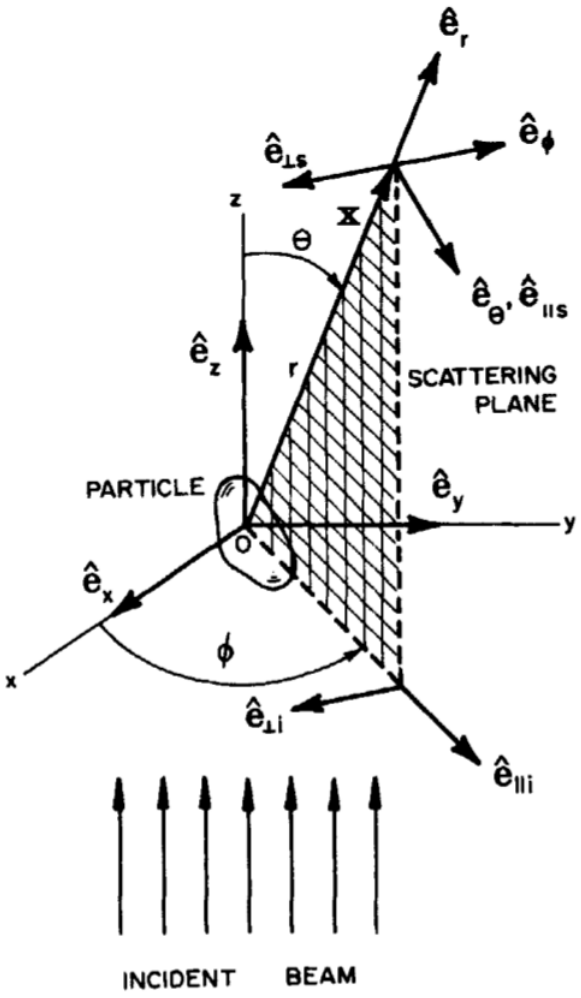

Figure 2.1: Diagram showing the base vectors and how the scattering plane is defined in the case of scattering from an arbitrary particle. Figure taken from (Bohren & Huffman, 1998)

$$E_i = \left(E_{0\|}\hat{e}_{\|i} + E_{0\perp}\hat{e}_{\perp i}\right)\exp\left(ikz - i\omega t\right) = \mathrm{E}_{\|i}\hat{\mathrm{e}}_{\|i} + \mathrm{E}_{\perp i} + \hat{\mathrm{e}}_{\perp i} \tag{2.36}$$

Where the base vectors

$$\hat{e}_{\|i} = \cos(\phi)\hat{\mathrm{e}}_{\mathrm{x}} - \sin(\phi)\hat{\mathrm{e}}_{\mathrm{y}} \tag{2.37}$$

$$\hat{e}_{\perp i} = \sin(\phi)\hat{\mathrm{e}}_{\mathrm{x}} - \cos(\phi)\hat{\mathrm{e}}_{\mathrm{y}} \tag{2.38}$$

and these form a right handed triad with $\hat{e}_z$ so that $\hat{e}_{\|i} \times \hat{e}_{\perp i} = \hat{e}_z$.

Also

$$\hat{e}_{\perp i} = -\hat{e}_\phi \hat{e}_{\|i} = \sin(\theta)\hat{\mathrm{e}}_r + \cos(\theta)\hat{\mathrm{e}}_r \tag{2.39}$$

where the base vectors $\hat{e}_r$, $\hat{e}_\theta$, $\hat{e}_\phi$ are associated with the spherical polar co-ordinates.

At sufficiently large distance from the origin ($kr \gg 1$) the scattering electric field E_s is approximately transverse ($\hat{e}_r \bullet E_s \simeq 0$) and has the asymptotic form (Jackson, 1975)

$$E_s \sim \frac{\exp(\mathrm{ikr})}{-ikr} A \qquad kr \gg 1 \tag{2.40}$$

where $\hat{e}_e \bullet A = 0$

Therefore the scattering field may be rewritten as

$$E_s = E_{\|s}\hat{e}_{\|s} + E_{\perp s}\hat{e}_{\perp s} \tag{2.41}$$

$$\hat{e}_{\|s} = \hat{e}_\theta \qquad \hat{e}_{\perp s} = -\hat{e}_\phi \qquad \hat{e}_{\perp s} \times \hat{e}_{\|s} = \hat{e}_r \tag{2.42}$$

where the base vectors $\hat{e}_{\|s}$ and $\hat{e}_{\perp s}$ are parallel and perpendicular respectively. The relation between incident and scattered waves can be written in the matrix form.

$$\begin{pmatrix} E_{\|s} \\ E_{\perp s} \end{pmatrix} = \frac{\exp(}{-ikr} \begin{pmatrix} S_2 & S_3 \\ S_4 & S_1 \end{pmatrix} \begin{pmatrix} E_{\|i} \\ E_{\perp i} \end{pmatrix} \tag{2.43}$$

The elements S_1, S_2, S_3 and S_4 form the amplitude scattering matrix and depend in general on θ, the scattering angle, and the azimuthal angle ϕ. Rarely are all these elements of this matrix measured as to do so requires measuring the amplitude and phase of the light scattering in all directions.

Once we have obtained the electromagnetic field scattering by the particle we can determine the Poynting vector at any point. The time averaged Poynting vector **S** at any point can be described as the sum of 3 terms

$$S = \frac{1}{2} Re(E \times H^*) = S_i + S_s + S_{ext} \tag{2.44}$$

$$\tag{2.45}$$

where S_i, S_s and S_{ext} are

$$S_i = \frac{1}{2} Re\left(E_i \times H_i^*\right) \tag{2.46}$$

$$S_s = \frac{1}{2} Re(E_s \times H_s^*) \tag{2.47}$$

$$S_{ext} = \frac{1}{2} Re\left(E_i \times H_s^* + E_s \times H_i^*\right) \tag{2.48}$$

where $Re(\cdots)$ signifies the real part and * signifies the complex conjugate.

S_i is the Poynting vector associated with the incident beam and is independent of the position, if the medium is non-absorbing, S_s is the Poynting vector of the scattered field, s_{ext} is the Poynting vector of the extinction and can be interpreted as being the interaction between scattered and incident waves.

If we now place a detector at a distance r from the particle, with a surface area ΔA aligned normal to $\hat{e}_r$, the scattering direction, the detector should record a signal proportional to $S_s \bullet \hat{e}_r \Delta A$. The detector should only record the scattered light provided the detector doesn't see the source of the radiation. From Equation 2.40, 2.46, 2.47 and 2.48 the detector should measure

$$S_s \bullet \hat{e}_r \Delta A = \frac{k}{2\omega\mu} \frac{|A|^2}{k^2} \Delta\Omega \tag{2.49}$$

where $\Delta\Omega = \Delta A / r^2$ is the solid angle subtended by the detector.

By using suitable polarisers between the particle and the detector we can record the irradiances and hence record the four Stokes parameters of light scattered by an arbitrary particle.

$$I_s = \left\langle E_{\parallel s} E^*_{\parallel s} + E_{\perp s} E^*_{\perp s} \right\rangle \tag{2.50}$$

$$Q_s = \left\langle E_{\parallel s} E^*_{\parallel s} - E_{\perp s} E^*_{\perp s} \right\rangle \tag{2.51}$$

$$U_s = \left\langle E_{\parallel s} E^*_{\perp s} + E_{\perp s} E^*_{\parallel s} \right\rangle \tag{2.52}$$

$$V_s = \left\langle i\left(E_{\parallel s} E^*_{\perp s} - E_{\perp s} E^*_{\parallel s}\right) \right\rangle \tag{2.53}$$

The relation between the incident and scattered stokes parameters follows that of the amplitude matrix

$$\begin{pmatrix} I_s \\ Q_s \\ U_s \\ V_s \end{pmatrix} = \frac{1}{k^2 r^2} \begin{pmatrix} S_{11} & S_{12} & S_{13} & S_{14} \\ S_{21} & S_{22} & S_{23} & S_{24} \\ S_{31} & S_{32} & S_{33} & S_{34} \\ S_{41} & S_{42} & S_{43} & S_{44} \end{pmatrix} \begin{pmatrix} I_i \\ Q_i \\ U_i \\ V_i \end{pmatrix} \tag{2.54}$$

This 4×4 matrix above is often referred to as the Scattering Matrix and is also sometimes referred to as the "Muller Matrix" when referring to the scattering of a single particle. Each one of these 16 matrix elements contained within the scattering matrix is an angle dependent function of wavelength, particle size, shape and composition. There is a great deal of information contained within the scattering matrix and only recently have all the elements been fully investigated. In general there are 16 non zero independent matrix elements although this number can be reduced by symmetry. The scattering matrix above has been defined for a single particle but it can also be applied to many separate particles as Stokes parameters for a collection of particles is simply the sum of the Stokes parameters for the individual particles, so the scattering matrix for a collection of particles is simply the sum of the individual scattering matrices. In the following section we will look at the different approaches to model the scattering from a particle or collection of particles by solving the various elements within the scattering matrix.

2.1.2 Modelling of scattered light

A nice analogy appears in the text book by Bohren & Huffman (1998) that describes the difficultly of modelling the observed scattered light. We take it that there are two

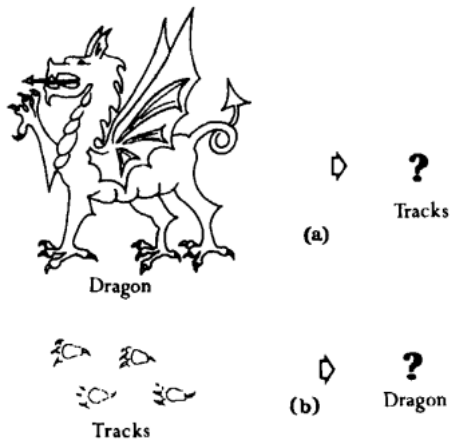

Figure 2.2: Analogous view of the difficulty modelling scattered light to determine what caused the scattering event. Figure taken from (Bohren & Huffman, 1998)

general classes of problems when it comes to modelling scattered light and these are the direct and the indirect problem. The direct problem would be; for a given particle of known shape, size and composition which is illuminated by a known irradiance, polarisation and frequency of electromagnetic radiation, determining the scattered electric field everywhere. This is the so called "easy" problem where all the incident parameters are known and is analogous to, given a dragon to study, determining the tracks it would leave behind, (see Figure 2.2). The inverse problem is to describe the particle or collection of particles responsible for the scattering given the scattered field. This is the "difficult" problem due to the many unknown aspects there are to calculate and is analogous to describe what the dragon looked like given the tracks left behind, (see Figure 2.2). As is usually the way in life the inverse or difficult problem is what interests us most. In recent years our understanding of light scattering methods has greatly increased. The most probable reason for this is the steady increase in computer processing power, speed and relative ease of access to them. Another reason is the increase in the accuracy of models over the past few years. As mentioned previously there is a large amount of information contained within the 16 matrix elements of the scattering matrix, such that any one of these elements can be related to an unknown physical quantity as a function of the scattering angle. Before any light scattering results for any object can be calculated a

preliminary choice of the object's morphology must be made. Is the particle of a known shape like a sphere or does it have to be modelled as well? Furthermore given the shape of the object one must then ask the question is the object solid or of a particulate nature? For a particulate material there are extra parameters that have to be considered, like size shape and packing density, that again have to be known or varied within the model. It can be seen from these small considerations why the modelling of scattered light can be quite a complicated and lengthy process. There are several models that can be used to model the observations of scattered light but the main three used are the T-matrix (Waterman, 1971), Discrete Dipole Approximations (DDA) (Purcell & Pennypacker, 1973), and the Radiative Transfer and Coherent Backscattering (RT-CB) approach (Muinonen et al., 2002a).

2.1.3 T-matrix

The T-Matrix method was first presented by Waterman in 1971 as a numerically exact technique by adapting the concept of Mie theory by expanding all the fields into Vector Spherical Wave Functions (VSWF). The framework of the T-matrix approach stems from our previous definition of the amplitude scattering matrix. In this instance the incident and scattered fields are expressed in terms of VSWF M_{mn} and N_{mn};

$$E_{inc} = \sum_{n=1}^{\infty} \sum_{m=-n}^{n} [a_{mn} RgM_{mn}(kR) + b_{mn} RGN_{mn}(kR)] \tag{2.55}$$

$$E_{sca} = \sum_{n=1}^{\infty} \sum_{m=-n}^{n} [ap_{mn} M_{mn}(kR) + q_{mn} N_{mn}(kR)], \;\; R > R_{>} \tag{2.56}$$

where $R_{>}$ is the radius of the smallest circumscribing sphere of the scatterer centred at the origin of the coordinate system. The mathematical properties of the two VSWF's above are well known. The functions RgM_{mn} and RgN_{mn} are finite at the origin, while the use of the outgoing functions M_{mn} and N_{mn} in the above equation ensures that the transverse component of the scattered electric field decays as $1/R$, whereas the radial component decays much faster than $1/R$ with $R \to \infty$. The expansion coefficients of the incident plane wave are given by simple analytical expressions. Due to the linearity of Maxwell's equations and the constitutive relations,

the relation between the scattered field expansion coefficients p_{mn} and q_{mn} on the one hand and the incident field expansion coefficients a_{mn} and b_{mn} on the other must be linear and is given by the transition matrix T as follows

$$p_{mn} = \sum_{n'=1}^{\infty} \sum_{m'=-n'}^{n} (T^{11}_{mnm'n'} a_{m'n'} + T^{12}_{mnm'n'} b_{m'n'}) \tag{2.57}$$

$$q_{mn} = \sum_{n'=1}^{\infty} \sum_{m'=-n'}^{n} (T^{21}_{mnm'n'} a_{m'n'} + T^{22}_{mnm'n'} b_{m'n'}) \tag{2.58}$$

In compact notation these can be written in the form

$$\begin{bmatrix} p \\ q \end{bmatrix} = T \begin{bmatrix} a \\ b \end{bmatrix} = \begin{bmatrix} T^{11} & T^{12} \\ T^{21} & T^{22} \end{bmatrix} \begin{bmatrix} a \\ b \end{bmatrix} \tag{2.59}$$

The above equation is the cornerstone of the T-matrix formulation. For a complete derivation and review of the T-matrix method see Mishchenko et al. (1996a). If the T-Matrix is known then you can find the scattered field everywhere outside the smallest circumscribing sphere of the the object.

A fundamental feature of the T-matrix method is that the T-matrix depends only on the physical and geometrical characteristics of the scattering particle. Therefore the model only depends on the particle size, shape, refractive index and orientation to the reference direction but it is completely independent of the propagation direction and polarisation state of the incident radiation. This means that the T-matrix needs only to be calculated once and then can be used in calculations for any direction of incidence and scattering and for any polarisation state of the incident field.

The Waterman T-matrix was later improved by Mishchenko et al. (1996b) to drastically increase the computational speed and the applicability of the approach. These improvements have added to the popularity of the T-matrix approach and made a very powerful and efficient numerical technique.

Since the Mischenko formulation approach is a publicly available model it has been used in many applications from the modelling of cell nuclei to aerosols in the atmosphere to cometary particles. It also remains a bench mark test to determine the

accuracy of other models that try to use different approaches to model the scattering of particles.

2.1.4 Discrete Dipole Approximation

The DDA approach is a general method to model the scattering and absorption of electromagnetic waves by particles of arbitrary geometry and composition. Purcell & Pennypacker (1973) initially proposed the idea of replacing the scatterer with a series of point sized dipoles to aid in their study of interstellar dust grains. These dipoles will interact with each other and the incident electric field giving rise to a set of linear equations, which can be solved to calculate the scattering matrices as well as scattering, absorption and extinction cross sections for a given problem. It was later shown that this method of using point dipoles could be derived from the integral equation for the electric field when the scatterer is divided up into small discrete sub-volumes. This approach is known as the Volume Integral Equation Method (VIEM). Both approaches give the same result but the interaction with dipoles helps to give a physically clear view whereas the VIEM gives insight to the mathematical approximation and ability to further improve the method (Lakhtakia & Mulholland, 1993).

DDA's popularity grew when Draine and co-workers developed a publicly available computer code DDSCAT (Draine & Flatau, 2008). Since then many different research groups have implemented their own DDA some of which are publicly or commercially available. These codes all have their unique features based on accuracy and speed. For a review of these different codes see Penttilä et al. (2007). The DDA model is typically associated with looking at the scattering from dust grains, for example those in the interstellar medium or from cometary dust. The main reason for this is the ability to shape the collection of dipoles into irregular shaped particles such that they become an accurate representation of the shape of the actual particle as shown in Figure 2.3 (Zubko et al., 2005). This greatly increases the accuracy of the model when comparing it to observational data.

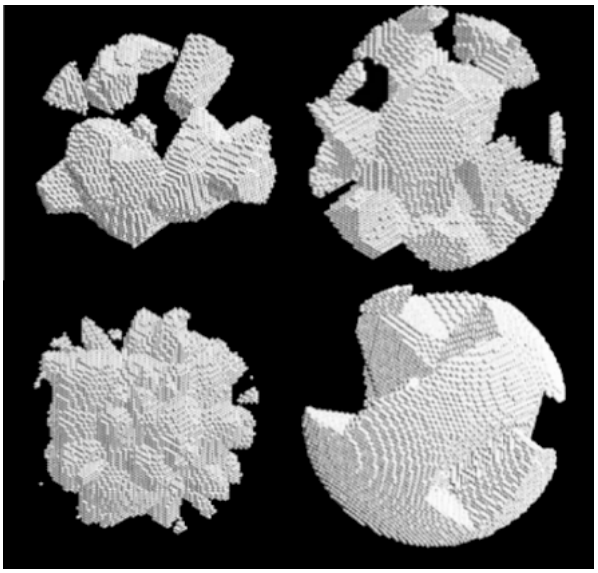

Figure 2.3: Examples of how DDA can be used to mimic different types of scatterer. Figures taken from Zubko et al. (2005)

2.1.5 Radiative Transfer & Coherent Backscattering

Unlike the other two models discussed that focus on solving the scattering mechanism for a single or collection of particles, the RT-CB approach tries to model the scattering for regolithic surfaces of atmospheric-less bodies. The scattering of electromagnetic waves by such a complex media is dictated by the macroscopic Maxwell equations. These equations need to be solved in order to successfully model the observational polarisation of an atmosphericless body. However, to solve such equations by direct computational modelling of electromagnetic scattering by such a surface is impractical even today. This means that some approximations have to be considered.

For many years one such approach used was the Radiative Transfer method (RT). The RT method does an adequate job of describing the diffuse multiscattering of light by many particle objects. However there are some features that are observed that RT alone can't explain. So recently RT theory has been paired up with the Coherent Backscattering mechanism (CB) to aid in the explanation of some of these features. One of these features that CB has been suggested to have an effect on is a narrow peak in brightness centred at the exact backscattering direction. An-

other feature that CB is thought to play a role in is a negative polarisation branch at small phase angles which, according to more recent observations by Rosenbush & Mishchenko (2011) can be accompanied by an extremely narrow and sharp minimum at phase angles approaching zero.

The RT-CB method developed by Karri Muinonen and co-workers is based on the Monte Carlo integration of the ladder and cyclical diagrams (Muinonen, 2004) pertaining to an imaginary spherical volume of radius R, that contains many identical non overlapping spherical particles of radius r. The size parameter of the volume is kR, and the particle size parameter is kr, where k is the wave number in the homogeneous media.

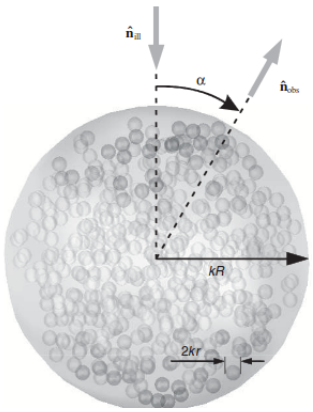

Figure 2.4: The imaginary spherical volume which is randomly filled with small spherical scatterers.

During the Monte Carlo integration the CB part of the approach is calculated alongside the RT method by incorporating the reciprocity relation in the electromagnetic scattering and keeping the relative phase information of the wave components. The concept of ladder and cylindrical diagrams is most conveniently introduced in the framework of the so called Foldy-Lax equations. These equations describe the electromagnetic scattering by a group of N discrete, arbitrary particles and is mathematically equivalent to the macroscopic Maxwell equations (Mishchenko et al., 2011). The Foldy-lax equations allow you to split the total electric field **E**, and the magnetic field **H**, at an observation point **r**, into the respective incident fields and individual particle contributions. This means the observed **E** and **H** field is

the summation of the incident field and the individual contributions of the scattering particles. The essence of the ladder diagram is to make sure that when the incident electromagnetic wave interacts with a sequence of spherical particles, the electric and magnetic fields both interact with same common group of particles. If they don't interact with the same common particles then these are ignored for the contribution at the observation point. The cylindrical diagrams composed of such conjugate multi-particle sequences usually provide little contribution to the scattering intensity but they do cause a significant CB effect when in the vicinity of the back scattering direction($\hat{n}_{obs} = -\hat{n}_{ill}$), see Figure 2.5. The phase difference between these conjugate multi-particle paths disappears and the result is constructive interference which produces an intense peak in intensity.

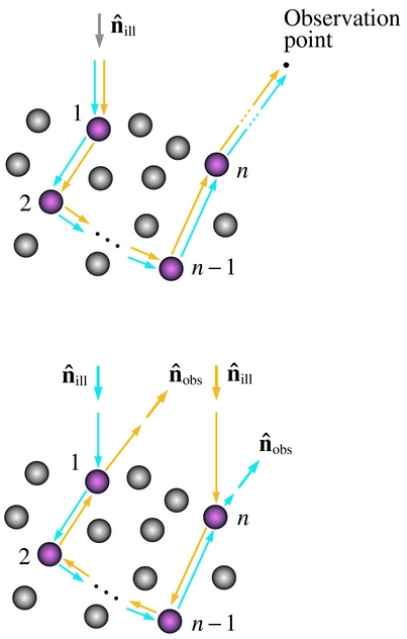

Figure 2.5: Example of a simple ladder diagram, upper panel, and a cylindrical diagram, lower panel. Blue arrows represent the direction of the magnetic field interactions and the yellow arrows represent the direction of the electric field interactions.

The two coherent backscattering phenomena previously mentioned have been verified numerically for the approach outlined in the previous paragraph and using the exact superposition T-matrix (Muinonen, 2004; Muinonen et al., 2012). This verification means that it is possible to develop models that utilize the sparse media

approach in RT-CB to describe the scattering characteristics of a densely packed medium like a planetary regolith.

More recently the RT-CB model has been further simplified to utilize the double Henyey-Greenstein function for the scattering phase function so that the computations are more transparent to the user (Muinonen & Videen, 2012).

$$P_\theta \propto P_{11}(\theta)[w_+\mathbf{M}_+(\theta) + w_-\mathbf{M}_-(\theta)] \tag{2.60}$$

$$w_+ = \frac{1}{2}(1 + P_{max}) \tag{2.61}$$

$$w_- = \frac{1}{2}(1 - P_{max}) \tag{2.62}$$

Where $\mathbf{M}_+$ and $\mathbf{M}_-$ are the scattering matrices of the modified electric-dipole and magnetic dipole respectively. w_+ and w_- are the normalised weights for the electric-dipole and magnetic-dipole. $P_{11}(\theta)$ is defined as the double Henyey-Greenstein function below;

$$P_{11} = w\frac{1 - g_1^2}{(1 + g_1^2 - 2g_1 cos\theta)^{\frac{3}{2}}} + (1 - w)\frac{1 - g_1^2}{(1 + g_1^2 - 2g_1 cos\theta)^{\frac{3}{2}}} \tag{2.63}$$

$$g = wg_1 + (1 - w)g_2 \tag{2.64}$$

$$w = \frac{g - g_2}{g_1 - g_2} \tag{2.65}$$

In the above equation w is the normalized weight of the first Henyey-Greenstein function, g is the total asymmetry parameter for the full double Henyey-Greenstien function, g_1 and g_2 are the forward and backward asymmetries, the parameter P_{max} is the maximum polarisation the scatterer would exhibit at a phase angle of 90 degrees. A factor not in any of the equations above is $\tilde{\omega}$, this is an additional free parameter in the model that represents the absorption of the incoming scatterers. Another factor that doesn't appear in the equations above is the distance between the constituent particles inside the scattering medium, the mean free path kl. This means that single scattering is described by 6 quantities, $\tilde{\omega}$, kl, g, g_1, g_2, and P_{max}.

In the forthcoming Figures I will show the effect that changing some of these parameters has on the resulting modelled polarisation phase curve. For all the graphs relating to the output of the model the y axis $-P_{21}/P_{11}$ corresponds to the matrix element that is responsible for Stokes Q, and the x axis is the phase angle. The input parameters that are not being varied have the fixed values of; $\tilde{\omega}$ = 0.5, kl = 60, g = 0.4, g_1 = 0.8, g_2 = -0.1 and P_{max} = 0.8.

In Figure 2.6 we see the effect that the number of incident photons has on the model's output when all other parameters are held constant. Even though this parameter is not related to the theory that the RT-CB model is based on it does have a large effect on the quality of the resulting polarisation phase angle relation. From Figure 2.6 it can be seen that with very low number of incident photons there are a lot of noise features on the curves which are purely caused by poor statistical averaging. As the numbers of photons increase these features begin to disappear. Like any computational model one would ideally like to have a very high or an infinite number of incoming photons but this not feasible due to time required to compute the final result. So in this respect a compromise between accuracy and time has to be made and typically the number of photons chosen is 200,000. Even though from Figure 2.6 it could argued that 50,000 photons is enough to obtain reasonable accuracy we shall see in the coming graphs that using this number of photons isn't enough as other parameters change.

In Figure 2.7 we allow the mean free path to change and we hold all other parameters constant. Firstly we can see that by increasing this factor increases the jaggedness of the graph indicating for high mean free paths we require more incident photons than the 50,000 used. The increase in mean free path also has the effect of moving the polarisation minimum to smaller phase angles and causes it to become quite acute in nature. This would indicate that this parameter has an effect on the CB mechanism within the model.

In Figure 2.8 we allow the polarisation maximum to change and we hold all the other parameters constant. By increasing this parameter the only major change is the increase in the absolute polarisation outputted to the model, i.e both amounts

of positive and negative polarisation increases. This is not surprising as the polarisation maximum controls the weighting of the double Hanyey-Greestein function.

In Figure 2.9 we allow the single scattering albedo to change and we hold all the other parameters constant. By increasing this parameter we can see two effects. The first is an increase in polarisation minimum observed as the albedo gets larger. The second is a slight decrease in the phase angle at which this polarisation minimum occurs. This again suggests that this parameter has an effect on the level the CB mechanism plays within the model.

Although this approach is still in its infancy compared to the other 2 models mentioned, it does show a lot of promise for future modelling of planetary regoliths.

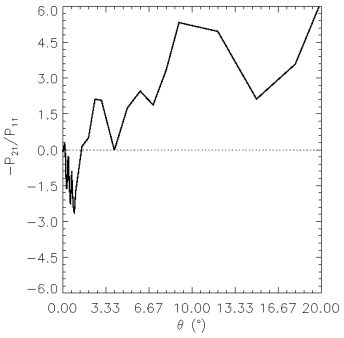

(a) Number of photons = 100

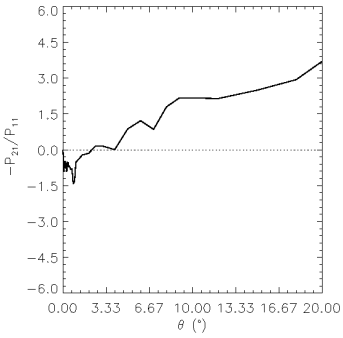

(b) Number of photons = 500

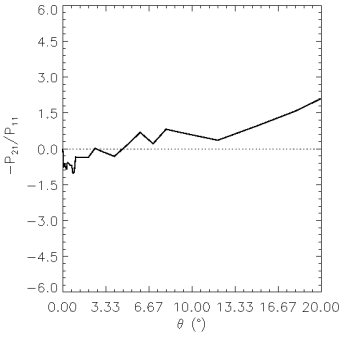

(c) Number of photons = 1000

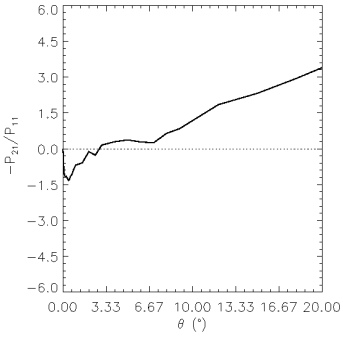

(d) Number of photons = 10,000

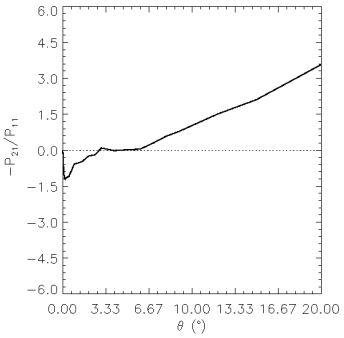

(e) Number of photons = 50,000

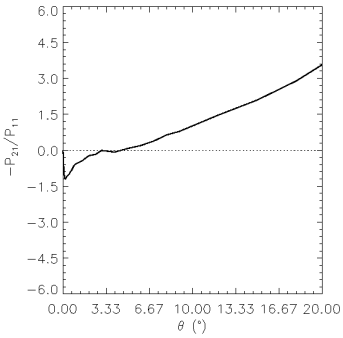

(f) Number of photons = 100,000

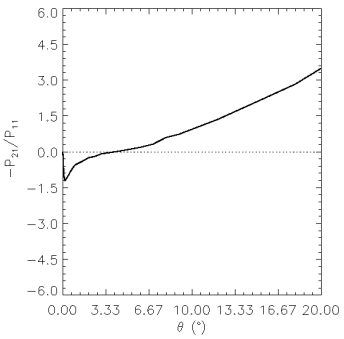

(g) Number of photons = 200,000

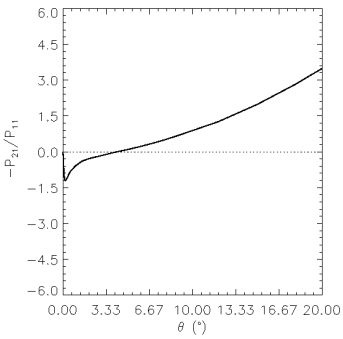

(h) Number of photons = 1,000,000

Figure 2.6: Variations on the output from the RT-CB code with increasing number of incident photons.

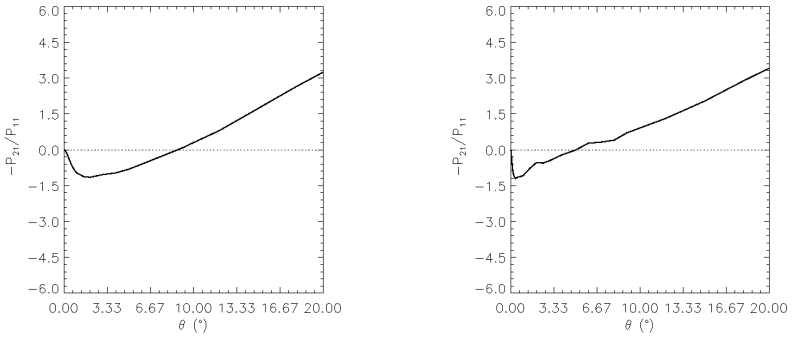

(a) kl = 10

(b) kl = 50

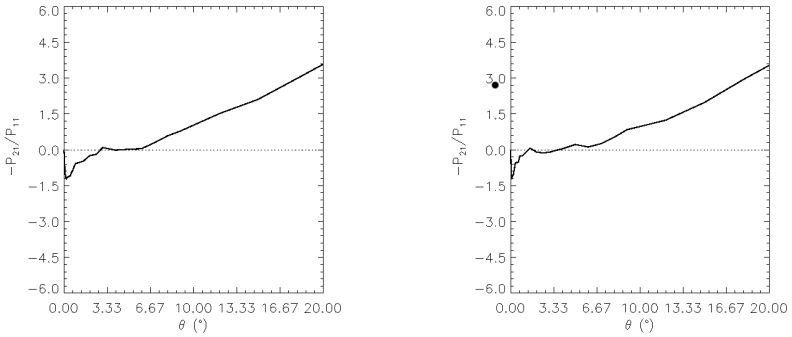

(c) kl = 100

(d) kl = 250

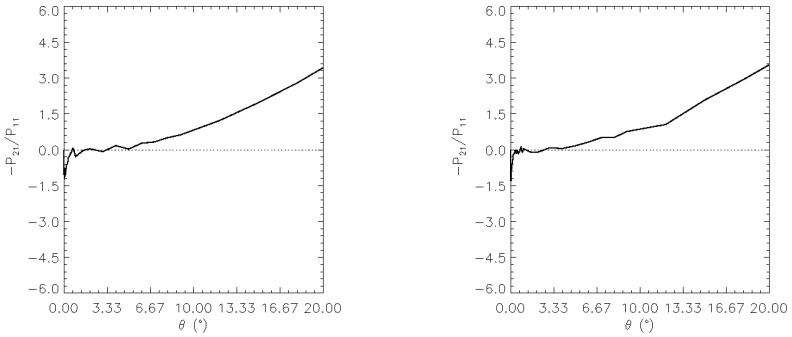

(e) kl = 500

(f) kl = 1000

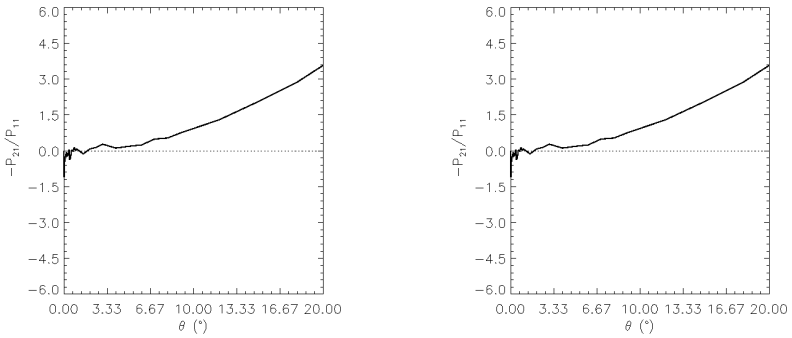

(g) kl = 2000

(h) kl = 3000

Figure 2.7: Variations on the output from the RT-CB code with increasing mean free path.

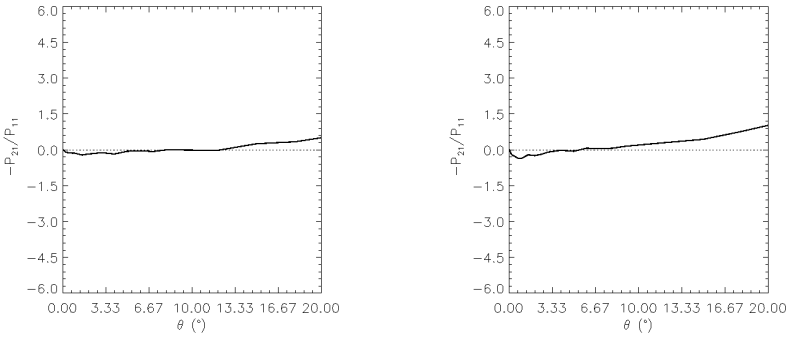

(a) $P_{max} = 0.1$

(b) $P_{max} = 0.2$

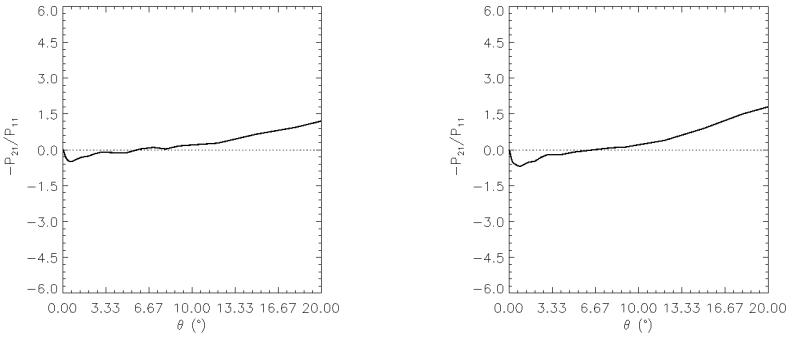

(c) $P_{max} = 0.3$

(d) $P_{max} = 0.4$

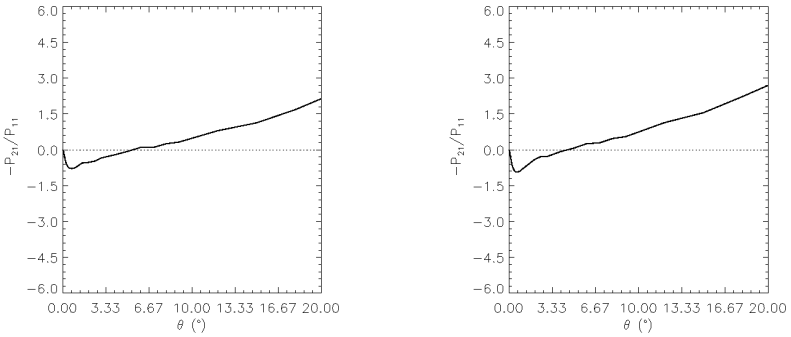

(e) $P_{max} = 0.5$

(f) $P_{max} = 0.6$

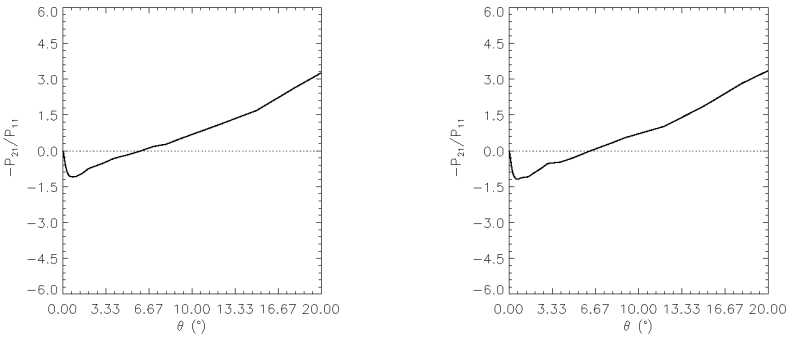

(g) $P_{max} = 0.7$

(h) $P_{max} = 0.8$

Figure 2.8: Variations on the output from the RT-CB code with increasing P_{max}.

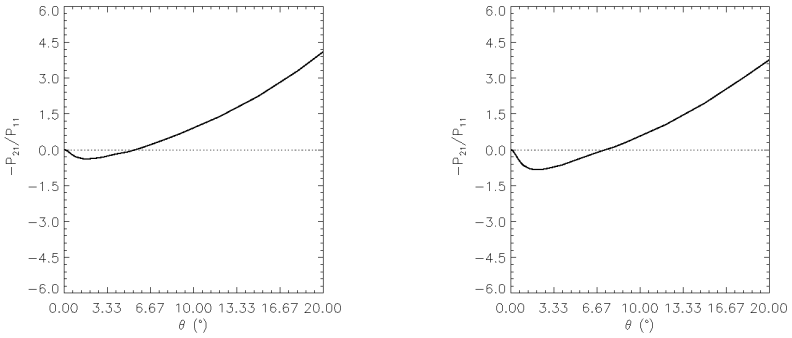

(a) $\tilde{\omega} = 0.1$ (b) $\tilde{\omega} = 0.2$

(c) $\tilde{\omega} = 0.3$ (d) $\tilde{\omega} = 0.4$

(e) $\tilde{\omega} = 0.5$ (f) $\tilde{\omega} = 0.6$

(g) $\tilde{\omega} = 0.7$ (h) $\tilde{\omega} = 0.8$

Figure 2.9: Variations on the output from the RT-CB code with increasing single scattering albedo.

Chapter 3

Instrumentation and planning of observations

In this Chapter we will go through the considerations, methods and tools used to measure Stokes parameters of astronomical sources. To measure the polarisation of light reflected from a Solar System body we rely on analysing the orientation of the electric field vector of an electromagnetic wave, i.e. the Stokes parameters. A very simple polarimeter would require only an analyser that allowed only certain orientations of the electric field to be transmitted and a CCD to measure the relative intensity as the analyser was rotated to define the Stokes parameters. This very simple polarimeter would be far from accurate but the concept is what all modern polarimeters are based upon. This very simple design could only be used to measure linear polarisation, but could be used measure circular polarisation with the addition of a quarter waveplate.

All polarimeters used in astronomy consist of three main components; a polariser, a retarder, and a detector. The information presented about each of these componets has been summarised from the following sources, (Keller, 2001) and (Kolokolova et al., 2015).

3.1 Polarisers

By definition a polariser is an optical element that produces linear, or circular, or elliptically polarised light when an unpolarised light source is passed through it.

There is a large variety of polarisers available to use. In this subsection I will briefly go through the various types.

3.1.1 Wire grid polarisers

These polarisers have been used for many years and are basically made from a grid of parallel conducting wires with a spacing of the order of the wavelength of the incoming radiation. Contrary to popular belief it is the polarisation perpendicular to the wires that is transmitted. This is due to the fact that the electric field component of the parallel beam will induce an electrical current in the wires. This induced current strongly reduces the transmission of the parallel component of the incoming radiation.

This type of polariser is typically used for infrared and longer wavelengths as it becomes difficult to make them for short wavelengths due to the wire spacing becoming very small.

3.1.2 Dichroic crystals

Dichroic crystals are type of crystal that preferentially absorb one polarisation state. The behaviour depends on the wavelength and the incident angle of the incoming radiation. Dichrosium arises from the anisotropy of the complex reflective index of the crystal. These crystals are found naturally but it is difficult to grow them artificially and in a uniform way to be able to use them for practical applications.

3.1.3 Polaroid-type polarisers

This type of polariser was first invented in 1928 by Edwin Land. The first design was based on using a suspension of dichroic crystals spread between two sheets. A strong magnetic field was then applied that aligned the suspensions to create a uniform dichroic layer. However, this design had a finite lifetime before the crystals became misaligned.

Decades later an improved design was constructed using molecular dichroism, which is analogous to the wire grid polariser mentioned earlier. This type of polariser was much more robust and was not affected by environmental changes such as temperature and humidity. It is this type of polariser that is widely used in po-

laroid sunglasses and camera lenses today.

3.1.4 Crystal-based polarisers

These polarisers are based on uniaxial crystals, i.e crystals that have a different refractive index in one axis compared to the other two. When light is transmitted through the uniaxial crystal it will be split into two rays. These rays are often described as the ordinary and extraordinary rays. In the case of a single uniaxial crystal the extraordinary ray is displaced by a small amount depending on the birefringence of the crystal. Both rays will have orthogonal polarisation states. The simplest example of one of these polarisers is a simple block of calcite sometimes referred to as a beam splitter.

The first crystal polariser was used in the 19th century; since then the design of such polarisers has become considerably better. Today there are three types that are commonly used in polarimetric optics and these are the Wollaston prism, the Savart plate, and Foster Prism (Glan-Thompson polariser).

Wollaston prisms are made from two calcite or quartz prisms that are cemented together with their optical axes perpendicular to each other. This works in a similar way to the beam splitter described earlier except both beams are displaced relative to the incoming ray.

Savart plate is essentially a beam splitter with a few additions. Since in a beam splitter the extraordinary ray is separated by the birefringent properties of the crystal it undergoes a slightly longer optical path. This additional distance travelled by this ray can cause focusing problems between the two rays on the detector. Hence a Savart plate consists of two plates that are rotated by 90 degrees with respect to each other, so that the beams travel the same distance.

The Foster prisms consists of two calcite prisms that are cemented together in such a way that the ordinary beam undergoes total internal reflection and can be absorbed by black paint on the crystal edge or passed through other optics to be measured, whereas the extraordinary beam is simply transmitted straight through the polariser.

The optical paths taken by the incoming and outgoing radiation are shown in

Figure 3.1.

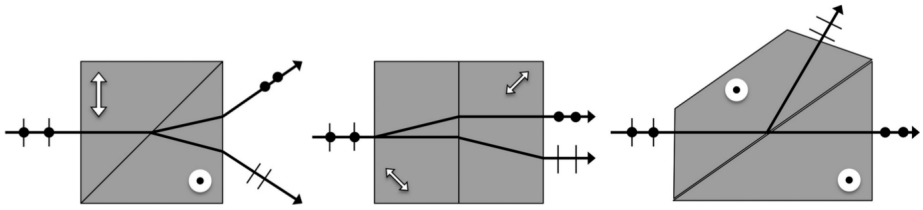

Figure 3.1: Optical path of light being transmitted through a Wollaston prism (left), a Savart plate (middle) and a Fosters prism (right). Figure taken from Kolokolova et al. (2015)

3.2 Retarders

Retarders are optical elements that introduce a phase shift between two perpendicular components of the electromagnetic field. They can convert linear polarisation to circular polarised and rotate the angle of linear polarisation. They can do this by using another property of birefringent crystals. When a birefringent crystal is cut with its optical axis parallel to the entrance surface the parallel and perpendicular electric field components of incident light will propagate at different velocities. This happens because the crystal will have two different refractive indexes, so when the input polarisation parallel to the axis will have the smallest refractive index it will travel faster than the light in the perpendicular direction, hence this adds a phase retardance. In the ideal case a retarder should not absorb any of the incoming radiation nor should it change the degree of linear polarisation.

There are two special cases of retarder wave plate and these are the half and quarter waveplate. The half and quarter refers to how much the phase has been changed, for a half waveplate this is 180 degrees or half the wavelength and for a quarter waveplate it is 90 degrees out of phase or quarter of a wave length. The half wave plate simply rotates the angle of the polarisation whereas a quarter wave plate transforms the linear polarisation into circular polarisation.

Typically these retarders are made of birefringence crystals such quartz, mica, MgF_2 etc or birefringent polymer sheets such as polyvinylchloride, polycarbonate. However there are some retarders that are constructed using more exotic techniques

like liquid crystals that can be manipulated with use of electric fields. For a complete list of retarders available see Keller (2001). All of these retarders only truly work for one wavelength, but they accept a broad wavelength range to be transmitted. Any chromatic effects have to be accounted for after the measurement depending on the wavelength of light being transmitted.

3.3 Detectors

As is the case for many other astronomical instruments the main requirement for polarimetry is a detector that has:

- A large quantum efficiency.
- Low readout noise.
- Low dark current.
- High linearity.
- Small gain variations.

For most astronomical applications linearity of the detector is of the utmost importance. However, since in polarimetry we are measuring small differences in the flux parallel and perpendicular it is important that the main source of error in the detector is from photon statistics.

3.4 Instrumentation

These three components: a polariser, a retarder, and a detector make up the basis of all polarimetric instruments. However there are many different design variations that exist that all essentially measure Stokes parameters but in different ways depending on the type of targets they were designed to observe, see Serkowski (1974) for information on different polarimetric designs. There are basically four different types of modern polarimeter:

- High-sensitivity polarimeters - These are polarimeters used to measure small polarisations or to measure small variations in an object's polarisation.

- High spectral resolution polarimeters - These polarimeters are mainly used to study the magnetic field of different stars by analysing the Zeeman splitting in spectral lines.

- High contrast polarimeters - These are relatively new types of polarimeter that are used to try and directly image exoplanets or circumstellar discs.

- High time resolution polarimeters - These are polarimeters that try and measure the polarimetry of very dynamic events such as the afterglow of a gamma ray burst.

The preferred mounting point for all these polarimeters would be at the Cassegrain focus of a telescope rather than the Nasmyth focus. The reason for this is to simply reduce the amount of instrumental polarisation generated, as every reflection can add a small amount of polarisation measured. However it is not always possible to mount optics on the Cassegrain focus due to weight restriction or the fact another instrument is already mounted there. Even if the polarimeter is mounted on the Cassegrain there is still the possibility of instrumental polarisation from some element along the optical path prior to entering the polarimeter. To calibrate for this instrumental polarisation it is customary to observe stars with a known amount of polarisation. Typically both unpolarised and high polarisation stars are observed to determine the instrumental polarisation. Provided that the instrumental effects are stable then any instrumental polarisation can simply be removed from future measurements.

In the following sections I will describe some of the instruments I have used during the course of this work, for a detailed list of all current polarimeters available for astronomical research see Table 4.1 in Kolokolova et al. (2015)

3.4.1 The FORS instrument

One of the most useful polarimeters for Solar System science is FORS2. FORS[1] is the visual and near UV FOcal Reducer and low dispersion Spectrograph mounted

[1] http://www.eso.org/sci/facilities/paranal/instruments/fors/

at the Cassegrain focus of UT1 of the Very Large Telescope (VLT) (Appenzeller et al., 1998).

FORS is equipped with a quarter and half waveplate. The quarter waveplate can be rotated in 90° steps, whereas the half wave plate can be rotated in steps of 22.5°. This is followed by a Wollaston prism that splits the incoming radiation into two orthogonally polarised beams (Appenzeller, 1967). These two beams are prevented from overlapping by a mask consisting of nine 22 arcsecond strips which is used before the light reaches the prism (Scarrott et al., 1983), as shown in Figure 3.2 (Appenzeller et al., 1998).

3.4.2 The RINGO instrument

RINGO was a novel optical polarimeter designed by Clarke & Neumayer (2002) and was mounted to the robotic Liverpool telescope in La Palma. In this design the instrument consisted of a polaroid filter that was rotated at 500 rpm and placed in the path of the incoming radiation. This creates a time variable signal depending on the polarisation state of the incident light. This time variable signal is transformed into a spatial signal on the CCD by use of a small angle prism rotating with the polaroid. The resulting image of the target forms a ring on the CCD with certain segments of the ring referring to certain Stokes parameters. The aim of this design was to enable the observation of bright sources without the need of neutral density filters and hence a longer exposure time. However, the major flaw with this design was that if two sources were close together the resultant rings would overlap on the CCD. The two overlapping rings can not be disentangled from one another causing the polarisation information to be lost. In 2009 RINGO was decommissioned and upgraded to form RINGO2.

RINGO2 was designed to be a fast readout imaging polarimeter aimed to rapidly gather information on Gamma ray bursts. The design was altered so that it no longer created rings on the CCD but rather the detector was read out 8 times a second synchronized with the rotation of the polaroid. The resultant 8 images could be combined to determine the polarisation characteristic of the target.

RINGO2 was decommissioned in 2012 and again upgraded to form RINGO3.

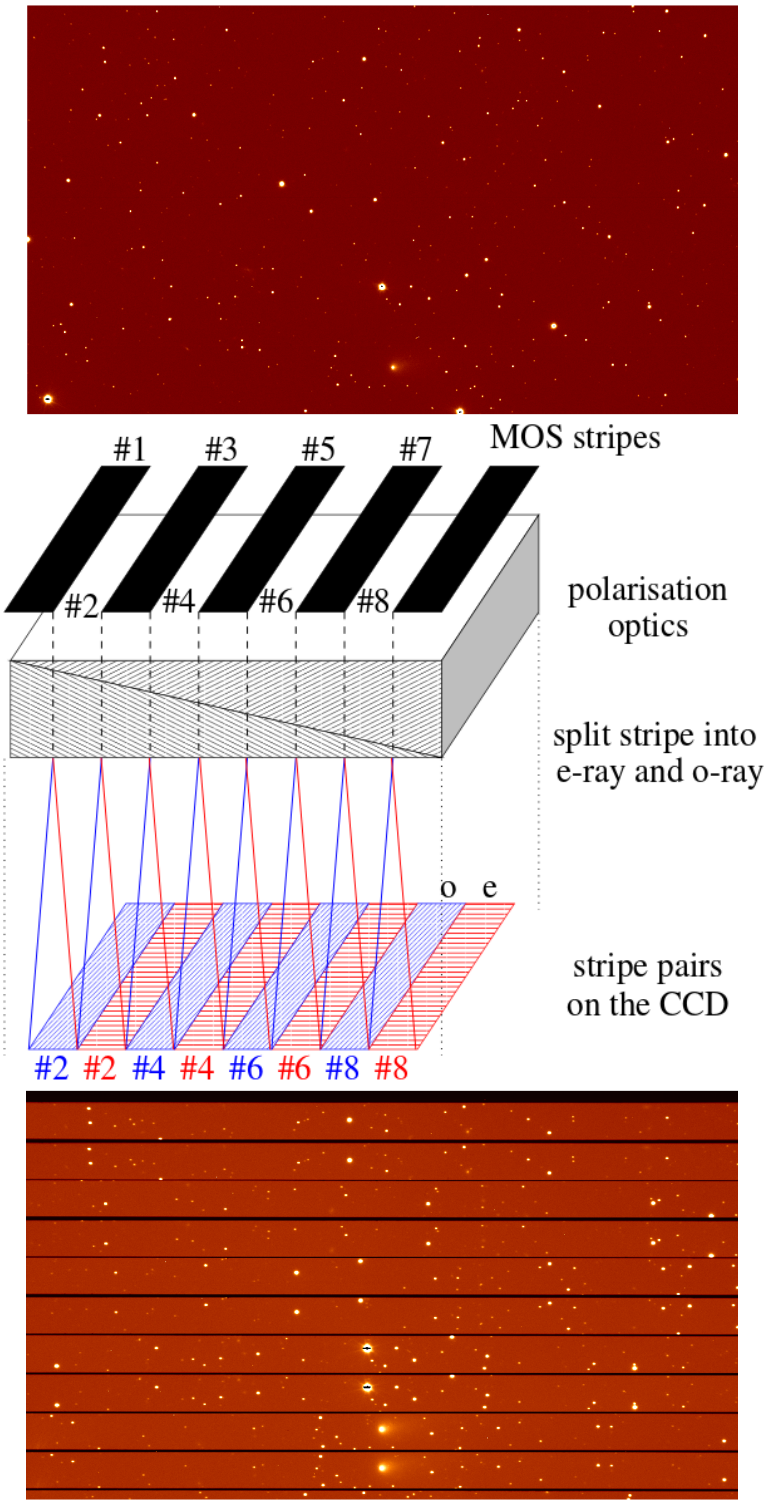

Figure 3.2: Top panel is the field of view of the FORS instrument with no polarimetric optics. Middle panel shows the optics that prevent the polarimetric beams from overlapping on the CCD. The bottom panel is the resulting polarimetric FORS image.

(a) FORS2 (b) SINFONI

Figure 3.3: FORS2 and SINFONI instruments.

In this incarnation the main bulk of the instrument remained unchanged. However, the addition of a pair of dichroic mirrors and two additional CCDs means that RINGO3 can carry out simultaneous RGB imaging polarimetry of a target.

3.4.3 The SINFONI instrument

Another instrument that I have used for Solar System science is SINFONI. SINFONI is the Spectrograph for INtegral Field Observations in the Near Infrared installed on the Cassegrain focus of UT4 of the VLT. Even though the majority of this thesis is based on polarimetric measurements I have also used SINFONI (Chapter 6) to measure the infrared spectra of cometary dust. SINFONI is fed by adaptive optics and operates over the wavelength range of 1.1-2.45μm. The spectrograph operates with 4 gratings (J, H, K, $H+K$) providing a spectral resolution around 2000, 3000, 4000 for J, H, and K respectively, and 1500 for $H+K$. The SINFONI field of view on the sky is sliced into 32 slitlets. The pre-optics allow the user to choose the angular size of the slices of the sky. The three choices are 250, 100 and 25 milli-arc-seconds, which lead to fields of view of 8”×8”, 3”×3”, 0.8”×0.8”. The typical limiting magnitudes (S/N = 10 in 1 hour on source) are around 17-18$^{\text{th}}$ magnitude in J, H, K. SINFONI can be used with or without adaptive optics guide stars, when used without, the adaptive optics modules acts as relay optics. The full

power of the instrument is only truly utilised when adaptive optics is being used. The FORS and SINFONI instruments are shown in Figure 3.3.

3.5 Observing strategies

Polarimetric observations take longer than most other observing techniques due to the reasons described here. Polarimetric measurements require very high signal to noise ratios to get accurate results. If we assume the flux and standard deviation from both parallel and perpendicular beams are approximately equal, Bagnulo et al. (2009) showed that the signal to noise ratio required to obtain a certain accuracy can be approximated using the equation

$$S/N = \frac{100}{\Delta P} \tag{3.1}$$

where ΔP is the required polarimetric accuracy in percent. For example to measure with an accuracy of 0.1 % polarisation one would require a signal to noise ratio of $\sim$ 1000. Depending on the relative brightness of the target this can require a very long exposure time to get the required accuracy. In addition to long exposure times typically in polarimetry we measure very small differences in the flux in the parallel and perpendicular beams, hence the detector readout has to be done slowly so as to not add additional readout noise to our measurements. This leads to long overheads waiting for the CCD to readout the detector. Also, this must be carried out at least 4 times to get measurements of P_Q and P_U via the beam swapping technique. The reason for using the beam swapping technique is to suppress instrumental effects and will be discussed later in Chapter 4. All of this means a typical polarimetric observing sequence can take upwards of 30-60 mins depending on the target's brightness. However, this is only one measurement for a single phase angle but we require several measurements spaced over the entire visible phase angle range to maximize the amount of information from our targets. Typically this can take several observations over the course of a few months.

3.5.1 Service and Visitor mode at the ESO VLT

For observations carried out at the VLT, two observation modes are offered, service and visitor mode. Visitor mode observations means the observer physically has to go to the telescope. Service mode observation's means the submission of Observing Blocks (OBs) for the telescope operator to carry out on the observers behalf. Service mode observations offers much more flexibility as it allows us to submit OBs over a period of months to be carried out without physically having to be at the telescope. Rationale, characteristics, and advantages of service mode observations are discussed in various articles of the ESO journal "The Messenger" (Comeron et al., 2002). For polarimetric observations this allows us to sample the available phase angle range without actually having to be at the telescope several times in a month to carry them out.

These observing blocks are submitted to the telescopes using the Phase 2 Proposal Preparation tool (P2PP), where one can outline preferred date and time of observations, the number of observations to be carried out, the filters to be used, exposure time and the amount of retarder wave plate positions to be used etc. In addition to this information, accurate ephemeris data containing co-ordinates and differential tracking which is important for moving targets must be sent. This information is readily available using the Jet Propulsion Laboratory (JPL) horizons web-interface [2].

3.5.2 Preventing background confusion

For moving targets we must also pay particular attention to where they are moving in relation to stars in the background. During visitor mode observations one can see if there any background stars interfering with the observations and can switch target if necessary. However, this is not the case for service mode observations. Clearly if we submit an OB to be carried over a few days to obtain polarimteric measurements for a certain phase angle, we don't want to have any stars close to our target that could contaminate our measurements. For this reason I used the Xephem[3] software which

[2] http://ssd.jpl.nasa.gov/horizons.cgi
[3] http://www.clearskyinstitute.com/xephem/

allows one to trace the trajectory of the moving target through the sky. This lets us identify the dates on which our target is close to a bright background star. In Figure 3.4 we can see the software trace out the movement of the comet 74P/Smirnova-Chernykh, through a night and display the background stars. In this example we can see that there are a few faint stars very close to the comet's path as well as bright stars above and below the comet. These bright stars could potentially cause CCD saturation and bleeding. Also bright stars like these tend to exhibit diffraction spikes that could overlap with our observation of the comet. This night is far from ideal so it would be better to avoid if possible. Once we choose dates that are free from background stars we have to pay attention to the influence of the Moon. When observations are carried out in the presence of the Moon, the background sky is highly polarised, so the dates in which the Moon is in close proximity to our target and/or has a large fraction of illumination are avoided. The high background sky polarisation can be a major cause of CCD saturation if the target is faint i.e long exposure time.

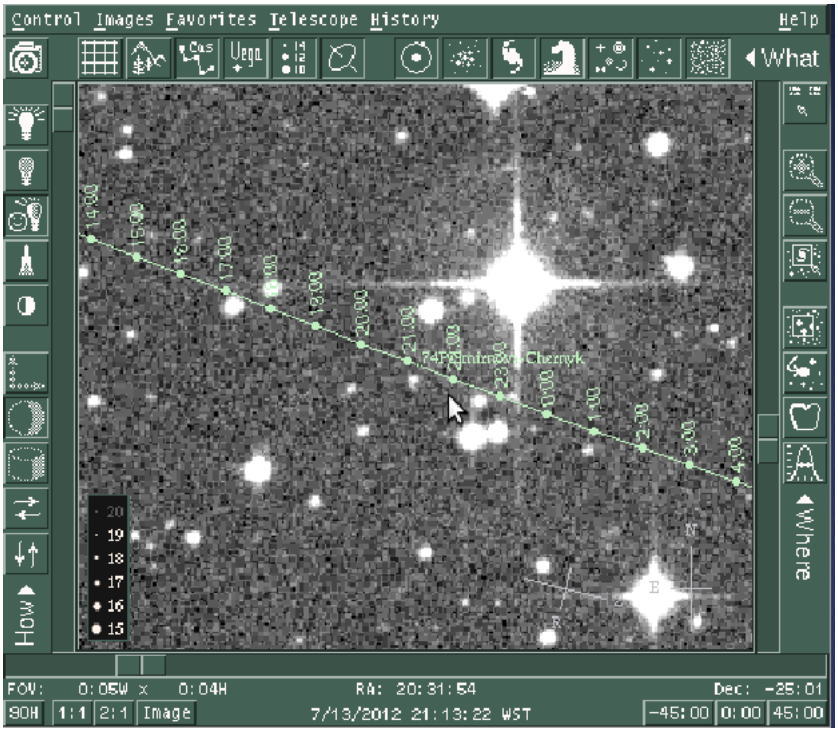

Figure 3.4: The path of the comet 74P/Smirnova-Chernykh across the sky over the course of a night.

Chapter 4

Data reduction techniques

Polarimetry is a technique based on the measurements of very small differences between very large signals; therefore, even if data have a very large signal to noise ratio, the relative error of the polarimetric measurements may still be large. The optimisation of the techniques used to carry out data reduction and measure the signals from the data is a crucially important step to avoid spurious measurements, minimise systematic errors, and achieve robust results. This chapter is dedicated to describing my attempts to maximise the data quality. This will include both image reduction and how polarimetric measurements are obtained from these images. I will also outline the importance of how the background sky contribution is estimated. This will involve the use of three different methods, utilizing Image Reduction and Analysis Facility (IRAF) and Source Extractor (SE) software packages that are routinely used in astrophysics.

Using these three different methods I will investigate how they affect different scenarios that can be encountered when measuring the polarimetry of Solar System objects. All the data investigated were obtained by the FORS2 instrument and the data will look at four different types of polarimetric observations, a low polarisation target, a high polarisation target, an extended source target, and a target which is effected by a high background polarisation. During this investigation I will detail how each piece of software calculates the flux from the target and background sky level. In addition to this I explore different techniques inside each piece of software to try and get the most accurate results possible. Ultimately the end results of this

chapter will be to decide which technique gives the best results for each of the four different type of observation.

4.1 CCD image correction

Before we begin to use data taken with FORS instrument, or any data taken with a CCD, we must first follow a few simple steps to remove the bias and correct for flat field effects.

The bias is a small positive offset that is added to the CCD electronics to avoid negative pixel counts. Negative pixel counts can occur if the CCD had an initial zero count across all pixels; due to small pixel to pixel variation some pixels would have an initial count slightly above or below zero. A negative count causes a problem for the analog-to-digital converter which would read the negative count as the maximum counts that the pixel can hold. Hence it is more convenient to apply a small positive offset that we can remove later and this offset is called the bias of the image. To remove this bias for the science data, several images are taken with zero exposure time with the shutter to the CCD closed. This means the counts in these images are of the bias only. Several of these images are combined and averaged to produce a master bias image which is statistically better than a single image and can negate the effects of cosmic rays. This master bias is then removed from all other CCD images.

Flat field effects occur in an image due to the fact that not every pixel has the exact same gain or quantum efficiency when compared to its neighbour. For example if a group of pixels were exposed to the same incoming photon flux, some may record more electrons than their neighbour or visa versa. In order to calibrate the response for each pixel, we must obtain a flat field image. There are a few ways in which this can be obtained: one method is to illuminate a screen inside the dome of the telescope and point the telescope at it; another method is to expose the CCD to a twilight sky. The goal of these observations is to expose the CCD to an approximately uniform source of light to fill the pixels of the detector with a large number of electrons to see the pixel variation.

It is important to note that these exposures are of the order of a few seconds to a few minutes, depending on light conditions. This allows the CCD to accumulate a large number of counts per pixel but low enough number so that the CCD does not become saturated. As before a series of these exposures are taken to create a master flat field. To create a master flat field we remove the bias from each of flat field images obtained. These are then combined and averaged in the same way as the bias mentioned above. However if the flat fields are obtained by observing a twilight sky it is often better to take the median rather than the average because there can be bright stars visible during twilight. Even though telescopes undergo an offset between twilight flat field exposures, if stars are visible in these images the average combined master flat field images would show the star drifting across the image whereas the median combined master flat field will not as the star will appear in different locations on the CCD. Once this master flat field is created it needs to be normalized by dividing each pixel count by the average pixel count over the whole flat field image. The normalized flat field is then divided into the science image. This has the effect of flattening out the pixel to pixel variation across the CCD. The image reduction process can be summarized by Equation 4.1.

$$\text{Reduced Image} = \frac{\text{Raw image} - \text{Bias}}{\text{Normalised Flat Field}} \tag{4.1}$$

4.2 Measuring Stokes Parameters

To measure Stokes Q and U parameters from observations using FORS we use the background subtracted photon counts of the parallel ($f^{\parallel}$) and perpendicular ($f^{\perp}$) beams observed at various retarder waveplate positions, α. An example FORS image is shown in Figure 4.1; the strips that contain the flux parallel and perpendicular are also labelled. As previously mentioned in Chapter 1 it is customary to work in the reduced Stokes parameters so that we are working with a fraction of linear polarised light.

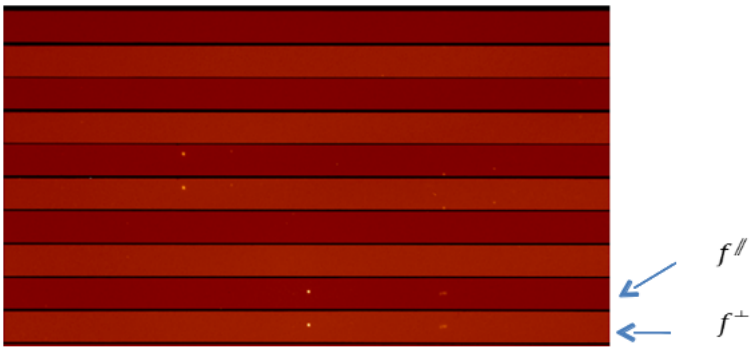

Figure 4.1: A typical image taken with FORS2 at a single retarder waveplate position.

$$P_Q = \frac{Q}{I} \tag{4.2}$$

$$P_U = \frac{U}{I} \tag{4.3}$$

In the case of an ideal polarimeter, P_Q is obtained by measuring the ratio;

$$r = (-1)^k \frac{f^{\parallel} - f^{\perp}}{f^{\parallel} + f^{\perp}} \tag{4.4}$$

With the half waveplate position $\alpha = k45^o$ where k=0, 1, 2 ... ,7. Likewise P_U is obtained by measuring the ratio at retarder waveplate positions at $\alpha = k45 + 22.5^o$.

In practice there are many deviations from the ideal case. For instance deviations in the waveplate angle or the actual retardance value of the retarder waveplate differs from π. As well as this the transmission of the parallel and perpendicular beam is not identical even after flat field correction. Also, there will be the possibility of small amounts of instrumental polarisation from reflections off mirrors and lens before it reaches the polarimeter.

The effect of these sources and others not mentioned can be significantly reduced at the first order by measuring the reduced Stokes parameters P_X (where X=Q or X=U) obtained using Bagnulo et al. (2009)

$$P_X = \frac{1}{2N} \sum_{j=1}^{N} \left[\left(\frac{f^{\parallel} - f^{\perp}}{f^{\parallel} + f^{\perp}} \right)_{\alpha_j} - \left(\frac{f^{\parallel} - f^{\perp}}{f^{\parallel} + f^{\perp}} \right)_{\alpha_{j+45}} \right] \tag{4.5}$$

where $f_{\parallel}$ is the flux in the parallel beam, $f_{\perp}$ is the flux in the perpendicular beam, N is the number of pairs of exposures, and α_j denotes the position angle of the retarder waveplate. For α = 0, 90, 180, and 270° Eq.(4.5) gives P_Q; for α = 22.5, 112.5, 202.5, 295.5° Eq.(4.5) gives P_U.

The uncertainty due to photon noise on P_Q and P_U from a pair of measurements is given by Bagnulo et al. (2009)

$$\sigma^2 = \frac{1}{(2N)^2} \sum_{j=1}^{N} [(g(\alpha_j))^2 + (g(\alpha_j + 45))^2] \tag{4.6}$$

where

$$g^2(\alpha) = \left(\frac{2 f^{\parallel} f^{\perp}}{(f^{\parallel} + f^{\perp})^2} \right)^2 \left(\frac{(\sigma^{\parallel})^2}{(f^{\parallel})^2} + \frac{(\sigma^{\perp})^2}{(f^{\perp})^2} \right)_{\alpha} \tag{4.7}$$

N is the number of pairs of exposures and $\sigma^{\parallel}$ and $\sigma^{\perp}$ are the uncertainty in the measurement of the $f^{\parallel}$ and $f^{\perp}$.

When these Stokes parameters are calculated using Equation 4.5 they will be measured using a reference direction dictated by the telescope optics. Usually in this case P_Q and P_U are measured with the instrument position angle = 0°. This means that the acceptance angle of the parallel beam is aligned to the north celestial meridian and the perpendicular beam normal to this. In Solar System science we prefer to have the Stokes parameters in a reference direction that is perpendicular to the plane containing the Sun, the target, and the observer (i.e. the scattering plane). The equations that transform P_Q and P_U from Equation 4.5 into this reference direction are given by Bagnulo et al. (2006)

$$P'_Q = \cos\left(2\left(\varphi + \frac{\pi}{2}\right)\right) P_Q + \sin\left(2\left(\varphi + \frac{\pi}{2}\right)\right) P_U \tag{4.8}$$

$$P'_U = -\sin\left(2\left(\varphi + \frac{\pi}{2}\right)\right) P_Q + \cos\left(2\left(\varphi + \frac{\pi}{2}\right)\right) P_U \tag{4.9}$$

where φ is the angle between the direction object-north pole and the object-Sun direction. For minor bodies of the Solar System such as asteroids, comets etc, φ can be easily obtained from NASA's Horizons web interface[1]. However, Horizons does not calculate φ for Planets and Moons. The angle, φ, can be calculated by

[1] http://ssd.jpl.nasa.gov/?horizons

applying the four parts formula to the spherical triangle defined by the object (with coordinates α_T, δ_T), the Sun (with coordinates $\alpha_\odot$, $\delta_\odot$) and the north celestial pole

$$\sin(\delta_\mathrm{T})\cos(\alpha_\odot - \alpha_\mathrm{T}) = \cos(\delta_\mathrm{T})\tan(\delta_\odot) - \sin(\alpha_\odot - \alpha_\mathrm{T})\frac{1}{\tan(\varphi)} \tag{4.10}$$

After this transformation P'_Q is the flux parallel to the Sun-target-observer minus the flux perpendicular to it, divided by the sum of the two. P'_U will equal zero due to the symmetry of the system and acts as a good quality check.

An additional quality check that can be used is the null parameters. The null parameters are the difference between two measurements of the same Stokes parameter. For example the null of P_Q (N_Q) is the difference between P_Q calculated using retarder positions 0° and 45° and P_Q calculated using 90° and 135°. If both these measurements where taken within a small time scale one does not expect the polarisation to change, (i.e. No rotational or phase angle change to affect the measured polarisation). Therefore both measurements should be identical and the difference between the measurements should be zero. If the null parameters deviate away from zero beyond the uncertainty of the measurement of either P_Q or P_U then something has went wrong with the data reduction, data analysis, or the stability of the polarimeter.

4.3 Aperture Polarimetry

Using Equations 4.5, 4.8 and 4.9 we can now begin to measure Stokes parameters of the target, but first we must calculate the photon counts for both the parallel and perpendicular beams from the CCD images. This is done by using simple aperture photometry. Aperture photometry is a simple technique that makes no assumption of the actual shape of the source's point spread function but simply collects and sums up the observed counts within a specific aperture centred on the source. The general method carried out to measure the photon count of the $f^{\parallel}$ and $f^{\perp}$ consists of measuring the flux in a wide range of circular apertures around the the target object. We vary the size of the aperture to make sure that all the flux from the object is collected. Outside of these apertures we use an annulus to estimate the average

background sky flux. This background sky estimate is then subtracted from each pixel contained inside the aperture around the target. This leaves only the flux that has came from the target object itself. A basic representation of this is shown in Figure 4.2. If we ignore read out noise of the CCD we can calculate the error of the flux measured in an aperture using the equation defined by Davis (1987)

$$\sigma^2 = f + A\sigma_B^2 + A^2\sigma_B^2/N_B \tag{4.11}$$

where f is the photon counts collected in the adopted aperture, A is the aperture area used to measure the photon counts expressed in pixels, σ_B is the standard deviation of the background estimate, N_B is the number of pixels used to estimate the background. The first term in Equation 4.11 is simple Poisson noise due to counting photons. The second and third terms are the uncertainties introduced when the background sky is being removed. When the target is bright and has a high number of photon counts the first term will be the dominant source of uncertainty, however if the target is faint and has a low amount of photon counts the second and third term will become significant. I note that if f and σ_B are originally measured in ADUs, they must be converted to electron counts by multiplying their original values by the number of electrons per ADU, before calculating Equation 4.11. Equation 4.11 will become inaccurate in later sections when I discuss the use of algorithms that estimate the background sky by creating a smooth interpolation map of the background sky over the entire CCD. The reason for this inaccuracy is because σ_B in the created background map will be very small compared to the original background sky in the science image.

The values obtained for P_Q and P_U using this method are slightly dependant on the size of the aperture used to measure the $f^{\parallel}$ and $f^{\perp}$. This effect can become more pronounced when the field of view around the target is crowded by background stars. It can also become more significant when the signal to noise ratio of the data is low. In Figure 4.3 we can see how the polarisation for a target varies with aperture size. In Figure 4.3 it can be seen that values of P_Q and P_U vary a lot at small aperture values before stabilizing at a value of $\sim -0.75\%$ for P_Q and close to zero for P_U

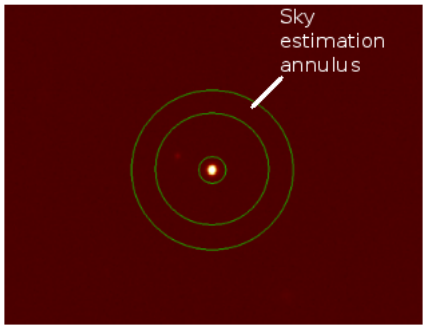

Figure 4.2: A basic representation of aperture photometry where we have the small inner aperture around the target and the annulus around the target to calculate the background sky.

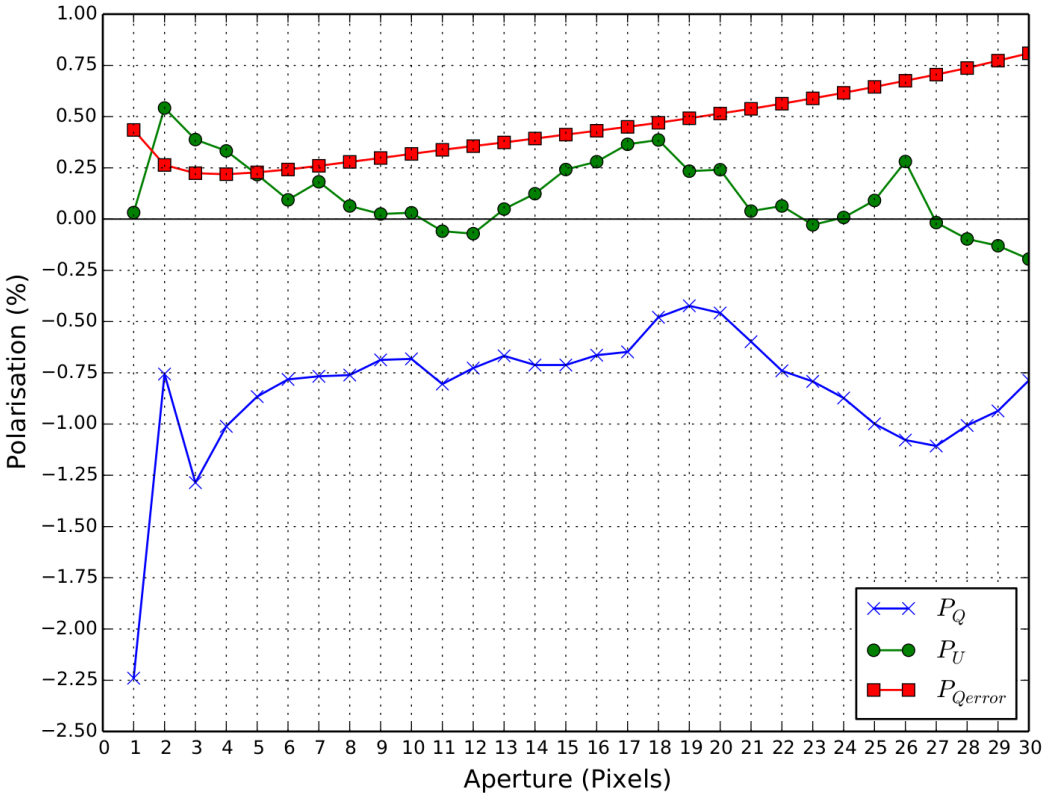

Figure 4.3: Change of polarisation with aperture size.

beyond an aperture of 6 pixels. In Figure 4.3 I have also plotted the errorbar and how the value changes as a function of aperture. It can be seen that the error decreases as more flux from the target is included in the aperture before increasing again as uncertainties in the background estimate begin to dominate. The final aperture size

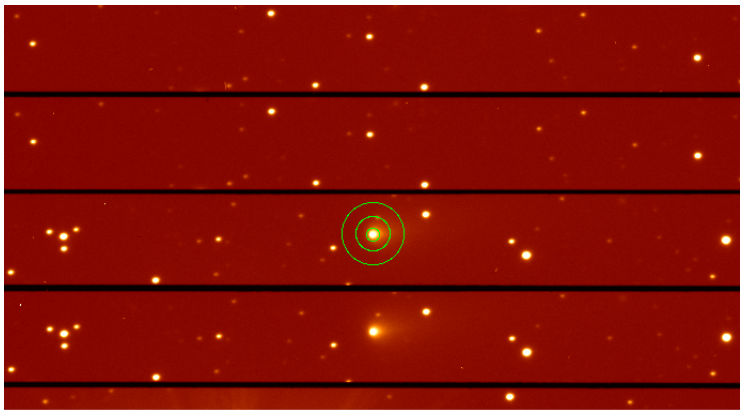

Figure 4.4: How the background flux calculation in the outer green annulus is impeded by the coma and tail of the target.

chosen to measure the polarisation in this example is one where the uncertainty on the measurement is low and the value of the polarisation versus aperture size is no longer still varying (Bagnulo et al., 2011). In this case an aperture of between 6-8 pixels would be acceptable as the polarisation is stable and the uncertainty is still small.

This method of data analysis is only suitable when the target is effectively a point source and is moving across the sky at a relatively slow rate. Things become a little more complicated when the target is an extended source and is fast moving, which is the case when we consider the polarimetric observations of comets (see Chapter 6). One difficulty that arises when dealing with an extended source is shown in Figure 4.4. We can see that the outer annulus used to calculate the background sky flux is contaminated by the coma and tail of the comet. This means that the average background sky estimate will contain an additional contribution and hence be an overestimate. This overestimate can alter the amount of polarisation we measure; this will be discussed later.

This issue can be alleviated if we detach the outer annulus from the target location and move it away to a safe place free from any contribution from the coma and tail. This new location also needs to be free of any background stars as they can also cause an additional contribution to the background sky calculation. The ideal location for this offset annulus would be close to the edge of the CCD in the opposite

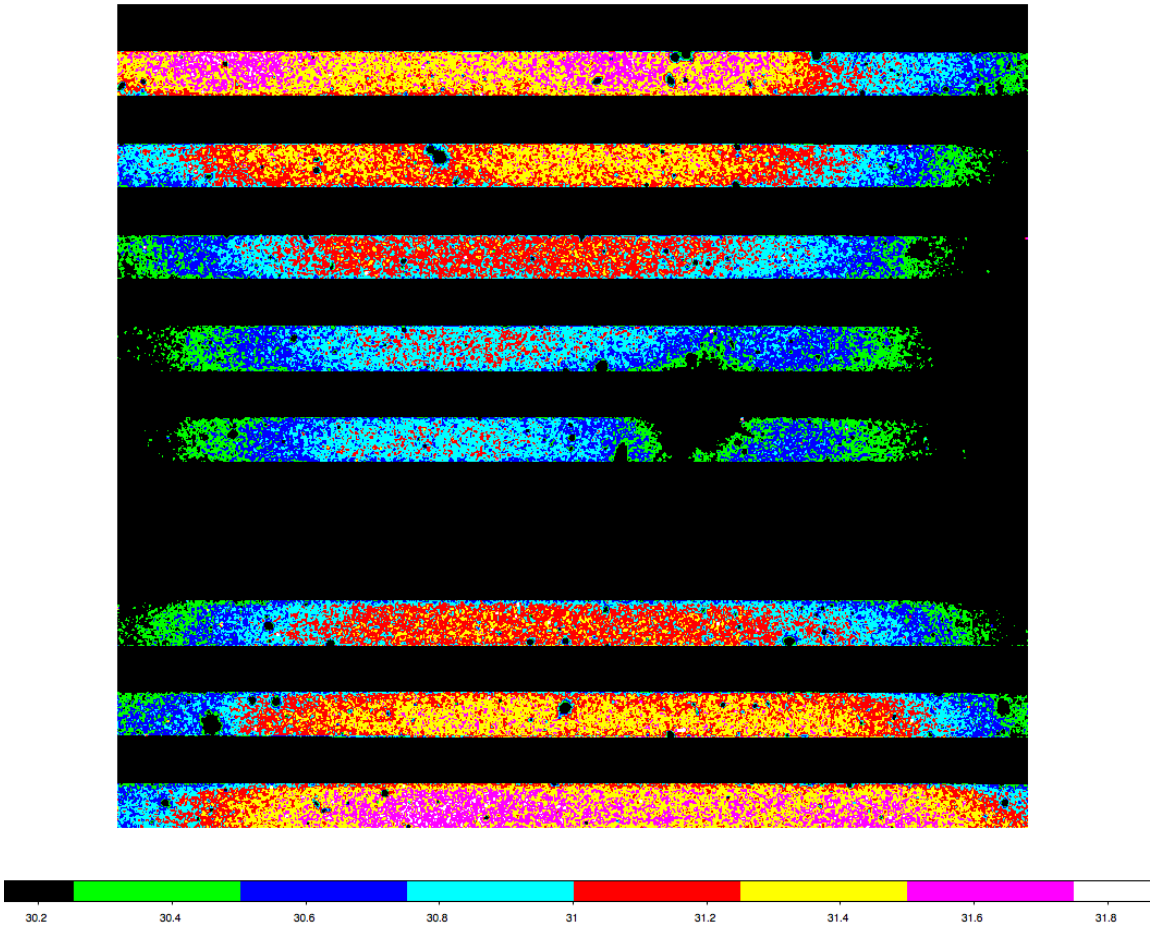

Figure 4.5: Different values of instrumental polarisation for the FORS instrument at different locations on the CCD. The scale bar shows the amount of polarisation in percent.

direction of the comet tail. This is due to the fact that the coma around the comet falls off as $\frac{1}{\text{Distance}}$ in the inner coma (assuming isotropic outflow) so it is effectively adding a small contribution to the field of view close to the comet. Beyond this inner coma area Solar radiation dominates dust dynamics which leads to formation of a tail, this is discussed in Finson-Probstein analysis in Chapter 6. However, FORS suffers from instrumental polarisation that varies the further you move from the centre of the CCD. This instrumental polarisation is best seen when the background sky is highly polarised, this is shown in Figure 4.5. This instrumental polarisation does not affect the amount of polarisation measured from the target as its always centred in the middle of the CCD where the instrumental polarisation is effectively

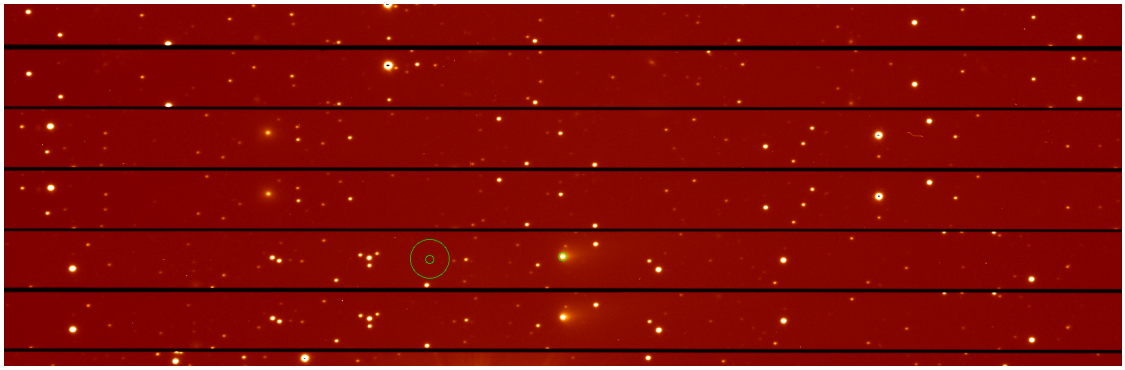

Figure 4.6: How the background flux can be calculated for extended targets if we move the outer green annulus away from contribution of the coma and tail.

removed when the background sky is estimated close to the target. So as you can see you have to choose a location for the background sky estimate that is far enough away from the comet so it is not being influenced by the coma but not that far away that it is being influenced by the instrumental polarisation. This "sweet spot" between both effects needs to be found and its location varies from target to target depending on the amount of activity shown by the comet. This process is shown in Figure 4.6.

This approach can be further complicated if the target is moving rapidly across the sky. The reason for this is that the time between first and last waveplate observation can be up to an hour apart depending on the exposure time of the observation. For a fast moving target the background stars can move a considerable distance relative to the target. So a place identified as a safe place at the start of the observations, Figure 4.6, may not be safe place by the end of the observations, Figure 4.7. Therefore we must continuously move the annulus to make sure we continue to obtain an uncontaminated background sky estimation.

4.4 Aperture Photometry

The ability to measure a celestial body's apparent brightness is done using aperture photometry, this technique was outlined in Section 4.3. The equation used to calculate the apparent magnitude (AM) is

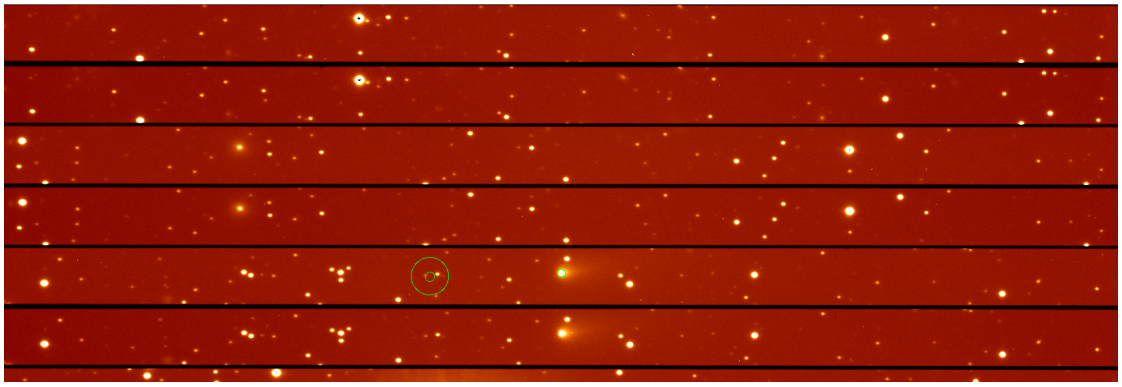

Figure 4.7: This is the last image taken on the same night as Figure 4.6 which now has a background star in green annulus used to calculate the background sky.

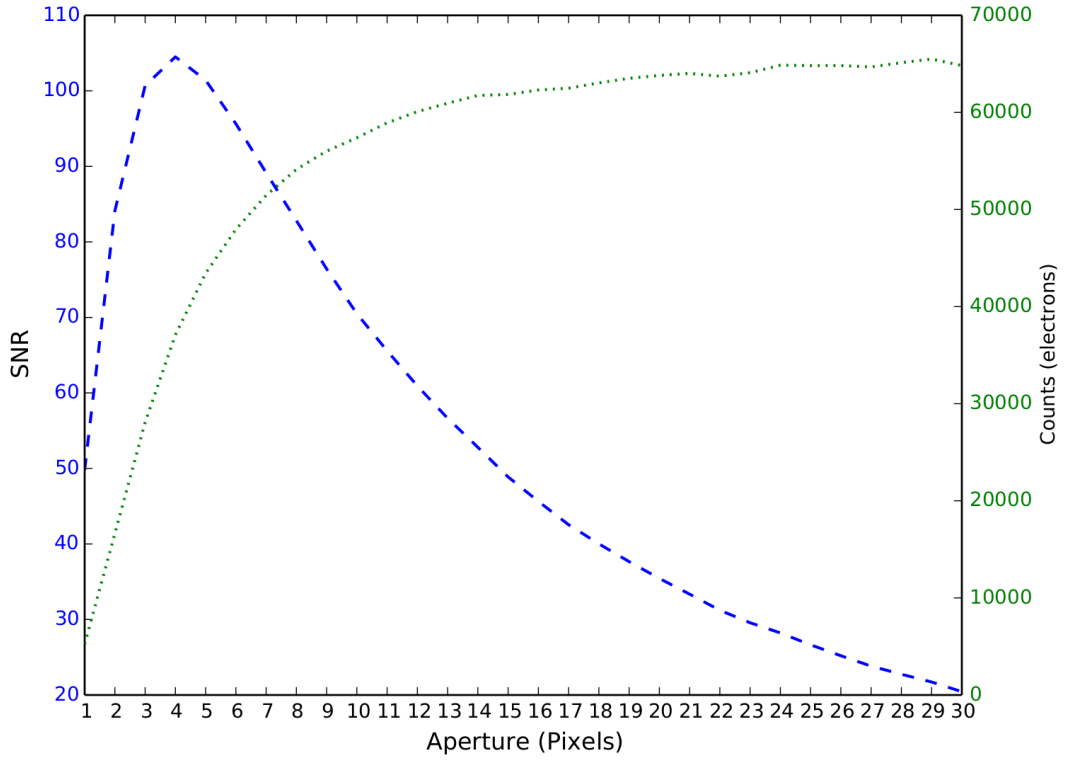

Figure 4.8: Change in SNR (blue dashed line) and counts collected from the source (green dotted line) with aperture size.

$$AM = Z_P - 2.5\log_{10}(F) + (A \times EXT) \tag{4.12}$$

where Z_P is the zero point of the night, F is the flux collected from the source in an aperture in e^-/s, A is the airmass, and EXT is the atmospheric extinction. The

choice of aperture used to measure the flux from a target is often a trade off between gathering all the flux from a source and keeping the uncertainties from estimating the background sky low. One demands you have a large aperture the other a small one. In Figure 4.8 I show this trade off between the flux gathered from the target and the change in the signal to noise ration (SNR). One could say the aperture that should be chosen is the point where the two lines meet. Others would argue the use of the point spread function (PSF) or the full width half max (FWHM) of the target on the CCD as the preferred method. In this work I do not use the PSF since I am mainly dealing with moving targets which causes background stars to become elongated in there direction of motion relative to the target during long exposures. The use of the PSF is also not very applicable to extended sources like comets.

4.5 High precision imaging polarimetry

Since we are typically measuring very small amounts of polarisation from objects it is very important that we get the most precise measurements that we can. In addition to the uncertainties described in Equations 4.11 and 4.6, there may also exist a systematic component.

For instance, if we neglected to remove the entire background sky contribution, F_B, from our data due to the use of a rough estimate, a simple manipulation of Equation 4.5 would introduce a factor

$$1 - 2\frac{F_B}{f^{\parallel} + f^{\perp}} \tag{4.13}$$

to our measured P_Q and P_U values.

Hence we can see the importance of calculating a very accurate estimation of the background sky when measuring Stokes parameters. As was the case in Equation 4.11 this uncertainty will be more influential on a faint low signal to noise ratio target rather than bright high signal to noise ratio targets. The main reason for this is the bottom line of the second term, i.e. when the flux is high it will tend to suppress any uncertainty caused by a poor background estimate, however it can still pose an issue if one is measuring a very small amount of polarisation

$\sim 0.1\%$. Since the estimation of the background sky is important for obtaining accurate polarimetric results in this section I will investigate various techniques used to estimate it.

There are many software packages that can be use to calculate the flux coming from a source in a CCD image. The three software packages that I have experimented with are IRAF[2], GAIA[3], and Source Extractor (SE)(Bertin & Arnouts, 1996).

IRAF is the Image Reduction and Analysis Facility which is a general purpose system for data reduction and analysis of scientific data. IRAF was written and supported by the National Optical Astronomy Observatories (NOAO) in Tucson, Arizona. IRAF offers a wide variety of packages to carry out reduction and analysis of scientific data but for this section we are only interested in the packages related to aperture photometry. In IRAF aperture photometry is carried out with a circular aperture surrounded by an annulus to carry out the measurement of the background sky. With a little bit of tinkering IRAF can also provide aperture photometry with an offset annulus.

GAIA is the Graphical Astronomy and Image Analysis tool. GAIA was created by the now closed Starlink UK project and has been supported more recently by the Joint Astronomy Center Hawaii. GAIA can be used to display and analyse images on an interactive level or it can be used from the command line. GAIA estimates the background sky using an annulus that can be offset to a user defined location.

Both IRAF and GAIA offer the same methods of calculating the flux and the background sky, so for the duration of this investigation I will only use IRAF for these methods, as it is more convenient to script.

Source Extractor offers a completely different method to calculate the background sky compared to IRAF and GAIA. SE was originally developed for the analysis of large scale galaxy survey data, but it also performs well in crowded star fields. Even though it was not strictly developed to do photometry for single targets it can be applied to them quite easily. Since it was primary designed to deal with

[2]http://iraf.noao.edu/

[3]http://star-www.dur.ac.uk/ pdraper/gaia/gaia.html

galaxy surveys it does offer non circular apertures which the software can change to best fit your source. This can be particularly useful for targets which are extended sources. SE calculates the background sky value by creating a background map that should be there, if the target and background stars were not present. It does this by assuming an estimate for the local background in every mesh of a grid that covers the whole CCD image. In each area, the mean and standard deviation of the distribution of pixels values is computed. The most deviant values are discarded and the median and standard deviation are computed again. This process is repeated until all the remaining pixels values are within $\pm\ 3\sigma$ of the mean. The background map created is a bi-cubic spine interpolation over all the area of the user defined mesh size. However polarimetric images taken with FORS have discontinuities as they are divided in strips of opposite polarization (the parallel and perpendicular beams). The background flux in these two strips is rarely the same due to the background sky polarisation caused by the Moon; this means that the interpolation will smooth the background estimation out essentially forming an average between the two background levels. This leads to an overestimate in one strip and an underestimate in the other therefore leading to a very poor sky estimate as shown in panel (b) of Figure 4.9. We can make the mesh size that SE uses to estimate the background smaller so it can cope with the stripped nature of the FORS images. However, reducing the mesh size to that level means background stars can appear in the background sky estimation and there is always a transition phase between the parallel and perpendicular strips, hence both methods create a poor estimate. This is shown in panel (c) of Figure 4.9.

Therefore we must first separate the strips that contain the flux parallel and perpendicular as used in Equation 4.5. Ideally we only need the strips in which the target appears. However the interpolation of the background sky in a single strip does not always give an accurate representation of the true background sky due to the instrumental polarisation of FORS. If the sky is highly polarised the background flux will follow a similar pattern as shown in Figure 4.5. It is this pattern that can cause issues with SE's interpolation algorithm. This is due to the

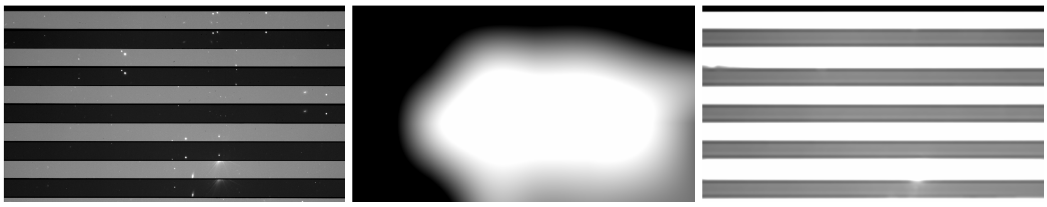

(a) Original image (b) Large mesh (c) Small mesh

Figure 4.9: Attempted background map of a FORS image using SE with the incorrect settings. The large mesh creates an average between parallel and perpendicular strips leading to poor representation of the background in the original image. A small mesh reproduces the stripped nature but at the cost of being influenced by background stars.

interpolation algorithm not having enough information to create an accurate smooth map of the background sky. For point sources this isn't really a serious issue as this region of the CCD is mapped quite well. However, if the target we are considering is an extended source like a comet, which can take up a considerable amount of the strip, SE has very little data over which to interpolate over which can lead to uncertainties in the background sky estimation. The only way to alleviate this issue is to give SE more data over which to interpolate. For this reason I stitch together several parallel or perpendicular strips to form a larger image. This is shown in panel (c) of Figure 4.10 where I have stitched together several parallel strips. If I use SE to create a background map using both a single strip and multiple strips, (panel (b) and (d) of Figure 4.10) we can compare the estimates. The best way to see the differences between the two estimates is to take one away from the other and examine the residuals; this can be seen in panel (e) of Figure 4.10. In this residual image the majority is the same (black region) where the count difference between the two maps is ± 1-2 counts, but in the centre where the comet lies the difference is around 100-150 counts or 4-6% higher in the single strip estimate compared to the estimate using several strips.

I will note that, depending on the intensity of the coma, SE can have problems deciphering what is coma and what is background sky, so it is important to pay attention to the background maps for any coma contribution in the maps and adjust the settings to compensate if there is.

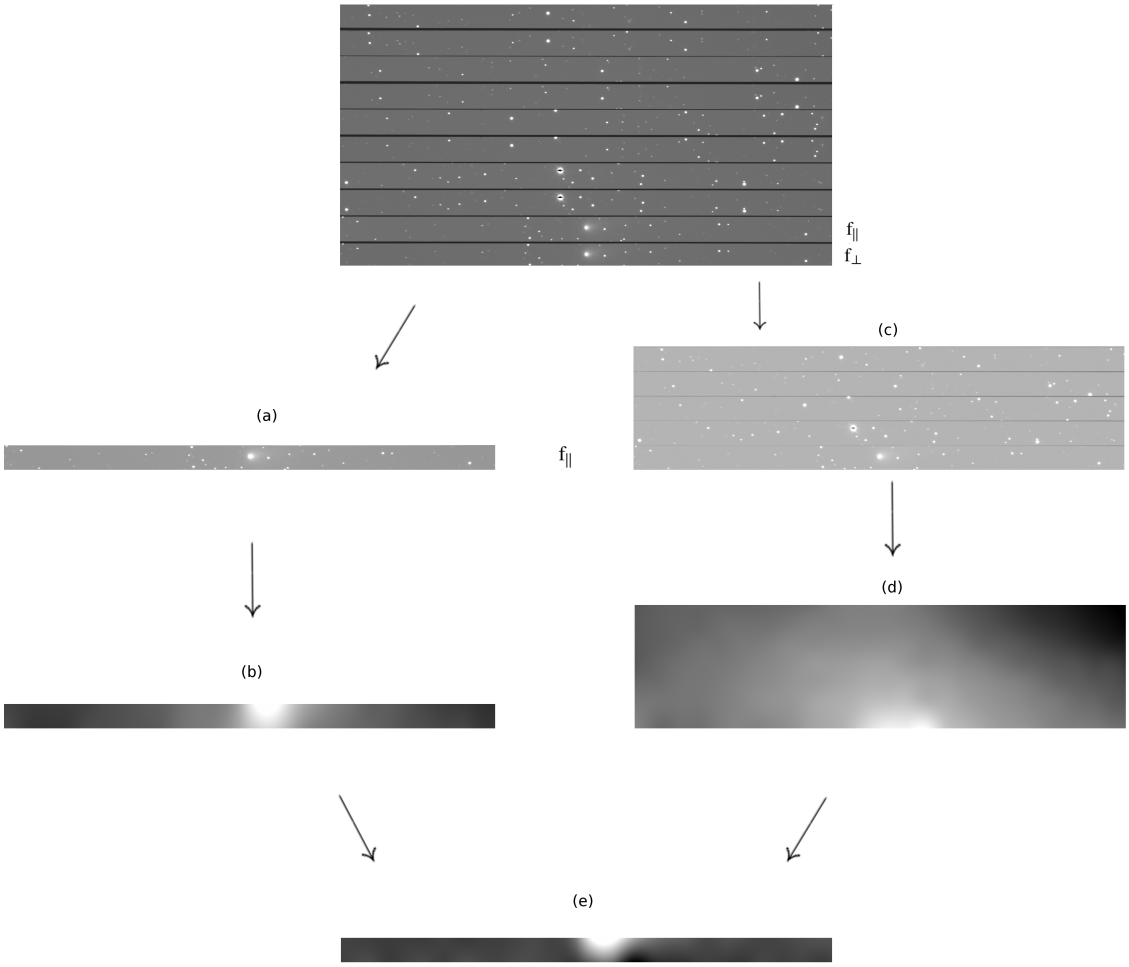

Figure 4.10: Two different approaches of estimating the background contribution using Source Extractor. Panel (a) considers only the parallel strip in which the target is located from the original image with its corresponding background estimate in Panel (b). Panel (c) considers all the parallel strips from the original image with its corresponding background estimate Panel (d). The difference between panel (b) and (d) is displayed as Panel (e).

Since in the coming sections I will be dealing with extended sources I will create the background maps for those targets using all the strips parallel/perpendicular. To further simplify things I will only use SE to calculate the background map for the data and then use IRAF to remove the background map from the data and to measure the flux. This way we only have one software package that measures the flux and we do not add any hidden systematic error that may occur when measuring the flux. The error for the SE measurements will have to be calculated slightly dif-

ferently from the other two methods outlined as we cannot use the value calculated for σ_B from Equation 4.11 from IRAF as the background has already been removed from the images. Instead we use the σ_B over a rectangular region around the target location. The result of this is a much lower σ_B calculated compared to the other methods and hence all measurements later discussed using this method will have a smaller error.

Using these two software packages and the three techniques to estimate the background sky mentioned above gives me the opportunity to investigate how background sky estimates affect polarimetric measurements.

4.5.1 Flat field effects on polarimetric measurements

The effect that flat fielding has on polarimetric measurements is quite subtle. Although correcting for flat field effects is important, one could argue that it is not a necessary step for polarimetric measurements since we use the beam swapping technique, summarised by Equation 4.5, meaning that the effect should cancel out as shown in Equation 4.14.

$$P_Q = \frac{1}{2}\left[\left(\frac{k_1 f^{\parallel} - k_2 f^{\perp}}{k_1 f^{\parallel} + k_2 f^{\perp}}\right) + \left(\frac{k_2 f^{\parallel} - k_1 f^{\perp}}{k_2 f^{\parallel} + k_1 f^{\perp}}\right)\right] \tag{4.14}$$

where k1 and k2 are the constants coefficients cause by the flat fielding in the parallel and perpendicular beams. We switch the notation of $f_{\parallel}$ and $f_{\perp}$ to $(I+Q)$ and $(I-Q)$ which are equivalent. Equation 4.14 then becomes

$$P_Q = \frac{1}{2}\left[\left(\frac{k_1(I+Q) - k_2(I-Q)}{k_1(I+Q) + k_2(I-Q)}\right) + \left(\frac{k_2(I+Q) - k_1(I-Q)}{k_2(I+Q) + k_1(I-Q}\right)\right] \tag{4.15}$$

With a little manipulation Equation 4.15 becomes

$$P_Q = \frac{1}{2}\left[\left(\frac{(k_1-k_2)I + (k_1+k_2)Q}{(k_1-k_2)I + (k_1-k_2)Q}\right) + \left(\frac{-(k_1-k_2)I + (k_1+k_2)Q}{(k_1+k_2)I - (k_1-k_2)Q}\right)\right] \tag{4.16}$$

By cross multiplying and simplifying Equation 4.16 we get

$$P_Q = \frac{IQ(k_1+k_2)^2 - IQ(k_1-k_2)^2}{I^2(k_1+k_2)^2 - Q^2(k_1-k_2)^2} \tag{4.17}$$

If we assume that $(k_1-k_2)^2$ will be a very small, and effectively zero Equation 4.17 becomes

$$P_Q = \frac{IQ}{I^2} = \frac{Q}{I} \tag{4.18}$$

The proof above shows that the flat field does not have an effect on the flux measured from the target. However, it does affect the estimation of the background sky. The reason for this is how the background sky is estimated. In the case of an annulus, a large area is used to estimate the background sky. Within this area there may be background stars or cosmic rays that get rejected as being deviant points. In the next set of images used to calculate the Stokes parameters these background stars will have moved and occupy a different location within the annulus. This means that two different sets of pixels have been used to calculate the background sky with two slightly different flat field characteristics. A similar situation occurs if the target moves by a small amount on the CCD, the annulus could encompass a different set of pixels. The same effect can occur when SE interpolates the background map, i.e different areas will have to interpolated over to generate the map. In this case it should not be as apparent as when using an annulus, as it is an interpolated fit rather than averaged value. Hence by not flat fielding one can over/under estimate the background sky estimate regardless of which software package is used. This also emphasises the importance of getting a good background estimation for polarmetric measurements. To show this effect I will compare the results of a 'before and after' flat field comparison for two types of target, with high and low signal to noise ratio.

The two targets used for this investigation are the Barbarian asteroid, 1998 RL_4, and a trojan asteroid of Jupiter, 1998 XO_{89}. In this case the barbarian asteroid is the faint, low signal-to-noise ratio target and the trojan asteroid is the bright high signal-to-noise ratio target. Both data sets have been reduced the same way using the procedure outlined in Section 4.1, once with flat fielding and once without. After the images have been reduced we use IRAF and SE to carry out aperture photometry on the targets and use Equation 4.5 to calculate P_Q and P_U. In Figure 4.11(a) and 4.11(b) we show how P_Q and P_U change as a function of aperture when flat fielding correction has and has not been applied for the trojan asteroid.

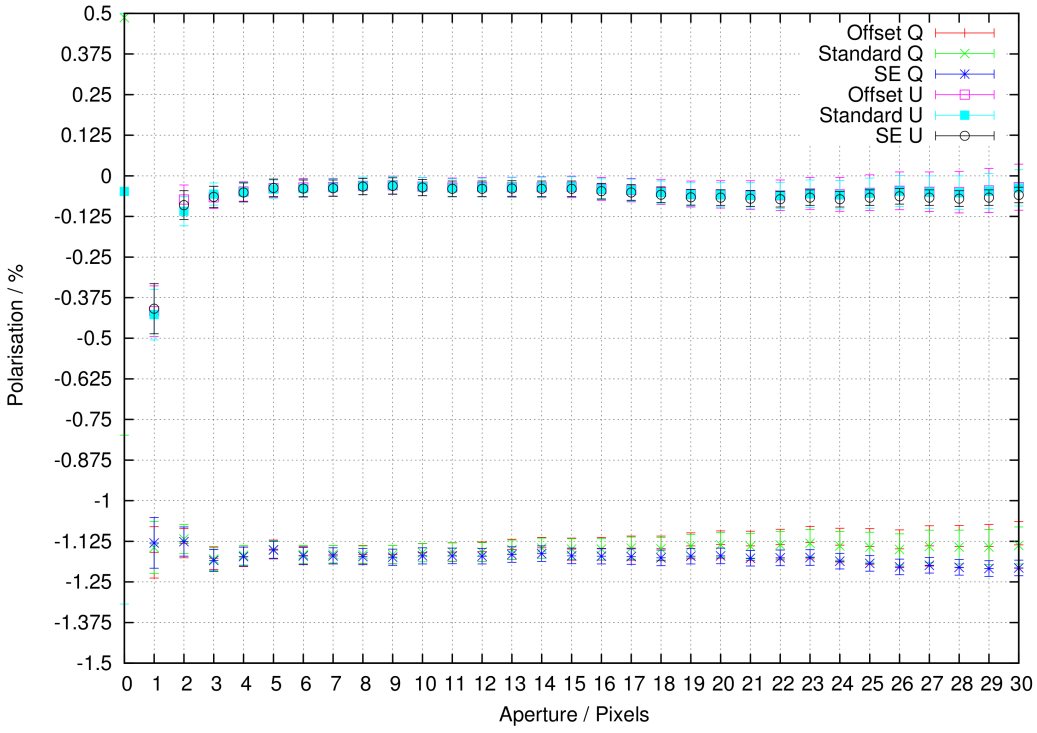

(a)

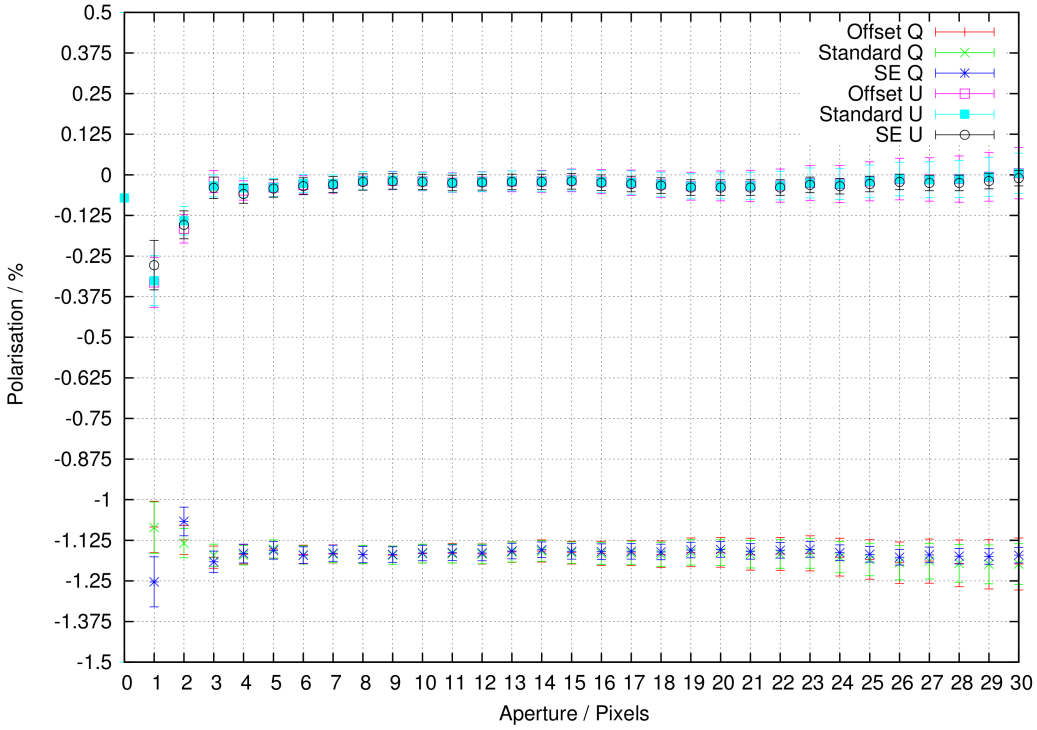

(b)

Figure 4.11: Stokes Q and U as a function of aperture when flat field correction has been applied (a) and when it hasn't (b) to a high flux count target.

In these figures data points labelled 'Offset' means that the background sky has been calculated using an offset annulus, 'Standard' means that the annulus was centred around the target in the standard way aperture photometry is typically carried out, and 'SE' means the background sky was calculated using Source Extractor. To make the difference between the two plots clearer I have taken the flat field corrected data away from the non flat field corrected data to best show the difference between them; this is shown in Figure 4.12.

From Figure 4.12 we can see that there is little difference whether we correct for flat field effects or not with this high flux count trojan data. Only slight differences occur at small apertures in P_Q. It is interesting that in P_U SE diverges from the other methods although both measurements are within the errorbars. This slight difference isn't surprising when we refer back to Equation 4.13; we can see from this formula that the error introduced by the incorrect background estimation will be damped down by the large number of flux counts, $f_{\|}$ and $f_{\perp}$, from the target. However, the error does start to become relevant and influence the measurement at large pixel apertures. This is due to these larger pixel apertures containing significantly more pixels,n(10 pixel aperture contains 314 pixels, 30 pixel aperture contains 2827 pixels) and so the error begins to build up.

If we now apply the same procedure outlined above to asteroid 1998 XO_{89}, in Figure 4.13(a) an 4.13(b) we can see the comparison between when flat field correction is applied and when it is not in the case of the low flux count barbarian asteroid. Again, to clearly outline the difference between these two plots, I have removed the flat field corrected data from the non flat field corrected data to show the difference between them; this is shown in Figure 4.14.

For this low signal to noise ratio target we can see there is a noticeable difference between the two methods. Both the standard and offset annulus method of background sky estimation show a noticeable difference, even at small apertures. A difference of approximately 0.125% for a 12 pixel aperture is a considerable amount on a polarimetric measurement. However SE shows the smallest difference in Stokes Q and Stokes U even for larger apertures, suggesting that the background

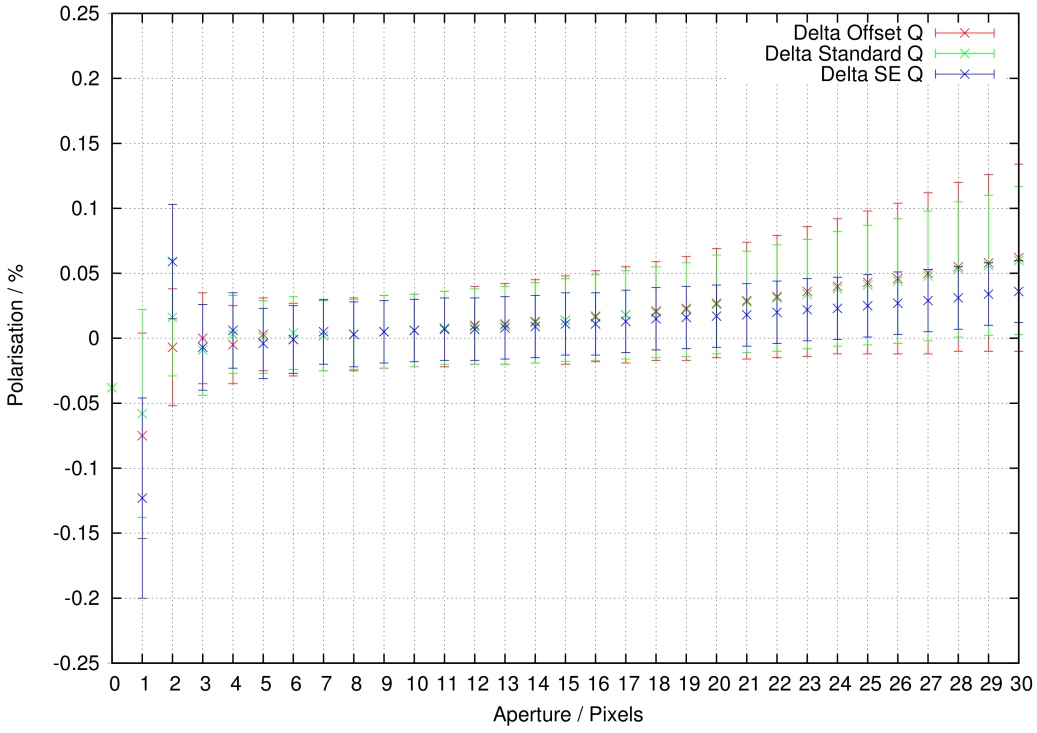

(a)

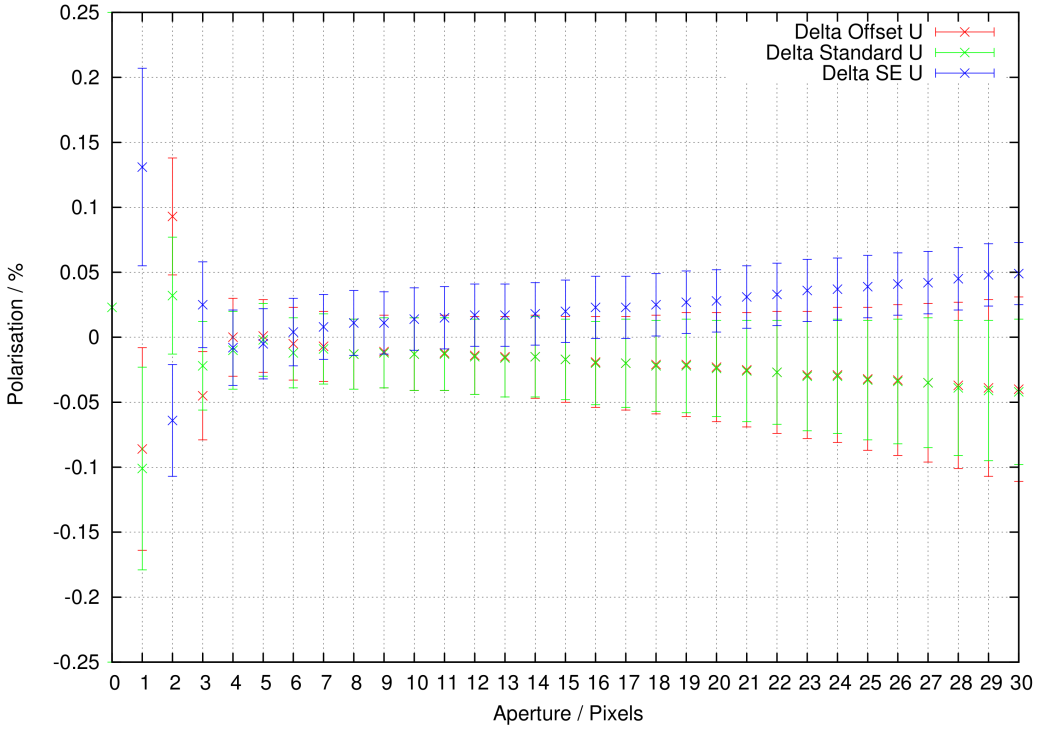

(b)

Figure 4.12: Difference plot between Stokes parameters of the trojan asteroid measured with and without flat fielding.

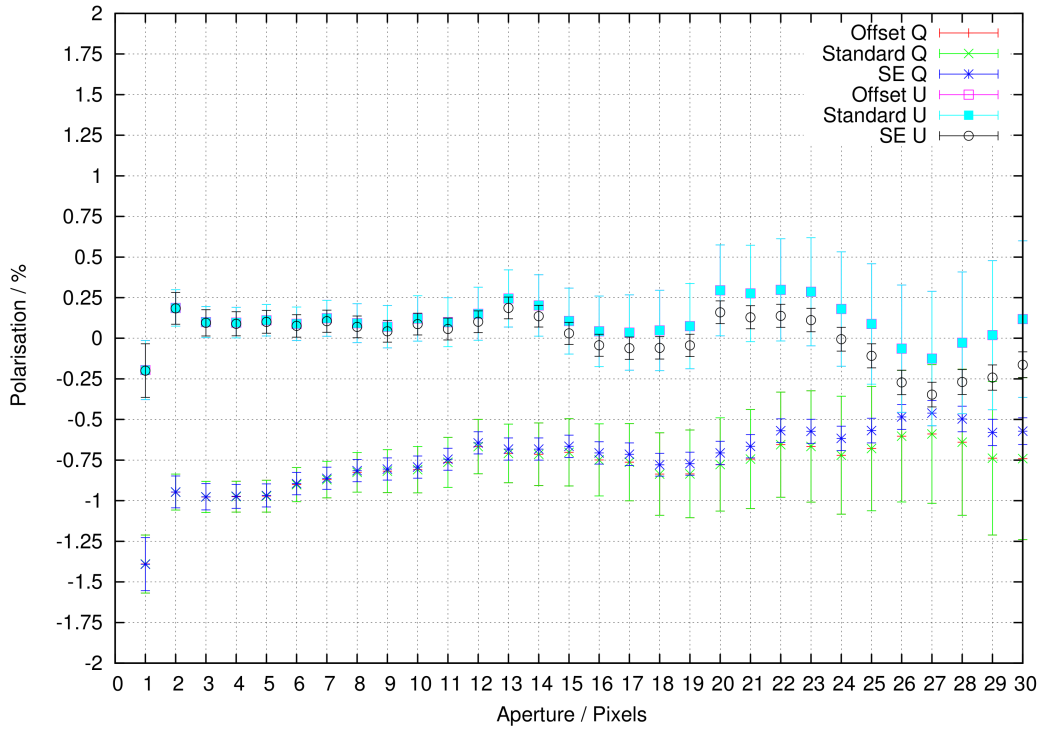

(a)

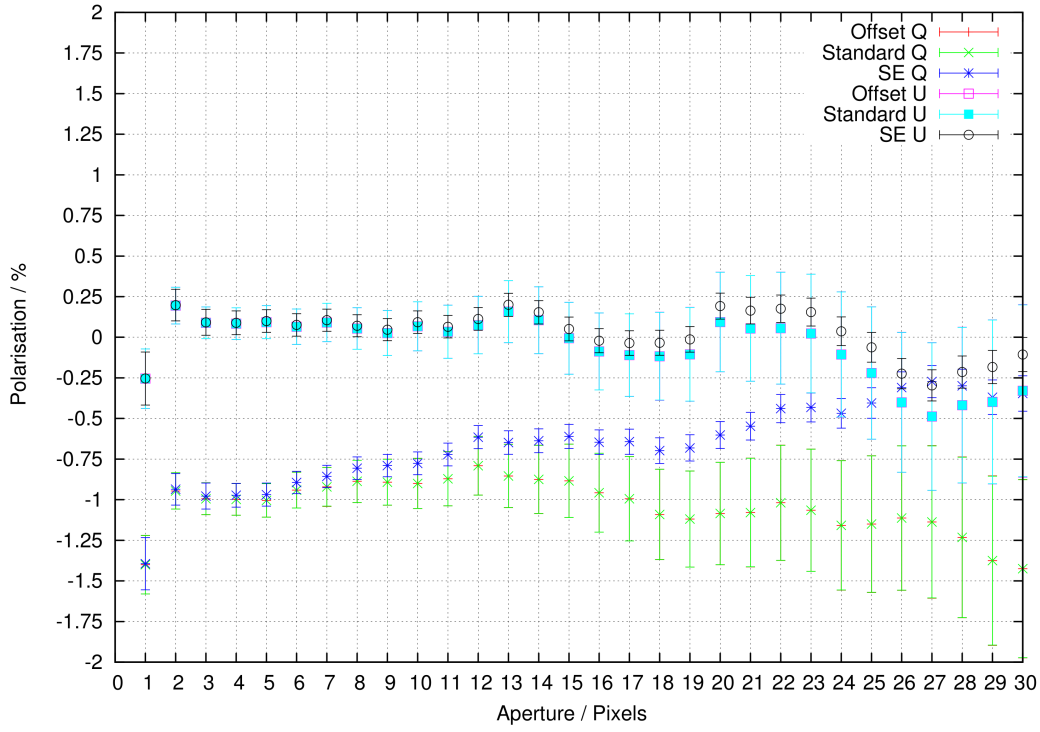

(b)

Figure 4.13: P_Q and P_U as a function of aperture when flat field correction has been applied (a) and when it hasn't (b) to a low flux count target.

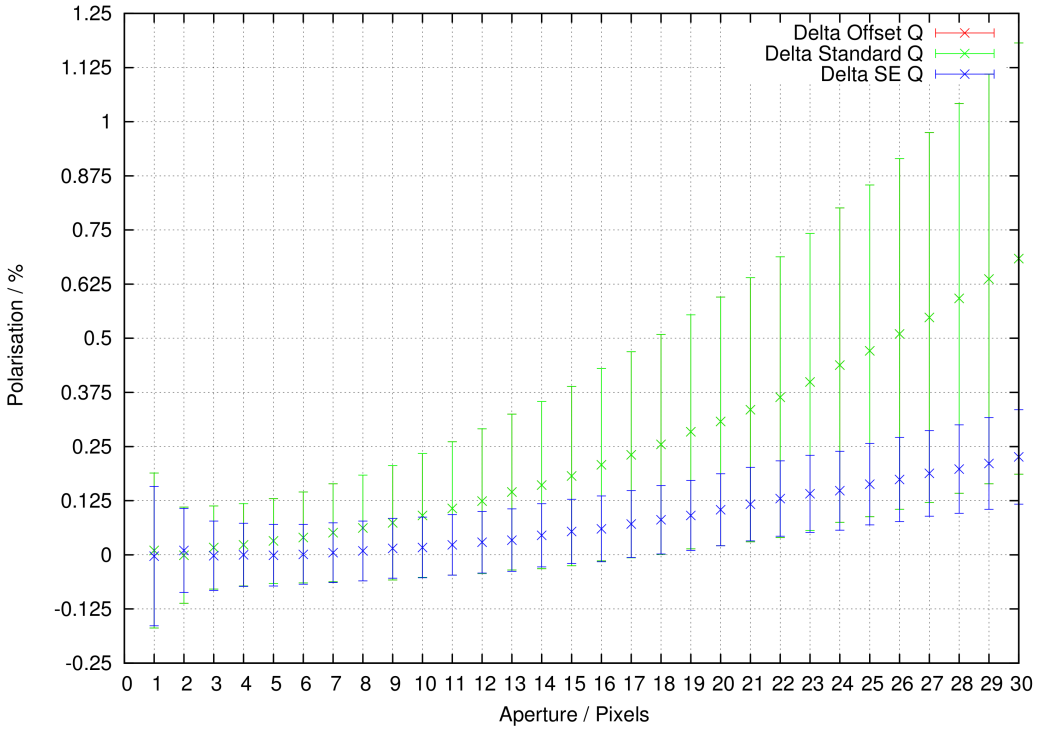

(a)

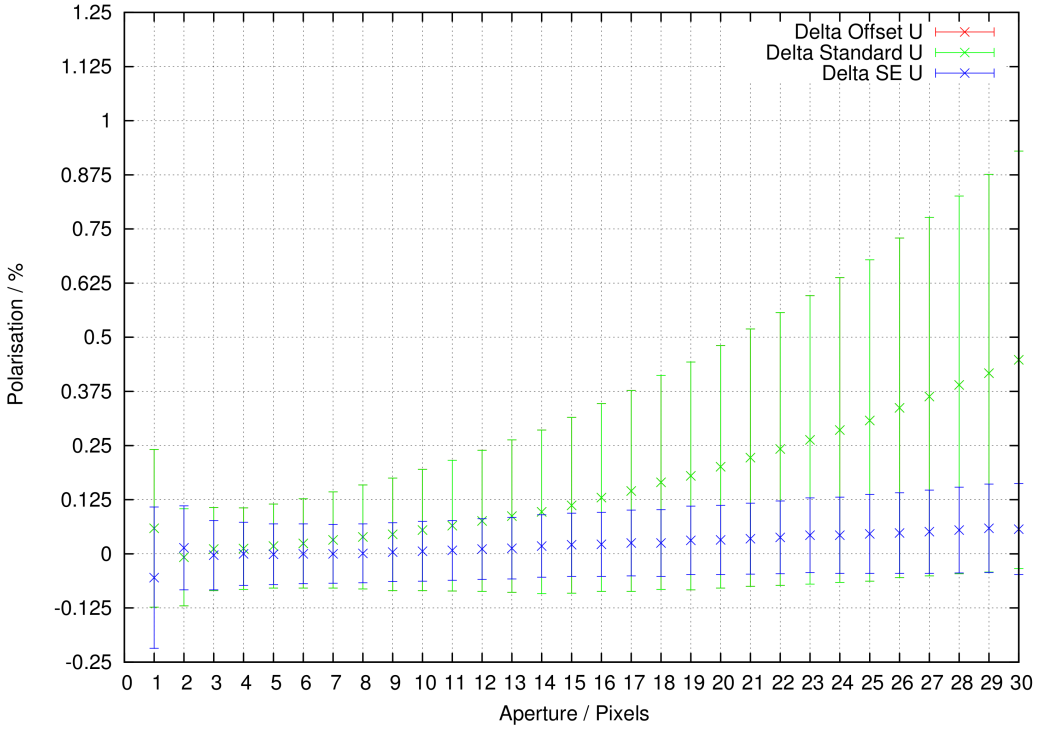

(b)

Figure 4.14: Difference plot between Stokes parameters of the barbarian asteroid measured with and without flat fielding.

estimations are less affected by the flat field effect. However yet again the measurements of all these methods are within the error of each other mainly due to the large uncertainty on the measurement. As mentioned before the reason for this larger error is due to the error in the estimate of the background sky being propagated though Equation 4.13, since the flux counts from the target are low, it is not being suppressed in the same way as in the example for the trojan asteroid. This 0.125% becomes very significant when measuring the polarisation from a target that may exhibit small amounts of polarisation, e.g., large TNOs. Even for asteroids that can have a polarisation of -1 to -1.5% at their minimum, it is a considerable amount, particularly if we are interested in determining the taxonomy of an asteroid, i.e. the value of the polarisation minimum and the slope of the curve through the inversion angle.

In this small investigation I have shown the importance of reducing the CCD images correctly when it comes to polarimetry. It also shows the importance of the background sky estimation when it comes to obtaining accurate polarimetric measurements. Furthermore it outlines the importance of observing a target with as high as possible signal to noise ratio to avoid large errors inferred by background sky estimation.

This now leads us to investigate which method of estimating the background sky is the best approach of the various scenarios one can encounter when measuring the polarisation properties of Solar System bodies.

4.5.2 Low polarisation targets

The first scenario we can encounter in Solar System science is when the object we are considering is a low polarised source, for example the TNO Makemake. Makemake is a relatively faint source with an apparent magnitude ~ 17. For this example the area around the target and the location of the offset annulus was free from any background stars. The effect of using the three different background estimate methods on the results is shown in Figure 4.15.

All three methods give slightly different values for Stokes Q and U but they are so slight they can be deemed to have calculated the same value within the un-

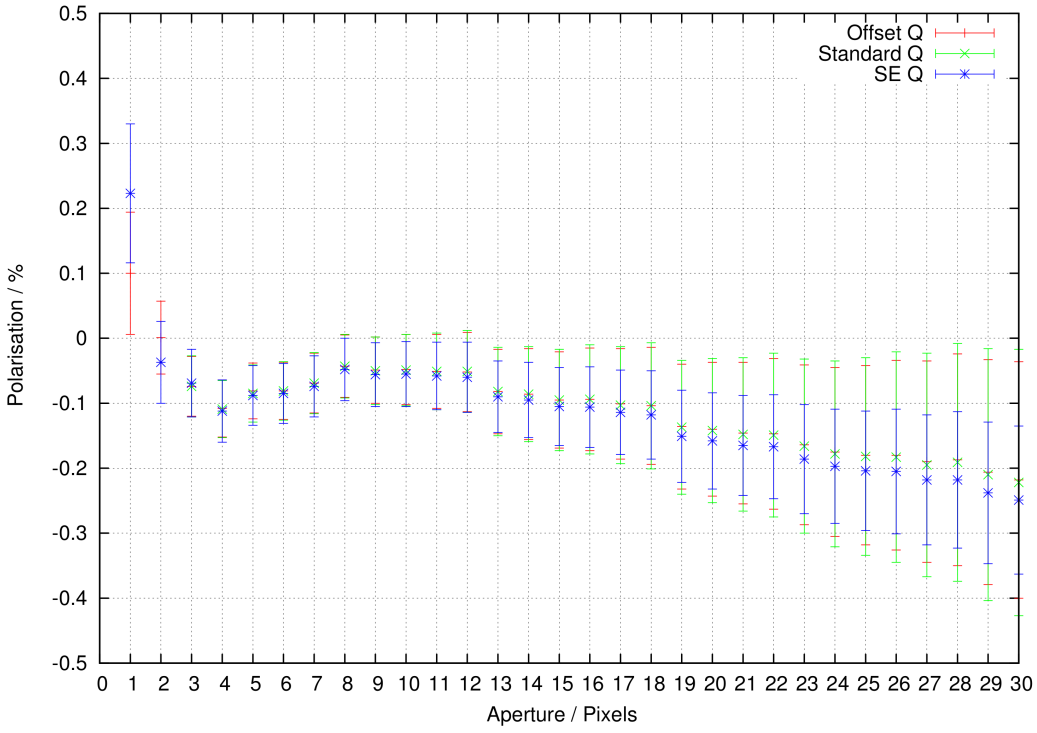

(a)

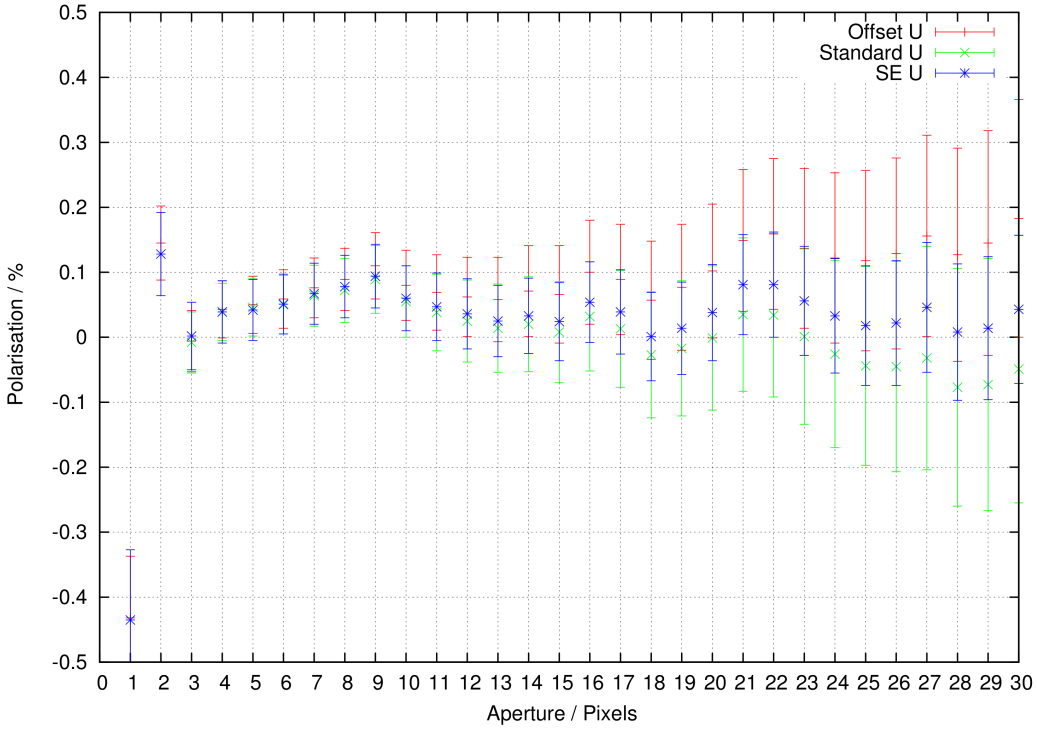

(b)

Figure 4.15: Stokes Q and U as a function of aperture for the low polarised large TNO Makemake.

certainty of the measurement. Any difference is purely down to a slight difference in the background sky estimation. The difference in the relative size of the errorbars is simply due to the standard deviation in the background sky. At low aperture size this difference is negligible but as we see at larger apertures it does begin to alter the size of the error bar simply due to Equation 4.11.

4.5.3 High polarisation targets

The second scenario that we may encounter is when the target shows high polarisation, for this example I will use data taken of the small TNO, Huya. Huya has an apparent magnitude ~ 19 which is fainter than Makemake, but the exposure time has been adjusted to reflect this, so that they have a comparable signal to noise ratio. As was the case for Makemake the background around the target and at the position of the the offset annulus was clear of any background stars. The results are shown in Figure 4.16. Both the standard and offset method had almost identical background sky estimations so the difference between the calculated values of Stokes Q and U is so small it cannot be seen in Figure 4.16. Using the SE method we get a slightly different value for Stokes Q, but as was the the case for Makemake the difference is so small they are practically the same result. However in Stokes U SE does begin to deviate from the other methods and from zero. Beyond an aperture of 12 pixels the deviation from zero starts to cause concern in the validity of the result. All three methods show the same variation, i.e peaks and troughs, as a function of pixel size used, showing they are being influenced in the same way. We can find no obvious reason for SE's deviation in the Stokes U measurement.

4.5.4 Extended source targets

The third scenario we may encounter is when the target is an extended source. For this example I have chosen data of the comet 74P/Smirnova-Chernykh. Needless to say the area around the target will be contaminated by the coma and tail of the comet. Because of this we expect the standard method to be incorrect due to the overestimation of the background sky. Additional attention should be given to Source Extractor's background estimation in this case as it can mistakenly try and

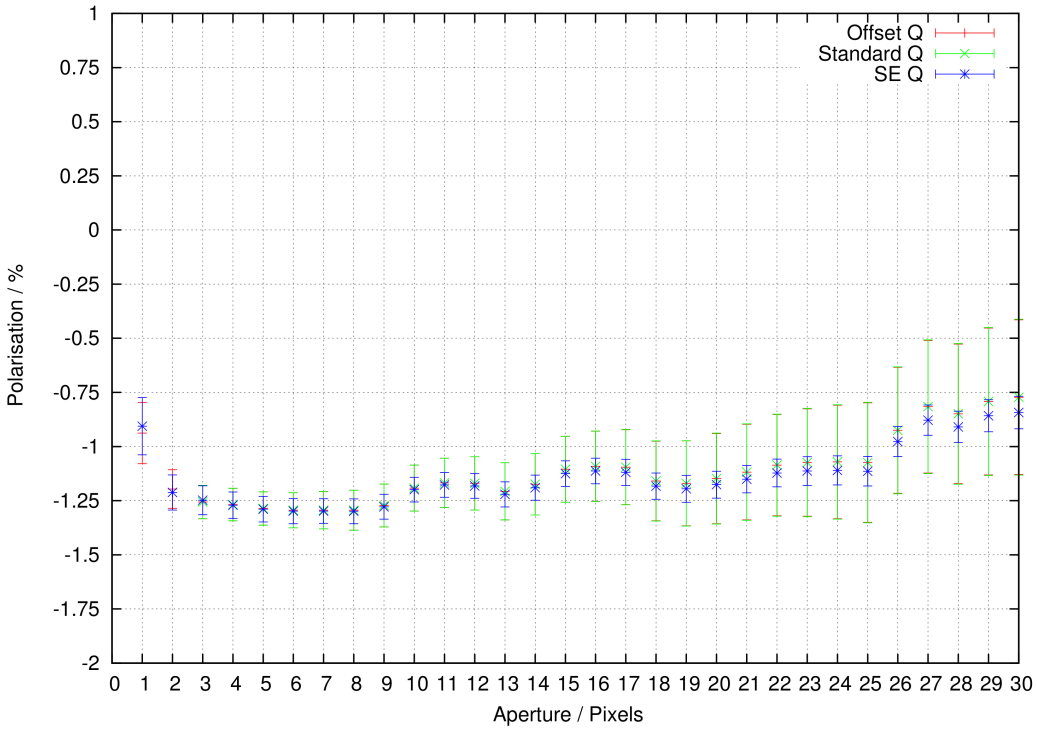

(a)

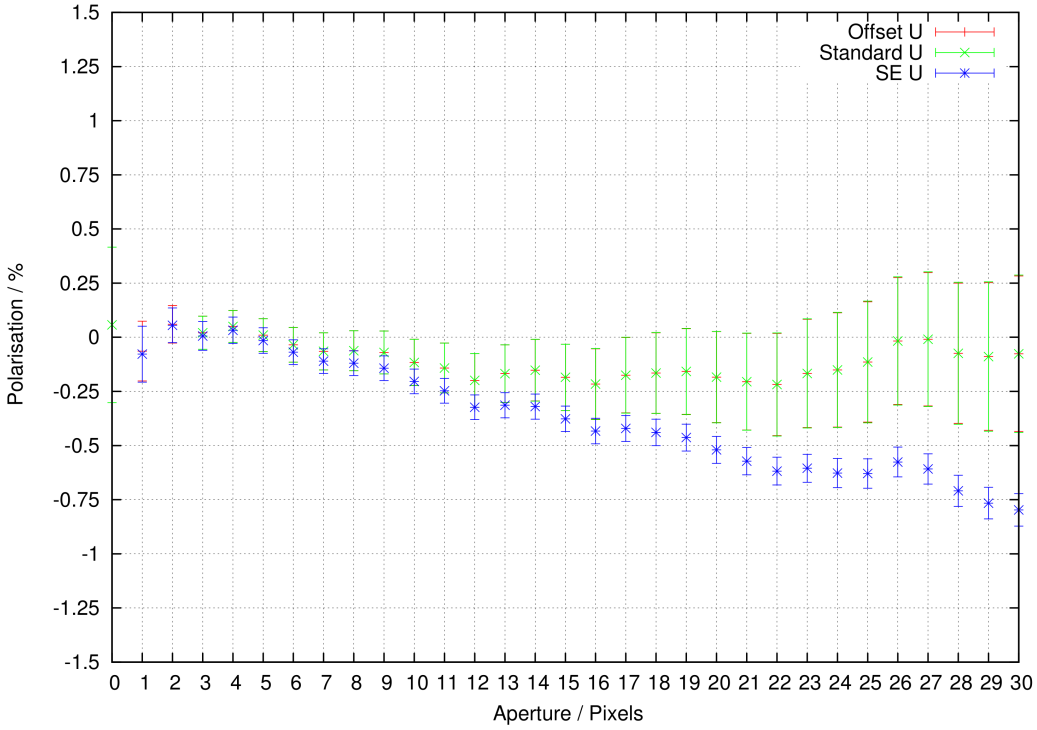

(b)

Figure 4.16: Stokes Q and U as a function of aperture for the high polarised small TNO Huya.

map the coma and tail if the settings in SE are not set correctly or if the coma/tail are very faint. So it is best to check the background maps that SE produces for any evidence of this. I will also note that the location of the offset annulus was contaminated by a few faint background stars, but the rejection algorithm inside IRAF should remove these with only a minimal contribution. The results are shown in Figure 4.17(a) and 4.17(b).

Even though the standard method is contaminated by the coma the Stoke Q does not deviate as much as expected and is quite similar at small apertures to the results from the other methods. Both the offset and SE methods give very similar results over all aperture sizes. Interestingly when we look at Stokes U results in Figure 4.17 we can see that regardless of the method used, Stokes U is approximately zero for the majority of the aperture sizes.

Source Extractor in theory offers the best form of background subtraction as it creates the background map without the comet and tail present provided the settings are correct. However this is not always the case as usually there is a contribution from the coma in the background maps. Even though the offset annulus can escape some of the contribution from the coma you are never guaranteed to be free from coma contamination and instrumental effects.

4.5.5 Highly polarised background sky

This scenario arises when polarimetric measurements are taken on nights when the Moon is nearly full or close to our target and are usually avoided due to the highly polarised background sky. However sometimes we have to endure this to get phase angle information or because of unlucky service mode observations. For an example of this we have selected data of the main belt comet 133P. The background flux in the parallel strip is approximately double that of the perpendicular strip. The coma and tail present was minimal and should not influence the results in any way, but I will note that the signal to noise ratio is low. The results for this example are shown in Figure 4.18(a) and 4.18(b). Both the standard and offset methods show very similar results. However Source Extractor gives a different result by around 0.5-1% in Q and $\sim 0.5\%$ in U. Since the signal-to-ratio of the data was low, I will

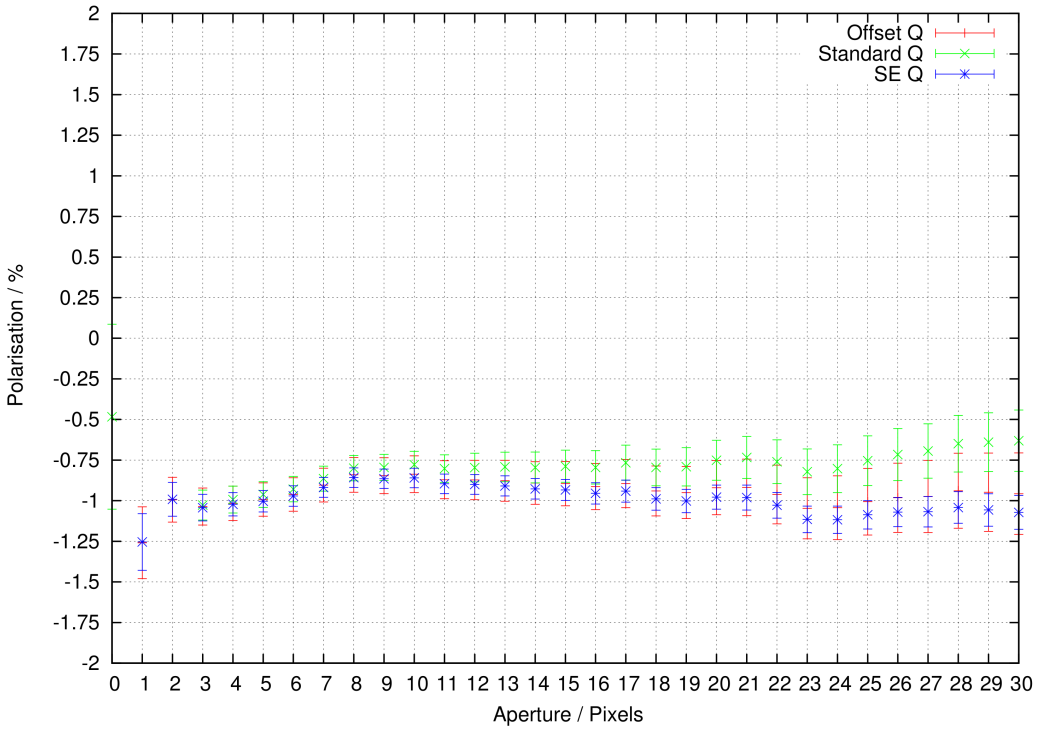

(a)

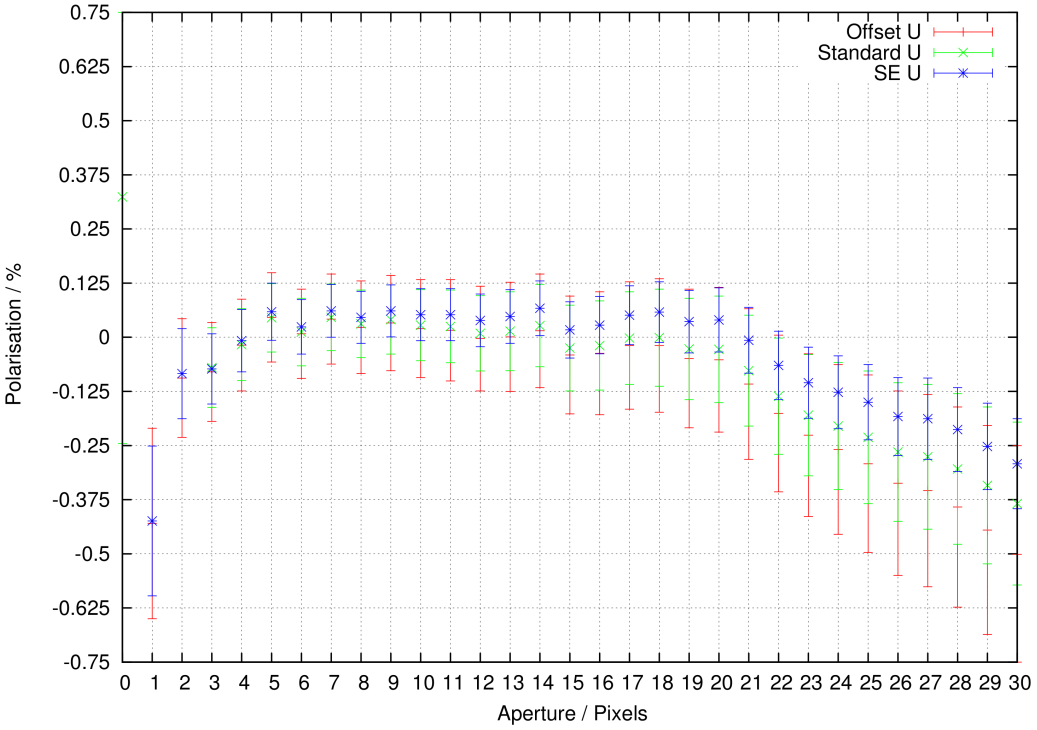

(b)

Figure 4.17: Stokes Q and U as a function of aperture for the extended source target comet 74P.

also do the same test on a high signal-to-noise case. The best example I found was of an observation of a gamma ray burst. Even though this has nothing to do with observations of a Solar System body, it is a good example of the high polarised sky. The results of these data are presented in Figure 4.19.

In this case at small aperture sizes all three methods give similar results. However, beyond an aperture of 8 pixels SE begins to deviate from the other two methods. In both the case of 133P and the GRB SE is influenced by features in the background. In the case of 133P there are many faint background stars close to the target location giving it less data to interpolate over and hence giving a rather poor estimation of the background. In the case of the GRB there is a very bright source that is blocked by the Wollaston mask although diffraction lines still appear close to the target area. Such is the shape of these lines the interpolation fails to deal with them correctly and hence we see a deviation beyond a 8 pixel radius.

Testing these three methods of estimating the background sky has led to some interesting results, namely, the difference shown between the results calculated using Source Extractor compared to the other two. An explanation for why the difference is so large in certain occasions is that we know that the error on results calculated by Source Extractor are an underestimate as the statistical errors on the creation of the background map are not fully revealed by Source Extractor. This means that the true error bar could be within the measurements of the other methods used to calculate the background sky. However it is clear that in the case of a crowded target region SE does not perform an accurate job of estimating the background sky. The reason for this is that SE was designed to work on galaxy survey data which comprised lots of data and the main goal was to do this quickly, with the sacrifice of accuracy.

With all these results it is hard to say whether one single method is better than the rest, however with the doubt on Source Extractor results in some cases, it would be probably best to use a combination of the standard and offset method when applied to polarimetry data.

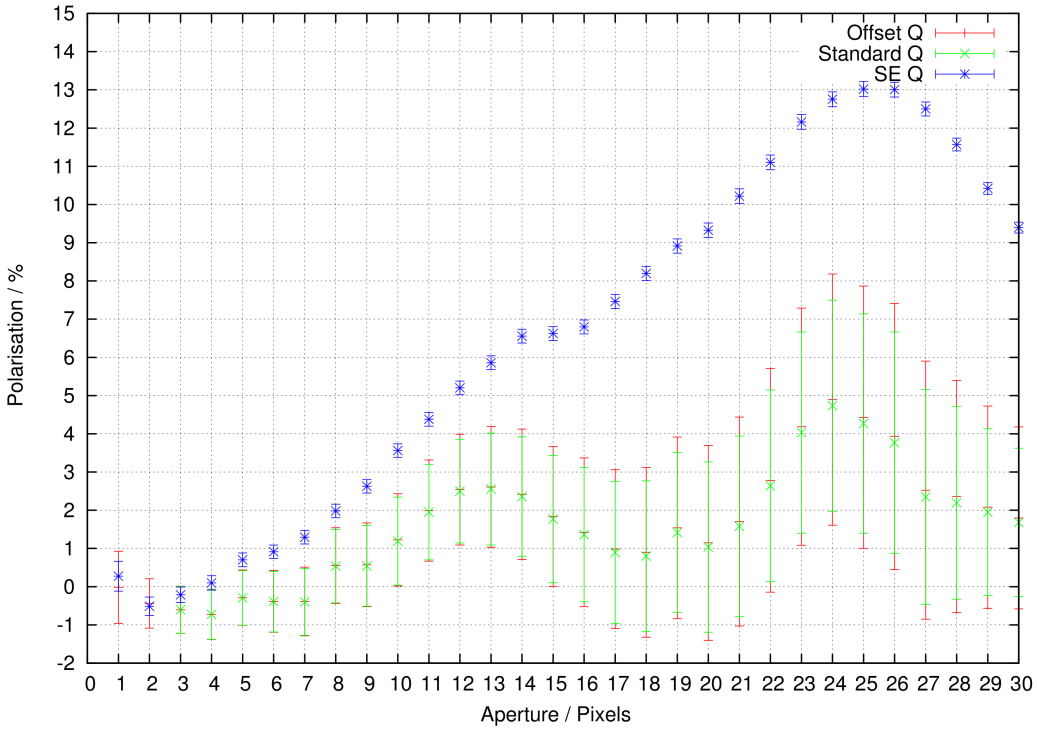

(a)

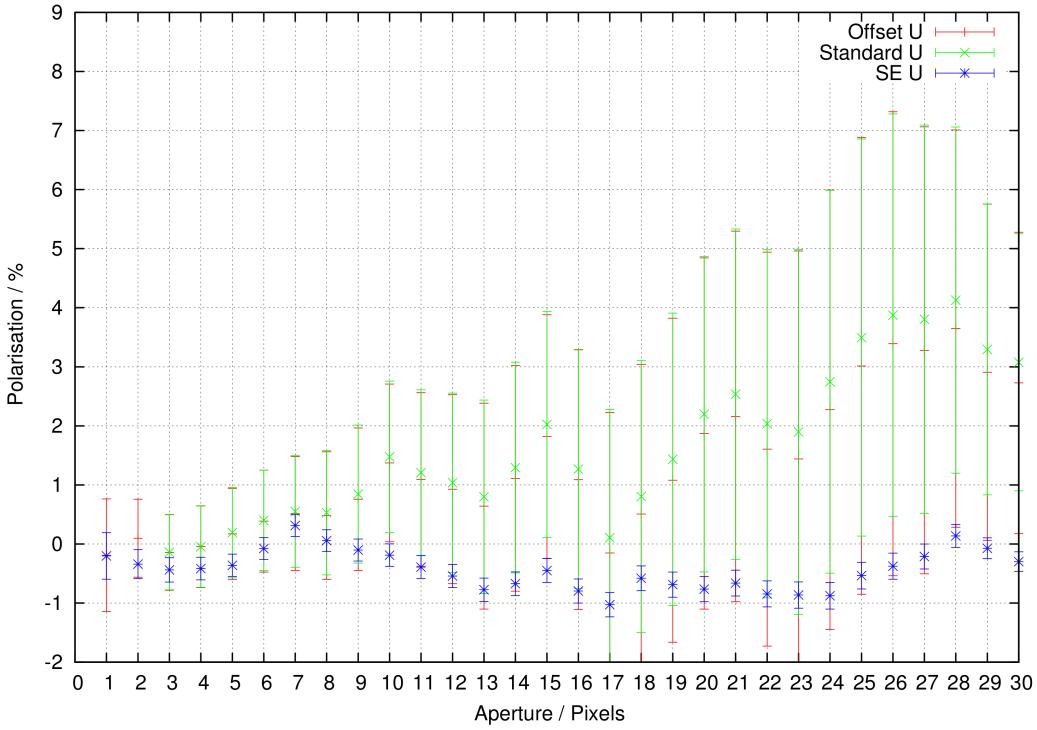

(b)

Figure 4.18: Stokes Q and U as a function of aperture when for the high background polarised main belt comet 133P.

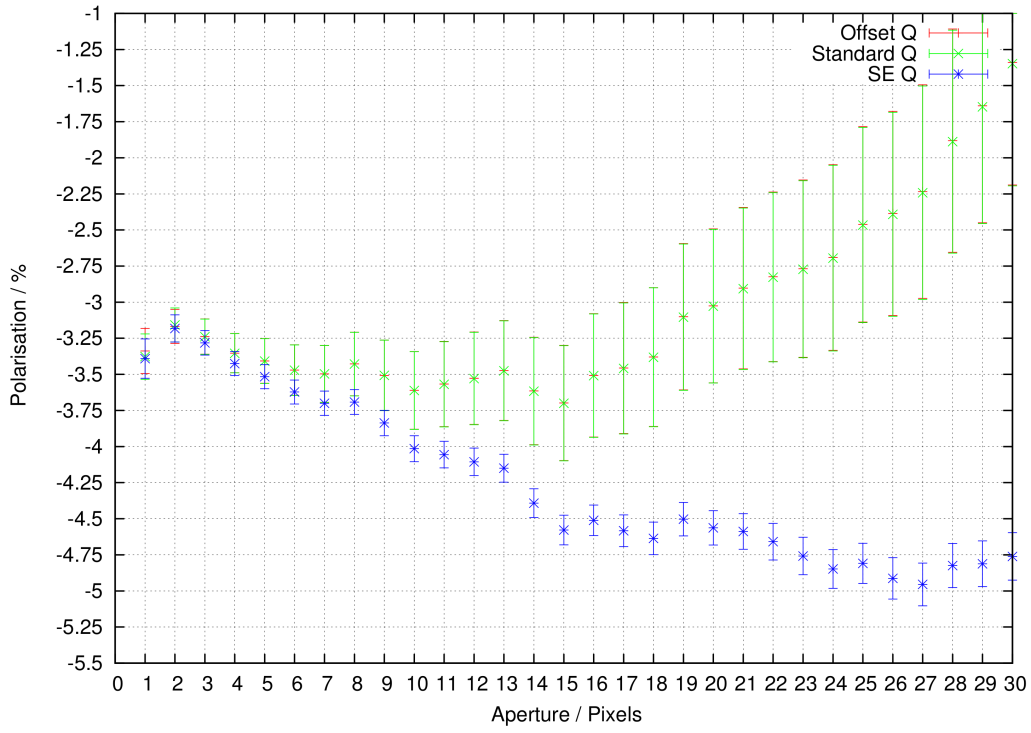

(a)

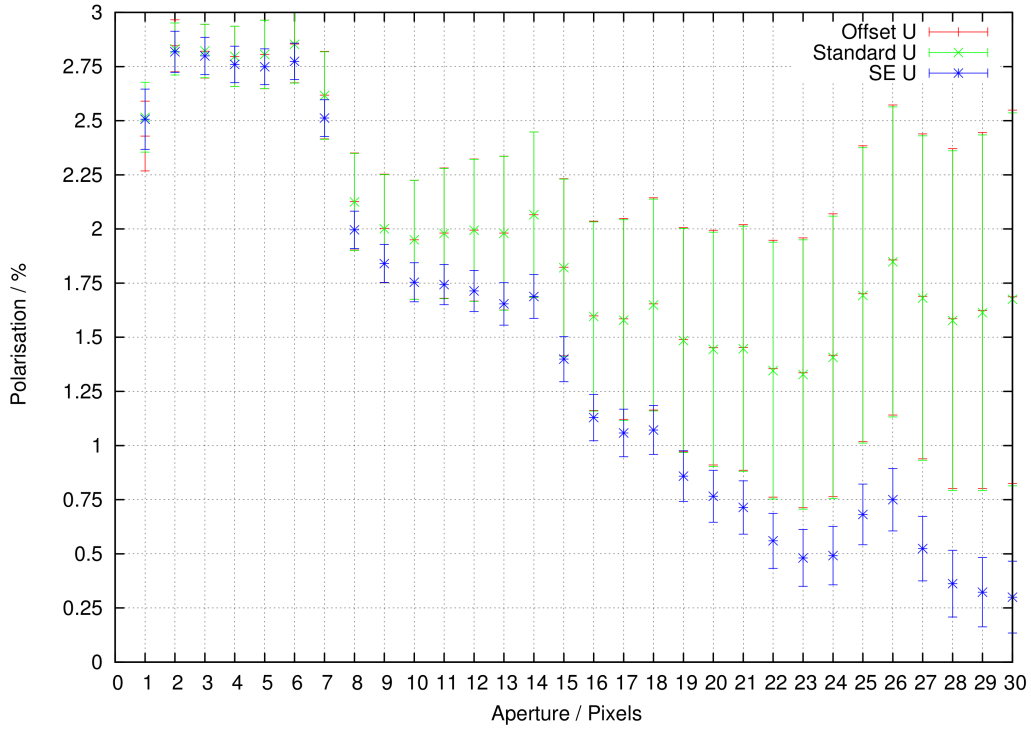

(b)

Figure 4.19: Stokes Q and U as a function of aperture for the high background polarised Gamma ray burst.

4.6 Deep imaging

This technique is a by product of polarimetric measurements. Since polarimetry requires a high signal to noise ratio and several different images to measure P_Q and P_U this means we have a series of many high signal to noise ratio images of the target. Combining all these images in the way we outline below will result in an image with an extremely high signal to noise ratio far above what one could achieve through a single exposure as this would likely saturate the CCD. It has been used in various publications, Boehnhardt et al. (2008) and Bagnulo et al. (2010), to search for faint coma activity around asteroids and comets that may not be clearly visible in the individual photometric or polarimetric images.

To form a deep image we consider the flux from the parallel and perpendicular beams as two separate images. From aperture polarimetry we have the location of the photometric centres of the target in both the parallel and perpendicular beams in all images. We can use these photometric centres to shift the parallel beam to an arbitrary fixed point, and then shift the perpendicular beam to the same arbitrary point. The result of this shifting is that we now have two new images from the original that have the target centred in the same point, as shown in Figure 4.20. This process is repeated for all polarimetric observations taken on the same night. For example if we have observed a target using 8 different retarder positions, we would have 16 images (8 parallel and 8 perpendicular images) each with the target in a common centre. We then subtract the background sky from each of these new images using the values calculated during the aperture photometry for the parallel and perpendicular beams. We also convert the flux from ADU to electrons and then divide by half the exposure time to get the number of photons per second. We divide by half the exposure time as each strip represents half of the total intensity I due to the Wollaston splitting the light into its parallel and perpendicular components. Therefore when we combine all the strips the flux should be in electrons per second. Since all these images have the target positioned at the same central location we can simply co-add the images together using an average σ clipping algorithm. This σ clipping algorithm is a rejection method for removing pixels that are not

representative of the pixel values, i.e. values that vary by more than a few standard deviations from the average pixel value. Additionally, because of the average sigma clipping algorithm we may also have the chance to remove the influence of some of the background stars if the field of view is moving quickly. This can occur because the average σ clipping algorithm will see the flux from the background star as out lying points and remove them from its consideration of the background value. This clipping algorithm isn't well suited when the background flux is comparable to the flux of the background star. However, we use a median σ clipping algorithm which will look for the middle value of all the considered background fluxes, and since the flux from a background star is likely to be the largest flux it would be rejected. In most cases an average σ clipping algorithm is used as it is more statistically robust compared to the median. However, if the target passes in the vicinity of near by stars that move slowly and influence the deep image the median σ clipping algorithm can remove the influence of these stars more effectively compared to the average σ clipping algorithm.

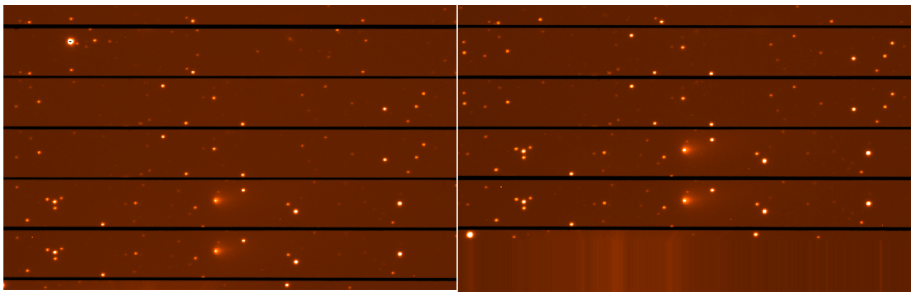

Figure 4.20: Illustrating the shifting of the parallel beam (left) to a fixed point and moving the perpendicular beam (right) to the same point.

4.7 Colour maps

Colour is often used in Solar System science to highlight differences in magnitude through different broadband filters or to define the spectral gradient of an object. This is done via aperture photometry, since for the majority of Solar System bodies, which are essentially point sources, this is the only meaningful way to measure the colour. However, for extended sources like comets it can be more fruitful to create

a colour map so that if a colour change is detected it is easy to investigate whether it occurs globally over the comet or in a localized area. For this reason we can create colour maps using the photometric frames in two different filters. In this section we discuss how these maps are created using observations taken with the FORS instrument.

Typically with observations from FORS we have multiple exposures taken using the same filter, so it is a good idea to combine these to get the highest signal-to-noise ratio colour map possible. To create the colour maps we first need to remove the background sky from each image separately. We must do this individually as the residual second order flat field effect present in FORS images varies as a function of distance across the CCD.

To remove the background sky from the photometric images we created a 'full resolution' background map using SE. Not only does this background map estimate the background sky but also fits the second order flat field effect. We prefer this method of background removal over a simple offset annulus estimation as the annulus only gives an estimation on a very localized spot on the CCD and typically a comet's tail will extend over a much larger distance. However, the background maps need to be carefully checked to ensure there is no coma contribution in the background sky estimation. If there is a coma contribution one can either change the settings in SE or use an offset annulus if the residual coma persists. The background estimate is then simply subtracted from the photometric images. The comet in each photometric image was then shifted to the same position using the photometric center of the comet calculated to one thousandth of a pixel. This is then done with the two broadband filters that the comet it has been observed in. After this has been done then it is a simple case of converting each pixel into a magnitude and creating the map by subtracting the two sets of images from each other. This technique will be used later in Chapter 6 when we discuss the results from the comets 74P/SmirnovaChernykh, and 152P/HelinLawrence.

4.8 Polarimetric maps

As mentioned in Section 4.7 creating maps over the whole comet allows us to investigate small scale structures within the coma and tail. Similar to the colour maps described previously, changes found in a polarimetric map would be due to changes in the size or composition of the scattering media.

Creating these maps is a much more laborious task than creating the colour maps of Sect. 4.7. The reason for this is that we can not easily remove the background sky from an entire polarimetric FORS because the background sky is polarised causing a discontinuity of the flux counts in the parallel and perpendicular beam. SE's interpolation algorithm cannot create an accurate estimation of the background sky due to this stripped nature. Depending on the settings used the interpolation will either contain an averaged out flux count from both strips or create a transition area where the background flux gradually changes from extreme to extreme, as seen in Figure 4.9. Even if we separate the strips into parallel and perpendicular strips SE's interpolation algorithm has trouble creating a background map if the target is an extended source. Hence in these cases we have used an offset annulus to calculate the background sky. This annulus should ideally be placed at a location where it should be free of coma contribution. However FORS suffers from instrumental errors the further you travel from the centre of the CCD due to a stressed element in the optical train. For this reason the annulus was placed in a location that minimized the instrumental effects and the contribution of the coma.

Once the background sky has been estimated and removed from these strips we use Equations 4.5 and 4.6 to create P_Q and P_U maps for each comet. This is summarized in Fig 4.21. The disadvantage with this method is that to utilize all the retarder positions used for these comets we will have to remove the background sky 16 times. If we assume we incur a small error each time we create a background estimate it could become significant to the accuracy of our results. A better method is to combine the images using Equation 4.19 and remove the background sky at the end, this is outlined in the equation

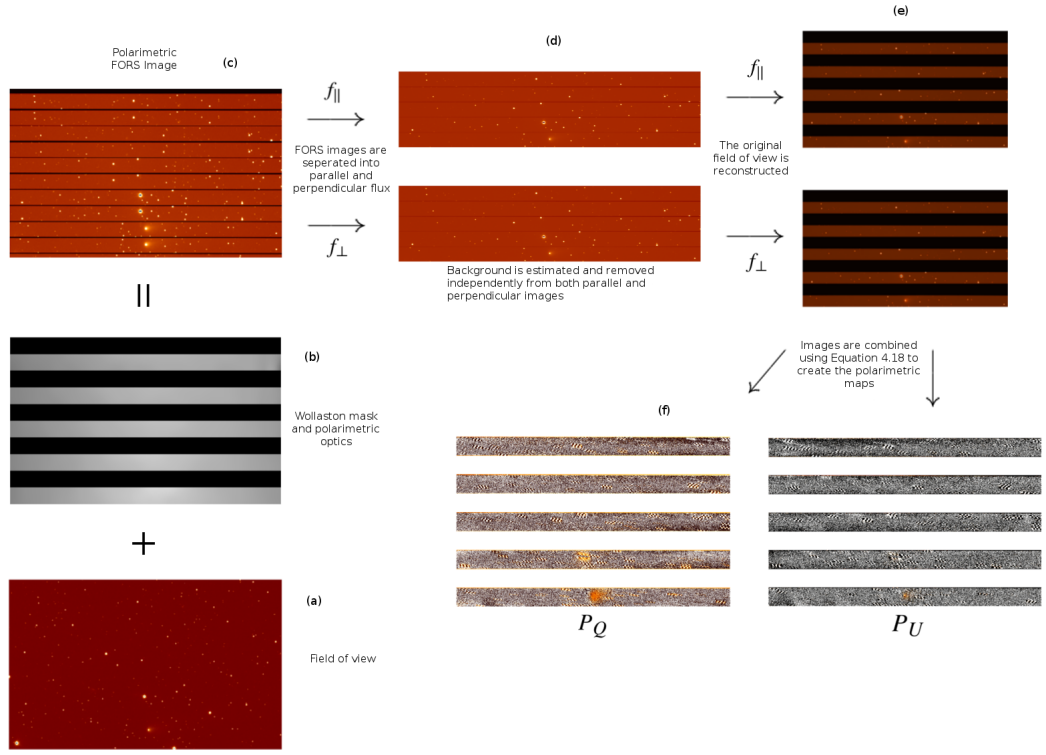

Figure 4.21: Basic representation of how the polarimetric maps were created from a FORS image.

$$P_X = \frac{\left(P_X^{\rm tot} \times I_X^{\rm tot}\right) - \left(P_X^{\rm sky} \times I_X^{\rm sky}\right)}{\left(I_X^{\rm tot} - I_X^{\rm sky}\right)} \tag{4.19}$$

where $P_X^{\rm tot}$ is the total Stokes parameter without any background sky subtraction, $I_X^{\rm tot}$ is the total flux counts of the images used to calculate the Stokes parameter, $P_X^{\rm sky}$ is the background estimate of $P_X^{\rm tot}$, $I_X^{\rm sky}$ is the background estimate of $I_X^{\rm tot}$. This method is numerically the same as Eq.(4.5) but here we only have to create two background maps instead of the 16 times previously, hence the error is reduced.

Chapter 5

Polarimetry of Atmosphereless bodies of the Solar System

5.1 Barbarian Asteroids

Barbarian asteroids are a type that exhibit unusual polarimetric properties. The phase angle when polarisation changes from negative to positive, $\alpha_{\rm inv}$, tends to occur at much higher phase angles than that of other asteroids. They are called barbarians after the first asteroid that was found to show this behaviour (234) Barbara (Cellino et al., 2006). Barbara belongs to the very rare L-type taxonomic class. Since the first discovery 5 more Barbarian asteroids have been found (Gil-Hutton et al., 2008; Masiero & Cellino, 2009). All 5 of these asteroids belong to the L, Ld, and K taxonomic class, however it should be noted that not all L, Ld, and K asteroids are barbarians. There have been several explanations put forward to help explain the unusual polarimetric properties, from peculiar surface composition to the presence of large craters on the surface; see Cellino et al. (2014) for more information. However, the exact reason why barbarians show this unusual behaviour is still unknown. In this section I present the observations of 9 candidate barbarian asteroids, (129) Antigone, (105) Artemis, (246) Asporina, (109) Felicitas, (444) Gyptis, (253) Mathilde, (201) Penelope, (5492) Thoma, and (729) Watsonia.

5.1.1 Observations

The observations of all 9 asteroids were carried out in service mode from August to December 2011 by the RINGO2 instrument mounted at the Liverpool Telescope in La Palma. For a description of the RINGO2 instrument see Section 3.4.2. For these observations we followed the recommendation of the instrument scientists and used the same instrumental setup as used to observe the standard stars. This means we can easily use the standard stars provided as part of the calibration plan for the instrument. Typically 3-4 zero and high polarised standard stars were observed every night to provide the necessary correction for the instrumental polarisation. Zero polarised standard stars are used to determine the instrumental polarisation where as highly polarised standard stars are used to determine the amount of instrumental depolarisation i.e. how much polarisation is absorbed by the instrument. The exposure time used for each asteroid varied from 30 - 120 seconds depending on the magnitude of the asteroid.

5.1.2 Data analysis

We followed the reduction pipeline suggested on the RINGO2 webpage[1]. We remind the reader that RINGO2 produces 8 frames per target which corresponds to 8 different positions of the rotating retarder waveplate i.e. frames 1 - 8. The data reduction consisted of calculating the background subtracted flux for the zero polarised standard stars in each of the 8 frames produced by RINGO2 using a suitable aperture. The same process is repeated for all 8 frames of our science targets and the highly polarised standard stars. To correct for the instrumental polarisation we take the background subtracted flux calculated for each frame of a zero polarised standard star and divide the corresponding science and high polarised standard star flux by it. For example the flux calculated from frame 1 of the zero polarised standard star is divided into frame 1 of the science or high polarised standard star.

Once this step has been carried out we can use the values calculated from the 8 frames to calculate P_Q and P_U using the equations outlined by Clarke & Neumayer (2002)

[1] http://telescope.livjm.ac.uk/TelInst/Inst/RINGO2/

$$P_Q = \pi\left(\frac{1}{2} - \frac{S_3}{S_1}\right) \qquad P_U = \pi\left(\frac{S_2}{S_1} - \frac{1}{2}\right) \tag{5.1}$$

where

$$S_1 = F_1 + F_2 + F_3 + F_4 + F_5 + F_6 + F_7 + F_8 \tag{5.2}$$

$$S_2 = F_1 + F_5 + F_2 + F_6 \tag{5.3}$$

$$S_3 = F_2 + F_6 + F_3 + F_7 \tag{5.4}$$

where F_{1-8} signifies the flux from 1-8.

Once the values of P_Q and P_U have been calculated using the above equations we must correct for the rotation instrument's position angle relative to North by using Equations 4.8 and 4.9 to rotate into the correct reference system. For our science data we must rotate again so that we are measuring P_Q and P_U relative to the scattering plane.

The uncertainty of P_Q and P_U is calculated using

$$\Delta Q = \pm\frac{1}{\sqrt{G}}\sqrt{\left(\frac{-\pi}{S_1}\sqrt{S_3}\right)^2 + \left(\frac{\pi S_3}{(S_1)^2}\sqrt{S_1}\right)^2} \tag{5.5}$$

$$\Delta U = \pm\frac{1}{\sqrt{G}}\sqrt{\left(\frac{\pi}{S_1}\sqrt{S_2}\right)^2 + \left(\frac{-\pi S_2}{(S_1)^2}\sqrt{S_1}\right)^2} \tag{5.6}$$

where S_1, S_2, S_3 have the same definition as previously and G is the conversion factor to transform from ADU's to electrons.

5.1.3 Results

The polarimetric results for all 9 asteroids are presented in Table 5.1

From Table 5.1 it is clear something is wrong with our measurements as P_U for almost all the asteroids deviates from zero beyond the uncertainty of the measurement. P_U should be zero in this reference system due to symmetry. Since the P_U results deviated from zero we double checked our reduction process and could find no errors in our method. At this point we decided to look at the high polarised standard stars to see if the polarisation values measured by RINGO2 match those

Table 5.1: The polarimetric results measured for 9 asteroids using RINGO2.

Target	Date	Time	Phase Angle	P_Q	P_U
	yyyy-mm-dd	hh:mm	(Degrees)	%	%
Antigone	2011-10-01	01:12	4.57	-0.71 ± 0.10	-0.40 ± 0.10
Antigone	2011-09-21	01:04	6.12	-0.41 ± 0.11	0.18 ± 0.11
Antigone	2011-08-31	03:23	12.42	-0.69 ± 0.10	0.14 ± 0.10
Antigone	2011-08-14	02:15	16.22	-0.76 ± 0.10	0.84 ± 0.10
Artemis	2011-08-15	05:15	22.22	0.41 ± 0.11	-0.67 ± 0.11
Artemis	2011-10-10	02:29	12.38	-0.86 ± 0.09	-0.07 ± 0.09
Artemis	2011-09-24	02:08	16.86	-0.15 ± 0.10	-0.68 ± 0.10
Asporina	2011-10-11	03:12	14.26	0.13 ± 0.10	0.37 ± 0.10
Asporina	2011-09-21	01:53	16.02	0.04 ± 0.08	-0.82 ± 0.08
Asporina	2011-09-21	02:02	18.11	0.27 ± 0.09	-0.87 ± 0.09
Asporina	2011-08-18	03:58	20.44	0.06 ± 0.12	-0.56 ± 0.12
Felicitas	2011-12-18	00:04	8.41	-1.84 ± 0.09	0.93 ± 0.09
Felicitas	2011-12-11	00:53	10.63	-1.41 ± 0.11	-0.21 ± 0.11
Felicitas	2011-12-06	02:12	12.70	-2.19 ± 0.09	0.31 ± 0.09
Felicitas	2011-11-30	03:17	15.35	-0.74 ± 0.09	-0.33 ± 0.09
Felicitas	2011-11-19	02:10	20.10	-0.30 ± 0.07	-0.69 ± 0.07
Felicitas	2011-11-01	02:40	26.18	1.10 ± 0.07	0.37 ± 0.07
Felicitas	2011-09-16	05:01	31.94	2.12 ± 0.10	-0.89 ± 0.10
Gyptis	2011-08-26	23:53	5.50	-1.03 ± 0.10	0.02 ± 0.10
Gyptis	2011-08-20	22:30	6.13	-0.70 ± 0.12	-0.43 ± 0.12
Gyptis	2011-08-07	22:41	10.45	-1.53 ± 0.11	-0.41 ± 0.11
Gyptis	2011-09-16	22:10	11.76	-0.40 ± 0.11	-0.01 ± 0.11
Gyptis	2011-09-24	02:08	14.41	0.26 ± 0.12	0.39 ± 0.12
Gyptis	2011-09-27	22:39	15.87	-0.04 ± 0.13	0.98 ± 0.13
Gyptis	2011-10-05	22:54	18.17	-0.37 ± 0.13	0.46 ± 0.13
Gyptis	2011-10-11	20:03	20.11	0.16 ± 0.14	-0.34 ± 0.14
Gyptis	2011-11-01	20:14	24.10	1.86 ± 0.15	0.04 ± 0.15
Mathilde	2011-12-19	05:18	15.82	-0.25 ± 0.28	0.25 ± 0.28
Mathilde	2011-10-28	05:19	16.90	0.28 ± 0.35	0.73 ± 0.35
Mathilde	2011-11-21	05:06	17.79	0.23 ± 0.31	-1.49 ± 0.31
Penelope	2011-08-11	02:57	5.49	0.60 ± 0.09	0.03 ± 0.09
Penelope	2011-10-31	02:24	6.37	-0.84 ± 0.08	-0.44 ± 0.08
Penelope	2011-10-26	00:23	8.50	-0.31 ± 0.12	-0.11 ± 0.12
Penelope	2011-10-17	23:40	11.91	-1.52 ± 0.10	-1.46 ± 0.10
Penelope	2011-10-01	02:54	17.89	0.31 ± 0.10	-0.35 ± 0.10
Penelope	2011-09-24	03:31	20.29	0.54 ± 0.09	-0.31 ± 0.09
Penelope	2011-09-16	04:45	22.23	1.22 ± 0.09	-0.31 ± 0.09
Penelope	2011-09-05	03:10	24.26	0.09 ± 0.21	-0.94 ± 0.21
Thoma	2011-12-28	03:36	14.32	-0.55 ± 0.17	-0.88 ± 0.17
Thoma	2011-12-26	03:04	14.82	-0.37 ± 0.18	0.29 ± 0.18
Thoma	2011-12-25	04:25	15.06	-0.93 ± 0.17	0.89 ± 0.17
Thoma	2011-12-24	03:40	15.29	-0.84 ± 0.19	-0.52± 0.19
Watsonia	2011-12-24	22:13	12.24	0.06 ± 0.14	0.73 ± 0.14
Watsonia	2011-12-27	23:35	12.96	2.35 ± 0.15	0.06 ± 0.15

seen in the literature. We found that they did not, and the polarisation measured varied in such a way that it could not be due to instrument depolarisation. This was a worrying discovery and we postulated that the reason for the deviation must be due to how the instrumental polarisation was calculated, and if instrumental polarisation was stable on a night to night basis. Therefore we downloaded all available observations of the zero polarised standard stars over the period 1st August to 31st December, which roughly corresponds to the period in which our asteroid observations were taken. This corresponds to approximately 100 nights and over 600 measurements of the zero polarised standard stars. Using Equation 5.5 we calculated the P_Q and P_U measurements for the zero polarised standard stars and plotted them as a function of time. This is shown in Figure 5.1.

We note that the approximate 2 week gap in the data at around $\sim$ 90 days in Figure 5.1 is due to the main mirror of the telescope being removed for cleaning. We can actually see that the mirror was dirty in the approximately 30 days prior to cleaning as there was a slight drop in the measured P_U value. From Figure 5.1 it is clear there is a large amount of scatter in the measured instrumental polarisation. Not only does the instrumental polarisation vary depending on the zero polarised standard used but also on a night to night basis. This variability is most likely the cause for our unusual polarisation values measured for our asteroids.

Following a lengthy conversation with the RINGO2 instrument scientists it was determined the probable cause for the varying instrumental polarisation was a combination of the retarder waveplate rotating at a non uniform speed and the possible non linearity of the fast readout detector at the sub 1% level i.e the difference in flux we need to measure for our asteroids.

RINGO2 was designed to rapidly measure the polarisation of gamma ray busts which can have polarisation values of $\sim$ 40%, If the uncertainty caused by inaccurately determining the instrumental polarisation is $\sim$1-2% it has very little impact on the $\sim$ 40% measured for the gamma ray burst, Essentially RINGO2 was not designed to measure small values of polarisation one would expects from asteroids.

5.1.4 Conclusions

Although our polarimetric measurements of these asteroids turned out to be unusable due to instrumental inaccuracies it was a very useful learning experience to determine the reason why our results were so poor.

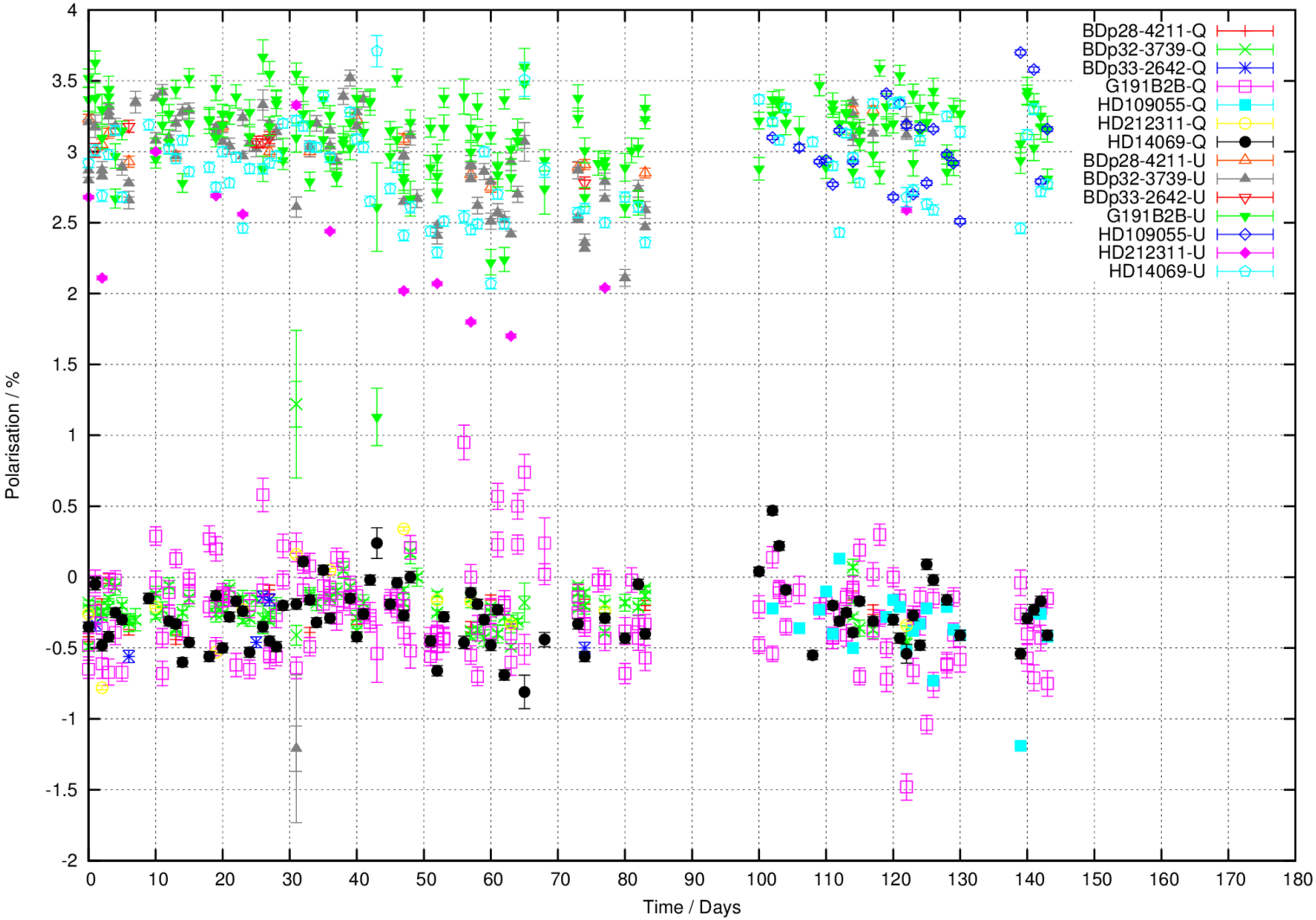

Figure 5.1: The P_Q and P_U measurements for zero polarised standard stars using the RINGO2 instrument.

5.2 Trojan Asteroids of Jupiter

5.2.1 Introduction

Asteroids that are confined to the L4 and L5 Lagrange points or 60° ahead and behind the planet's position along its orbit, Figure 5.2, are referred to as Trojan asteroids (Murray & Dermott, 1999).

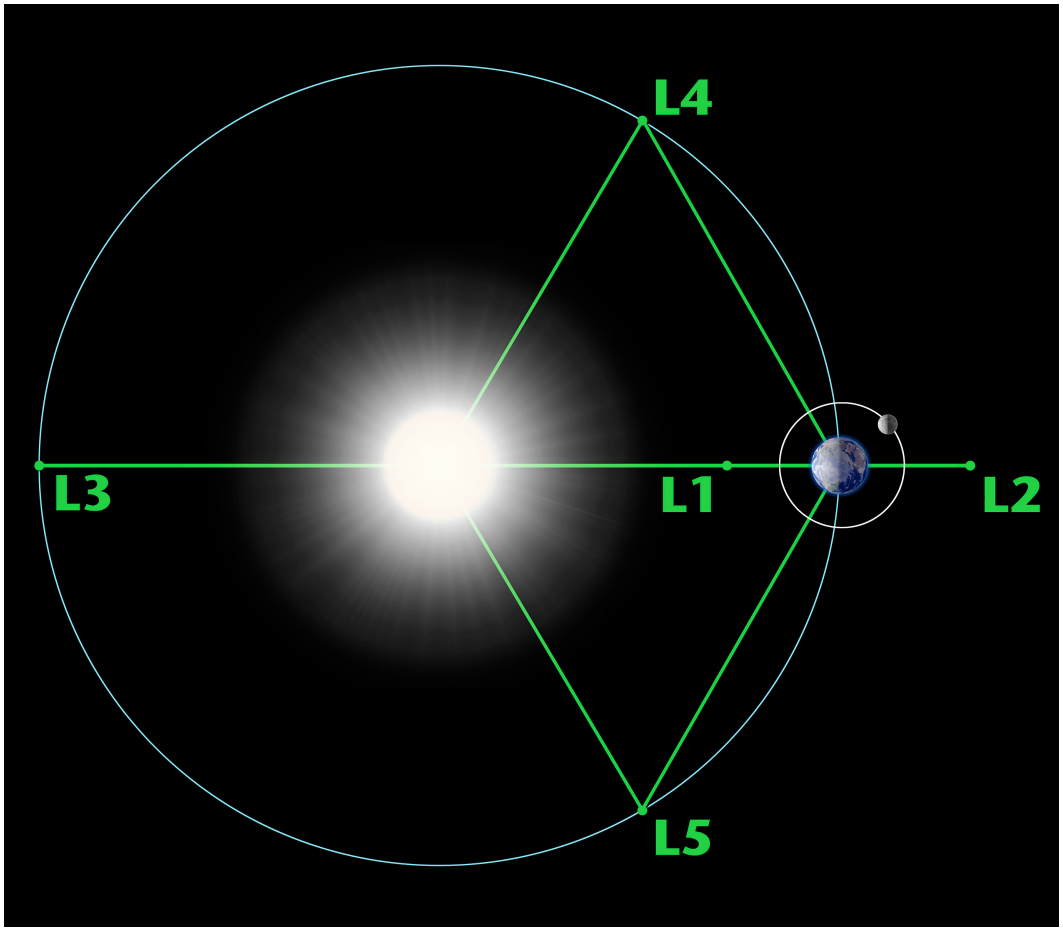

Figure 5.2: Diagram of the Lagrange Points associated with the Sun-Earth system. Image credit: NASA / WMAP Science Team

Dynamically stable Trojan populations have been found in the orbits of Mars, Jupiter, Neptune and two of the Saturnian moons (Tethys and Dione). Their stability allows us to look at objects that formed in the early Solar System. Both Saturn and Uranus do not support a stable Trojan population due to short term orbital perturbations compared to the age of the Solar System. The remaining terrestrial planets Mercury, Venus and Earth have the potential to host stable Trojan popula-

tions although no stable Trojan has been found. One Trojan has been discovered by Connors et al. (2011) in Earth's Lagrange point although it is not stable over the lifetime of the Solar System.

The largest stable population of Trojan asteroids is found around Jupiter with more than 6000 identified so far (Emery et al., 2015). An explanation for the origin of this population was first put forward by Morbidelli et al. (2005b) using the Nice model which describes the formation of our Solar System. This model predicted that as the gas giants began to slowly migrate away from the Sun they perturbed objects in the proto-Kuiper belt inwards and some were captured in the stable L4 and L5 orbits. The majority of the other objects perturbed inwards impacted planets and moons in the late heavy bombardment or were ejected from the Solar System. The Nice model was able to reproduce the final orbits of the gas giants that are very similar to their orbits in the current Solar System. However it did not accurately represent the orbits of the terrestrial planets (Brasser et al., 2009) and left the asteroid belt with an excess of high inclination asteroids (Morbidelli et al., 2010). Morbidelli et al. (2005b) results were later disproved by simulations by Nesvorný & Morbidelli (2012) and Nesvorný et al. (2013) under the so called Jumping Jupiter scenario. In this scenario an ice giant (Uranus, Neptune or an additional Neptune-mass planet) encounters Saturn and then Jupiter causing a step-wise separation of their orbits rather than a smooth migration of the original Nice model. Nesvorný et al. (2013) simulations were able to reproduce the observed distribution of orbital elements for the Jupiter Trojans. The Nesvorný et al. (2013) study also supports the idea of Morbidelli et al. (2005b) that the majority of the Trojans are captured objects from the proto-Kuiper belt region. However, Nesvorný et al. (2013) also predicts that a small fraction of the Jupiter Trojans originated from the outer asteroid belt.

Unfortunately we can not directly compare Jupiter Trojans to TNOs as they have very different optical properties. TNOs have moderate to high albedos while all known Trojan asteroids show a very low albedo. The difference in optical properties is likely due to the Jupiter Trojans experiencing higher irradiation and a different thermal environment compared to the TNOs (Emery et al., 2015). The majority

of Jupiter Trojans belong to the C-, D- and P-type asteroids which are typically associated to the outer part of the main asteroid belt and are considered to be quite primitive in composition.

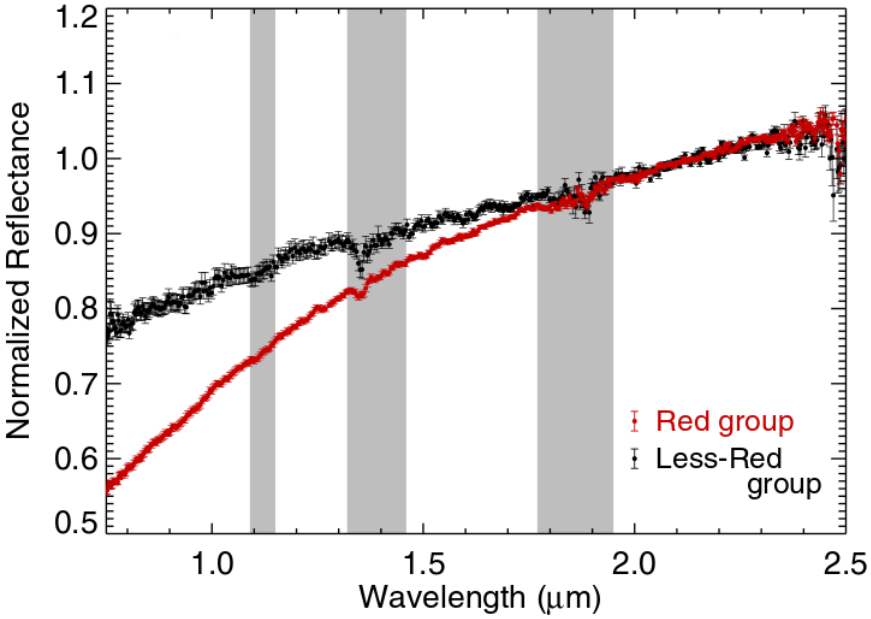

Figure 5.3: Averages of the spectra in each of the two near-infrared spectral groups of Jupiter Trojans. The grey bars near 1.2, 1.4, and 1.9 μm mark regions of strong water vapour absorption in Earth's atmosphere.

Studies of 58 Jupiter Trojans in the infrared have shown two different behaviours in the spectral slope and albedo; see Figure 5.3 taken from (Emery et al., 2011). This supports the predictions of Nesvorný et al. (2013) that the Trojans consist of at least two separate populations. Emery et al. (2011) interpreted that the Trojans that displayed a "less red" spectral slope as originating close to Jupiter or from the main belt while those that displayed a "redder" spectral slope originated beyond Jupiter's orbit. Even though only 58 Trojans were studied it gives us access to a reservoir of potential Kuiper belt objects as well as unique objects from the middle of the solar nebula to study.

In this chapter I present the first polarimetric study of six Jupiter Trojans from the L4 population: (588) Achilles, (1583) Antilochus, (3548) Eurybates, (4543) Phoinix (6545) 1986 TR6, and (21601) 1998 XO89. From this point on I will refer to these Trojans by name only i.e Achilles. Due to the heliocentric distance of

the Jupiter Trojans the maximum phase angle that can be observed is ∼12°. Our polarimetric observations of Jupiter Trojans cover the phase angle range between 7-12° and with an extremely high signal to noise ratio of ∼ 5000. The aim of these observations is to explore whether polarimetry can discern the two different populations and help provide additional information to help constrain the origin and composition of Jupiter Trojans. Additionally we utilize the deep imaging technique mentioned in Section 4.6 to search for coma activity.

5.2.2 Observations

The six Jupiter Trojans were observed in service mode over the period April - June 2013 using the FORS2 instrument under Program ID 091.C-0687(PI= Belskaya). For details about the FORS instrument see Section 3.4.1. The Polarimetric measurements consisted of a series of frames with the half-waveplate set at 8 different positions 0-157.5 in steps of 22.5. For all observations the *R*-special filter was used. Each Trojan was observed using different exposure times with range from 2-40mins for the entire observing series.

Since the Jupiter Trojans are relative bright targets for the VLT the signal to noise ratio is limited to the number of photons that can be measured with the FORS CCD i.e. CCD saturation limit. The standard FORS read out mode is a 2×2 binning readout with an ADU to electron conversion factor of 1.25 and a pixel scale of 1 pixel = 0.25". The maximum number of ADU counts per pixel allowed by the analogue to digital converter is 2^{16}. If we assume a seeing of 1" the limit to the signal to noise ratio of each frame is ∼ 350. To increase the efficiency of our observations we opted for the non-standard 1×1 readout mode with an ADU to electron conversion factor of 1.25 and a pixel scale of 1 pixel = 0.125". In this readout mode we can achieve a signal to noise ratio of ∼ 500 per frame.

Due to the non standard readout mode, special flat fields were requested with the same 1×1 readout as the polarimetric data.

5.2.3 Data analysis

All polarimetric and photometric images were reduced using the methods outlined in Chapter 4.

5.2.4 Aperture photometry

No dedicated photometric images were requested in the observing proposal, however, to align the target with the centre of the polarimetric optics it is customary to take an acquisition image without the polarimetric optics. Therefore we obtain a short exposure photometric image without losing any of the allotted observing time. Each FORS acquisition frame is taken using the same filter as the forthcoming polarimetric observations and are hard coded to be taken with the 2×2 pixel readout mode. Even though the signal to noise ratio will not be very high it does yield a good approximation of the target's apparent magnitude. Aperture photometry was performed using an aperture of up to 15 pixels (3.75") with the background sky estimated using an annulus with an inner radius of 20 pixels and an outer radius of 30 pixels which corresponds to an area between 5" and 7.5" from the target.

In general, it is not possible to give accurate night-by-night values for the zero point or extinction coefficients because photometric standard stars are not taken by default under the FORS calibration plan for polarimetric observations. Therefore, we use the nightly zero point and extinction coefficient available on the ESO quality control and data processing web page. These were calculated using all the photometric standard stars observed over a period of about 28 nights centred at each night under consideration. We associated an uncertainty of 0.05 mag with the magnitude measurements, which is consistent with the uncertainties of the zero points. The uncertainties due to photon noise and background subtractions are negligible in comparison with those of the zero points.

Finally the apparent magnitudes for different epochs were converted to absolute magnitudes using

$$H = m - 5\log_{10}(r \times \Delta) \tag{5.7}$$

where m is the apparent magnitude, r is the heliocentric distance and Δ is the geo-

centric distance.

The photometric results are presented in Table 5.2.

5.2.5 Aperture Polarimetry

Aperture polarimetry was carried out in a similar way to that described in Section 5.2.4. The flux parallel and perpendicular were measured using apertures up to 30 pixels in radius (3.75"). Since the signal to noise ratio for all observations was high the choice of aperture is not crucial as the polarimetry was stable over all apertures, but to minimize errors an aperture between 7-9 pixels was used for all Trojans. The background sky was estimated in an annulus of inner radius of 28 pixels and an outer radius of 58 pixels (i.e in an area between 4.5" and 7.25" from the target). The parallel and perpendicular flux were used to calculate P_Q and P_U using Equation 4.5 as outlined in Section 4.2.

5.2.6 Results and Discussion

5.2.6.1 Polarimetry

The polarimetric results for all six Trojans are shown in Table 5.2 and plotted in Figure 5.4. Overall we measure polarisation values between -1.0 and -1.3 % over the phase angle range 7-12°. The variations in the measured polarisation are small but thanks to the extremely high signal to noise ratio of the observations it is possible to distinguish some different polarimetric behaviours.

In Figure 5.4 we present the polarisation results of all six Trojans, each with a best fit line through them to aid visual inspection. The best fit expression used is a trigonometric function that was introduced by Lumme & Muinonen (1993) and outlined by Penttilä & Lumme (2005) and is defined in Equation 1.4 (Page: 45). This equation can be used for extrapolation only within a phase angle range where well distributed data points are available. For this reason I plot the polarimetric results and the fits around a range close to 10°. Beyond this the fits become untrustworthy and are heavily influenced by the data points at 10°.

All the Trojans observed belong to the D-type taxonomic class (Grav et al., 2012) apart from Eurybates which belongs to the C-type taxonomic class (For-

Table 5.2: Polarimetry and photometry of six Trojans asteroids in the special *R* FORS filter. P_Q and P_U are the reduced Stokes parameters measured in a reference system such that P_Q is the flux perpendicular to the plane Sun-Object-Earth (the scattering plane) minus the flux parallel to that plane, divided by the sum of the two fluxes. Null parameters N_Q and N_U are expected to be zero within error bars. *R* is the photometry and $H_R(\alpha)$ is the absolute magnitude in the *R* band, not extrapolated to phase-angle zero. Photometric error bars are estimated as being 0.05.

Date	Time (UT)	Exp (sec)	OBJECT	Phase angle α (°)	P_Q (%)	N_Q (%)	P_U (%)	N_U (%)	R	$H_R(\alpha)$
2013 04 12	04:40	400	588	9.31	-1.07 ± 0.02	−0.02	0.01 ± 0.02	−0.04	14.92	8.39
2013 04 18	01:16	96	Achilles	10.03	-1.07 ± 0.04	0.00	-0.07 ± 0.04	−0.06	15.00	8.43
2013 05 26	01:33	680	(1906 TG)	11.93	-0.98 ± 0.03	−0.02	-0.01 ± 0.03	0.01	≤ 15.59	≤ 8.62
2013 04 11	02:26	560	1583	9.15	-1.22 ± 0.02	0.02	-0.01 ± 0.02	−0.01	15.74	8.87
2013 04 18	04:13	480	Antilochus	9.75	-1.23 ± 0.03	−0.01	0.01 ± 0.03	0.02	15.89	8.98
2013 05 13	00:52	400	(1950 SA)	11.07	-1.25 ± 0.03	0.00	0.00 ± 0.03	0.02	15.96	8.90
2013 04 12	03:31	1280	3548	7.35	-1.18 ± 0.03	−0.02	-0.04 ± 0.03	0.03	16.73	9.93
2013 04 18	03:41	1450	Eurybates	8.21	-1.25 ± 0.03	−0.05	-0.04 ± 0.03	0.03	16.78	9.95
2013 04 19	04:31	1420	(1973 SO)	8.35	-1.31 ± 0.03	−0.03	0.02 ± 0.03	−0.04	16.72	9.88
2013 06 01	01:30	1760		11.18	-1.28 ± 0.04	−0.00	0.03 ± 0.04	−0.08	≤ 17.29	≤ 10.16
2013 04 11	03:00	1440	4543	7.32	-0.91 ± 0.03	−0.02	0.00 ± 0.03	−0.02	≤ 16.71	≤ 9.82
2013 04 19	01:24	1660	Phoinix	8.40	-0.91 ± 0.03	0.02	-0.02 ± 0.03	0.01	16.78	9.85
2013 06 04	01:56	1920	(1989 CQ1)	10.96	-0.97 ± 0.03	−0.02	0.04 ± 0.03	−0.02	17.39	10.14
2013 04 12	04:08	1080	6545	8.79	-1.20 ± 0.03	0.03	0.02 ± 0.03	−0.04	17.24	10.43
2013 04 25	02:58	2400	(1986 TR6)	10.13	-1.04 ± 0.09	0.07	0.11 ± 0.10	−0.01	≤ 17.37	≤ 10.49
2013 06 05	01:25	2400		11.14	-1.25 ± 0.04	0.07	0.02 ± 0.04	−0.01	17.81	10.64
2013 04 11	03:40	1360	21601	6.83	-1.17 ± 0.03	0.02	-0.02 ± 0.03	−0.01	16.84	10.14
2013 04 19	05:10	1390	(1998 X089)	7.85	-1.18 ± 0.03	0.11	0.01 ± 0.03	−0.06	16.93	10.20
2013 05 26	02:27	1920		11.07	-1.13 ± 0.09	0.10	-0.07 ± 0.09	−0.01	≤ 17.67	≤ 10.72
2013 06 05	02:20	1920		11.36	-1.19 ± 0.03	−0.05	0.04 ± 0.03	0.05	17.59	10.58

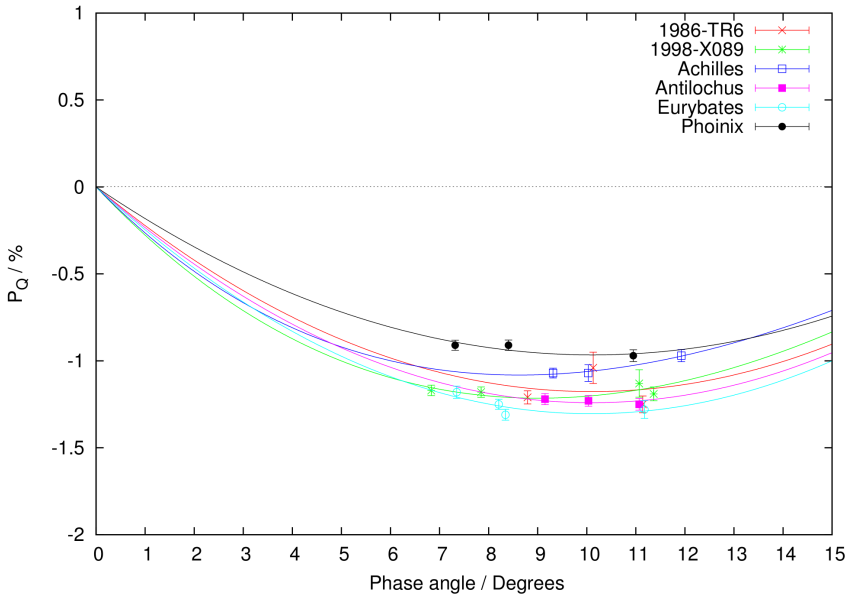

Figure 5.4: P_Q measurements of six Jupiter Trojans

nasier et al., 2007). Hence Eurybates shows the deepest negative polarisation of the six observed Trojans with a minimum of ~-1.3 %. Achilles and Phoinix exhibit a smaller polarisation in absolute terms compared to the other Trojans. Antilochus, 1986 TR6, and 1998 XO89 all exhibit a very similar polarimetric behaviour with a minimum of polarisation of ~ 1.2 %.

From Figure 5.4 we can see that we tentatively suggest we have at least two different polarimetric behaviours. However, first we must check these results are real and not due to a source of photon or instrumental noise. The influence of the photon noise on these measurement is very low at ~ ±0.03 % due to the high signal to noise ratio of the observations. Since the error due to photon noise is so small, any small error contribution due to the instrument may not be negligible in this case. To check the stability of the instrument we look at two parameters, P_U and the null profiles. As mentioned in Section 4.2 we know that P_U should equal zero in this reference system. The null profiles are a good quality check on the stability of the instrument. The null profile basically means we compare two sets of P_Q and P_U measurements taken on the same observing epoch with each other. For example the null of the P_Q measurement (N_Q) would consist of comparing the P_Q measured using retarder positions 0° and 45° minus the P_Q measured using retarder positions

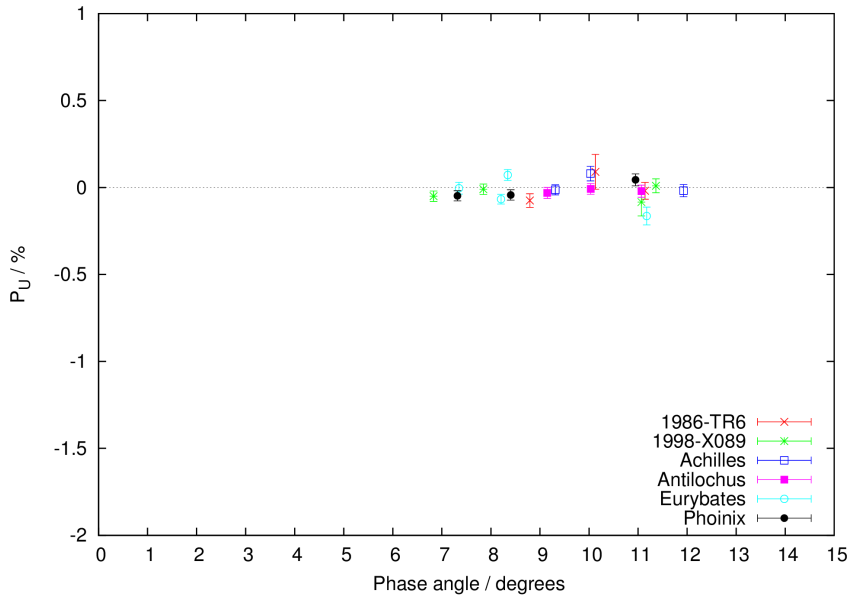

Figure 5.5: P_U measurements of six Jupiter Trojans

90° and 135°. A similar null profile (N_U) exists for P_U measurements by using the retarder positions associated with the P_U measurements. If the instrument is stable the difference between two consecutive P_Q and P_U measurements should be zero. As the measurements of P_U and the null profiles are almost all zero within the errorbars (see Figure 5.5 and 5.6) we can assume that the instrument is stable and our error are mostly due to photon noise.

In Figure 5.4 there are two measurements that appear to be slightly different from the others measured for the same Trojan. One is the measurement of Eurybates at a phase angle of 8.4° and the other is the measurement for the Trojan 1986 TR6 at a phase angle of 10.1°. Both these points deviate away from the normal changes one would expect to see with changing phase angle which are indicated by the best fit curves in Figure 5.4. The reason for the difference in measurement is puzzling. In the case of 1986 TR6 the difference is probably due to a high polarised background sky. In Figure 5.7 I have plotted how P_Q and P_U values vary as a function of aperture size in pixels. The failure of P_Q and P_U to converge around a single value is probably the main reason for the difference compared to the other measurements.

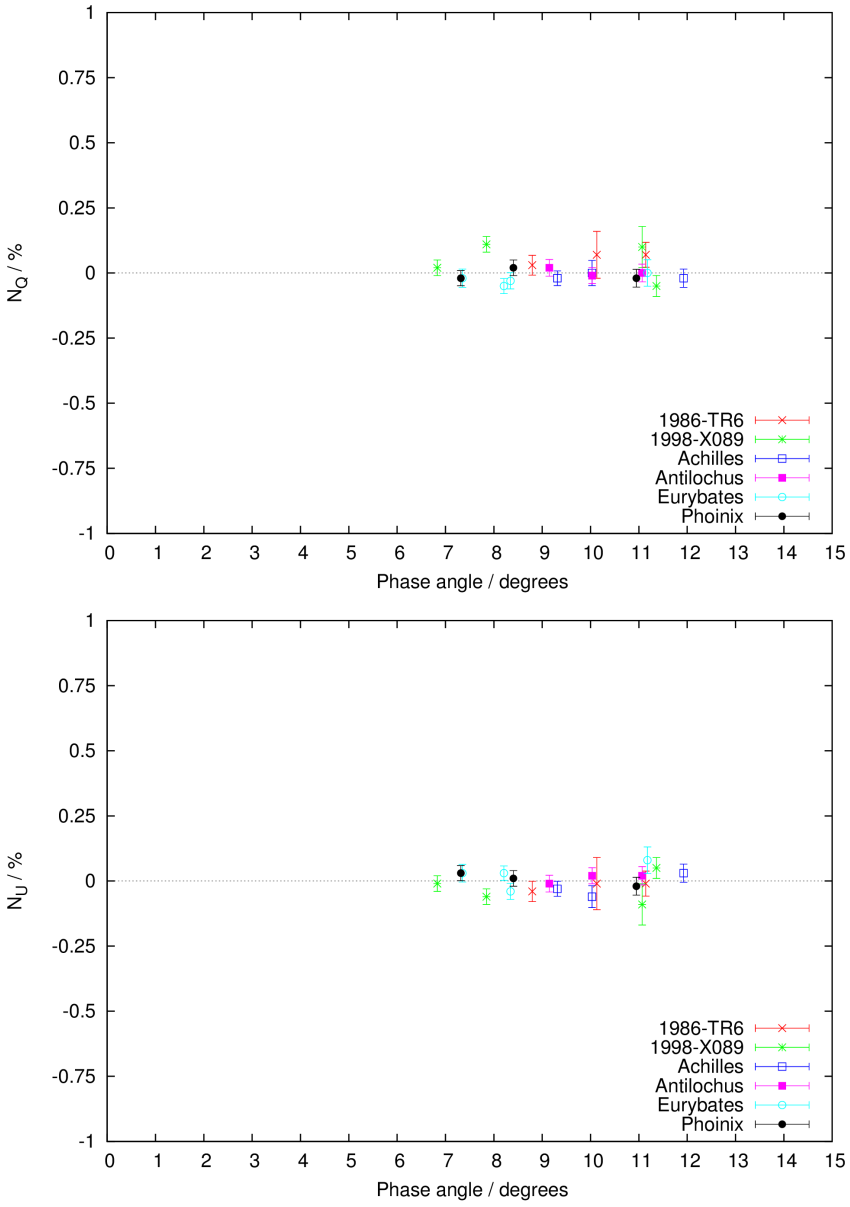

Figure 5.6: Top: Null profile of P_Q measurements of six Jupiter Trojans, Bottom: Null profile of P_U measurements of six Jupiter Trojans

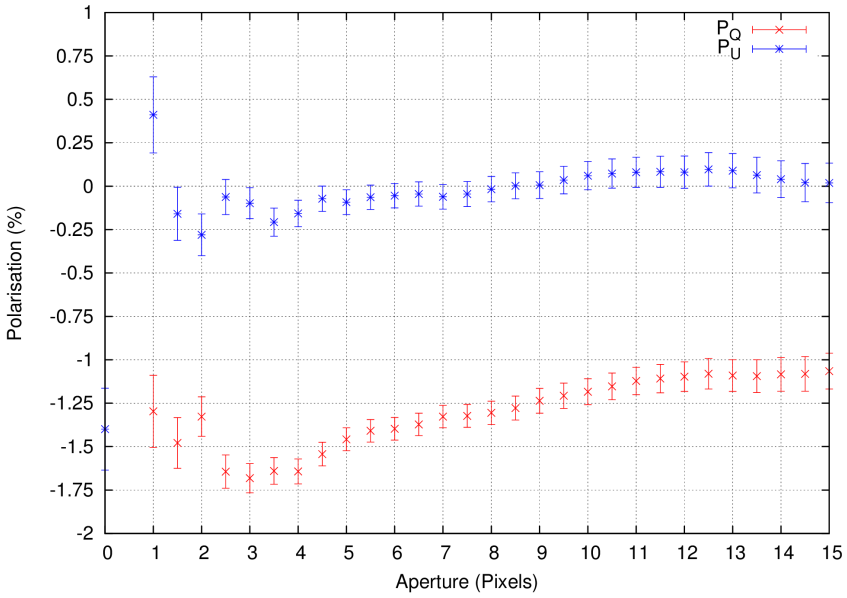

Figure 5.7: P_Q and P_U measurements of 1986 TR6 on the night of 2013-04-25

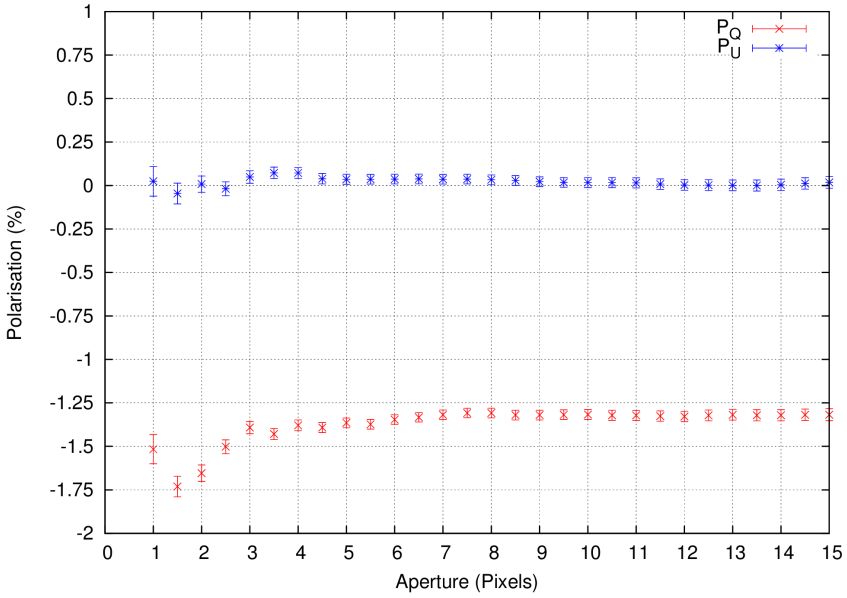

Figure 5.8: P_Q and P_U measurements of Eurybates on the night of 2013-04-19

If we carry out the same analysis for Eurybates as shown in Figure 5.8 we do not see the same instability suggesting that the polarimetric measurement is accurate. This means the change in P_Q from a phase angle of 8.1 to 8.4° could be due to a change in surface characteristics possibly the result of the Trojan rotating between observations. Eurybates has a rotation period of 8.711 ± 0.009 hours (Mottola et al., 2011) meaning that the rotation phase difference between the P_Q at a phase angle 8.1° and 8.4° is only 0.1 rotation cycles. The other Trojans are all observed at different rotational phases yet do not show any form of change in polarimetry due to rotational behaviour. There are only a few known cases were an object's rotation has changed the level of polarisation. The most noticeable of these was Vesta which experienced a change of 0.03 % (Wiktorowicz & Nofi, 2015) to 0.1 % (Lupishko et al., 1988) through its rotation cycle.

Although it is possible for Trojans to have changes in their surface characteristics it is unlikely to influence the measured polarisation over a 0.1 phase change in rotation. Therefore it could be possible that the difference observed for the polarimetry for Eurybates could be down to a fluctuation produced by photon noise or a small amount of instrumental polarisation.

5.2.6.2 Search for coma activity

All polarimetric images were stacked together to form a deep image as outlined in Section 4.6. To search for a coma contribution we can easily compare the PSF of the Trojan with that of a background star. However for a more quantitative evaluation of the potential coma contribution measured around the Trojan asteroids we can follow the strategy first developed by Tozzi & Licandro (2002), Tozzi et al. (2004), and later outlined in Bagnulo et al. (2010). This strategy assumes that the number of detected electrons from the object per unit time within a circular aperture of radius a is the sum of the contribution from the nucleus, the coma, and potentially a surplus amount due to non-perfect background subtraction. From the work of A'Hearn et al. (1984) if we assume the flux from a weak coma (F_C) around the nucleus in a certain wavelength band can be written as

$$F_C = Af\left(\frac{\rho}{2\Delta}\right)\frac{r_e^2}{r^2}F_\odot \tag{5.8}$$

where A is the mean albedo (unit-less), f is the filling factor (unit-less), Δ is the geocentric distance expressed in cm, r_e is the Earth-Sun distance expressed in AU, r is the heliocentric distance expressed in AU, ρ is the projected distance from the nucleus (which corresponds to the size of the aperture used to measure F_C), and $F_\odot$ is the solar flux at 1 AU integrated in the same wavelength band as F_C.

Based on the hypothesis from A'Hearn et al. (1984) if there is a uniform and isotropic ejection of dust at a constant velocity, then the product of $Af\rho$ should be constant with ρ. It is assumed that the contribution from the background should be constant when measured in a small region around the object. Tozzi et al. (2004), and Bagnulo et al. (2010) have shown that if the derivative of the flux with respect to the aperture converges to a constant value $k^{(C)}$, then the size of the coma contribution can be transformed into a meaningful value using the quantity $Af\rho$ introduced by A'Hearn et al. (1984) using the equation,

$$Af\rho = 1.234\times10^{19}\,10^{0.4(m_\odot - Z_P)}\,r^2\left(\frac{\Delta}{d_p}\right)k^{(C)} \tag{5.9}$$

where m is the apparent magnitude of the Sun (i.e., at 1 AU) in the considered filter, Z_P is the zeropoint in wavelength band for the observing night, d_p is the CCD pixel scale in arcseconds (0.125 in our case), r and Δ are both measured in AU, $k^{(C)}$ is measured in electrons per second and $Af\rho$ is measured in cm.

It has been suggested by Guilbert-Lepoutre (2014) that Trojans could have water ice just a few metres under their surfaces. A similar study by Prialnik & Rosenberg (2009) suggested that main belt asteroids could retain water ice $\sim$ 50 - 150m beneath their surfaces. Since a few asteroids in the main belt have been known to show cometary activity it could be suggested that some Trojans could also show activity. Using Equation 5.9 we found that in all cases, $Af\rho$ is consistent with zero within a typical error bar of 10 to 50 cm (see Figure 5.9). Therefore we conclude that there is no evidence for coma activity for these Trojans.

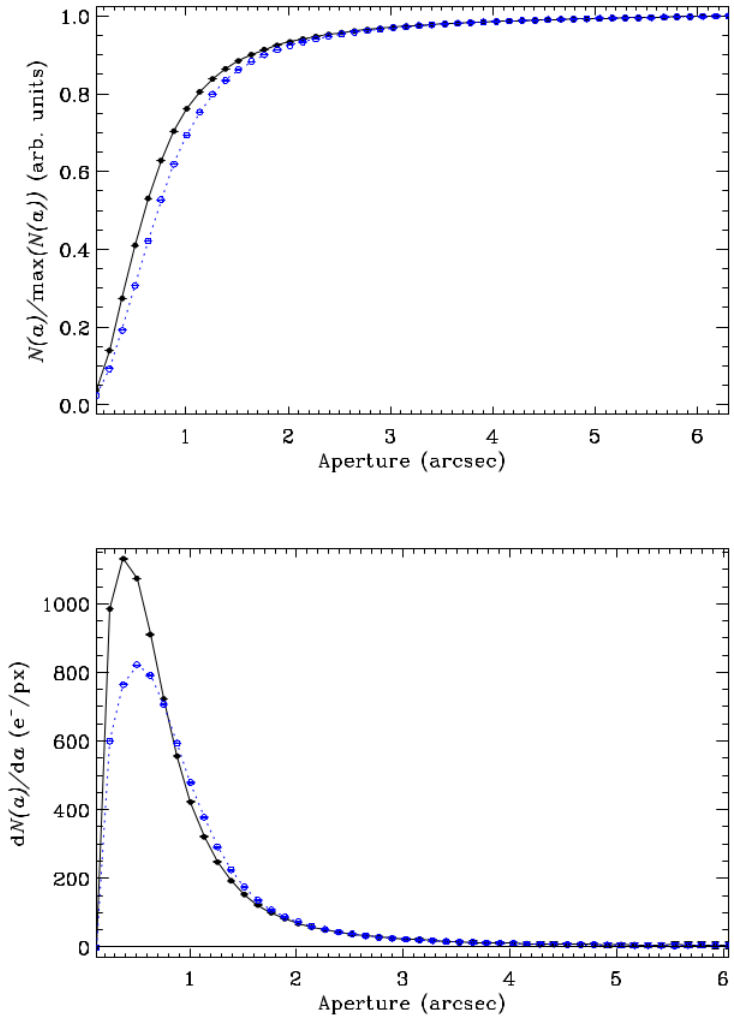

Figure 5.9: Flux (top panel) and its derivative (bottom panel) as a function of the aperture for asteroid (6545) 1986 TR6 observed on 2013-06-05 (black solid circles and solid lines) and for a background star of similar brightness (blue empty circles and dashed lines).

5.2.6.3 Albedo

As stated in Section 1.2.3 it is possible to link an asteroid's polarisation minimum ($P_{\rm min}$) and its slope through inversion (h) to its albedo. Since for these Trojans observations we do not have any information on h we shall only concentrate on $P_{\rm min}$. Using Equation 1.5 and the minimum of polarisation we calculate albedos of the order of 0.08-0.12. This range of albedo is inconsistent with pre-existing albedos calculated from the WISE (Grav et al., 2012) and the AKARI (Usui et al., 2011) mid-infrared surveys which calculate the albedos in the 0.04 - 0.1 range. The

reason for this inconsistency is that Equation 1.5 is only an estimate so there is a degree of uncertainty on the calculated albedo. Additionally, in this case Equation 1.5 is not well suited to estimating the albedo for the darkest objects as a saturation effect occurs for the value of $P_{\min}$. Normally as albedo decreases the value of $P_{\min}$ increases in absolute terms. However laboratory experiments have shown that as the albedo drops below ~ 0.05 the value of $P_{\min}$ remains approximately constant (Shkuratov et al., 1992). This effect has been polarimetrically observed for the very dark F-type asteroids by Belskaya et al. (2005). Hence it is reasonable to state that the albedos calculated for these Trojans using Equation 1.5 are in the same saturated regime as the F-type asteroids.

5.2.6.4 Comparison with other asteroids

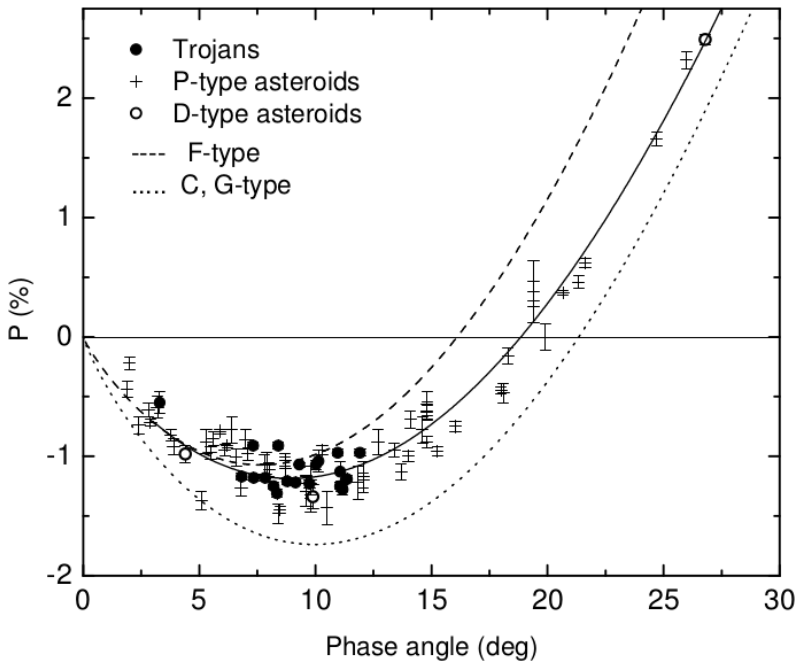

Figure 5.10: Polarisation plotted as a function of phase angle for Jupiter Trojans, D-type asteroids and P-type asteroids. The best fit curves are shown for the F-type (dashed line), P-type (solid line), and C,G type (dotted line) asteroids.

In Figure 5.10 we compare the polarimetric properties of the Trojan asteroids with those of other asteroids of varying taxonomic class. The data for these other taxonomic classes are taken from the asteroid polarimetric database (Lupishko,

2014). The classes included in Figure 5.10 are the P-, F-, G- and the C-type asteroids which all have similarly low albedo. To prevent overlapping points I have replaced the data points of the C- and F-type asteroids with best fits using Equation 1.4. Both the P-type, D-type and our Trojan observations have a very similar polarimetric behaviour. F-types exhibit a polarisation minimum that occurs at a smaller phase angle than that of the Trojans hence we can assume that the inversion angle for the Trojan asteroids also occurs at a larger phase angle compared to the F-types. The only D-type asteroid to be observed at large phase angles is the asteroid 944 Hidalgo (Fornasier et al., 2006). Hidalgo has an unusual orbit with a semi-major axis of 5.74 AU and eccentricity of 0.66. This means that Hidalgo has a perihelion distance of 1.94 AU hence giving access to a large observable phase angle range compared to other D-type asteroids. The polarisation measured for Hidalgo by Fornasier et al. (2006) at a phase angle of 26.8° lies exactly on the fitted phase curve for the P-type asteroids. This further confirms the similarity of the polarisation properties of P- and D-type asteroids within the accuracy of polarimetric measurements.

5.2.7 Conclusions

In this Section I have presented the first polarimetric measurements of six L4 population Jupiter Trojan asteroids. From these measurements at least two distinct polarimetric behaviours can be seen. Trojans Achilles and Phoinix show a shallower polarimetric phase curve compared to the others with polarisation minima of $\sim 1\,\%$. Antilochus, 1986 TR6, and 1998 XO89 are D-type asteroids and all exhibit a very similar polarimetric behaviour with a minimum of polarisation of $\sim 1.2\,\%$. Eurybates belongs to a different taxonomic class (C-Type) and so has the deepest minima of polarisation of $\sim 1.3\,\%$ but is still quite similar to the D-type Trojans. All six Trojans appear to have their polarisation minimum around a phase angle of $\sim 10°$; whether this is due to the small phase angle range of these observations we can not say. All six Trojans throughout all the observations showed no signs of coma activity within the uncertainty of the measurements.

Table 5.2 and Figures 5.9 and 5.10 where reproduced from Bagnulo et al. 2016, A&A, 585, A122 with permission from ©ESO

5.3 The TNOs Makemake and Orcus

5.3.1 Introduction

As previously mentioned in Section 1.2.6, Trans-neptunian objects are the most distant objects which we can observe in our Solar System. These are thought to be the remnants from the formation of the outer Solar System and possibly represent the most pristine population of objects that can be observed in our Solar System. Investigating the surface properties of these bodies can begin to give us an insight to the formation and evolution of the Solar System and the composition of the proto-planetary disk.

Over the past 25 years the investigation of the surface properties of these objects has intensified. This has been mainly due to the creation of the largest ground based telescopes like the Very Large Telescope and Subaru, and space telescopes Hubble, Spitzer and Herschel.

At the moment almost 1400 TNOs have been discovered, according to the latest figures from the Minor Planet Center. These objects have been heavily perturbed dynamically which is indicated by the presence of bodies that have highly inclined and eccentric orbits and the existence of widely different dynamical classes. The four main dynamical classes for TNOs (Elliot et al., 2005) are

- Resonant objects: these are trapped in resonances with Neptune, with the majority discovered in or around the 3:2 mean motion resonance with Neptune.
- Scattered disk objects: these objects have high-eccentricity and high-inclination orbits and a perihelion distance close to 35 AU
- Detached objects: these are located outside of interacting gravitational encounters with Neptune
- Classical objects: these are non-resonant and scattering objects with low eccentricity.

Even though these objects reside in the same region of the Solar System they exhibit a wide variety of different surface characteristics with only a few appar-

ent links between their orbital paths and surface properties (Doressoundiram et al., 2008).

Infrared and visible spectroscopy carried out on a small number of these TNOs confirms the presence of several types of ices (Barucci et al., 2011), such that we can classify TNOs into 3 groups.

- Water-ice rich.
- Volatile rich.
- Featureless.

As the name suggests, water-ice rich objects are objects that show a high abundance of water-ice in their surface spectra with approximately 30 objects that fall into this category. Volatile rich are a group of objects that show the presence of volatile-ices like nitrogen ice and methane ice. We call these ices volatile as they can be melted into their gaseous states easily and be removed from the object. These volatile rich objects tend to be the largest TNOs, for example Pluto, Eris and Makemake. Finally, featureless objects again as the name suggests are objects whose spectra do not show the presence of any type of ice on their surface although a few objects show additional features that perhaps could be attributed to ammonia or methanol.

Amongst these many TNOs reside some large objects that are classified as Dwarf planets. Of these large objects only a handful have been polarimetrically observed due to their distance from the Sun and relatively high apparent magnitude.

Bagnulo et al. (2008) discovered that the handful of polarimetry observed TNOs exhibit two distinct polarimetric behaviours. The two polarimetric behaviours depend on the size of the object. TNOs which have a diameter larger than 1000km tend to exhibit a flat and non varying polarisation phase curve as shown in the left panel of Figure 5.11. TNOs that have diameter less than a 1000km exhibit a sharp surge in negative polarisation reaching -1% at 1 degree of phase angle, as seen in the right panel of Figure 5.11.

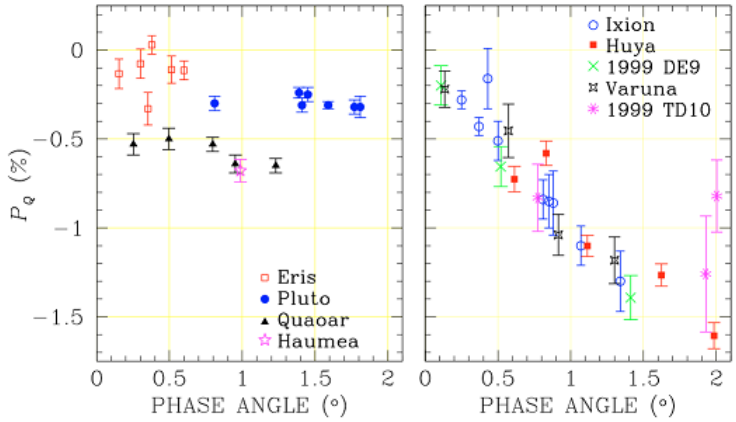

Figure 5.11: Polarimetric observations of large TNOs in the left panel and and small TNOs in the right panel. Figure taken from Bagnulo et al. (2008).

It is quite normal to think that these two different polarimetric phase relations are simply due to different surface compositions and structure. These groups of objects differ in surface albedo, where the largest TNOs have a high albedo and the smaller TNOs tend to have a low albedo. Perhaps the most important difference in the surface properties between these two groups of objects is the tendency of the large TNOs, that exhibit a small constant value of negative polarisation, to have the capability of retaining volatiles such as nitrogen, methane, and carbon monoxide. Eris, Pluto, and Makemake have surfaces that contain both methane and nitrogen ices. Whilst the other two objects, Haumea and Quaoar, exhibit a slightly more negative polarisation and have spectra dominated by water ice and are believed to be in a transition phase where they have lost their nitrogen and methane ices but have not yet lost their water ice as shown in Figure 5.2 taken from Brown et al. (2011). This evolutionary phase may also explain their different albedo as well as their different polarimetric behaviour compared to small TNOs.

Since only a handful of these TNOs have been polarimetrically observed I present the observations of two more large TNOs, whose diameter is around 1000 km, to help study surface properties, and further look into the dependence of polarisation degree on diameter and in relation to the capability of retaining volatiles. The two observed TNOs are Makemake and Orcus. In the following I will outline the information that we have about these objects.

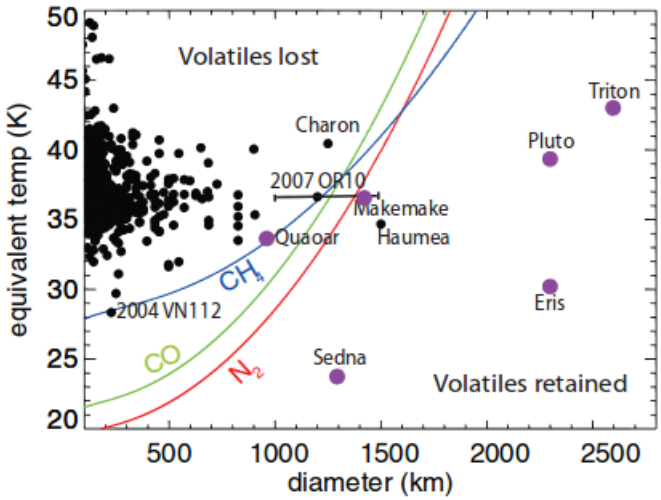

Figure 5.12: Plot of volatile retention and loss in the Kuiper belt. Objects to the left of the CH_4, CO and N_2 lines are too small and too hot to retain any of those volatiles over the age of the Solar System. Figure taken from Brown et al. (2011)

5.3.1.1 Makemake

Makemake is one of the largest known TNOs with a diameter of ~ 1400 km (Brown, 2013) with a semi-major axis of 45.97 AU. Due to this distance from the Sun the observable phase angle range for Makemake is between 0.6-1.1°. This range would place it between the data on Eris and Pluto on Figure 5.11. Makemake has no known moon which is unusual for a TNO of this size. Makemake has a rotational period of 7.771 ± 0.003 hours (Heinze & de Lahunta, 2009). As well as this the amplitude in Makemake's light curve has been found to be very small at $\Delta V = 0.029 \pm 0.002$ which means there is very little variation over Makemake's surface. However, it is assumed that Makemake's surface is made up of bright terrains with an albedo of $0.78 \leq p_v \leq 0.90$ and dark terrains with albedo $0.002 \leq p_v \leq 0.12$ to fit thermal data taken with the Herschel space telescope (Lim et al., 2010a). Lim et al. (2010a) proposed 3 different possible surface features that could be responsible for these bright and dark terrains and still exhibit only a small change in light curve.

- The surface is comprised of evenly distributed dark and bright terrains.
- The dark terrain is a band at a constant latitude or a polar spot.

- The dark terrain could be a yet undiscovered moon of Makemake.

Out of these various scenarios the most plausible is the fact that we are looking at Makemake at an almost pole-on orientation and we are seeing some kind of polar spot.

Further observations of Makemake using Spitzer and Herschel space telescopes have confirmed its unusual thermal emission spectrum, which is different from all the other TNOs (Lim et al., 2010b).

Spectroscopic observations of Makemake have revealed strong absorption bands associated with methane ice (Barkume et al., 2005; Licandro et al., 2006; Brown et al., 2007; Tegler et al., 2007). Brown et al. (2007) also reported the presence of ethane features and no apparent evidence of other volatiles like nitrogen or carbon monoxide ice. However Tegler et al. (2008) have reported that there is a small shift in the methane bands in their spectra of Makemake in comparison with a model fit, which could suggest the presence of trace amounts of nitrogen ice on the surface.

5.3.1.2 Orcus

Orcus has a Pluto-like orbit in the 3:2 resonance with Neptune. All objects which orbit within this 3:2 resonance are called Plutinos of which Orcus is one of the largest known with a diameter estimated at 850km ± 70km (Lim et al., 2010b) and 940km ± 70km (Brown et al., 2010). Orcus has a satellite, Vanth, with an apparent magnitude 2.6 fainter in the V-band filter, and has a diameter of 280-380km (Brown et al., 2010). Orcus has a spectrum which is dominated with water ice features suggest a water-ice rich surface with an albedo of about 0.3 (Lim et al., 2010b). Spectral modelling of Orcus shows that the water-ice is present in its crystalline form and contains an estimated 2% methane and 5% nitrogen.

5.3.2 Observations

Both Makemake and Orcus were polarimetrically observed between April and May 2011 using the FORS2 instrument attached to UT1 of the Very Large Telescope (VLT) under the program ID: 087.C-0615 (PI=Bagnulo).

These observations consisted of simultaneous polarimetric and photometric measurements. Both polarimetric and photometric observations were carried out using the R-special filter (central wavelength of 655nm with a FWHM of 165nm). For Makemake, the photometric images had an exposure time of 15 seconds and the polarimetric images had an exposure time of 38 seconds. For Orcus, the photometric images had an exposure time of 60 seconds and the polarimetric images had an exposure time of 340 seconds. Makemake used the full set of retarder waveplate positions available, 0 - 337.5°. Due to Orcus's long exposure time we only used the waveplate positions between 0-157.5°.

Over the observing period we observed Makemake at five different epochs and Orcus at only one epoch. As previously mentioned due to the TNOs having a large heliocentric distance > 30 AU the observable phase angle range is less than 2 degrees. For Makemake we sampled phase angles between the range of 0.60 - 1.07 degrees and Orcus at a phase angle of 1.0 degrees.

5.3.3 Results

The polarimetric measurements for Makemake and Orcus are presented in Table 5.3; they are also plotted against their phase angle in Figure 5.13. The aperture used to calculate the polarimetry varied between 5-8 pixels for Makemake and 6 pixels for Orcus.

From the results presented in Table 5.1 we can see that Makemake exhibits a small negative polarisation over the phase angle range 0.6-1.1° with an average polarisation value of $0.160 \pm 0.05\%$. The polarisation measurement at phase angle of 0.8° differs from the average value by a significant margin but it is perhaps showing a scatter in our results similar to that exhibited by Eris in Figure 5.13 rather than some real change in the surface properties. We can also assume the same is true for the value measured at a phase angle of 0.9°. When we compare Makemake's polarisation phase curve in Figure 5.13 to other large TNOs we can see that it exhibits a similar behaviour to that of Eris and Pluto but different from that of Haumea and Quaoar. From this we can say that Makemake's polarimetric properties are similar to the two other large TNOs that have a surface dominated with methane. The fact

Table 5.3: Observations of Makemake and Orcus using the R-Special filter.

Target	Date (dd/mm/yyyy)	Time hh:mm	Phase angle (degrees)	r AU	Δ AU	P_Q (%)	P_U (%)	R	H_R
Makemake	03/04/2011	04:56	0.600	52.207	51.369	-0.170 ±0.045	0.000 ±0.045	16.81 ±0.05	-0.332 ±0.05
	25/04/2011	01:30	0.802	52.201	51.517	-0.316 ±0.048	-0.044 ±0.048	16.86 ±0.05	-0.288 ±0.05
	10/05/2011	01:31	0.940	52.212	51.676	-0.050 ±0.052	0.089 ±0.052	16.77 ±0.05	-0.385 ±0.05
	14/05/2011	00:29	0.972	52.213	51.725	-0.151 ±0.085	-0.093 ±0.086	16.80 ±0.05	0.0357 ±0.05
	29/05/2011	01:07	1.066	52.215	51.926	-0.114 ±0.095	-0.110 ±0.087	-*	-*
Orcus	24/04/2011	03:26	1.08	47.932	47.482	-1.062 ±0.092	0.115 ±0.092	18.83 ±0.05	2.044 ±0.05

* Photometry was affected by thin clouds making the data unusable.

that Makemake's polarisation is not as negative compared to Pluto is because the polarisation measurements of Pluto are of the unresolved binary of the Pluto-Charon system. We denote the reduced Stokes parameter Q/I as if we were observing Pluto alone with $P_Q^{(\mathrm{P})} = Q^{(\mathrm{P})}/I^{(\mathrm{P})}$ (measured with respect to the direction perpendicular to the scattering plane Sun-Pluto-Earth). Similarly, we denote the reduced Stokes parameter Q/I as if we were observing Charon alone with $P_Q^{(\mathrm{C})} = Q^{(\mathrm{C})}/I^{(\mathrm{C})}$ (measured with respect to the direction perpendicular to the plane Sun-Charon-Earth. We can assume that at each phase angle, Pluto, Charon, the Sun, and the Earth define an identical scattering plane, so that $P_Q^{(P)}$ and $P_Q^{(C)}$ are expressed in the same reference system. This allows use to write, for the observed polarisation of the double system, $P_Q^{(P+C)} = (Q^{(P)} + Q^{(C)}/(I^{(P)} + I^{(C)})$. Taking into the account the ratio of the reflected light of the two objects is ~ 0.17, we deduce (Bagnulo et al., 2008)

$$P_Q^{(P)} = P_Q^{(P+C)} + 0.17(P_Q^{(P+C)} - P_Q^{(C)}) \tag{5.10}$$

If we assume that Charon has an intrinsic polarisation similar to that of Quaoar and Haumea of -0.7%, we can estimate that the intrinsic polarisation of Pluto is -0.2%. We can assume Charon has a polarisation value similar to Quaoar and Haumea because all three of these object have surface spectra dominated by water-ice. If this assumption is correct it means Makemake and Pluto have very similar polarisation phase angle behaviour. Also the polarimetric phase behaviour of TNOs with a methane dominated surface is different from those that have a water-ice dominated surface. This difference is not simply due to the objects having a different albedo because both Haumea and Makemake have approximately similar albedos of 0.8 yet we have a 0.5% difference in polarisation.

Photometry for Makemake was also carried out on the acquisition images just before the polarimetric observations. Even though these acquisition images are not specifically designed for photometry they still give good photometric estimates. However not all observing series were carried out during photometric nights. The sky transparency at Paranal is monitored by the Line Of Sky Absorption Monitor

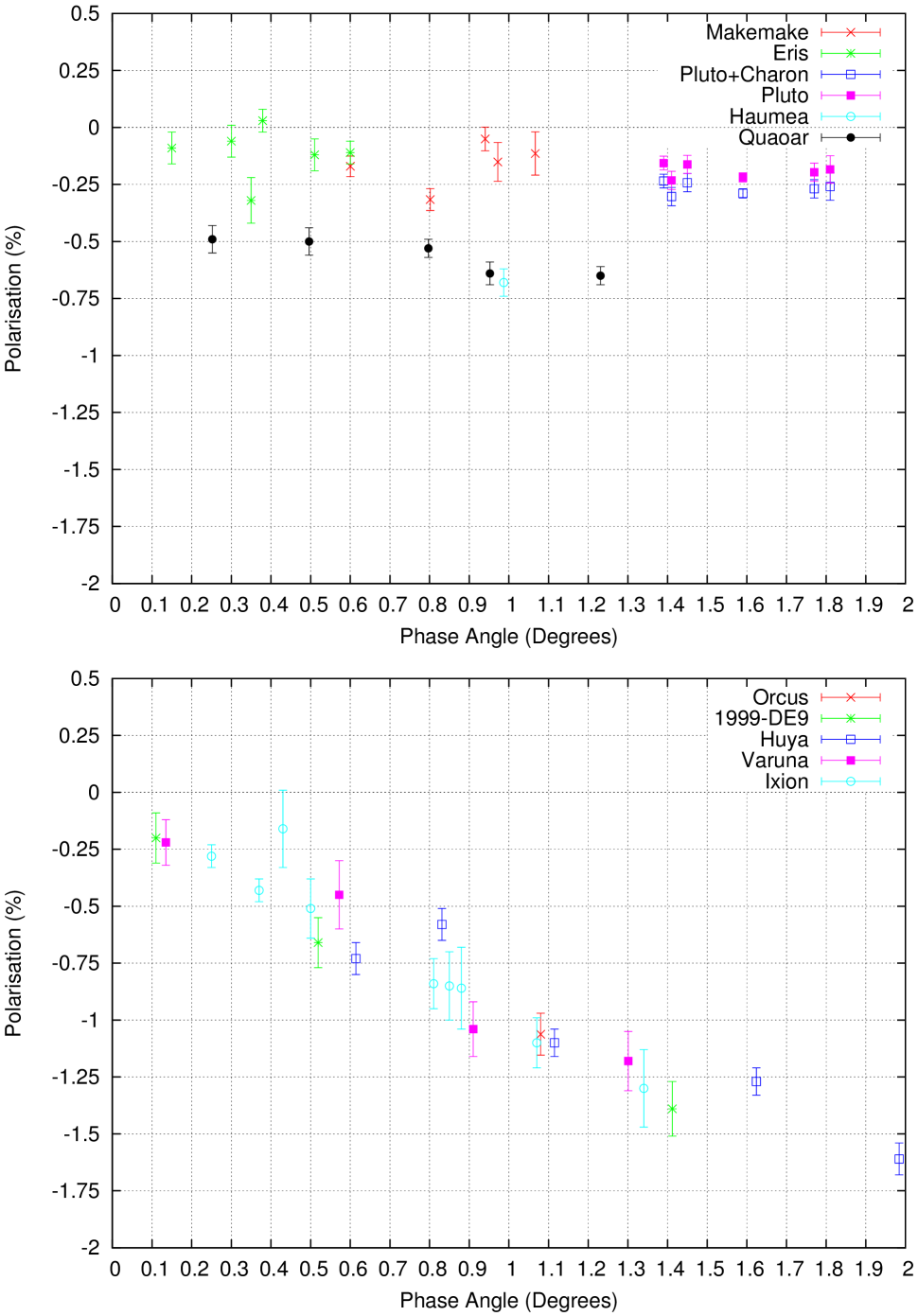

Figure 5.13: In the upper panel we have the linear polarisation as a function of phase angle for Makemake (red cross) and other large TNOs (Bagnulo et al., 2008; Breger & Cochran, 1982). In the lower panel we have linear polarisation as a function of phase angle for Orcus (red cross) and the other TNOs smaller than 1000 km in diameter (Bagnulo et al., 2006, 2008; Boehnhardt et al., 2004).

(LOSSAM), whose data can be retrieved on the ESO web-page[2]. In Figure 5.14 we show an example of a LOSSAM plot detailing the sky conditions.

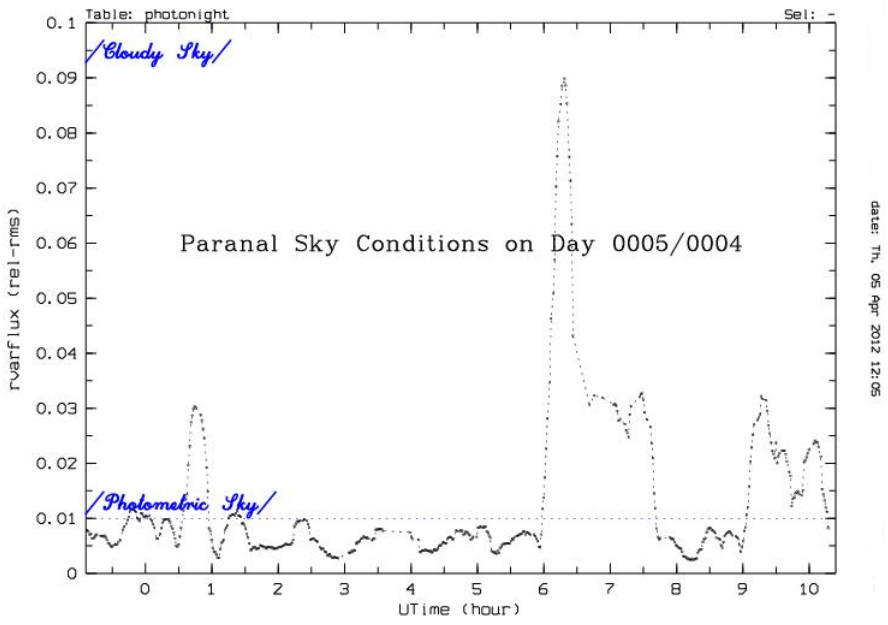

Figure 5.14: LOSSAM plot showing the sky conditions of Paranal during a specific observing night.

For all observations in this section and future sections I have checked the LOSSAM plots, and denote an * beside any magnitude that was observed during a night that was not photometric.

Photometry for Makemake over the observed phase angle is presented in Figure 5.15. For all nights I used a 10 pixel aperture to measure the flux from the the target. We can see from this that it shows very little variation over the observable phase angle range. I also note that I have omitted the magnitude measured on the night 2011-05-29 because the photometry on that night was impeded by clouds.

The single polarimetric observation we have for Orcus at a phase angle of 1.08° gave a measured polarisation value of $-1.062 \pm 0.092\,\%$. This single observation would place it firmly in the small TNO category of polarimetric behaviours. Like for Pluto, our polarimetric observations of Orcus are of the unresolved binary of Orcus and its moon Vanth. If we apply the same treatment as we did for the

[2]http://archive.eso.org/asm/ambient-server?site=paranal

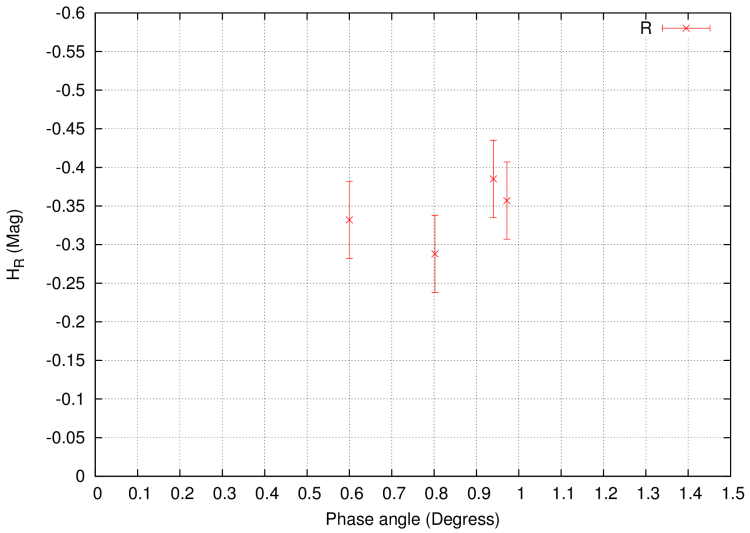

Figure 5.15: The absolute magnitude of Makemake as a function of phase angle in the R-special filter.

Pluto-Charon system and assume a polarisation value for Vanth we can estimate the value of Orcus's polarisation. Even if we assume a polarisation of $-1.5\,\%$ for Vanth (a very large negative polarisation for an object at 1 degree of phase angle) the contribution to the overall system is still very small at $\approx 0.04\%$. Even though Orcus is approximately 1000 km in diameter it doesn't quite show the same polarimetric behaviour as Haumea and Quaoar which are slightly larger than 1000 km, ~1240 km and ~1073 km respectively, but yet all have spectra dominated by water-ice spectra. With only one observation of Orcus there is a the possibility that Orcus could also exhibit a similar non varying polarisation like Haumea and Quaoar.

The Deep imaging technique described in Section 4.6 was applied to both Makemake and Orcus to search for a possible coma or outgassing activity. Neither Makemake or Orcus can be seen to exhibit any outgassing or a coma around them within the depth of these images. Analysis of their point spread function (PSF) is shown in Figure 5.16.

5.3.4 Discussion

The observation of these two objects has increased the total number of TNOs polarimetrically observed to 10. Even though these observations represent objects

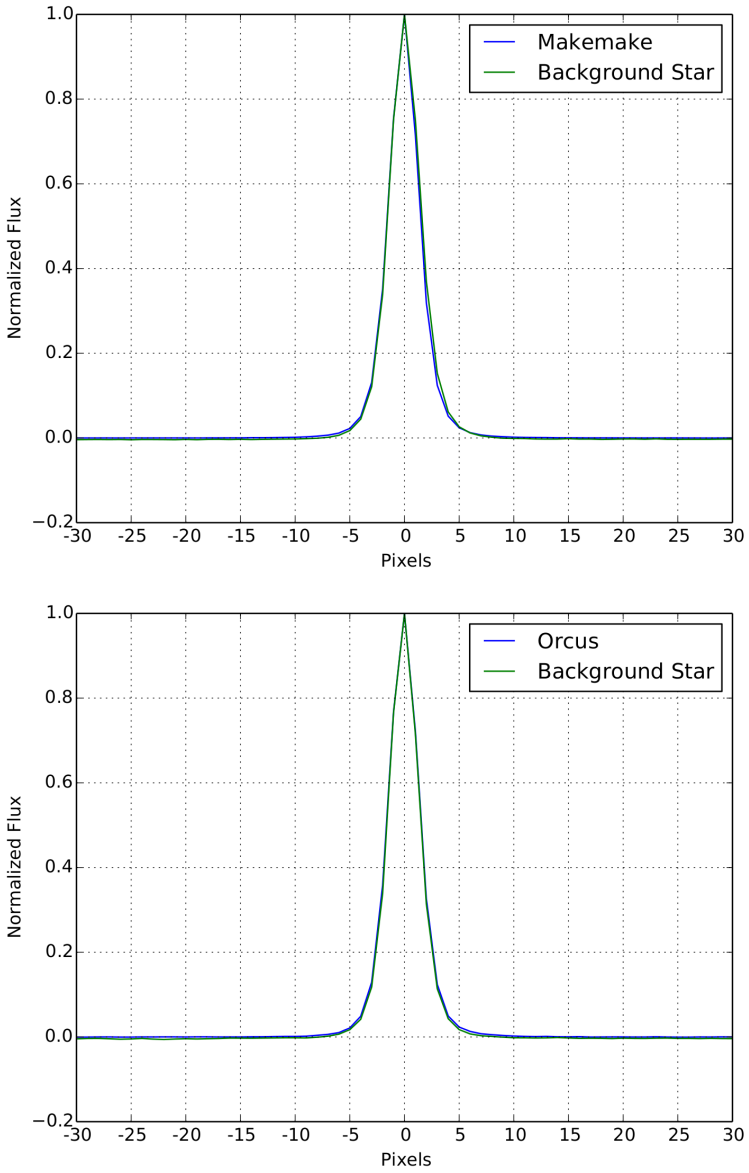

Figure 5.16: The PSF of Makemake and Orcus compared to the profile of a background star.

from all dynamical classes we do not observe considerable differences in their polarisation due to this. Instead we notice a significant difference in the polarisation measured between large and small objects and show a remarkably different polarimetric behaviour compared to asteroids in the inner Solar System, see Section 1.2. We also see a difference between large TNOs that have water-ice dominated surfaces and methane dominated surfaces.

From all the observed large TNOs we do not see any opposition effects associated with observations at small phase angles. These opposition effects show themselves as a sharp increase in the brightness of the object as well as a sharp surge in the amount of negative polarisation observed which is predicted by coherent backscattering theory. Even Eris, which has been polarimetrically observed at a phase angle as low as 0.15° (Belskaya et al., 2008) shows no sign of an increase in negative polarisation. A possible reason why we do not see this is that Eris has a very bright albedo of ~ 0.97 (Sicardy et al., 2011) and this tends to push the opposition surge to smaller phase angles as shown in the coherent backscattering models in Chapter 2. This is also true for our observations of Makemake. Even though it has a sightly lower albedo than that of Eris we still do not see opposition effect in either the polarimetry or photometry. Most probably the opposition surges for these objects are very narrow and unfortunately occur over very small phase angles which we can not sample from ground based observations. However, in the past few years observations of Neptune's moon Triton have exhibited a photometric opposition surge at phase angles less than 0.1°. Triton also has a surface dominated by methane-ice (Tegler et al., 2012) and is believed to be a captured Kuiper belt object due to its retrograde orbit. This supports our suggestion that there may also be a opposition surge for Makemake, Eris, and Pluto.

We can also see that for Makemake, Eris, and Pluto we only see a very small amount of negative polarisation. A hypothesis put forward by Breger & Cochran (1982) was that the small value of negative polarisation observed for Pluto was due to the presence of a thin atmosphere that suppresses the polarisation from the surface. Pluto's atmosphere most probably consists of nitrogen with some carbon

monoxide and methane with a pressure of a few microbars at the surface, when Pluto is at perihelion. The presence of an atmosphere has been confirmed by stellar occultations (Dias-Oliveira et al., 2015). However, we will not know the atmospheric conditions until the New Horizon probe transmits back it analysis of the atmosphere. A pressure of a few microbars is too small to warrant atmospheric effects on the surface polarisation. Even for Mars, that has an atmosphere of several millibars, the influence is rather small in the visible wavelength range. The only time when Mars's atmosphere influences the polarisation is when there are contributions due to the presence of dust clouds and an aerosol component. Since we can hardly expect the out-gassing for a dwarf planet to be larger than for Mars, we may exclude the atmospheric influence on the measured polarisation for Pluto and hence Makemake and Eris.

As we believe it reasonable that we are looking at the surface polarisation and not anything in the atmosphere we can begin to get an idea of what the surface structure of these objects is like and look at the properties of materials that can cause small levels of polarisation and opposition surges. Laboratory measurements at small phase angles have shown that narrow opposition spikes are found in materials that have bright and fluffy surfaces consisting of very small particles (Psarev et al., 2007). These narrow spikes in negative polarisation are usually accompanied by small amounts of polarisation. This has been shown in work done by Shkuratov et al. (1994, 2002) on polarimetric observations of fluffy samples of SiO_2, shown in Figure 5.17. The width of polarisation surge also depends on the porosity of the sample as shown in Figure 5.17. After the sample has been compressed the surface porosity would have been significantly reduced causing the peak to become broader and more visible at larger phase angles. Another possible explanation for any noticeable negative polarisation surges is that the surface particles are large compared to the wavelengths of visible light. Figure 5.17 shows the results presented by Shkuratov et al. (2002) of Al_2O_3 powders of different average grain size with the same high albedo. From this Figure we can see that as the grain size increases we tend only to see a small amount of polarisation.

Of these two possibilities the idea of small sized particles that create a fluffy porous surface is the most likely to be found on the surface of these objects. The reason we believe this is the case is because the surface spectra of Makemake, Eris and Pluto are dominated by frozen volatile gases; nitrogen, carbon monoxide, and methane, that may form a porous hoarfrost from their dilute atmospheres. We could perhaps think of the atmosphere freezing up seasonally as they move further away from the Sun. As is the case for both Makemake and Pluto we could imagine the frosts preferentially evaporate on the darker (warmer) regions of their surfaces and refreeze on the brighter (colder) regions perhaps creating an atmospheric transport of volatiles.

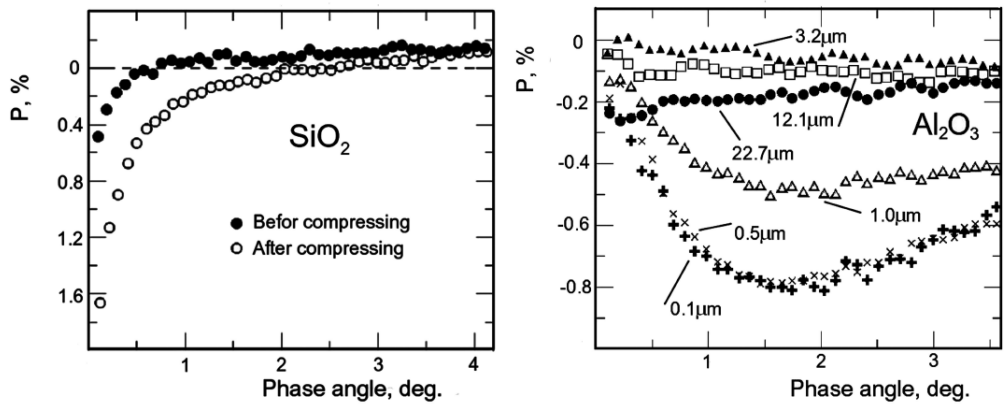

Figure 5.17: Left panel shows super fine SiO_2 particles before and after compression. Right panel shows size separated Al_2O_3 powders. Figure taken from Shkuratov et al. (2002)

The single polarimetric data point of Orcus is very similar to that of the other small TNOs despite belonging to a different dynamical class. This suggests that all these objects have very similar polarimetric properties. The polarisation phase relation for these small TNOs is very similar to that displayed by the major moons of Uranus (Ariel, Umbriel, Titania, and Oberon) as shown in Figure 5.18. All four of these moons have moderate albedos 0.19-0.35 (Avramchuk et al., 2007), which are slightly larger than than that of the small TNOs at < 0.12.

Both the Uranian moons and the small TNO's polarimetric behaviour differs from that of the other icy moons of Jupiter and Saturn despite the presence of water

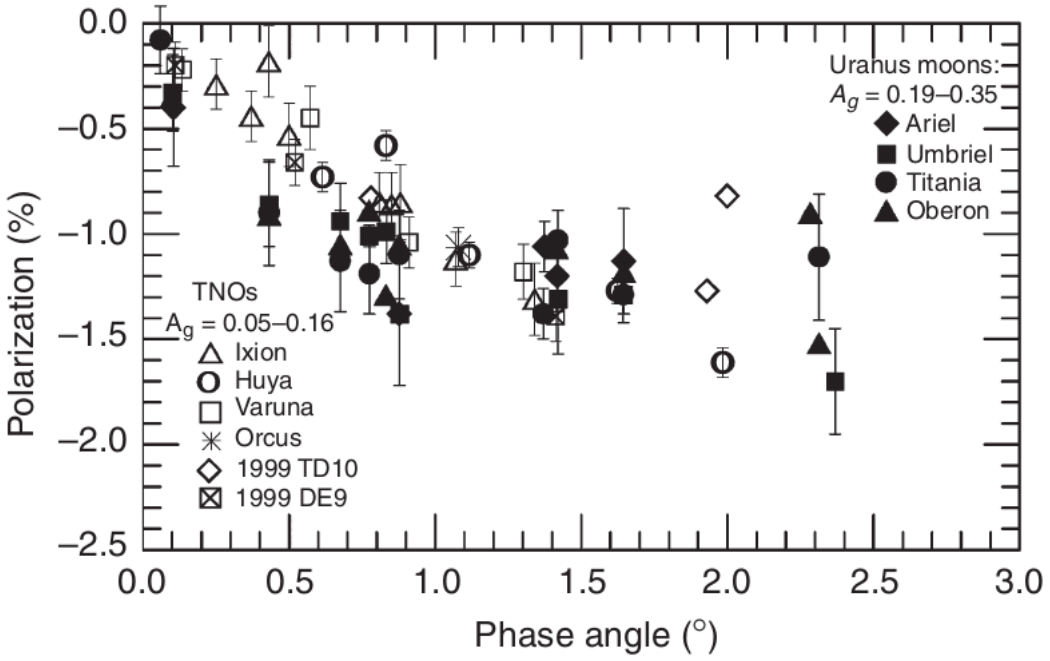

Figure 5.18: Comparison of the polarisation of the Uranian moons (dark symbols) and TNOs (open symbols). Figure taken from Kolokolova et al. (2015)

on all their surfaces. The shift of the minimum of polarisation towards smaller phase angles and the very narrow opposition surge demonstrated by these bodies suggest they have a peculiar surface composition and / or micro-structure. Since both the Uranian moons and the small TNOs are very far from the Sun it can be assumed that these objects consist of a primitive and unprocessed material compared to the icy moons of Jupiter and Saturn.

We can now also begin to interpret the polarimetric observations of both the large TNOs and small TNOs using the RT-CB method outlined in Chapter 2. The numerical computations have been carried out for 6272 spherical media of optical thickness approaching infinity. These media consist of varying several of the parameters within the model as listed here.

- The single scattering albedo is varied $\tilde{\omega}$ = 0.3, 0.4, 0.5 ...., and 0.9.
- The asymmetry parameter g = 0.3, 0.4, 0.5, and 0.6. Where g_1 =0.8,g_2=-0.2 or g_1 = 0.8 g_2 =-0.1.
- The polarisation maximum P_{max} = 0.4, 0.5, 0.6, and 0.7.

- The mean free path, in size parameter scale, k$l \in$ [30,10000]

This gave us a pre-computed grid over which we can compare our observational results. In Figure 5.19 we show the variation envelopes as established from these pre computed RT-CB models by tentatively allowing the geometric albedos 0.1-0.3 and 0.4-0.9 for the small and large TNOs respectively. For the small TNOs we allowed the rms error of the model fit to be smaller than 0.16%; whereas for large TNOs the rms was set at less than 0.3%. These rms values represent the difference in the variation of the observations around the mean value for small and large TNOs, but these values are not based on any rigorous statistical criteria. The geometrical albedo p_v corresponding to the best fits for the small and large TNOs are $p_v \approx 0.2$ and $p_v \approx 0.4$. Based on this analysis, we have $\tilde{\omega} \approx 0.6$, kl ≈ 60 for small TNOs and $\tilde{\omega} \approx 0.9$, kl ≈ 4000 for the large TNOs. As mentioned before the difference in parameters could be due to the presence or absence of volatiles such as, methane or nitrogen, on the surfaces of large and small TNOs.

Apart from the obvious difference in albedo between large and small TNOs the main result of this modelling is the large mean free path between scattering events which suggests a fluffy or frosty surface. The latest images of Pluto from the New Horizons space probe have shown a thin atmosphere escaping from the surface of Pluto. Since Pluto has recently (27 years ago) passed its perihelion passage we could be seeing a transient atmosphere which has began to cool and condense forming frost deposits back on the surface. Recent stellar occultations of Eris and Makemake observed by Sicardy et al. (2011) and Ortiz et al. (2012) showed that both these bodies failed to show any evidence of an atmosphere suggesting that the atmosphere has condensed back to the surface and an atmosphere will not be present until they pass close to their perihelion passage.

5.3.5 Conclusion

Our new polarimetric observations of Makemake and Orcus confirm the two different types of polarisation phase behaviour of the large and small TNOs. The polarisation of Orcus is similar to that of smaller sized TNOs but with only one observation we do not know if it exhibits polarimetric behaviour similar to that of

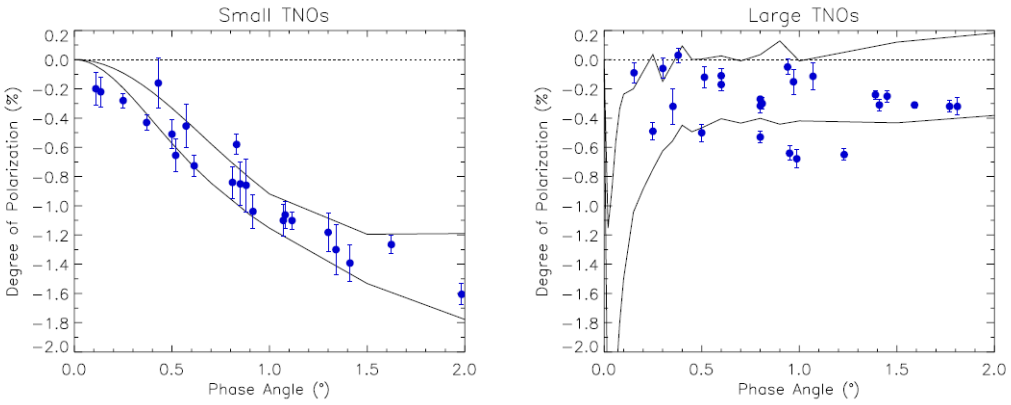

Figure 5.19: RT-CB modelling for large and small TNOs.

the large TNOs. The polarimetric properties of Makemake are very close to those of Eris and Pluto, and different from those of Haumea and Quaoar. To explain the small polarisation of Pluto, Makemake and Eris we assume that their surfaces are covered by a thin layer of hoarfrost masking the surface structure that might produce prominent negative polarisation.

Tables 5.3 was reproduced from Belskaya et al. 2012, A&A, 547, A101 with permission from ©ESO

Chapter 6

Active Comets

6.1 Active comets at large heliocentric distances

The light scattered by dust particles is linearly polarised by a small amount depending on the properties of the scattering media. By studying the polarized light reflected by cometary dust we can obtain information on the micro-structure and single scattering albedo of the cometary atmosphere (Muinonen, 2004).

The methods we use to study the dust ejected from comets is similar to techniques used to study the surface structure of atmosphereless bodies. However, it becomes more important to get additional information i.e. colour and spectral information rather than purely polarimetry. These additional pieces of information help determine the precise cause for polarisation trends in the coma and tail of a comet that may be the result of activity or changing properties of the dust grains i.e. particle size, composition, fragmentation, decomposition etc.

Comets are of particular interest as they are believed to be some of the most primitive objects in the Solar System and can give us information about the conditions in which they were formed.

Due to the geometry of the Solar System main-belt asteroids can be generally observed at phase-angles $< 30^{\circ}$. However, since comets can have eccentric orbits it is possible to measure much greater phase angles, especially if they have Earth crossing orbits. At phase angles $\lesssim 20^{\circ}$ the linear polarisation of cometary dust is usually negative, much like atmosphereless bodies.

Polarimetry has been used to classify active comets into two main categories, dust rich and gas rich (Levasseur-Regourd et al., 1996). The distinction between the two types occurs at phase angles beyond 40 degrees. At this point a fork in the polarimetric phase function occurs with dust rich comets showing a much higher amount of linear polarisation compared to gas rich comets. At phase angle ranges $\lesssim 20^{\circ}$ the main bulk of observational data consists of well sampled data for comets 1P/Halley and Hale-Bopp. From the database of comet polarimetry (Kiselev et al., 2006) only comets 47P/AshbrookJackson (observations carried out by Jockers et al 1993, unpublished), 22P/Kopff (Myers, 1985), and 67P/ChuryumovGerasimenko (Myers & Nordsieck, 1984) have been observed within this phase angle range. In addition, low phase-angle measurements of the nucleus of comet 2P/Encke have been presented by Boehnhardt et al. (2008)

Almost all of these observations have been taken at heliocentric distances < 2 AU when comets become more active, and hence brighter meaning they are much easier to observe with small telescopes. Beyond this heliocentric distance they become much harder to observe and it becomes difficult to investigate the properties of the dust.

In this section I present the first colour and polarimetric measurements of three Jupiter Family Comets (JFCs) 67P/Churyumov-Gerasimenko (hereafter 67P), 74P/Smirnova-Chernykh (hereafter 74P), and 152P/Helin-Lawrence (hereafter 152P) at a heliocentric distance > 3 AU. Only 67P has been polarimetrically observed previously by Myers & Nordsieck (1984). All three comets have been photometrically observed to varying extents. 67P has been observed and modelled by numerous authors in recent years as it is the target of the European Space Agency's (ESA) ROSETTA spacecraft. Photometry of 74P has been carried by Lowry & Fitzsimmons (2001) and Lamy et al. (2011). Lamy et al. (2011) observations were carried out with the Hubble Space Telescope as the comet was travelling outbound at a heliocentric distance of 3.55 AU. From these measurements Lamy et al. (2011) were able to derive a nucleus radius of 2.25 ± 0.1 km, which exhibited an axis ratio a/b = 1.14 and a rotational period of 28 ± 6 hours. On the other hand,

152P has not been observed in as much detail with only one publication mentioning photometric observations (Lowry et al., 1999). From these observations Lowry et al. (1999) were able to find an upper limit on the size of the nucleus of 3.3 ± 0.9 km assuming a standard albedo of 0.04. The rotational period for 152P is unconstrained.

6.1.1 Observations

6.1.1.1 Optical photometry and broadband polarimetry

The comets were observed in service mode between February - March 2010 for comet 67P, and April-September 2012 for comets 74P and 152P using the FORS2 instrument installed on Unit Telescope 1 (UT1) of the ESO Very Large Telescope (VLT); see Section 3.4.1 for a description of the FORS instrument. The observations for comets 67P, 74P, and 152P consisted of both quasi-simultaneous photometric and linear polarimetric measurements. The photometric observations for 67P consisted of two 60s exposures in the *R*-Special filter, whereas for 74P and 152P it consisted of four 60s exposures, using both the *R*-Special and *v*-high filters. Due to the exposure time, differential autoguiding of the telescope at the apparent velocity of the objects was applied to the observations. Between each exposure a different offset was applied to the telescope; this was to ensure that the image of the comet does not fall on the same pixels during each exposure.

The photometric observations were immediately followed by the linear polarisation measurements using the *R*-Special filter only. In our initial set of polarimetric observations we obtained a series of frames with the half waveplate set at 8 different position angles 0 - 157.5° in steps of 22.5° each with an exposure time of 380s for 67P, 270s for 74P, and 300s for 152P. All comets' photocentres were found brighter than expected, and for 152P we eventually reduced the exposure time and increased the number of exposures to avoid saturation.

67P was observed at seven different epochs giving us access to a phase angle range 2-15°. 74P was photometrically observed on six different epochs and polarimetrically observed on eight different epochs giving us access to a phase angle range of 2-11°. 152P was photometrically observed on six different epochs and po-

larimetrically observed on seven different epochs giving us access to a phase angle range of 3-15°.

6.1.1.2 Infrared integral field spectroscopy

In addition to the photometric and polarimetric observations of comets 74P and 152P we also obtained infrared spectroscopic observations using the integral field spectrometer, SINFONI, installed at UT4 of the VLT (Eisenhauer, 2003; Bonnet et al., 2004). For a description of the SINFONI instrument see Section 3.4.3 . The spectra were obtained over the whole night of 2012/06/28 in visitor mode; see Table 6.1 for observing log. For these observations we used the *J* and *H*+*K* grating corresponding to the wavelength range 1.1 - 2.45 μm. We also chose the largest field of view of 8×8 arcseconds which gave us a spatial resolution of 125×250mas per pixel. Adaptive optics were not used for these observations as it is not an option for a moving target. The science observations were carried out using a fixed offset template, that shifted between the sky and the comet in a ABBA pattern where A is the sky and B is the target positions of the telescope. The exposure time used for both comets and the on sky observations was 300s. A total of 30 exposures were obtained for comet 152P, 16 in the *J* grating and 14 in *H*+*K* grating. For comet 74P a total of 19 exposures were obtained, 12 with the *J* grating and 7 with *H*+*K* grating. A number of telluric standard stars prescribed by the SINFONI calibration plan and our chosen solar analogue, Land (SA) 110-361, were observed using the same instrumental settings and at an airmass as close as possible to the comet's airmass to provide the necessary calibration.

6.1.2 Data analysis

6.1.2.1 FORS data pre-processing

The polarimetric and photometric images were reduced using the methods described in Section 4

6.1.2.2 FORS photometry

The comets displayed coma and dust tails in the images indicating recent or current activity. The signal from the bare nucleus is not detected. We used an aperture of

Table 6.1: Observing log of SINFONI observations of comet 152P on the night 28 June 2012. For all exposures the integration time was 300 seconds. The heliocentric distance is 3.12 AU and geocentric distance is 2.23 AU.

UT start	Grating	Airmass start	Airmass end
00:27:24	J	1.129	1.117
00:40:12	J	1.102	1.092
01:02:58	J	1.063	1.056
01:14:32	J	1.048	1.042
01:20:10	J	1.042	1.036
01:31:13	J	1.031	1.027
01:37:28	J	1.026	1.022
01:48:39	J	1.019	1.016
01:55:30	J	1.015	1.013
02:06:29	J	1.012	1.011
02:12:06	J	1.011	1.01
02:23:09	J	1.01	1.01
02:37:21	H+K	1.012	1.014
02:48:34	H+K	1.017	1.019
02:54:12	H+K	1.019	1.023
03:05:19	H+K	1.027	1.032
03:10:57	H+K	1.032	1.037
03:22:00	H+K	1.043	1.049
03:27:36	H+K	1.049	1.056
03:38:43	H+K	1.064	1.072
03:44:20	H+K	1.073	1.081
03:55:25	H+K	1.091	1.101
04:01:02	H+K	1.102	1.112
04:12:04	H+K	1.125	1.137

between 7 - 13 pixel which covers 10,000 km around the coma. This aperture included flux from the majority of the coma and some of the tail of the comet. The background sky was estimated using a detached annulus at a location close to the comet but free from contamination from the coma, tail, and background stars.

In general, it is not possible to give accurate night-by-night values for the zero point or extinction coefficients because photometric standard stars are not taken by default under the FORS calibration plan for polarimetric observations. Therefore, we used the nightly zero point and extinction coefficient available on the ESO quality control and data processing web page. These were calculated using all the photometric standard stars observed over a period of about 28 nights centred at each

night under consideration. We assigned an uncertainty of 0.05 mag to the magnitude measurements, which is consistent with the uncertainties of the zero points. The uncertainties due to photon noise and background subtractions are negligible in comparison with those of the zero points.

Finally the apparent magnitudes for different epochs were magnitude corrected for Sun and Earth distances of the comet using Equation 5.7 (Page: 146). This corrected magnitude allows us to investigate how the brightness of the comet changes independently of its distance but is still dependent on the phase angle. It should be noted that Equation 5.7 needs to be treated with care when applied to comets as they are extended sources. The aperture used to measure the flux from the comet should be a fixed distance aperture, in this case 10,000 km, rather than a fixed pixel aperture. The fixed distance aperture means we can compare the same extent of coma and tail in every observation whereas a fixed pixel aperture would be effected by changes in Δ as the aperture would encompass more or less of the coma/tail depending whether Δ was getting smaller or larger between observations. We can also use these magnitudes to calculate a *V-R* colour magnitude for the comets. This allows us to see if there are any fluctuations in the colour that would suggest a change in the dust particles emitted.

In addition to colour fluctuations we can use the flux from the comets to measure the relative dust production rate. This is done using a quantity $Af\rho$ first defined by A'Hearn et al. (1984). $Af\rho$ is a slightly aperture-dependent quantity which is roughly proportional to the dust production rate of a comet. $Af\rho$ is typically measured in cm and is determined from the observations using a rearranged version of Equation 5.8 (Page: 154). Since we are using a fixed aperture our value for ρ is 5×10^8 cm. The photometric results for comets 152P, 74P, and 67P are presented in Table 6.2 and plotted in Figures 6.1, 6.6, and 6.10 and the results will be discussed in Section 6.1.3.1, 6.1.3.6, and 6.1.3.10.

6.1.2.3 FORS intensity maps

FORS intensity maps are constructed by stacking all the photometric images taken using the same filter together. We can also use the polarimetric images to create

intensity maps as well, although due to the limited field of view of a FORS strip it is usually better to use photometric images if available. Analysis of the coma and tail to search for structure was performed using a combination of numerical techniques as well as visual inspection of the intensity maps. The first of these techniques was the Laplace filtering which highlights regions of intensity change which can be used to search for localised activity such as jets (Boehnhardt & Birkle, 1994). The second technique is radial renormalization, which highlights deviations in the mean coma brightness (A'hearn et al., 1986). The analysis of the structure of each comet is discussed in Sects. 6.1.3.2, 6.1.3.7, and 6.1.3.11.

6.1.2.4 Colour maps

Aperture photometry gives us information over a large portion of the active region of the comet. To inspect the colour of the coma and search for small scale features such as jets in the coma we created *V-R* colour maps using the photometric frames. For details on how these maps were created see Section 4.7.

The final *V-R* colour maps are shown in Figure 6.3 and 6.8 and are discussed in Sects. 6.1.3.3 and 6.1.3.8.

6.1.2.5 Aperture polarimetry

Aperture polarimetry is carried out in a similar way to that described in Sect 6.1.2.2. The $f_{\parallel}$ and $f_{\perp}$ from Equation 4.5 are measured from the polarimetric FORS images using aperture photometry. As mentioned in Section 6.1.2.2 the background sky level was estimated using an offset annulus that was close to the comet but far enough away so that influence from the coma, tail, and background stars was at a minimum. The size of the aperture chosen to measure the flux on a given night was based on the uncertainty on the measured P_Q and P_U, and if the values of P_Q and P_U were not varying with size of aperture used as shown in Section 4.3. The aperture typically chosen for the polarimetry varied between 6-8 pixels for comet 152P, 7-10 pixels for 74P and 4-6 pixels for comet 67P. The polarimetric results for comets 67P, 74P, and 152P are shown in Table 6.2. The polarimetric phase curve is discussed in Section 6.1.4 and plotted in Figure 6.12.

6.1.2.6 Polarimetric map

Any change in polarimetric characteristics would be due to changes in characteristics of the scattering medium, in our case, in size or composition of the dust particles in the coma. These polarimetric changes can then be compared to the *V-R* colour maps where variations are also related to variations in size or composition of the dust particles. The explanation of how these maps were created can be found in Section 4.8

6.1.2.7 IR spectrophotometry

The infrared spectra obtained by the SINFONI instrument were reduced using the ESO SINFONI reduction pipeline (version 2.3.2), with all the relevant calibration files provided by ESO. The pipeline was also used to extract all the spectra from the data cubes using a 6 pixel aperture centred around the approximate photometric centre of the comet.

The individual spectra extracted in the *J*- and *H*+*K*-bands were corrected for the exposure time and combined performing a resistant mean with a threshold of $2.5\,\sigma$. The same data reduction steps were applied to the solar analogue spectra. The target spectrum was divided by that of the solar analogue Land (SA) 110-361 observed at similar airmass to correct for telluric lines and remove the Sun's contribution, obtaining this way the comet relative reflectance spectrum . The latter was normalized to unity at 1.2 micron. Unfortunately we do not have near-infrared photometric data to verify the adjustment of the separate spectra taken in the J and H+K wavelength bands. We therefore need to rely on our data processing. In Fig 6.5 we present the relative reflectance spectrum of 152P only, since the signal-to-noise of the comet 74P spectrum was too low to yield any useful information.

6.1.3 Results

The results of the photometry and polarimetry for the comets are displayed in Table 6.2. Sect 6.1.3 is dedicated to the results of comet 152P, Sect 6.1.3.5 to comet 74P, and Sect 6.1.3.9 to comet 67P. In the Sects 6.1.3, 6.1.3.5, and 6.1.3.9 we present the

Table 6.2: Photometric and polarimetric results obtained for comet 152P, 74P, and 67P. Each magnitude has a standard error of 0.05 magnitude.

Target	Date (dd/mm/yyyy)	Time hh:mm	Phase angle (degrees)	r AU	Δ AU	R	V	H_R	H_V	$V-R$	P'_Q (%)	P'_U (%)
152P	05/04/2012	08:30	15.37	3.158	2.496	17.97	18.74	13.49	14.24	0.74	-0.922 ± 0.066	0.235 ± 0.065
	30/04/2012	06:15	9.80	3.139	2.239	17.51	18.02	13.29	13.79	0.57	-1.483 ± 0.039	0.006 ± 0.039
	21/05/2012	05:45	3.38	3.127	2.126	16.95	17.49	12.84	13.37	0.54	-1.121 ± 0.031	0.029 ± 0.031
	23/05/2012	03:15	2.86	3.126	2.122	16.87	17.47	12.87	13.36	0.60	-1.209 ± 0.031	0.035 ± 0.031
	15/07/2012	03:30	14.54	3.116	2.368	17.49	18.15	13.15	13.81	0.66	-1.096 ± 0.039	0.054 ± 0.040
	16/07/2012	00:57	14.91	3.116	2.368	-	-	-	-	-	-1.089 ± 0.038	0.117 ± 0.039
	24/07/2012	02:00	16.31	3.117	2.466	17.79	18.12	13.16	13.69	0.54	-0.926 ± 0.038	0.040 ± 0.038
74P	21/06/2012	07:05	7.74	4.557	3.705	19.34	20.12	13.20	13.99	0.79	-	-
	26/06/2012	09:04	6.70	4.561	3.666	19.37	-	13.26	-	-	-1.384 ± 0.087	0.182 ± 0.094
	17/07/2012	06:24	2.35	4.579	3.576	19.00	19.68	12.93	13.61	0.68	-1.231 ± 0.088	0.002 ± 0.088
	24/07/2012	06:11	1.36	4.585	3.574	18.89	19.58	12.82	13.51	0.70	-0.800 ± 0.078	0.031 ± 0.101
	18/08/2012	06:25	5.75	4.606	3.680	19.41	20.11	13.27	13.97	0.70	-	-
	19/08/2012	02:17	5.92	4.602	3.688	19.09	19.77	12.94	13.62	0.68	-1.222 ± 0.037	0.150 ± 0.037
	10/09/2012	03:55	9.72	4.602	3.920	-	-	-	-	-	-1.160 ± 0.114	0.210 ± 0.115
	16/09/2012	03:56	10.47	4.627	3.999	-	-	-	-	-	-1.400 ± 0.132	0.001 ± 0.131
67P	09/02/2010	06:54	15.37	3.447	2.951	21.08	-	16.05	-	-	-0.793 ± 0.53	-0.621 ± 0.53
	22/02/2010	05:41	13.14	3.523	2.850	21.12	-	16.11	-	-	-1.067 ± 0.49	0.178 ± 0.49
	06/03/2010	08:42	10.33	3.593	2.780	20.39	-	15.39	-	-	-1.116 ± 0.57	-0.227 ± 0.59
	07/03/2010	04:30	10.11	3.598	2.776	20.95	-	15.95	-	-	-1.959 ± 0.50	-0.621 ± 0.49
	09/03/2010	06:08	9.56	3.610	2.768	20.84	-	15.84	-	-	-2.031 ± 0.41	-0.178 ± 0.42
	16/03/2010	04:45	7.61	3.649	2.747	20.76	-	15.76	-	-	-1.428 ± 0.37	0.258 ± 0.38
	29/03/2010	03:50	2.72	3.721	2.744	19.85	-	14.81	-	-	-0.568 ± 1.17	-1.683 ± 1.18

results of aperture photometry, colour maps, $Af\rho$ and polarimetric maps. In Sect 6.1.4 we present the aperture polarimetry for 152P, 74P, and 67P.

Comet 152P/HelinLawrence

6.1.3.1 Aperture Photometry

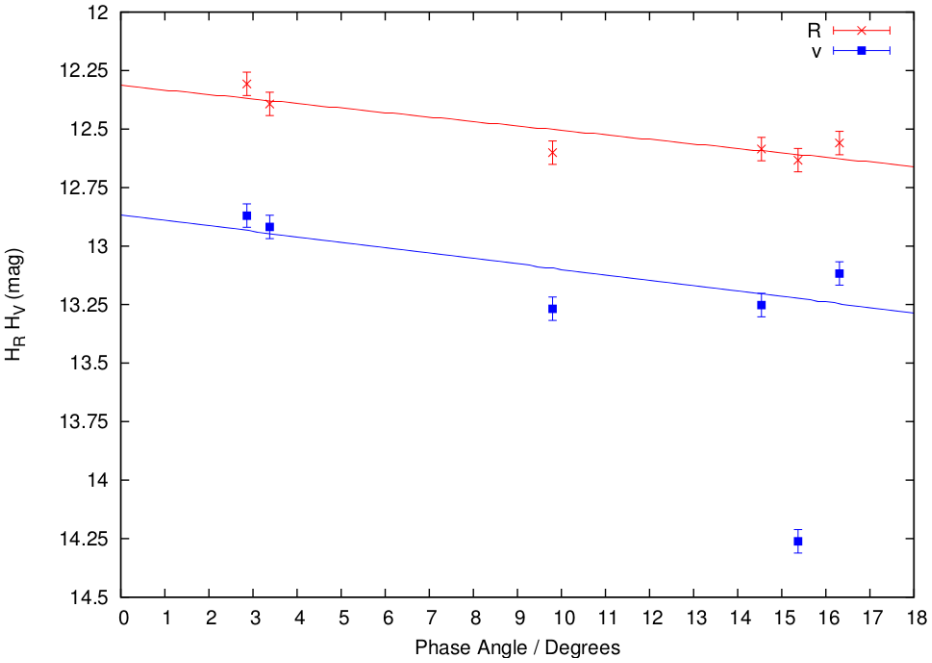

Figure 6.1: Magnitude corrected for the Sun and Earth distances of comet 152P as a function of phase angle.

In Figure 6.1 we have plotted the magnitude corrected for the Sun and Earth distances of comet 152P as a function of phase angle. If we ignore the results on the night 05/04/2012 and use a straight line fit the extrapolated average brightness at zero phase angle are 12.79 ± 0.13 and 13.32 ± 0.12 in the *R* and *V* filters assuming no opposition surge. This results in an average *V*-*R* colour of 0.53± 0.18 which is equivalent to a spectral gradient of 18.03 %/100 nm.

Lowry et al. (1999) photometrically observed 152P in *V* and *R* filters and found that 152P had a very red colour of 0.77 ± 0.12 when the comet was at 4.6 AU from the Sun. Within the errors the results are consistent with both measurements.

Using Equation 5.8 and the flux extrapolated back to zero phase in the *R*-Special filter and the average *r* and Δ distances to the comet yields an $Af\rho$ value of 195 ± 22 cm.

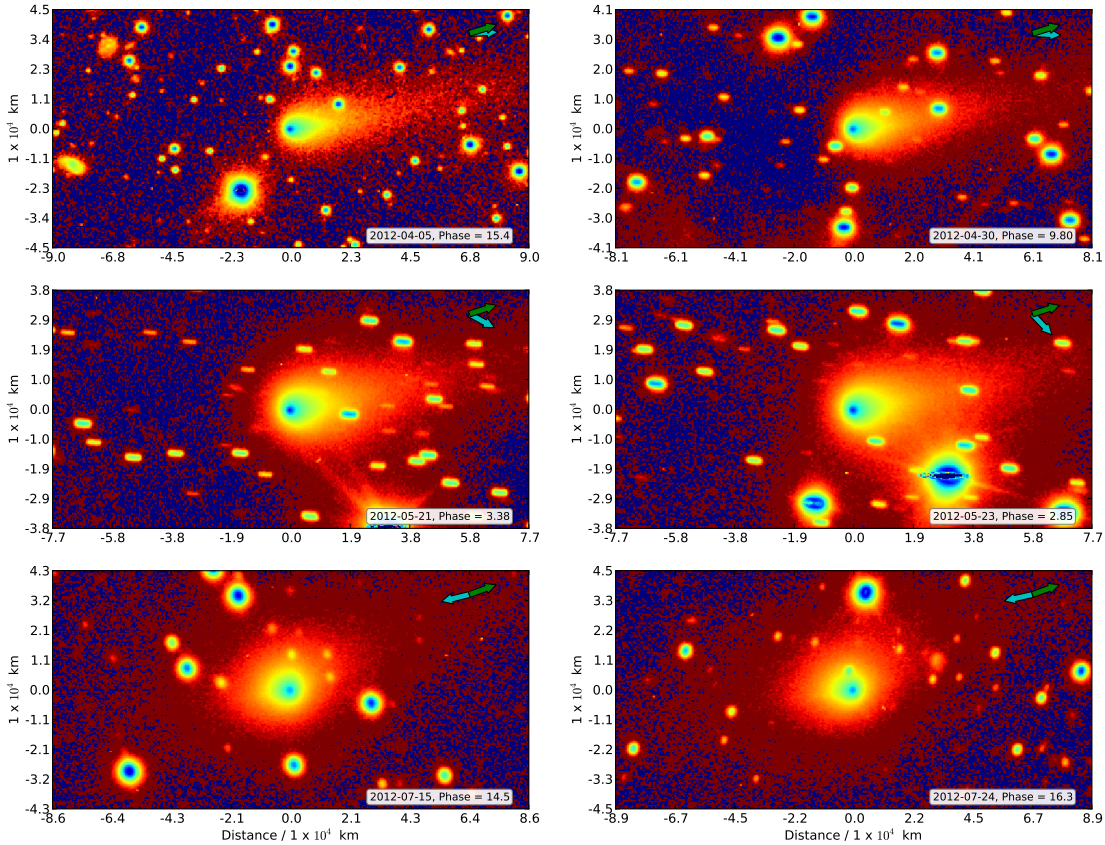

Figure 6.2: Intensity maps of comet 152P. Green arrow points in the direction of the negative target velocity as seen from the observer. The cyan arrow is the direction of the anti-solar direction. North is up and east is to the left.

Table 6.3: Comparison between measured position angle and Finson-Probstein synchrone analysis for comet 152P.

Date (UT)	PA Tail measured (deg)	PA Synchrone 30 days (deg)	PA Synchrone 60 days (deg)	PA Synchrone 120 days (deg)	PA Synchrone 240 days (deg)	PA Synchrone 360 days (deg)
2012-04-05	279-283	276	276	280	282	283
2012-04-30	278-283	273	275	280	282	283
2012-05-21	278-283	267	274	280	283	285
2012-05-23	278-282	266	274	280	283	285
2012-07-15	290-95	102	99	338	295	293
2012-07-24	290-100	101	96	24	297	294

6.1.3.2 Intensity maps

The intensity images for comet 152P are presented in Figure 6.2. Analysis of the intensity images showed that apart from slightly asymmetric coma extensions into northern and northwestern directions and from the main tail axis no distinct coma

structure (jet, fan or shell) was found in processed images. Given the wide wavelength range of the *R*-Special and *v*-high filters used, the coma and tail are mainly representing the dust distribution around the nucleus. Features that could be attributed to gas and plasma, for instance tail rays, are not seen in the images. Tail-like extensions of the coma pointed westward in April and May 2012 and appeared in two parts during the 2nd half of July, one towards West-North-West and one towards East.

Finson-Probstein calculations (Finson & Probstein, 1968; Birkett, 1988) (Table 6.3) for the dust tail geometry show that the dust tail is orientated westward during April and May 2012. The appearance of two dust tail features in the 2nd half of July 2012 indicates that young dust grains, i.e. typically released less than 2 months before observing epoch, project into the eastern sector between angles of 90 and 100°, while much older dust, typically released more than 8 months before the observing date, is found in the West-North-Western coma region. Dust produced by the nucleus in between 2 to 8 months projects as seen from Earth into the Northern coma hemisphere and creates the asymmetric appearance in the coma.

6.1.3.3 Colour maps

Figure 6.3 shows the colour maps of comet 152P. The colour scale has been centred about the solar reflectance colour of 0.35 for *V-R*. Any feature redder or bluer than this value appears in the figure as red or blue, respectively. We note the occurrence of some red-blue "dipole" features, especially in the background. These are artifacts due to the presence of background stars that, due to the differential tracking of the telescope, appear offset in the *R* and *V* images. The exceptions are the top two maps in Figure 6.3 where the colour scale has been extended to accommodate their slightly redder colour compared to the other data, although the colour scale is still centred about 0.35.

The colour maps created show little to no structure apart from the nights 30th of April, 21st and 23rd May. On the 30th April the photometric centre of the comet has a bluer colour compared to that of 5th April. This suggests either the comet

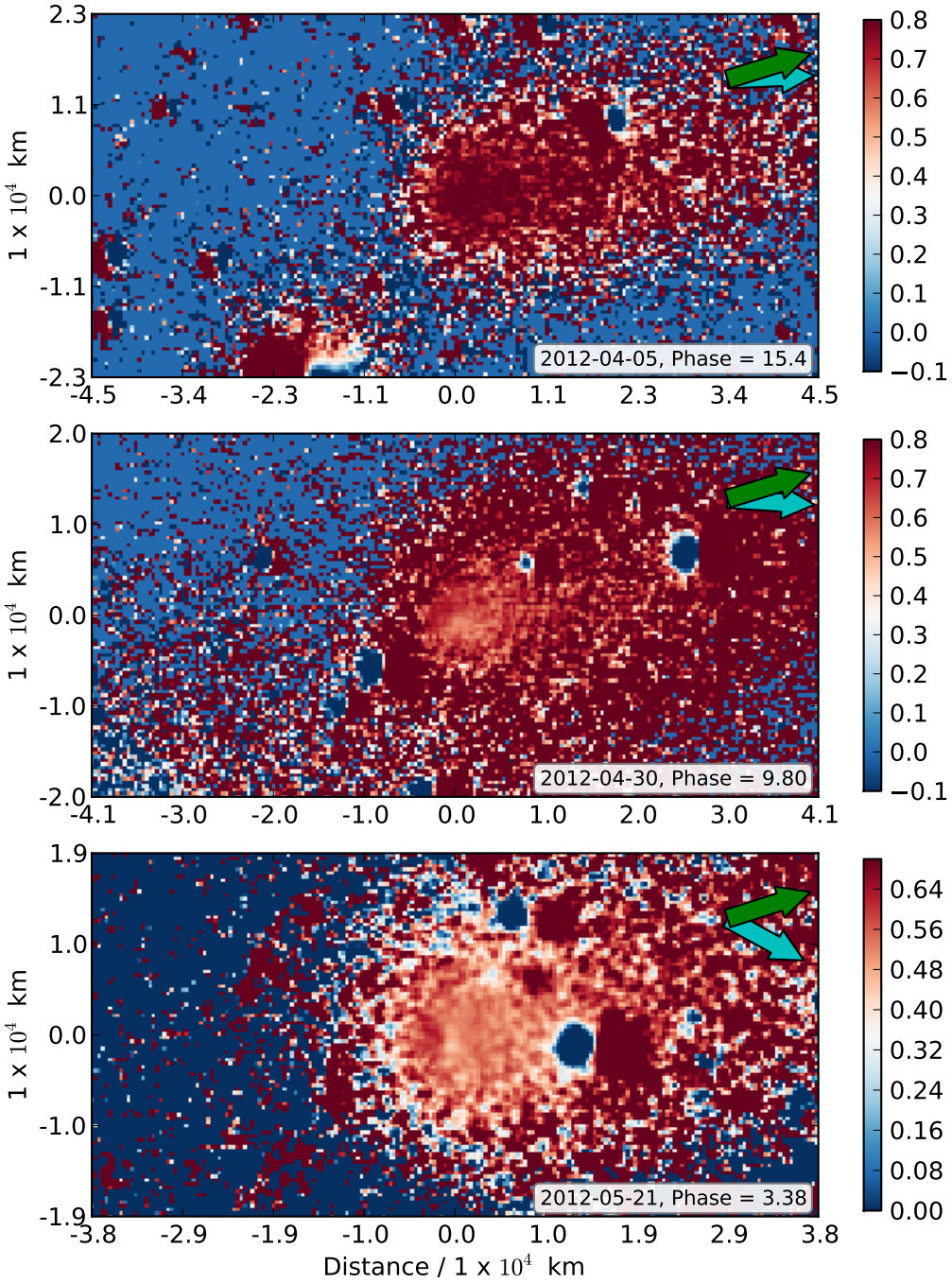

Figure 6.3: *V-R* colour map of comet 152P. Green arrow points in the direction of the negative target velocity as seen from the observer. The cyan arrow is the direction of the anti-solar direction. North is up and east is to the left.

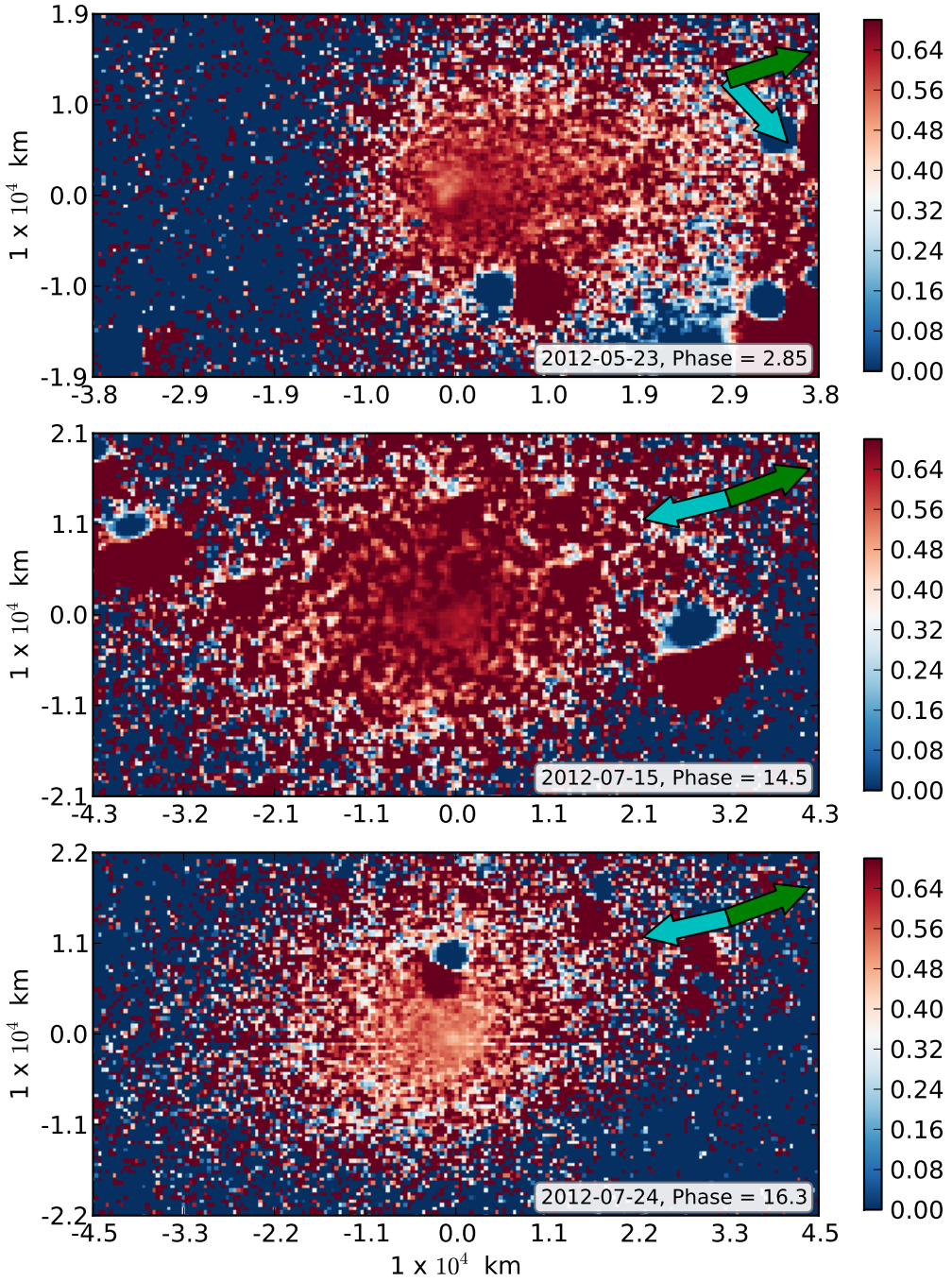

Figure 6.3: *V-R* colour map of comet 152P. Green arrow points in the direction of the negative target velocity as seen from the observer. The cyan arrow is the direction of the anti-solar direction. North is up and east is to the left.

was producing more red material on the 5th April compared to the 30th April or producing bluer material on 30th April. On the 21st May the average coma colour is ~ 0.54. However, there is a small spot at the photometric centre with a colour of ~0.43; north-west of this there is a much redder feature with a colour ~0.63. This could be an indication of activity, jet or outburst, in the inner coma. Two days later on the 23rd May the average colour of the coma has increased to ~ 0.60 perhaps indicating results of the activity, noticed on May 21st. On 23rd of May there is a feature in north-west of the photometric center of the coma as was the case on the 21st May. However, the colour of this feature has changed to a value ~0.43, this could be due to particle movement and nucleus rotation. These features are not a simple case of image misalignment as this would result in a dipole feature which is seen in the background of all these colour maps which are due to stars moving in the background with respect to the comet. Also the images used to calculate these colour maps were carefully selected to ensure that they had very similar seeing conditions. After the 23rd May the coma continues to increase in colour to an average colour of ~ 0.66 which is fairly uniform across the coma. Unfortunately the *V* and *R* images are taken under different seeing conditions making it impossible to see if there was any activity to cause the colour to drop to ~ 0.54 in the coma.

6.1.3.4 Polarimetric maps

The polarimetric maps for comet 152P are presented in Figure 6.4; on the left side are the P_Q maps and on the right side are the P_U maps. On the night 05/04/2012 the background sky was highly polarised, which made getting an accurate background sky estimate difficult which can be seen in the background features in the polarimetric maps. In spite of this there are no unusual polarimetric values that coincide with the red colour seen in the colour maps in Figure 6.3.

The polarimetric maps created for the nights of 21st and 23rd May can be compared to the colour maps created in Figure 6.3 to determine if the same features are present. Figure 6.4 shows that on the night of 21st May the amount of polarisation becomes more negative ~ 3% in the direction of the outburst seen in the colour map in Figure 6.3. In the P_U map for the same night we see an increase in P_U in the

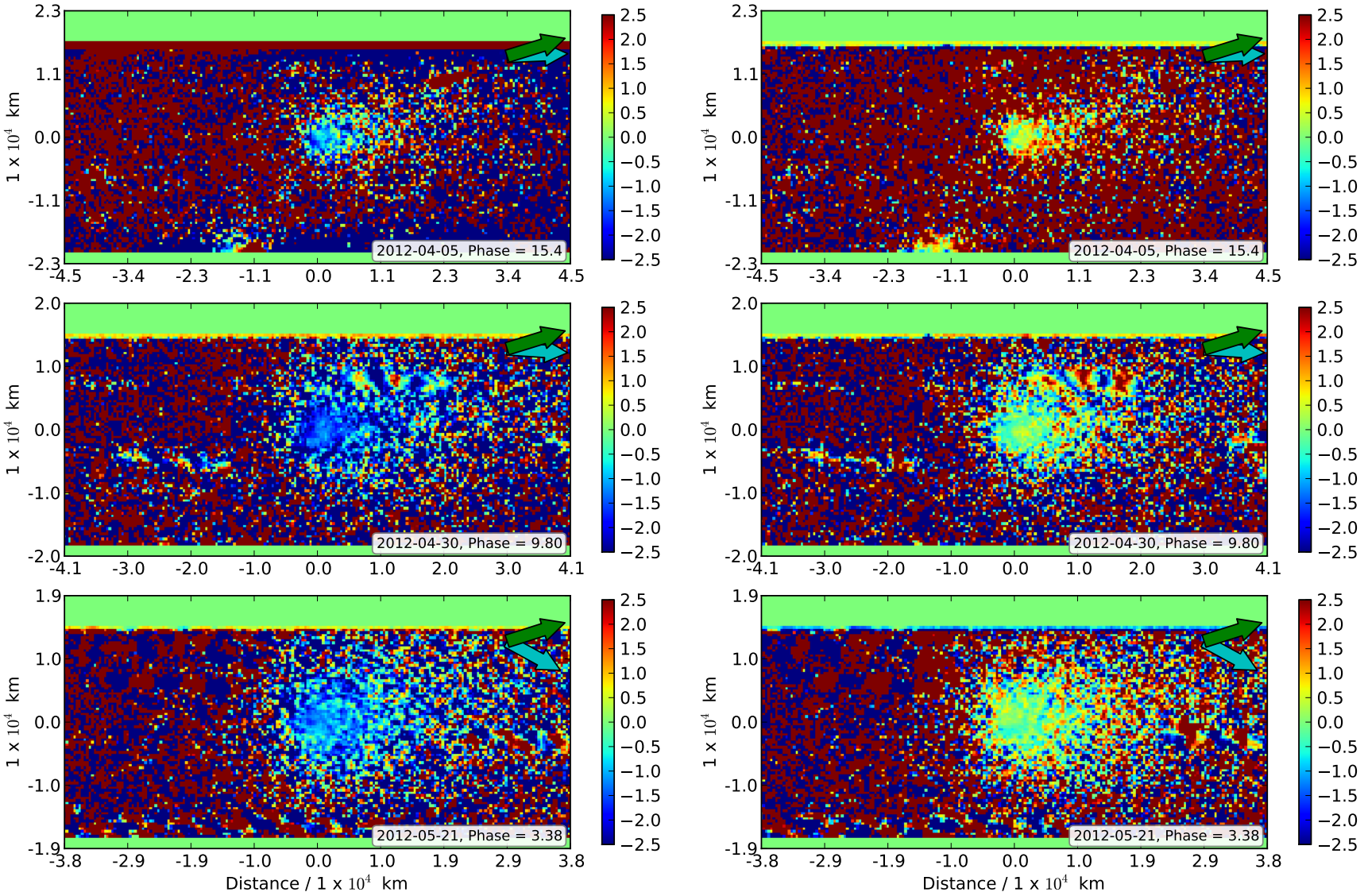

Figure 6.4: P_Q (left) and P_U (right) polarimetric maps for the comet 152P. Green arrow points in the direction of the negative target velocity as seen from the observer. The cyan arrow is the direction of the anti Solar direction. North is up and East is to the left.

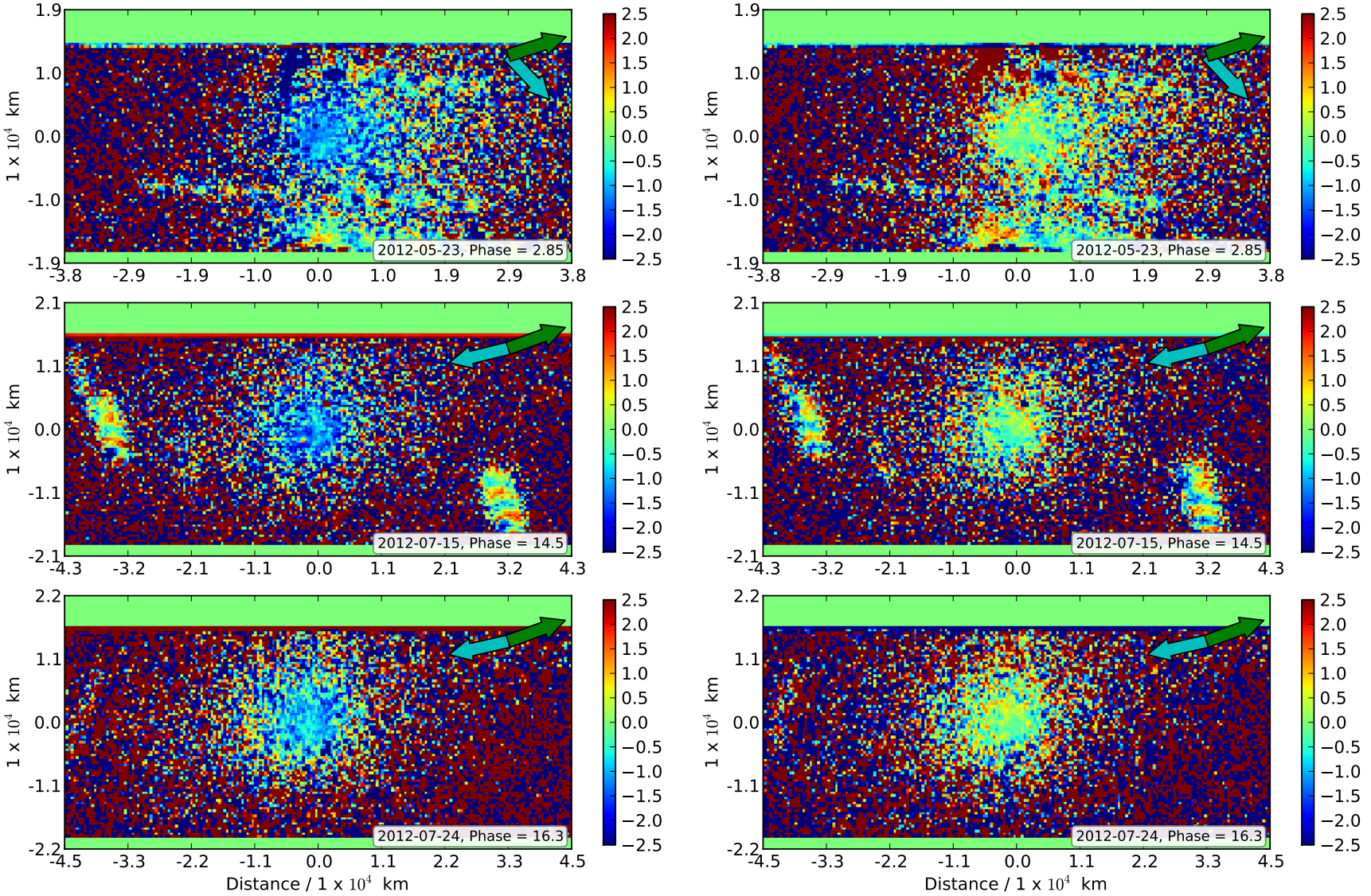

Figure 6.4: P_Q (left) and P_U (right) polarimetric maps for the comet 152P. Green arrow points in the direction of the negative target velocity as seen from the observer. The cyan arrow is the direction of the anti Solar direction. North is up and East is to the left.

location of the outburst region of ~ 0.5%. Again this suggests that the outburst is composed of a different material or has a different morphology to the surrounding coma.

On 23rd May there is a slight hint of structure in the coma in the P_Q map for this night. In the north-western direction from the photometric centre there is a slightly more negative polarisation compared to the south-eastern direction. This polarisation difference occurs in the same location as the colour feature seen in the colour maps of Figure 6.3.

In the last two maps in July as seen in Figure 6.4 both maps in P_Q show very few features of note. In the P_U maps on the same nights there are small fluctuations in polarisation of around ± 0.1%, consistent with noise.

6.1.3.5 SINFONI infra-red spectra

Figure 6.5 shows the relative reflectance spectrum of comet 152P. The target spectrum presents a positive spectral slope. We looked for the presence of water ice absorption features at 1.5 and 2.0 μm, displayed by other JFCs' spectra such as Hartley 2 (A'Hearn et al., 2011) and the outbursting comet P/2010 H2 (Vales) (Yang & Sarid, 2010). However, 152P's spectrum does not display clear water-ice absorptions and resembles, to a first order, the spectrum of a dark and featureless refractory component (e.g., amorphous carbon, dashed blue line).

Comet 74P/SmirnovaChernykh

6.1.3.6 Aperture photometry

74P shows a constant Solar *V-R* colour throughout all our observations. The only exception is the night 21/06/2012 which is contaminated by two nearby saturated stars particularly when the *R* filter observations were carried out.

In Figure 6.6 we have plotted the magnitude corrected for the Sun and Earth distances of comet 74P as a function of phase angle. If we ignore the result on the night 21/06/2012 and use a straight line fit the extrapolated average brightnesses at zero phase angle are 12.76 ± 0.13 and 13.43 ± 0.15 in the *R* and *V* filters assuming no opposition surge. This results in an average *V-R* colour of 0.67 ± 0.20 which is

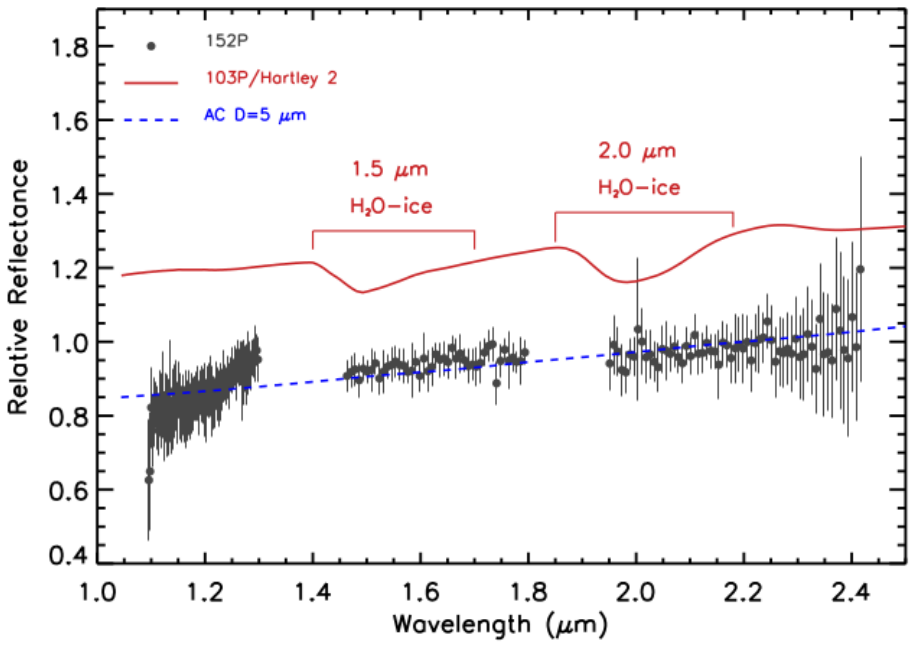

Figure 6.5: Relative reflectance spectrum of comet 152P (grey dots). For comparison, a synthetic spectrum of amorphous carbon (AC) grains (particle diameter of 5 μm, blue line) and the synthetic spectrum used to represent the Hartley 2 coma (solid red line) composed of 1 μm water-ice grains and dust not in thermal equilibrium (Protopapa et al., 2014).

equivalent to a spectral gradient of 34.28 %/100 nm.

Lowry & Fitzsimmons (2001) observed 74P and found that it had a *V-R* colour of 0.44 ± 0.10 which is not quite as red as suggested by our findings.

Using Equation 5.8 and the flux extrapolated back to zero phase in the *R*-Special filter and the average r and Δ distances to the comet yields an $Af\rho$ value of 201 ± 23 cm.

6.1.3.7 Intensity maps

The intensity images for comet 74P are presented in Figure 6.7. We note that the intensity images for the nights 2012-06-26 and 2012-09-10 are missing due to the presence of close background stars that interfere with the analysis of any structures in the tail region. Additionally the intensity image for the night 2012-08-19 has been omitted as it is very similar to that of the night 2012-08-18. Also for the night 2012-09-16 no photometric images were available therefore we have created the intensity map using the polarimetric images.

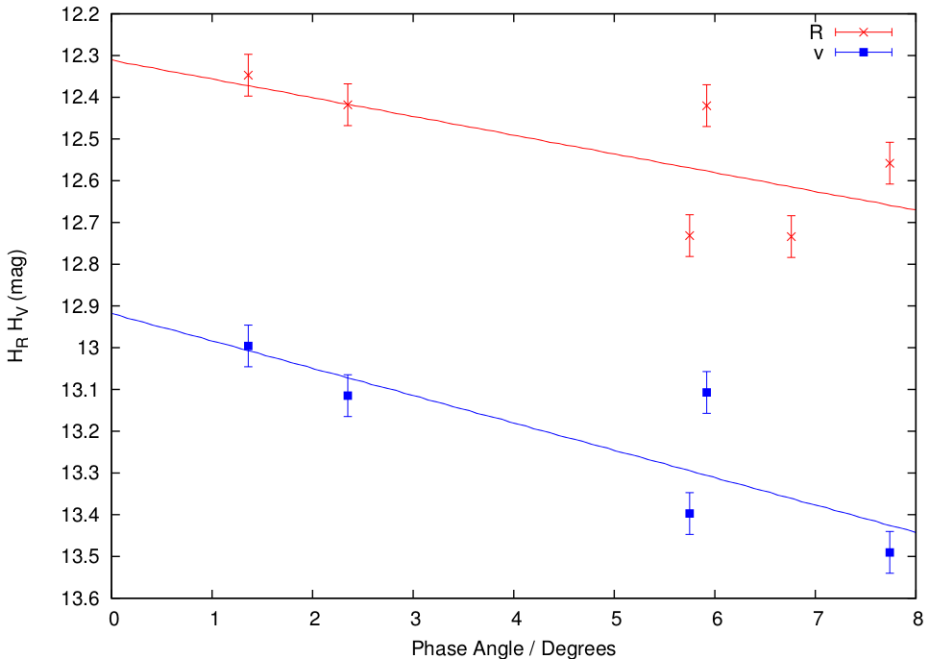

Figure 6.6: Magnitude corrected for the Sun and Earth distances of comet 74P as a function of phase angle.

Table 6.4: The Finson-Probstein synchrone analysis for comet 74P.

Date (UT)	PA Tail measured (deg)	PA Synchrone 30 days (deg)	PA Synchrone 60 days (deg)	PA Synchrone 120 days (deg)	PA Synchrone 240 days (deg)	PA Synchrone 360 days (deg)
2012-06-10	264-264	262	261	261	261	261
2012-06-26	260-264	267	266	266	266	266
2012-07-17	263-268	290	277	270	268	267
2012-07-24	267-269	315	287	274	269	268
2012-08-18	268-272	66	55	320	275	270
2012-08-19	268-272	67	56	323	275	270
2012-09-10	272-280	75	72	53	283	272
2012-09-16	272-280	77	74	60	285	272

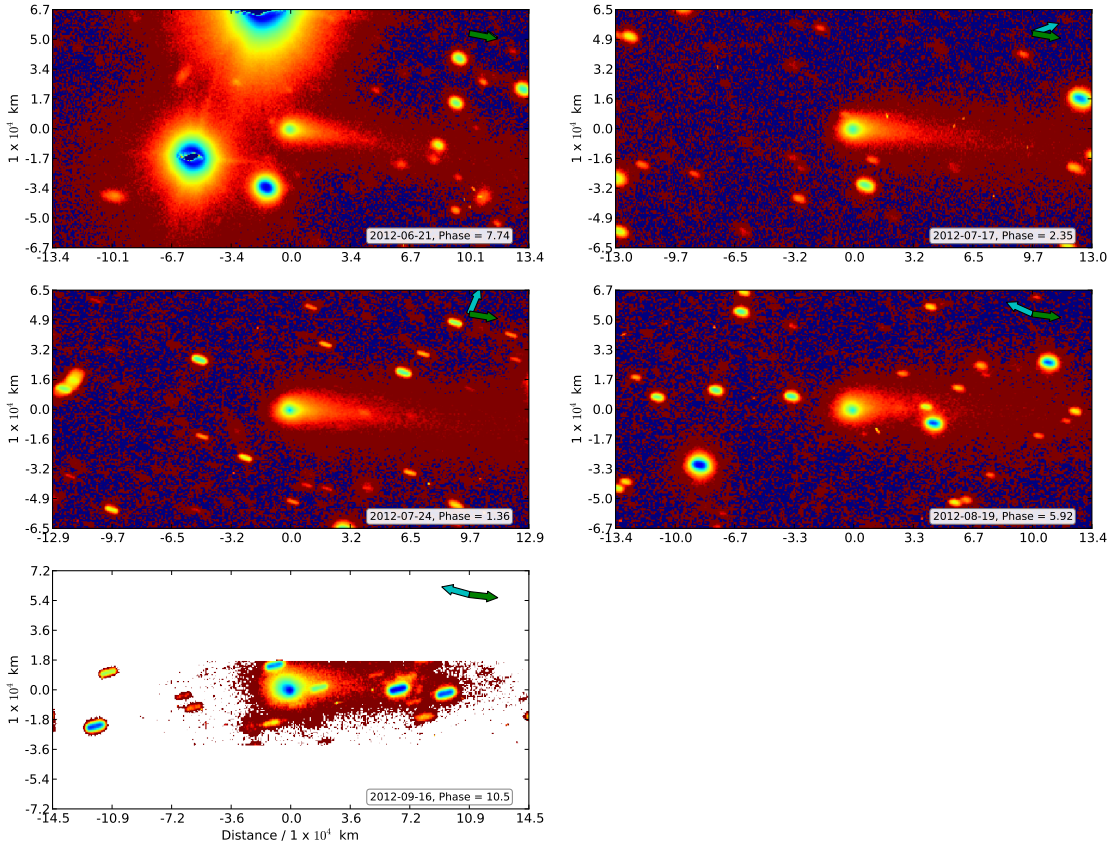

Figure 6.7: Intensity maps of comet 74P. Green arrow points in the direction of the negative target velocity as seen from the observer. The cyan arrow is the direction of the anti-solar direction. North is up and east is to the left.

No distinct coma structure was found in processed images indicating no localized activity on the nucleus. Again given the broad wavelength range of the filters used the coma and tail are mostly representing the dust distribution around the nucleus. Features that could be attributed to gas and plasma (for instance tail rays) are not seen in the images. A dust tail is present throughout the observing period in a westward direction. At the beginning of the observing period this dust tail was also slightly curved towards the south. In late September 2012, and possibly in August 2012, there is a noticeable additional coma extension into the north-western quadrant.

The Finson-Probstein analysis of the dust tail geometry (Table 6.4) suggests that there is a coma asymmetry in the north-western coma section in September 2012 maybe due to dust grains released during the previous 2 months before obser-

vations and projected into that coma quadrant as seen from Earth. The westward pointing tail at this time consists of very old dust emitted by the nucleus about a year earlier. The old dust overlaps with the more recent grains during the June and July observing epochs forming a brighter and wider slightly curved dust tail as seen in the images.

6.1.3.8 Colour map

The colour maps produced for comet 74P are shown in Figure 6.8. The blue and red spots exhibited on the nights 2012-06-21 and 2012-07-24 are artificial features caused by a large seeing difference between V and R images. On the other nights not affected by seeing changes there is no clear evidence of colour variation within the coma or tail region of the comet.

6.1.3.9 Polarimetric maps

In Figure 6.9 we present the polarisation maps for 74P. Since 74P was fainter and exhibited a narrow coma and tail the signal to noise ratio is lower than for 152P. Additionally, the comet passes close to background stars which makes it difficult to search for features in the coma and tail region especially when the 3 by 3 box car is applied. The quality of the observations for 74P is lower as our photometric and polarimetric measurements did not always occur on the same night and the presence of background stars changed throughout our polarimetric observations.

On the nights 26/06/2012, 19/08/2012, and 10/09/2012 the comet passed close to or in front of the background stars which affects our search for structures within the coma and tail of the comet. The least affected nights are the two nights in July. In the P_Q maps for the observation on 17th and 24th, Figure 6.9, we see no clear evidence of structure or change in the amount of polarisation across the coma. In the P_U maps on both nights there is a small residual polarisation which, however, shows no definite structure that suggests a jet or an outburst is present.

On the night 16/09/2012 there was a tracking issue which caused the target offsetting toward the edge of the strip during the exposures. Nothing clear can be seen on this night, most likely due to the low signal to noise ratio from the data.

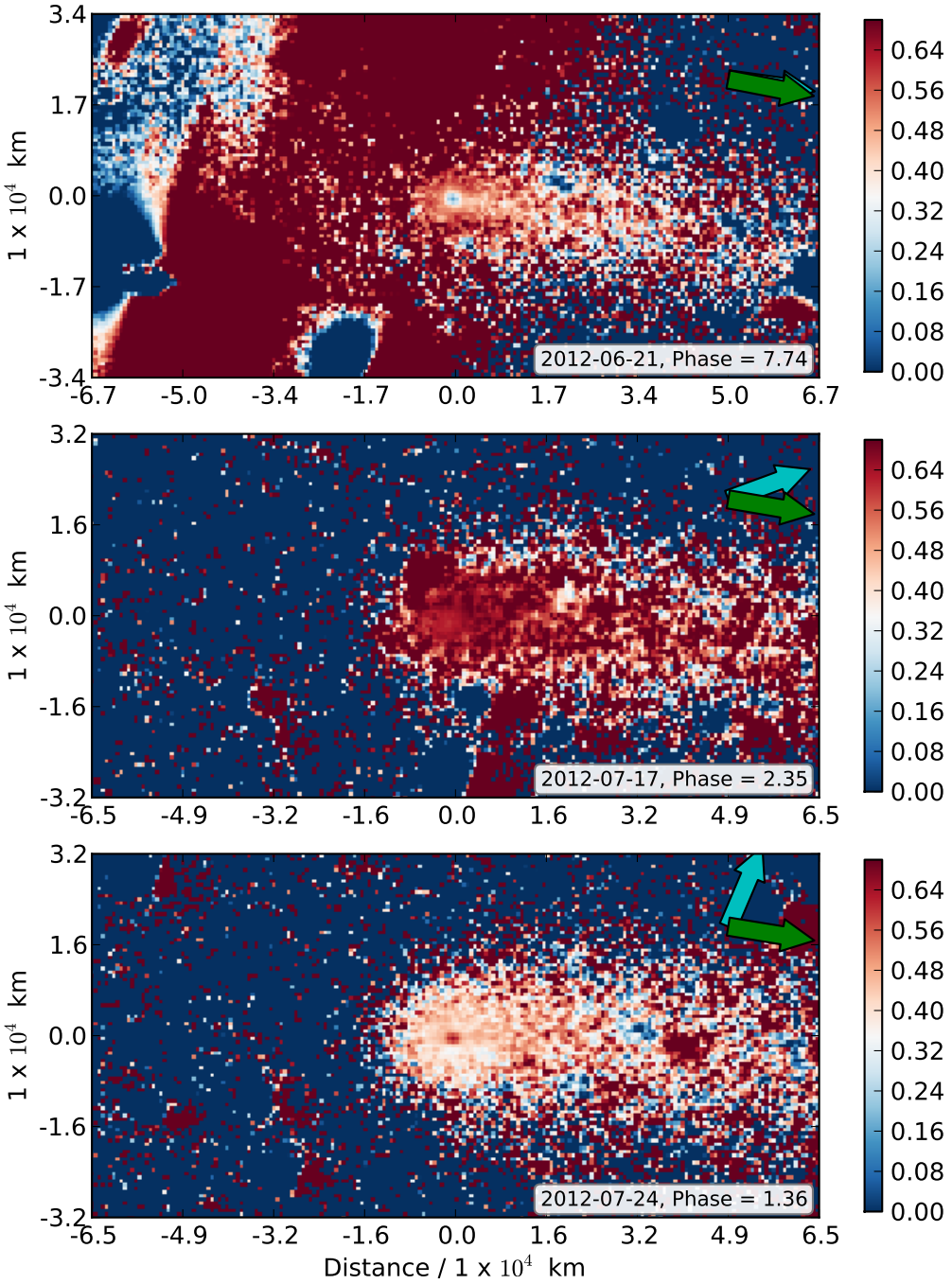

Figure 6.8: *V-R* colour map of comet 74P. Green arrow points in the direction of the negative target velocity as seen from the observer. The cyan arrow is the direction of the anti-solar direction. North is up and east is to the left.

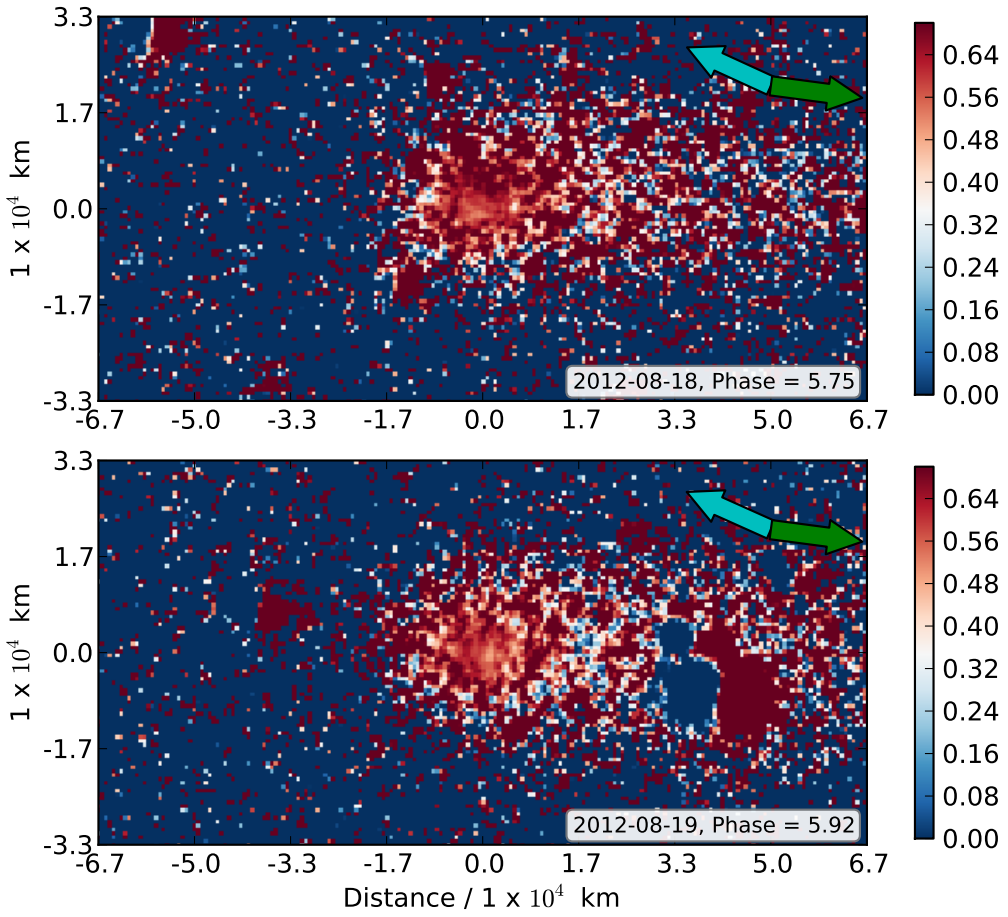

Figure 6.8: *V-R* colour map of comet 74P. Green arrow points in the direction of the negative target velocity as seen from the observer. The cyan arrow is the direction of the anti-solar direction. North is up and east is to the left.

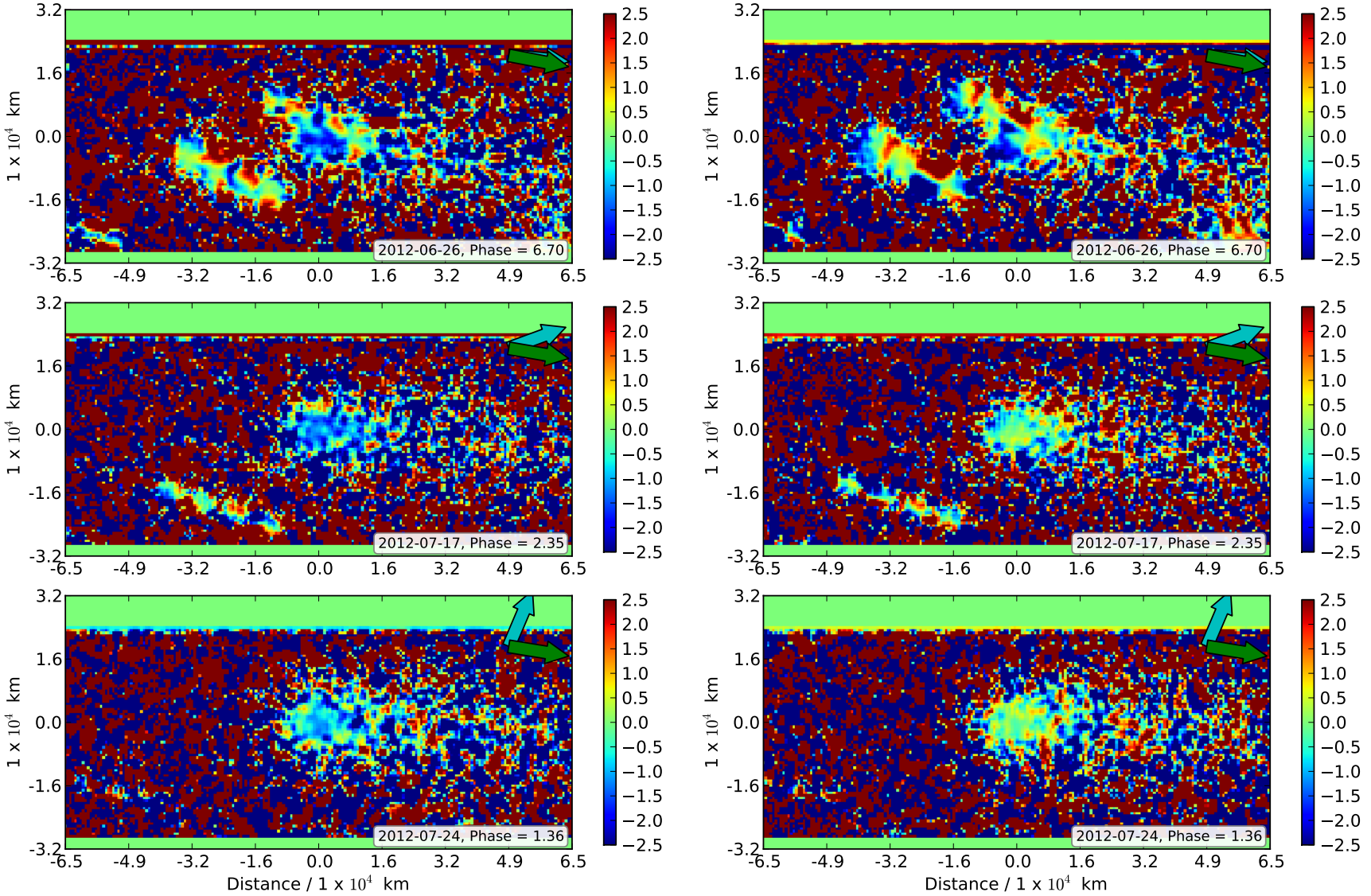

Figure 6.9: P_Q (left) and P_U (right) polarimetric maps for the comet 74P. Green arrow points in the direction of the negative target velocity as seen from the observer. The cyan arrow is the direction of the anti-solar direction. North is up and East is to the left.

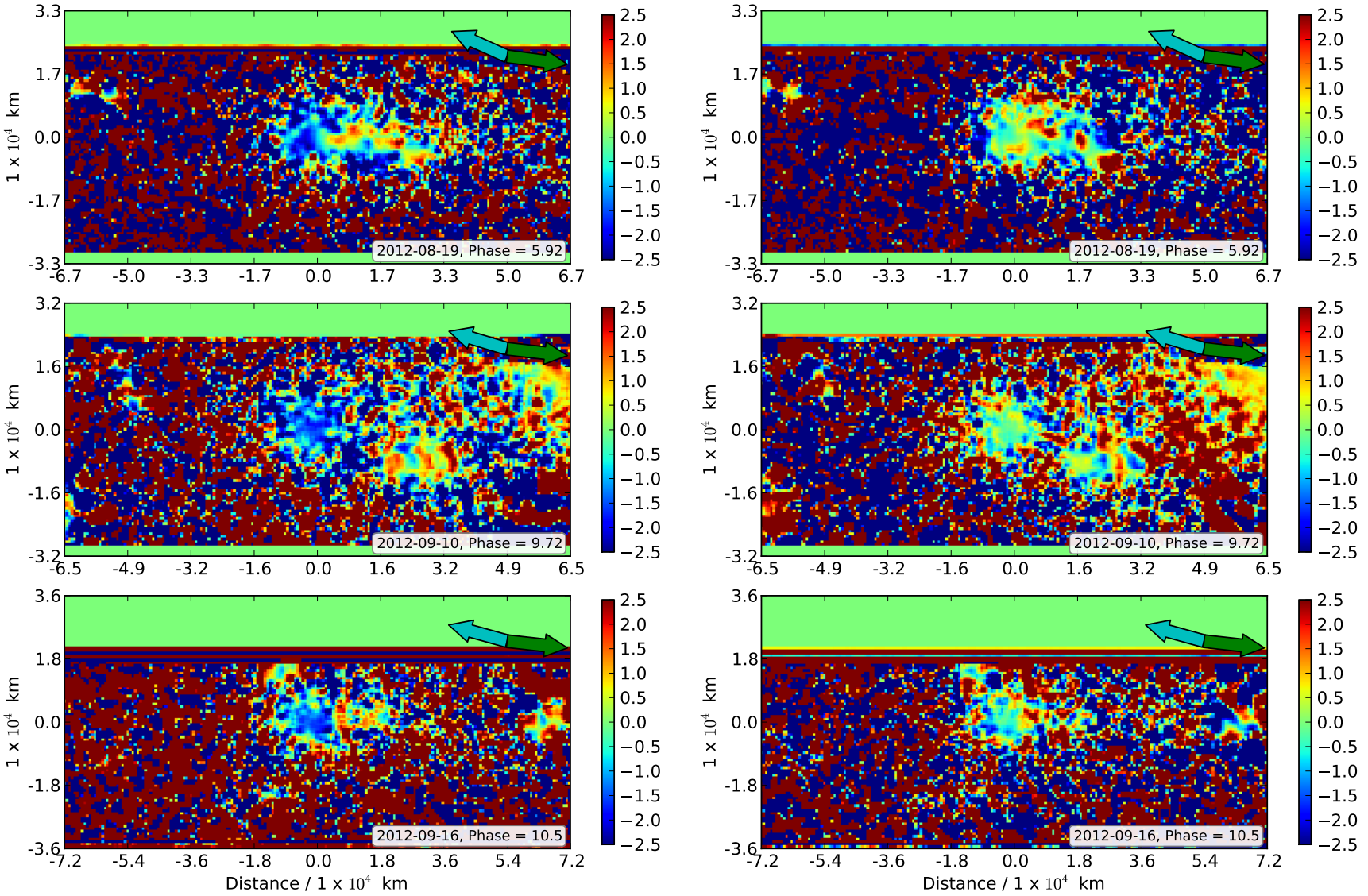

Figure 6.9: P_Q (left) and P_U (right) polarimetric maps for the comet 74P. Green arrow points in the direction of the negative target velocity as seen from the observer. The cyan arrow is the direction of the anti-solar direction. North is up and East is to the left.

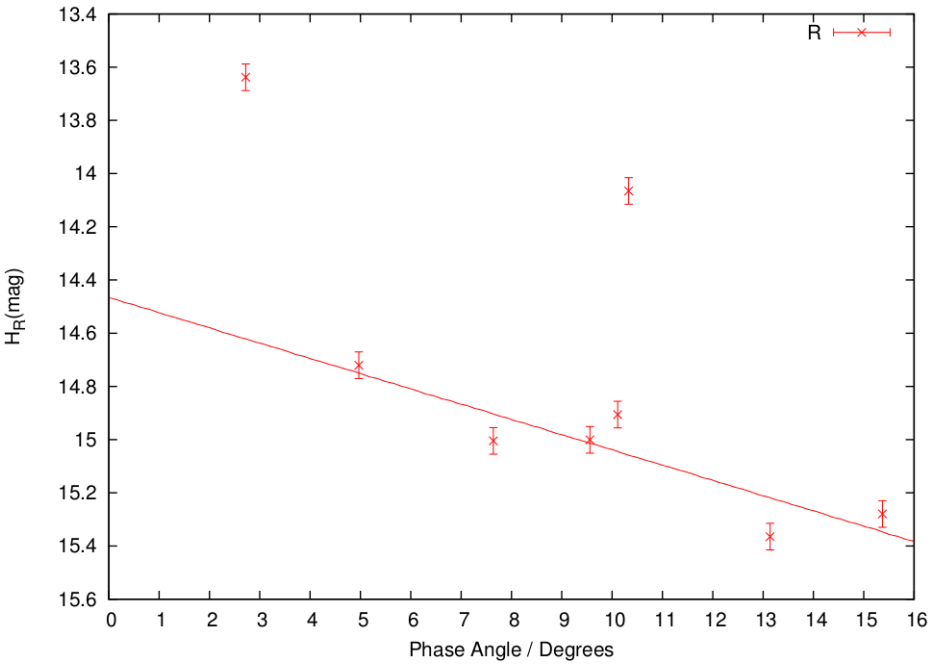

Figure 6.10: Magnitude corrected for the Sun and Earth distances of comet 67P as a function of phase angle. We note the points at phase angles 2.7° and 10.3° are contaminated by background sources and are ignored.

Comet 67P/ChuryumovGerasimenko

Since 67P was only observed in the R filter we can not create *V-R* colour maps. Additionally 67P appeared 2-3 magnitudes fainter than the other comets meaning the signal to noise ratio of the polarimetric measurements was so low that the polarimetric maps generated showed no clear structure.

6.1.3.10 Aperture photometry

The results for comet 67P are shown in Table 1. In Figure 6.10 we have plotted the magnitude corrected for the Sun and Earth distances of comet 67P in the *R*-Special filter as a function of phase angle. In this figure there is no evidence of an opposition surge at small phase angles. We note the points at phase angles 2.7° and 10.3° are contaminated by background sources and are ignored. If we extrapolate the average brightness at zero phase angle is 15.33 ± 0.11 in the *R* filter.

Using Equation 5.8 and the flux extrapolated back to zero phase in the *R*-Special filter and the average r and Δ distances to the comet yields an $Af\rho$ value of 19 ± 2 cm.

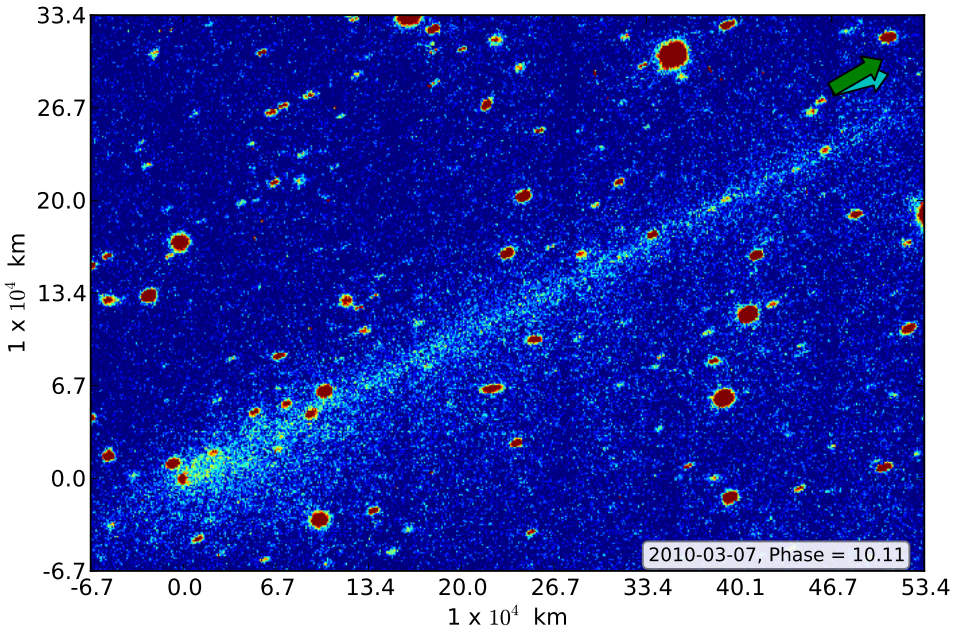

Figure 6.11: Intensity map of comet 67P. Green arrow points in the direction of the negative target velocity as seen from the observer. The cyan arrow is the direction of the anti-solar direction. North is up and east is to the left.

Table 6.5: The Finson-Probstein synchrone analysis for comet 67P.

Date (UT)	PA Tail measured (deg)	PA Synchrone 30 days (deg)	PA Synchrone 60 days (deg)	PA Synchrone 120 days (deg)	PA Synchrone 240 days (deg)	PA Synchrone 360 days (deg)
2010-02-09	298	290	291	293	295	297
2010-02-22	297	288	290	293	295	297
2010-03-06	295	286	288	292	295	297
2010-03-07	296	286	288	292	295	297
2010-03-09	296	285	288	291	295	297
2010-03-16	295	284	287	291	295	297
2010-03-25	295	276	284	290	295	297
2010-03-29	296	272	283	290	295	297

6.1.3.11 Intensity maps

An intensity image for comet 67P is presented in Figure 6.11; we only present a single intensity image as all exposures look quite similar. The coma of 67P does not show any sign of structure. However, it is noted that the dust coma extends asym-

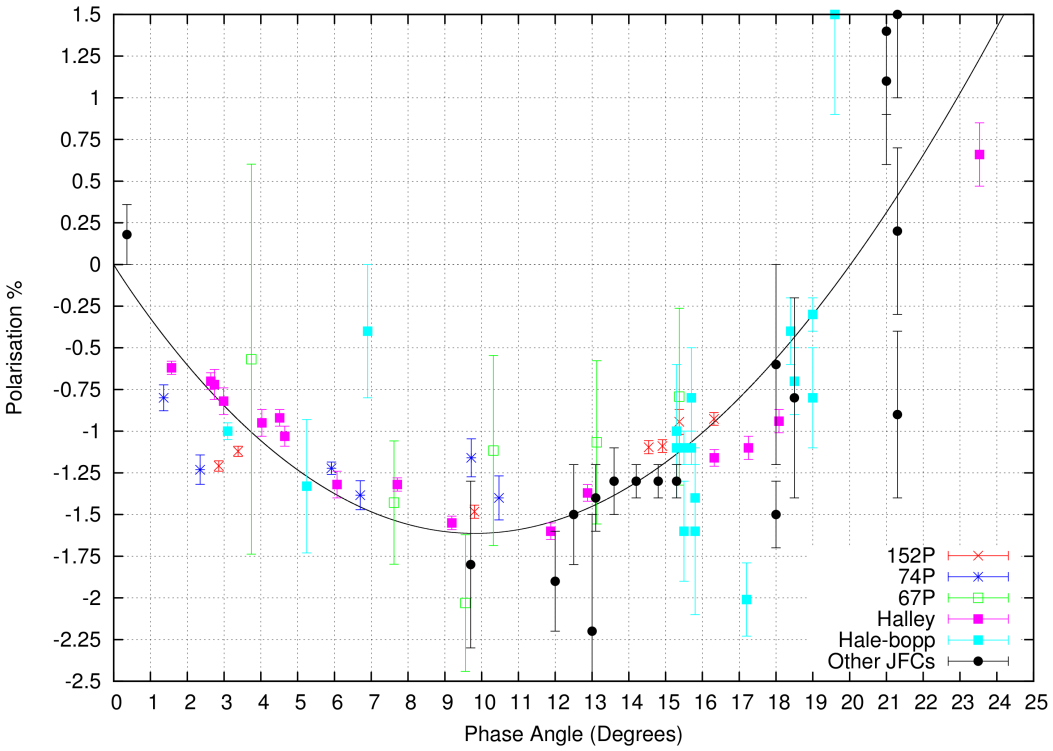

Figure 6.12: P_Q as a function of phase angle for comets 67P, 74P, and 152P. Solid black line is a best fit of previously observed comets long period comets and black circles are previous observations of other Jupiter family comets.

metrically and is larger in the southern direction suggesting ongoing activity in the southern part of the nucleus. There is also a significant but weak ~25" coma peak into Sun direction. The overall appearance of the coma and tail does not change over the course of our observations. The tail orientation is very constant at position angle ~296-297° with a small trend to lower position angles with time.

Finson Probstein calculations of the dust tail (Table 6.5) indicate that the material defining the main tail axis appears to be old and may have been produced by the nucleus about 1/2 to 1 year before observation.

6.1.4 Aperture Polarimetry of 152P, 74P, and 67P

In Figure 6.12 we present the aperture polarimetry for 67P, 74P, and 152P. The solid black line is a best fit representation of previously observed *R*-band polarimetric data of active comets taken from the polarimetric comet database (Kiselev et al., 2006). The best fit we used is a trigonometric function that was introduced by Lumme & Muinonen (1993) and outlined by Penttilä & Lumme (2005) and is

defined in Equation 1.4 (Page: 45).

As we can see from Figure 6.12 all three comets show a very similar polarimetric phase relationship. However, polarimetric measurements of comet 67P have a large uncertainty due to poor signal to noise, so it is difficult to make any firm conclusions from these data. Both comets 74P and 152P show a slightly different polarimetric behaviour compared to the best fit curve. They both exhibit an excess in negative polarisation at phase angles $< 3^{\circ}$. The deviation from the best fit at the small phase angles for comet 152P corresponds to the data points on the 21st and 23rd May which showed the presence of activity in the colour maps, see Figure 6.3. We are unable to state the cause for the deviation at small phase angles for comet 74P as we lack both good polarimetric and colour data for these nights, but it is likely due to activity or statistical scatter around the best fit. Also presented in this graph are other JFCs observed in a similar wavelength range compared to our observations. These observations are within the errorbars of both our observations and the best fit line. However there are points that deviate from the best fit and this is likely due to either being observed at slightly different wavelengths or at different heliocentric distances. Therefore, when we compare comet polarimetry in broadband filters we must be treated with caution as there are many factors that can influence the amount of polarisation measured, i.e gas contamination, outbursts of activity etc.

6.1.5 Discussion and conclusions

To investigate whether we see any polarimetric and colour trends along the solar anti-solar direction we have taken scans through the photometric centre of the comets. Since comet 74P has few simultaneous photometric and polarimetric observations and 67P has no colour information, we only carry out this analysis for comet 152P. The scans are presented in Figure 6.13 along with a contour plot showing exactly which region of the coma is being scanned.

For 152P we do not see any colour or polarisation trends with cometocentric distance, see Figure 6.13. For the majority of the observations of 152P we see an average colour $\sim$ 30-40%/100 nm while the polarisation, although varying from

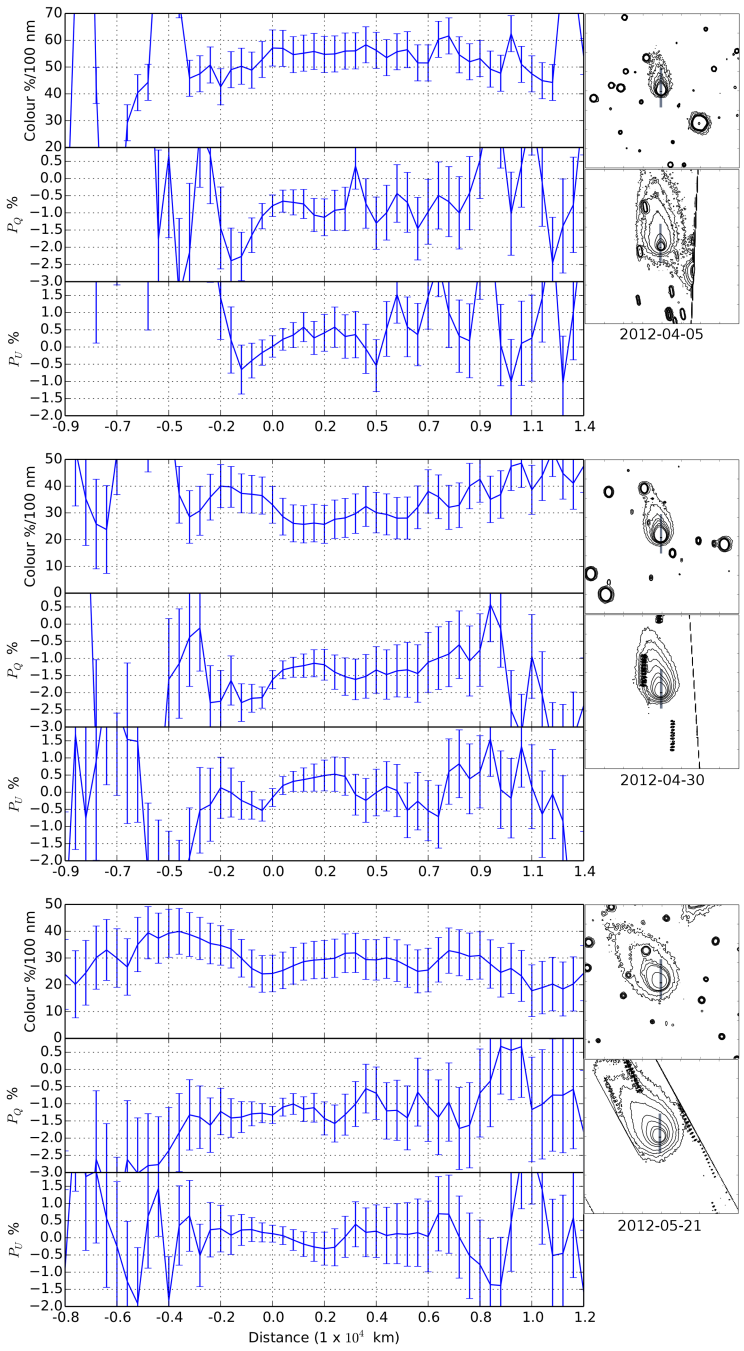

Figure 6.13: Scans of comet 152P's colour, P_Q, and P_U along the solar anti-solar direction. Positive distance is in the antisolar direction, and negative distance is in the solar direction. The zero is at the photometric centre of the comet. The upper contour plot is the intensity of the comet in the photometric images and the lower contour plot shows the intensity of the comet in the polarimetric images, the levels are arbitrary. The small grey shaded area in each contour plot shows the area scanned.

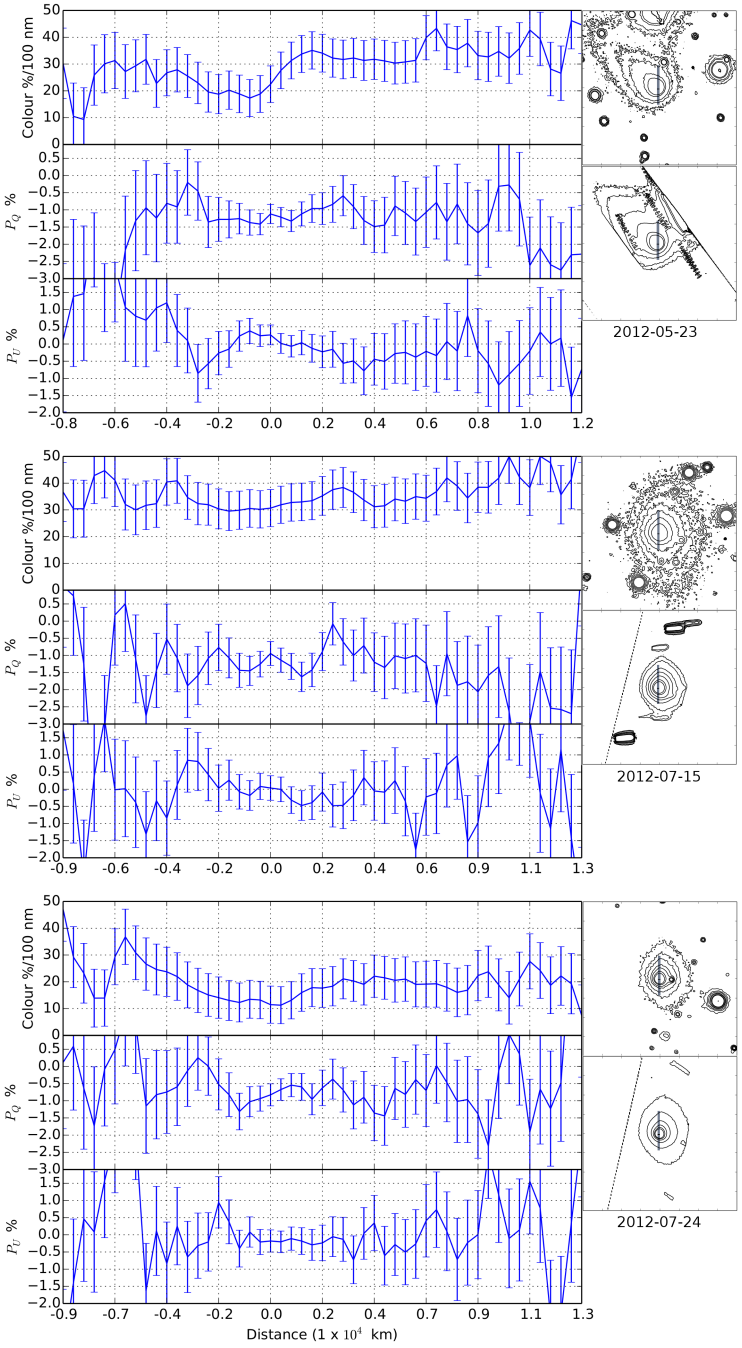

Figure 6.13: Scans of comet 152P's colour, P_Q, and P_U along the solar anti-solar direction. Positive distance is in the antisolar direction, and negative distance is in the solar direction. The zero is at the photometric centre of the comet. The upper contour plot is the intensity of the comet in the photometric images and the lower contour plot shows the intensity of the comet in the polarimetric images, the levels are arbitrary. The small grey shaded area in each contour plot shows the area scanned.

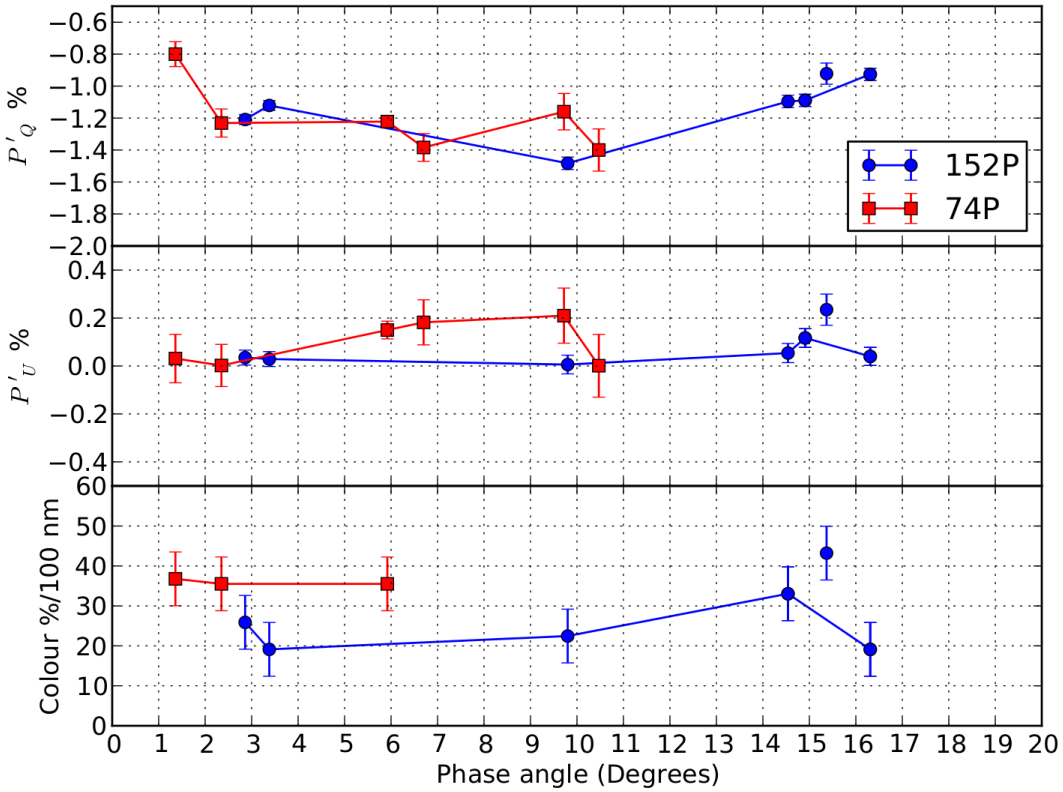

Figure 6.14: P_Q, P_U, and colour changes as a function of phase angle for comets 74P and 152P.

epoch to epoch due to changing phase angle, remains constant across the coma. We fail to see any trend in blue to red colour that would suggest the sublimation of water ice in our observations which supports our near infrared observations where we see no water absorption (Kolokolova et al., 2001). The exception is possibly the scan on the 23rd May where we see a change in colour about the photometric centre of the comet, however we do not see a corresponding trend in polarisation which we would expect to see. The reddish colour and the lack of water ice in the coma suggests that the dust is possibly made up of dirty ice or organic particles. Again if this was the case we do not see any trends that suggest the decomposition or fragmentation of the dust that would show itself as a change in colour from red to blue as the particles get smaller and become more efficient Rayleigh scatterers. The lack of any trends could be a special feature of distant comets. At these large heliocentric distances, sublimation and fragmentation of the dust particles are very slow due to less intense solar radiation, and this may be the reason why we do not

see any gradual cometocentric changes in colour and polarisation. Beer et al. (2006) modelled the lifetime of dust particles at a similar heliocentric distance and found that dirty ice particles live a maximum of 2-3 hours before the ice sublimates. On the other hand Beer et al. (2006) showed that grains of pure water ice can survive many years before sublimation. However, since the probability of getting pure water ice grains is very small and the fact that we have found no water ice in the near infra-red spectrum suggests this is not the cause for our lack of variation.

If we consider how the polarisation and colour properties changed as a function of phase angle (Figure 6.14) we can see two interesting anomalies for comet 152P. The first occurs at the two small phase angles of 2.9° and 3.4° where we see both an increase in P_Q in absolute terms and an increase in colour. The increase in P_Q is the opposite behaviour we expect to see at these phase angles, indicating something unusual is happening on this night. The combination of this with an increase in colour suggest that either at the phase angle 2.9° the comet produced more ice than usual or that at a phase angle of 3.4° it produced less ice than usual. The second anomaly occurs at large phase angles between July 15th and July 24th where the colour shows a large decrease. We note that the data point at phase angle 15.4° has to be ignored as it corresponds to observations taken 3 months earlier, hence why this data point is not connected to the others. The decrease in colour is accompanied by a decrease in absolute terms of P_Q although this decrease in polarisation is expected with the change in phase angle. Since the colour maps for this night are influenced by different seeing conditions we are unable to tell if there is a jet or that an outburst has occurred around the time of observation.

Very little can be said about 74P; the lack of quasi-simultaneous colour and polarisation measurements means we can not draw any firm conclusions. There are two uncharacteristic dips in P_Q between 5-7° and 9-11°. The first is due to observations being two months apart and are not a good comparison. However the second dip is a little more interesting as the observations are taken a week apart and clearly something unusual is occurring in the coma that has caused an increase of $\sim 0.25\,\%$ in absolute terms. This could be caused by smaller particles being emitted from the

nucleus or the sublimation of ice (Kolokolova et al., 2001), although without colour information we can not decipher which.

Comparing the $Af\rho$ measurements for these three comets at these large heliocentric distances, 74P appears to be the most active comet closely followed by 152P with 67P showing the least activity.

Tables 6.2, 6.3 and Figures 6.1, 6.2, 6.3, 6.4, 6.5, 6.6, 6.7, 6.8, 6.9, 6.10, 6.11, 6.12, 6.13, and 6.14 where reproduced from Stinson et al. 2016, A&A, in press, DOI 10.1051/0004-6361/201527696 with permission from ©ESO

6.2 Polarimetry during the Deep Impact event

The Jupiter family comet 9P/Tempel 1 (hereafter 9P) will always be synonymous with the Deep Impact mission (DI). DI occurred on July 4 2005 when a 370kg impactor struck the surface of the comet excavating thousands of tons of cometary material from the nucleus. This event and its aftermath were observed from close distance by instruments on-board the DI fly-by spacecraft (A'Hearn et al., 2005), as well as by ground-based telescopes (e.g Meech et al., 2005), by orbiting satellites, and from interplanetary missions (e.g., Rosetta, see Keller et al., 2005, 2007; Feldman et al., 2007). This resulted in a wealth of publications in major scientific journals (e.g., Meech et al., 2005; A'Hearn, 2008; Meech et al., 2011) and special issues of Science (2005, Vol. 310, issue 5746) and of Icarus (2007, Vol. 187, issue 1).

Around the time of the impact, the comet was also monitored with polarimetric techniques. These polarimetric techniques tend to be more sensitive to changes in the scattering media than other methods. As such any change in the linear polarisation pre- and post-impact would suggest a change in composition, size or morphology of the scattering media.

Only three groups have published polarimetric results relating to the DI event: (Harrington et al., 2007; Furusho et al., 2007; Hadamcik et al., 2007).

Harrington et al. (2007) reported two sets of spectropolarimetric observations obtained with the HiVIS instrument attached to the AEWOS 3.7 m telescope on Haleakala, Maui. Both sets of observations occurred about 40 and 90 minutes after impact, in the spectral interval 637–968 nm. The target of these observations was the dust ejected from the nucleus after the impact, and no polarimetric measurements of the "quiet" (e.g. before impact) coma were obtained. Harrington et al. (2007) report for the first dataset a polarization falling from $\sim 4\,\%$ in the bluest spectral region to $\sim 3\,\%$ in the red, and for the second dataset a value from $\sim 7\,\%$ in the blue, falling to $\sim 2\,\%$ in the red.

Furusho et al. (2007) obtained imaging polarimetry in the Gunn i filter (686-837 nm band) using the Polarimetric Imager for COmets (PICO) of the 1 m Lulin

One-meter Telescope from July 3 to July 5. Integrating the signal in a 10 000 km aperture centred on the comet nucleus, Furusho et al. (2007) reported a polarization of about 7 % before impact (on July 3), which slightly raised after the impact (on July 4), and then decreased (July 7). The polarization maps obtained by Furusho et al. (2007) show that at a projected distance of about 4000 km, the fraction of linear polarization was higher in the direction of the ejecta (~ 9 %) than in the position opposite with respect to the nucleus (~ 6 %). At a projected distance of about 6 000 km from the nucleus the polarization started to decrease with distance, to reach about 5 % at about 12000 km.

Hadamcik et al. (2007) obtained two sets of imaging polarimetric data before impact (at -32 h and -7 h, respectively), and two after impact (at +43 h and +65 h, respectively) with the 0.8 m telescope at the Haute-Provence Observatory, using a red filter about 100 nm wide centred at 650 nm. For that temporal sequence, in a projected aperture of 3300 km, they report a fraction of linear polarization of about 5.7 ± 0.4, 9.9 ± 0.3, 9.9 ± 0.4, and 6.9 ± 0.4 %.

Here I present imaging polarimetric observations of comet 9P performed around the time of the DI event using the FORS1 instrument at the European Southern Observatory (ESO). The measurements were obtained in the framework of a coordinated observing campaign performed at the Cerro Paranal and Cerro La Silla Observatories in Chile. For an overview on the scientific goals and the observations of this campaign see, e.g., Kaufl et al. (2005). Results on the 9P dust component measured at ESO during the DI event are described by Boehnhardt et al. (2007), Bonev et al. (2009), and Tozzi et al. (2007) and those on the gas component by Rauer et al. (2006) and Jehin et al. (2006).

6.2.1 Observations

9P was observed in service mode over the period 3rd July - 7th July, or 50 hours before and 47 hours after the DI event. Both sets of observations were carried out by the FORs instrument of the ESO VLT, see Section 3.4.1. Since the goal of these observations was to observe the ejected dust excavated by the impactor the two filters chosen where FILT_485_37 + 68 and FILT_834_48 + 71 in their ESO

Table 6.6: Log of the polarimetric observations of the DI event obtained with FORS1. During the polarimetric observing campaign the Sun and Earth distances of the comet increased from 1.506 to 1.507 AU and from 0.888 to 0.926 AU, respectively.

Filter	Epoch (UT)	Time to DI (hours)	Exp (s)	Airmass	Seeing (arcsec)	Φ (deg)	Phase angle
F_{485}	2005-07-03.1469	-50.34	1000	1.85-2.05	0.7	111.52	40.84
F_{834}	2005-07-03.1704	-49.78	1200	2.25-2.77	0.6	111.51	40.85
F_{485}	2005-07-07.1484	45.68	1000	1.90-2.17	0.6	110.98	41.17
F_{834}	2005-07-07.1675	46.30	800	2.35-2.72	0.7	110.98	41.17

notation but hereafter I will refer to them as F_{485} and F_{834}. Both F_{485} and F_{834} are very narrow band filters centered on spectral ranges that should be free of gas contamination.

Each observing sequence consisted of a series of images with the retarder waveplate set at 4 different position angles 0-67.5 in steps of 22.5. The exposure time for each observing series varied from 800 to 1200 seconds. For both observering series after the DI event the polarimetric optics were rotated by 45°. The reason for this was to align the polarimetric optics so that the plume created by DI would be along the strip and not be cut off. A simple log of the observations can be found in Table 6.6

6.2.2 Data analysis

All science frames were reduced using the techniques outlined in Section 4.1. Polarimetry was measured using the beam swapping technique outlined in Section 4.2. As was the case in the previous Section, the area chosen to estimate the background sky for all observations was a region where the contribution from the coma and effects due to instrumental polarisation were at a minimum. This area was always on the opposite side of the comet where the DI plume would occur.

6.2.2.1 Correction for retarder chromatism

The FORS1/2 user manual warns about a source of systematic, wavelength dependent, uncertainty of the polarization angle that is introduced by the retarder waveplate. Typically for the most used filters they quote a correction value for the filter

in the user manual. However, for the F_{485} and F_{834} we must manually calculate the offset that must be applied. The user manual provides a correction function $\epsilon(\lambda)$ to be applied to the polarization position angle and has the form

$$\epsilon_{\Delta\lambda} = \frac{\int_{-\infty}^{+\infty} \mathrm{d}\lambda\ F(\lambda) T_{\Delta\lambda}(\lambda) \epsilon(\lambda)}{\int_{-\infty}^{+\infty} \mathrm{d}\lambda\ F(\lambda) T_{\Delta\lambda}(\lambda)} \tag{6.1}$$

where $F(\lambda)$ is the spectral energy distribution of a G2V star, $T_{\Delta\lambda}(\lambda)$ is the FORS filter transmission function or the extracted spectral region. Using this Equation the offset for the F_{485} filter was $\epsilon_{\mathrm{blue}} = +3.4709$, and for the F_{834} filter $\epsilon_{\mathrm{red}} = -2.7582$. These correction offsets can be added to the position angle used to transform into the scattering plane or used as a second transformation after the polarimetric measurements are in the scattering plane.

6.2.2.2 Gas contamination

Prior to the analysis of the imaging polarimetric data, we examined the low resolution spectra obtained with FORS2 at different position angles Rauer et al. (2006). The reason for this was to check the contribution to the emission due to the gas component versus the contribution due to the dust, at various distances from the comet nucleus. The importance of the gas contamination can be evaluated by setting the flux parallel and perpendicular in Equation 4.5 to

$$\begin{aligned} f^{\parallel} &= f^{\parallel}_{\mathrm{gas}} + f^{\parallel}_{\mathrm{dust}} \\ f^{\perp} &= f^{\perp}_{\mathrm{gas}} + f^{\perp}_{\mathrm{dust}} \end{aligned} \tag{6.2}$$

Since gas tends to be unpolarised, the net effect of having a large gas contribution is to dilute the polarisation measured for the dust resulting in an overall depolarising effect. The spectroscopic data obtained with FORS2 by Rauer et al. (2006) served to evaluate the gas to dust ratio $r_{\mathrm{g/d}} = f^{\parallel}_{\mathrm{gas}}/f^{\parallel}_{\mathrm{dust}} \simeq f^{\perp}_{\mathrm{gas}}/f^{\perp}_{\mathrm{dust}}$. In the wavelength interval covered by the F_{485} filter, the gas contribution to the polarisation is negligible in the inner part of the coma, but since the dust decreases with distance from the nucleus much faster than the gas, it is important at larger distances, as

we measured, e.g., $r_{g/d} \simeq 0.24$ at 5000 km. In this case the gas contamination is mainly due to the C_3 and NH_2 radicals. The amount of gas contamination depends not only on the distance from the nucleus but also on the position angle the polarisation is being measured. This is due to the spatial distribution of the dust being affected by radiation pressure compared to that of the gas distribution. For the F_{485} filter we estimated that the gas component is responsible for a 2 % dilution in the inner 2000 km, and for about 25 % at distance of $\sim$ 5000 km. Since it is difficult to evaluate more precisely the gas contamination, we decided not to use imaging polarimetric data obtained in the F_{485} filter.

By contrast, the contamination of the gas present in the coma is negligible in the F_{834} band at small and larger distances from the nucleus (e.g., $r_{g/d} \sim 0.04$ at 5000 km).

6.2.3 Results

For the polarimetric data pre and -post impact we can extract some spatial information about how the polarisation changes with distance. The quick way to do this is to create polarimetric maps of the comet pre- and post-impact and make a comparison. Polarimetric maps were created using the method outlined in Sections 4.8. In Figure 6.15 we present P_Q and P_U maps pre- and post-impact in the F_{834} filter. In both sets of maps North is up and East is to the Left. I will remind the reader that the polarimetric optics on the 7th July were rotated by 45° hence the different orientation of the polarmetric map. From Figure 6.15 it can be seen that there is a small gradient in P_Q with distance from the nucleus (ρ) on both observing epochs. To better show this gradient we have plotted the azimuthally averaged polarisation in Figure 6.16. Figure 6.16 shows a linear decrease of P_Q with increasing nucleocentric distance.

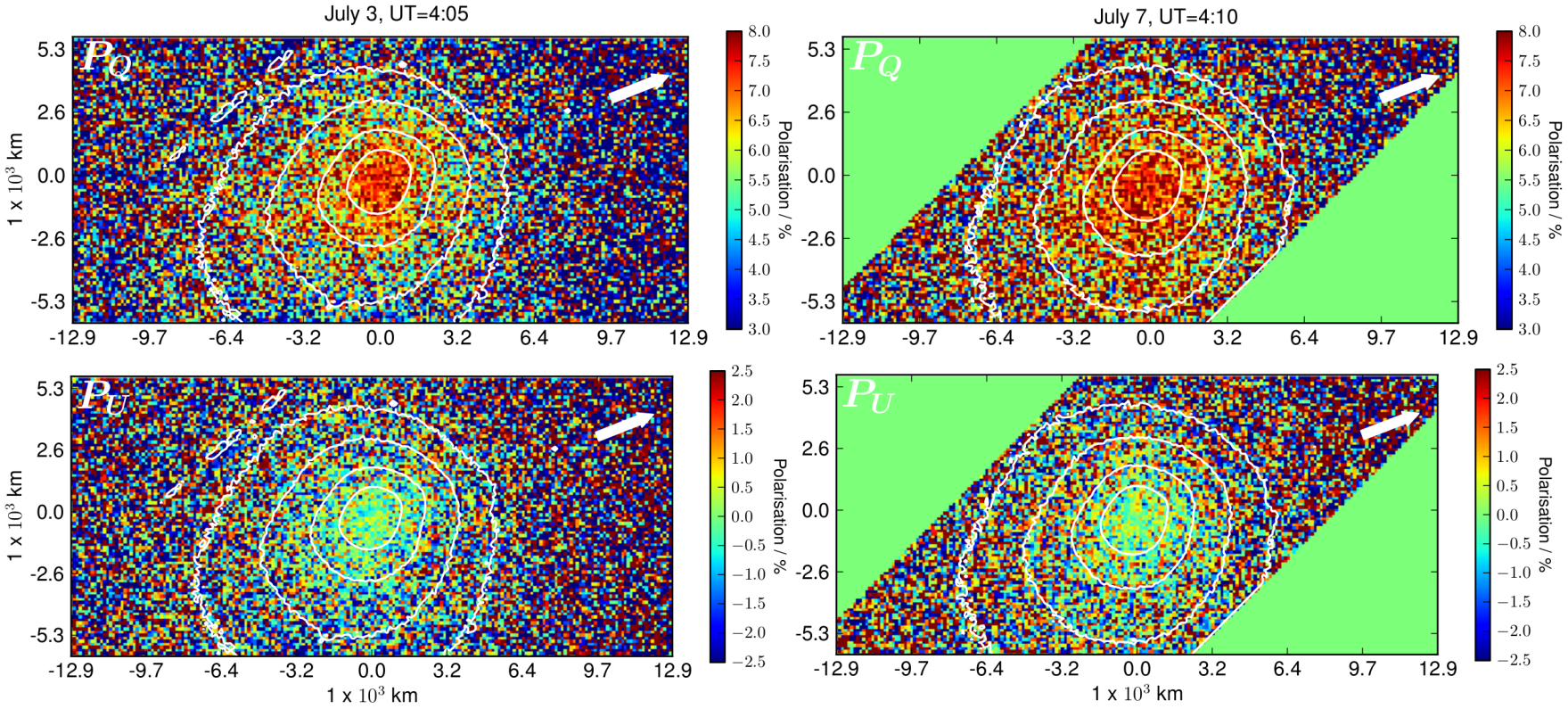

Figure 6.15: FORS1 maps of the Stokes parameter of the inner coma of comet 9P, measured through the F_{834} filters on 5 July 2005 (left), and on 7 July 2005 (right).

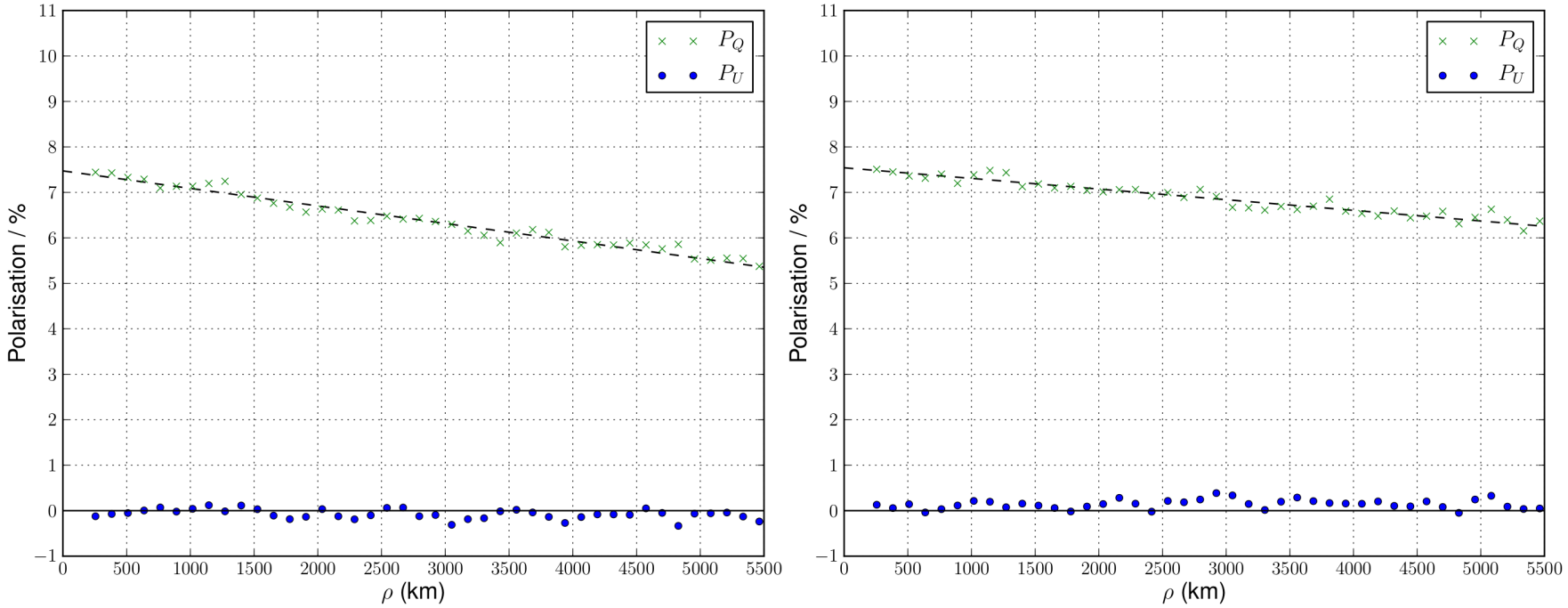

Figure 6.16: Stokes polarization parameters P_Q and P_U, integrated in azimuth, vs. the nucleocentric distance. The observations were obtained with the F_{834} filter on 3 July (left) and 7 July 2005 (right).

Table 6.7: Radial slopes of the P_Q parameters pre- and post-impact (in %/1000 km) in the four canonical coma sectors measured through the F_{834} filter. The uncertainties are about twice as high as for the azimuthally averaged results above. The ejecta produced by the impact was mainly in quadrant S3 (SW)

Coma sector	PA range	Slope k_Q^i (%/1000 km)	
		2005-07-03	2005-07-07
2π	$[0-360)$	-0.34	-0.20
S1 (NE)	$[0-90)$	-0.36	-0.23
S2 (SE)	$[90-180)$	-0.32	-0.21
S3 (SW)	$[180-270)$	-0.43	-0.29
S4 (NW)	$[270-360)$	-0.31	-0.21

Linear fitting of the P_Q spatial profiles allows us to estimate the gradient of the slope with radial distance ρ from the nucleus. Defining Q_0 the fraction of linear polarization at the coma centre, and ρ_{1000} as the distance to the nucleus expressed in units of 1000 km, we calculated

$$\int_{2\pi} \mathrm{d}\phi\,(\rho,\phi) = Q_0 + k_Q \rho_{1000} \tag{6.3}$$

For the pre-impact measurements (3 July 2005) we get, in F_{834} filter,

$$Q_0 = 7.51 \pm 0.17\,\% \quad k_Q = -0.25 \pm 0.06\,\%(1000\,\mathrm{km})^{-1} \tag{6.4}$$

For the post-impact measurements (7 July 2005), we obtain

$$Q_0 = 7.64 \pm 0.07\,\% \quad k_Q = -0.04 \pm 0.03\,\%(1000\,\mathrm{km})^{-1} \tag{6.5}$$

which shows a decrease of 0.2 % in 5000 km with respect to 1.25 % pre-impact.

We tested the gradient fitting against systematic effects, the largest of which might come from incorrect background subtraction. By changing the background levels by ± 15 ADU about their best estimate, we found that the results remain within the errors. An independent quality check for the reliability of our results is that of P_U, which is always around zero for all distances.

In order to investigate whether the change of the slope with radial distance

from the pre- and post-impact is related to the dust ejected by the DI event, we measured the average Stokes parameters as a function of distance from the nucleus (ρ) in the four canonical sectors: Sector 1 (S_1, with $0 \leq \mathrm{PA} < 90$, counted from North to East), Sector 2 (S_2, $90 \leq \mathrm{PA} < 180$), Sector 3 ($S_3$, $180 \leq \mathrm{PA} < 270$), and Sector 4 ($S_4$, $270 \leq \mathrm{PA} < 360$). Note that most of the material produced by the impact was ejected in sector 3.

Similarly to what was done in Equation 6.3 we have calculated the radial slope k_Q^i for each Sector S_i using

$$\int_{S_i} \mathrm{d}\phi(\rho, \phi) = Q_0^i + k_Q^i \rho_{1000} \tag{6.6}$$

The sectoral slopes for F_{834} filter observations are given in table 6.7. Note that the slight difference between the values in this table and the gradient measured over 2π is due to the different method applied, i.e. intensity measurements in a full annulus for the global gradients and transformation to polar coordinates and simple averaging over the respective position angle (PA) range for the sectoral slopes. We conclude that slope change of about the same quantity from pre- to post-impact with the change being slightly higher in the S3 ejecta quadrant.

6.2.4 Discussion and Conclusions

If we considering the uncertainties of the polarimetry of the dust coma, we can conclude that there is a definite detection of both spatial and temporal variability of the polarization. The strongest P_Q spatial gradient is found in the southwestern sector of the coma (Sector 3). It is at this PA range where the DI dust ejecta cloud appeared projected in the sky. However, the spatial gradient changes occurred in both pre- and post-impact data. Since for this sector the variation of the slope is the same as the other three coma quadrants, a correlation of the spatial gradient with the DI event appears to be unlikely.

Instead, we note that the southwestern coma sector displayed - before, during and after DI - the strongest features of a localized “normal” activity in the dust coma (Boehnhardt et al., 2007). It is also in this quadrant where organic grains

are supposed to be present (Tozzi et al., 2007). The projected scale length for the sublimation of organic grains was found to be 6300 km, i.e. of the same order as the size of the polarimetric map. Hence, a scenario involving sublimation of such grains, or the sublimation of organic matter embedded on silicates grains, might be compatible with our finding of stronger gradient of P_Q in the southwestern coma quadrant of 9P. After impact the P_Q gradients appear to be $\sim 35\%$ shallower in all sectors, but the relative amplitudes remained about the same. This implies that whatever the reason for the phenomenon, it appears to affect the dust more or less by the same amount in the inner regions of the coma around the nucleus. This excludes the expanding ejecta cone of the DI event as a possible origin of the effect since it was produced mainly in the southwestern quadrant and, moreover, it had already left the field of view of the central FORS1 polarimetry mask slit where the linear polarization of the dust was measured (Tozzi et al., 2007).

The amount of polarisation measured at a phase angle of $\sim 41^\circ$ for 9P is consistent with the amount of polarisation measured for other dusty comets based on models by Levasseur-Regourd et al. (2008). In conclusion, our measurements characterize the normal coma dust rather than the material ejected by DI. The absence of clear DI induced changes in the average linear polarization of the coma dust of 9P in our measurements is also consistent with the rather constant polarization found in broadband imaging polarimetry of the comet around the 4 July 2005 (see Furusho et al., 2007; Hadamcik et al., 2007). The failure to detect any noticeable change in polarisation related to the DI event is most likely due to the dust being sufficiently dispersed 45 hours after the DI collision leaving only the polarised signal of a normal comet.

Chapter 7

Cometary nuclei

As was the case when we analysed the dust of active comets, the study of cometary nuclei is of particular interest in Solar System science. However observing these relatively small faint objects is very difficult. It is no surprise that comet nuclei have not been polarimetrically observed to a large extent. Since cometary nuclei are very faint objects this means that only the largest telescopes in the world can get the required signal to noise ratio. This problem is not only confined to polarimetric observations but other observing techniques such as spectroscopy, which yield very little information about the cometary nucleus. Only recently as cometary nuclei have been observed by space telescopes, such as Spitzer and insitu measurements from spacecraft such as Stardust, Deep Impact, Deep Space 1 and most recently Rosetta, has our understanding of these primitive bodies begun to move forward. These missions have allowed us not only to get some of the first resolved images of the surfaces of these bodies but also allowed us to derive the size and albedo, and place constraints on the composition. The most interesting of these missions is the currently ongoing Rosetta mission. Not only has this mission accompanied the comet throughout its perihelion passage but it has also deployed a lander called Philae that could potentially give us the first insitu measurements of the surface composition, grain size and grain morphology. Rosetta and Philae's' results will not be ubiquitous to all comets but will provide an invaluable a bench mark to compare with other comets.

This brings us back to the usefulness of polarimetric observations; from these

measurements we can gain information on global surface properties, which we can directly compare to other comets and to other objects in our Solar System.

Only two cometary nuclei have been polarimetrically observed, 2P/Encke (Boehnhardt et al., 2008) and the main belt comet 133P/Elst-Pizaro (Bagnulo et al., 2010). Results from these observations linked these bodies with F-type asteroids although the polarimetric phase curve did differ in quite a few significant ways from that of the F-types, such as the phase angle of the polarisation minimum (P_{min}) and the slope of the curve at the inversion from negative to positive polarisation (h).

Both the values for P_{min} and h can be used to calculate the albedo of the body via a semi-empirical relation first proposed by Zellner & Gradie (1976) and mentioned in detail in Section 1.2.3. Using the values measured from comet 2P/Encke Boehnhardt et al. (2008) found that the geometric albedo was estimated as 0.145 using h and 0.08 using P_{min}. These values for the albedo are significantly higher than those calculated using more realistic visual (Fernández et al., 2000) and thermal infra-red (Lamy & Weaver, 2004) measurements which yield a value of 0.043. A possible reason for this inconsistency is that the value of P_{min} for 2P/Encke was not well defined. Additionally in this case Equation 1.5 also has problems estimating the albedo for the darkest objects as a saturation effect occurs for the value of P_{min} (Shkuratov et al., 1992).

In the following chapter I present the polarimetric observations of two cometary nuclei: 9P/Tempel-1 (hereafter referred to as 9P) and 19P/Borrelly (hereafter referred to as 19P). The aim of these observations is to further test the empirical relation between albedo and polarisation parameters and see if 2P/Encke is a special case or if all cometary nuclei display similar polarimetric behaviour. Also 9P and 19P have both been observed by spacecraft flybys which have given us accurate measurements of the albedo of these bodies and this gives us a direct comparison between these values and the ones calculated using the empirical relation. I will also compare the available photometric and polarimetric data for comet nuclei to those of other Solar System bodies in the hope of finding other objects with similar properties.

7.1 Observations

The observations of comet 9P and 19P were carried out in service mode over the period between October - December 2006 for comet 9P, and July - September 2007 for comet 19P using the FORS1 instrument attached to unit two (UT2) of the ESO VLT, (see Section 3.4.1 for instrumental description). The observations of the comet consisted of quasi-simultaneous photometric and polarimetric exposures using both the *R*-Bessel and *V*-Bessel filters. Comet 9P was observed at 5 different epochs covering a phase angle range between 3.8-14.1°. At each epoch the comet was photometrically observed using the *R* and the *V* with an exposure time of 60 seconds. For the first two observing epochs 9P was polarimetrically observed through both *V* and *R* filters using the retarder positions 0 - 157.5° in steps of 22.5 ° with an exposure time of 350 seconds. For the remaining epochs on which 9P was polarimetrically observed through the *R* filter only, the retarder waveplate positions used were 0-337.5° in steps of 22.5° each with an exposure of 360 seconds.

Comet 19P was observed on 4 different epochs covering a phase angle range between 7.9 - 17.3°. At each of these four epochs 19P was both photometrically and polarimetrically observed using the *V* and *R* Bessel filters. An exposure time of 60 seconds was typically used for the photometric observations in both the *R* and *V* filters, although some exposures were increased to 120 to 300 seconds.

For the polarimetric observations of 19P we adopted an exposure time of 200 seconds for both the *V* and *R* Bessel filter using the retarder waveplate angles 0 - 247.5°

7.2 Data Analysis

The data reduction steps applied to these data are outlined in Chapter 4.

A few special considerations had to be applied for the data of comet 9P. On the nights 2006-11-18 and 2006-12-31 there was a slight tracking problem with these observations. This caused the target to move up the FORS strip until the target was on the edge of the strip. Due to this we had to employ a small aperture to encompass as much light from the comet but without going off the edge of the strip.

This also meant we had to detach the annulus from the aperture used to measure the target flux, as we would get a poor background sky estimation due to the striped nature of the FORS images. This issue was compounded by the observing strategy used for these comets, where the same retarder waveplate positions were repeated after each other to reduce overheads e.g (0, 0, 22.5, 22.5, ...°). This meant that the final retarder positions in the series were the worst affected.

7.3 Results

In the following sections I present the results of the aperture photometry and polarimetry. In Table 7.1 and 7.2 I present the photometric and polarimetric results.

Table 7.1: Photometric results obtained for comet 9P and 19P. Each magnitude has a standard error of 0.05 magnitude.

Target	Date (dd/mm/yyyy)	Time hh:mm	Phase angle (degrees)	r AU	Δ AU	R	V	H_R	H_V	$V-R$
19P	16/07/2007	09:02	7.972	3.579	2.657	20.67	21.33	15.77	16.43	0.66
	19/08/2007	01:05	12.315	3.382	2.594	20.78	21.49	16.06	16.77	0.71
	31/08/2007	01:00	14.658	3.309	2.633	20.68	21.37	16.00	16.66	0.66
	18/09/2007	00:30	17.307	3.198	2.730	20.80	21.34	16.15	16.63	0.48
9P	02/10/2006	08:30	6.346	3.650	2.712	20.09	20.79	15.11	15.82	0.71
	11/10/2006	06:15	3.898	3.687	2.713	19.85	20.60	14.87	15.68	0.81
	02/11/2006	05:45	4.683	3.772	2.817	20.62	21.14	15.48	16.08	0.60
	18/11/2006	03:15	8.590	3.832	2.298	20.67	21.27	15.39	15.98	0.59
	31/12/2006	03:30	14.049	3.929	3.687	21.28	21.96	15.44	16.12	0.68

Table 7.2: Table showing the polarimetric results obtained for comets 9P and 19P

Target	Date (dd/mm/yyyy)	Time hh:mm	Phase angle (degrees)	r AU	Δ AU	R-Special P_q (%)	R-Special P_u (%)	v-high P_q (%)	v-high P_u (%)
19P	16/07/2007	09:02	7.972	3.579	2.657	-0.60 ± 0.43	0.08 ± 0.34	-1.55 ± 0.40	-0.31 ± 0.400
	19/08/2007	01:05	12.315	3.382	2.594	-1.13 ± 0.28	0.02 ± 0.27	-1.44 ± 0.34	0.59 ± 0.36
	31/08/2007	01:00	14.658	3.309	2.633	-0.90 ± 0.39	0.47 ± 0.38	-0.92 ± 0.36	-0.37 ± 0.34
	18/09/2007	00:30	17.307	3.198	2.730	0.04 ± 0.34	0.05 ± 0.36	-0.70 ± 0.45	-0.68 ± 0.45
9P	02/10/2006	08:30	6.346	3.650	2.712	-0.82 ± 0.24	-0.25 ± 0.20	-0.77 ± 0.25	-0.05 ± 0.23
	11/10/2006	06:15	3.898	3.687	2.713	-0.80 ± 0.19	-0.16 ± 0.19	-0.79 ± 0.28	-0.01 ± 0.28
	02/11/2006	05:45	4.683	3.772	2.817	-1.11 ± 0.51	-0.26 ± 0.44	-	-
	18/11/2006	03:15	8.590	3.832	2.298	-1.09 ± 0.19	0.26 ± 0.18	-	-
	31/12/2006	03:30	14.049	3.929	3.687	-0.18 ± 0.89	-0.12 ± 0.88	-	-

7.3.1 Photometry

The aperture used to measure the flux from each comet varied between 8-10 pixels depending on the seeing conditions.

7.3.1.1 9P

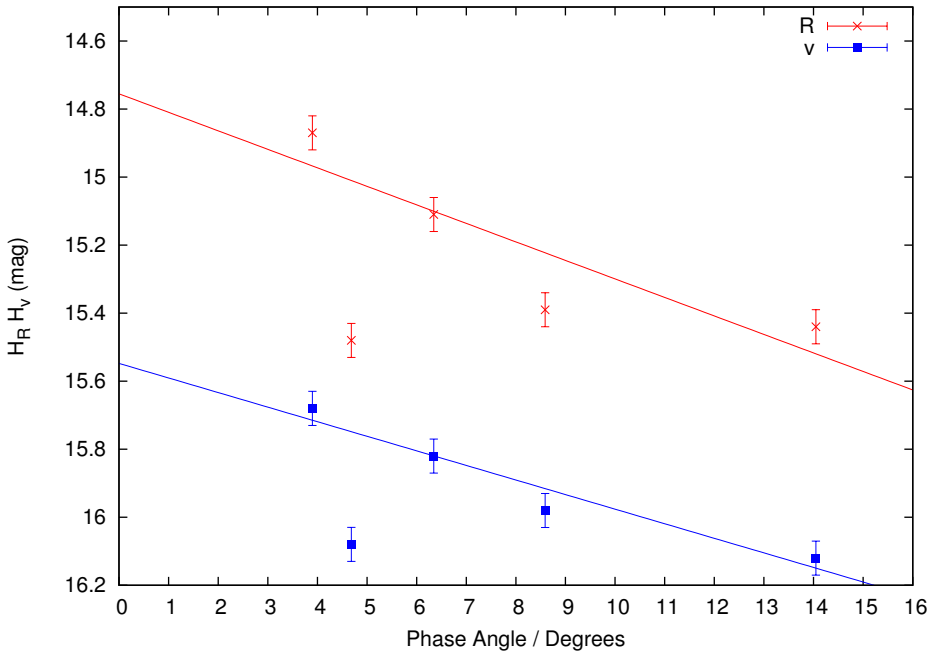

Figure 7.1: Absolute photometry of comet 9P in the *R* and *V* filters

From Figure 7.1 we can see that the Sun and Earth distance corrected magnitude of the nucleus of comet 9P shows an approximate linear brightness increase with decreasing phase angle. The scatter of the measurements may be due to different viewing geometries of the irregular-shaped rotating nucleus. The variation amplitude could be up to 1.28 mag for an approximate axis ratio of the nucleus of 3.27 as concluded from spacecraft results (Belton et al., 2007). Assuming a constant rotation axis orientation with time as determined during the spacecraft flybys (Thomas et al., 2007) an approximate side-on viewing aspect of the nucleus is estimated for the observing period October to December 2006. With the rotation period of the nucleus being 41.85h (Belton et al., 2007) the measurements on 2nd and 11th

October as well as on 31st December 2006 had a similar viewing cross section of the rotating nucleus as seen from Earth, while the observations on 2nd and 18th November 2006 deviate in rotation phase from the others, such that at least qualitatively the scatter is consistent with the observations. Since the rotation period of the nucleus is not constant with time (Belton et al., 2011) it is open whether the rotation axis changes significantly with time and proper phasing of the measurements appears to be an academic exercise.

There doesn't appear to be any detectable opposition surge present in our photometry of the 9P nucleus. The inability to see an opposition surge could be due to our lack of data points at small phase angles. If we assume there is no opposition surge and use a linear fit we can extrapolate the approximate brightness of the comet at zero phase angle. For this linear fit we have ignored the data taken at a phase angle of 4.68° on 02-11-2006 as these observations were taken in very bad seeing and are most likely maximum out of the rotation phase of the rest of the data. From these linear fits we determine similar (within the error bars) slopes of 0.054 ± 0.019 mag/degree for the *R*-filter and 0.042 ± 0.007 mag/degree for the *v*-filter. The average slope of 0.48 ±0.02 mag/degree is very similar to that found by (Li et al., 2007b) of 0.046 ± 0.007 that was calculated with a combination of ground based observations, Hubble Space Telescope and Deep Impact measurements, using phase angles between 3-117°. Using the *R* and *V* filter phase slopes, the extrapolated magnitude at zero phase angle is 14.76 ± 0.18 in *R* and 15.54 ± 0.07 in *V*, respectively (*V*-*R* = 0.78 ± 0.19). The average *V*-*R* colour of the nucleus is determined from the 5 available measurement sets to be 0.68 ±0.11 mag which yields a spectral slope of 37 %/100nm. Our *V*-*R* colour is comparable - within the uncertainties - though slightly redder than those calculated by (Li et al., 2007b) and (Belton et al., 2005) who calculated 0.50 ± 0.02 and 0.56 ± 0.02. Compared to other cometary nuclei (see (Hainaut et al., 2012) and the MBOSS2 database at http://www.eso.org/ ohainaut/MBOSS) the nucleus of comet 9P appears to be very red.

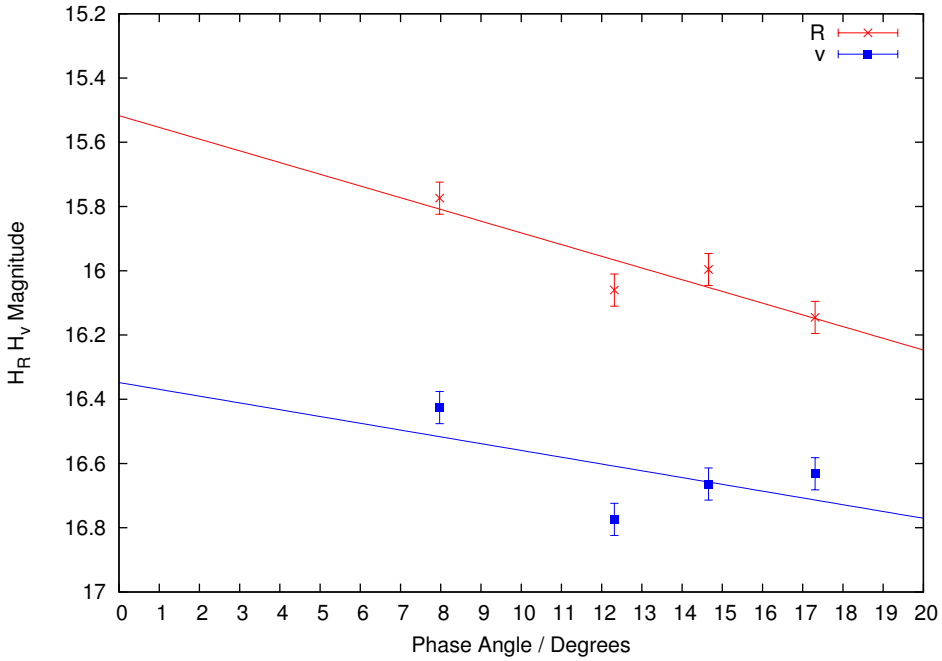

Figure 7.2: Absolute photometry of comet 19P in the *R* and *V* filters.

7.3.1.2 19P

The Sun and Earth distance corrected magnitudes of the nucleus of 19P show an approximately linear increase with decreasing phase angle (Figure 7.2). The scatter is well within the range set by the axis ratio of the nucleus (Buratti et al., 2004): The axis ratio of 19P is 2.53 which results in a maximum amplitude for rotation variability of about 1.0 mag. Using the rotation axis parameters of Farnham & Cochran (2002) a more face-on viewing geometry of the nucleus, as seen from Earth, is to be assumed for our observing period of the comet, which is compatible with our measurement results for the phase function. For a rotation period of 1.08 days (Mueller et al., 2010) our observing epochs of 19P result in close to full or close to half rotation cycles of the nucleus; thus nucleus cross section variations should be small.

In the *R* and *V* filter photometry of 19P (see Figure 7.2) apparent evidence of an opposition surge is absent. Again the inability to see an opposition surge is

likely due to our lack of data points at small phase angles. According to Buratti et al. (2004), the opposition surge of 19P had occurred for phase angles well below 5 deg during the DS1 flyby at the comet, which is beyond the phase angle coverage of our data. Applying a linear best fit to the filter photometry we calculate a slope of 0.036 ± 0.11 and 0.0212 ± 0.021 mag/deg in *R* and *V*, respectively. This compares to a slope of 0.043 mag/deg found by (Li et al., 2007a) who used a combination of ground based observations and data taken from the Deep Space 1 probe in a similar *R*-band filter. The determination of our slope value was based on data points between 10 - 30°. If we extrapolate our linear best fit back to zero phase angle we get an absolute magnitude of 15.51 ± 0.18 mag in *R* and 16.38 ± 0.29 mag in *V*. (Li et al., 2007a) reported a magnitude of 14.79 mag in the *R* band at zero phase angle also assuming no opposition surge. The reason for the large difference in derived magnitude at zero phase angle is likely due to different nucleus cross sections being considered. Li et al. (2007a) derived their measurements from the maximum nucleus cross section, whereas for our measurements we do not know the view geometry in which our measurements were taken but it is unlikely to be at the maximum.

Averaging the results at different phase angles provides a mean *V-R* colour of 0.63 ± 0.10 mag for the nucleus of 19P. Our result for *V-R* indicates a much redder nucleus surface - similar to the nucleus of 9P - than found by the mean colour value for 19P of Lowry et al. (2003), although their measurements show a very large uncertainty (in fact, both results for the *V-R* are consistent within the uncertainties).

7.3.2 Aperture Polarimetry

The polarimetric results for comets 9P and 19P are presented in Table 7.2. The apertures used to measure the polarimetry varied between 4-8 pixels for comet 9P and 4-6 pixels for comet 19P. In Figure 7.3 we plot the polarimetric results of the *R* filter and in Figure 7.4 we plot the polarimetric results of 9P and 19P in the *V* filter. In these plots we include polarimetric observations of 2P/Encke and the main belt comet 133P/Elst-Pizarro. We use a semi-empirical function that has been widely used for the fitting of polarimetric phase curves of asteroids, see ((Muinonen et al.,

2002b)), and is defined as

$$P(\alpha) = A_0 \left[exp\left(\frac{-\alpha}{A_1}\right) - 1 \right] + A_2\alpha \tag{7.1}$$

where, A_0, A_1, A_2 are free parameters, and α is the phase angle. This equation should only be used to fit data within a phase angle range where there are a well distributed set of data points available. This function yields very similar results to Equation 1.4 used to fit the phase curve of cometary dust in Section 6.1.4. The benefit of Equation 7.1 is that it only has three free parameters compared to Equation 1.4 which has four and since we are dealing with few data points it is slightly better constrained. We exclude data points from 133P from this best fit as it is usually considered as an F-type asteroid with a water ice reservoir, and may influence the plot for actual cometary nuclei, but is useful for comparison purposes.

In Figure 7.3 we have plotted polarimetric measurements through the *R* band filter and used Equation 7.1 to fit the data. In Figure 7.3 we can see that for the *R* filter all 3 comet nuclei and 133P/Elst-Pizarro show a very similar polarimetric behaviour. There is some scatter away from the best fit but this could be due to the large uncertainties on the measurement or simple statistical scatter about the best fit.

In Figure 7.4 we have plotted polarimetric measurements through the *V* band filter. For comparison purposes the best fit in Figure 7.4 is the best fit for the *R* band polarimetry. In Figure 7.4 we can clearly see there is a noticeable difference in the polarimetric behaviour between 2P and 19P. With only 2 data points for 9P it is impossible to tell which of the comets is showing an odd behaviour. However using 133P as a comparison would suggest that 2P is the comet showing a unique behaviour compared to the others. A re-analysis of the 2P/Encke using the same data reduction techniques used for 9P and 19P yielded similar results to those published by Boehnhardt et al. (2008). The difference in behaviour between the *R* and the *V* filter is rather strange. One possible suggestion for the drop in polarisation

seen in the *V* filter is the presence of gas contamination. At the time of the polarimetric observations of 2P/Encke the comet was around 1.5 AU from the Sun. At this distance from the Sun gas emission can occur with C_2 sometimes measured around other comets. So, if 2P/Encke produced C_2, it could have contaminated the *V* filter causing a depolarising effect. However, the problem with this explanation is that Boehnhardt et al. (2008) did not detect any significant dust production and it is very unusual to have gas emission without the detectable presence of dust. The only conclusion we can draw is that the *V* band polarimetry of 2P/Encke is very unusual.

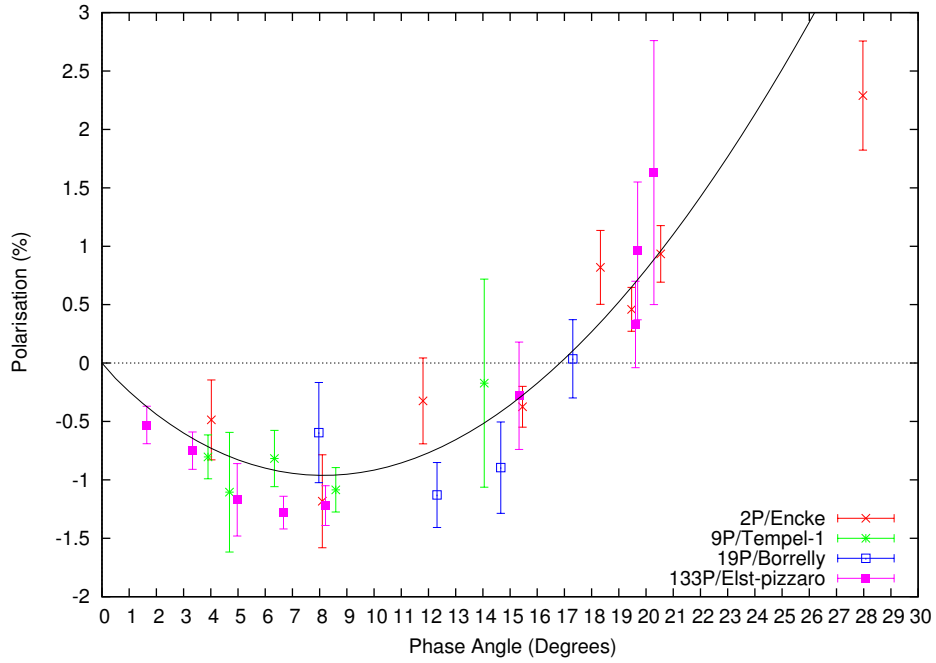

Figure 7.3: Polarisation phase relationships for cometary nuclei in the *R* filter.

7.3.3 Albedo

Since the *R*-filter data yield the most consistent results we can use the best fit for the comet nuclei in this filter to test the empirical relationships between polarimetric properties and albedo that has been developed for asteroids. These relationships were first proposed by Zellner & Gradie (1976) and have since been updated by Cellino et al. (1999); Cellino et al. (2012). These relationships rely on two quantities

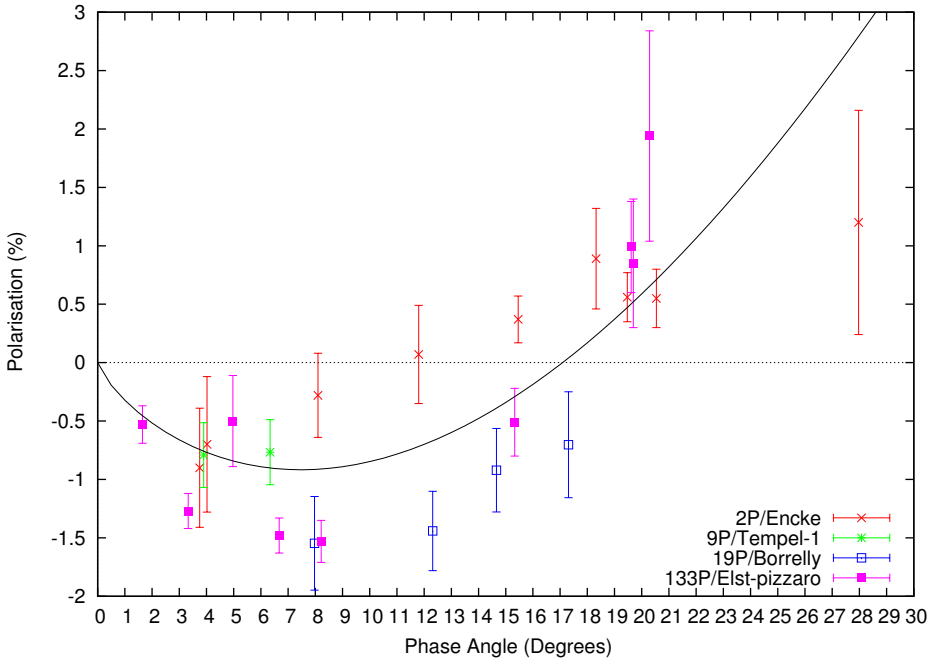

Figure 7.4: Polarisation phase relationships for cometary nuclei in the *V* filter.

from the polarimetric phase curve namely, $P_{\min}$ the absolute value of minimum polarisation and h the slope of the phase curve as it passes from negative to positive polarisation. These relationships are defined in Equations 1.5 and **??** (Page 45. Using the latest constants derived by Cellino et al. (2012) and the parameters from our best fit we derive a geometric albedo of 0.075 when we use the slope of the curve at the inversion point and a geometric albedo of 0.125 using the polarisation minimum. These derived values for albedo are much higher than the average values of geometric albedo measured using more traditional techniques which is ~0.05. The large difference in derived albedo using $P_{\min}$ is likely due to the saturation effect experienced by very dark objects (Shkuratov et al., 1992). The albedo derived using h is very close to the albedo of 9P although it is almost double that of 19P and 2P/Encke. The negative result of this empirical relationship suggests that the relationship is not very well constrained for objects with the darkest albedos or the surfaces of cometary nuclei differ from those of main belt and near earth asteroids

which have been used to constrain the values of the empirical relation.

7.4 Discussion

In the previous sections we have presented the photometric and polarimetric results from the cometary nuclei of 9P and 19P. From the photometry both comet nuclei appear to be very red with average colours of 0.68 and 0.63 for 9P and 19P respectively. Normally a red colour can be explained by space weathering (Chapman, 2004) where over the course of many millions of years the surface begins to redden due to exposure to solar radiation. However this explanation has problems explaining our measurements since comets show periodic activity, meaning their surfaces are constantly being renewed. This suggest that the red colour observed for these comets is not due to space weathering, but rather the nuclei of these comets are composed of a red material.

In Table 7.3 we compare the light scattering properties of many different classes of atmosphereless bodies of the Solar System. In Table 7.3 the albedo, spectral slope, the polarisation minimum P_{min}, the phase angle that the polarisation minimum occurs α_{min}, the phase angle when polarisation changes from negative to positive α_{inv} and the slope of the curve at the point where negative polarisation changes to positive polarisation. These four parameters related to quantities on the polarimetric phase curve are calculated using the best fit equations. The majority of the polarimetric data presented in Table 7.3 are taken in the *V* band. However the variation of polarisation parameters with colour should be quite small. In Table 7.3 we use the combined polarimetric results of 2P/Encke, 9P/Tempel-1 and 19P/Borrelly to form the "comet nuclei" entry.

Comparing the albedo and spectral slope properties of comet nuclei to those of other groups in Table 7.3 suggests that C-type asteroids show similar properties with both the spectral slope and albedo ranges consistent with those of comet nuclei. F-type asteroids share a similar albedo range although the bluish spectral slope measured for F-type asteroids differs.

Table 7.3: Comparison of photometric and polarimetric properties of comet nuclei and other small bodies

Object	Albedo	Spectral Slope %/100 nm	P_{min} %	α_{min} Degrees	Pol Slope	α_{inv} Degrees
Comet Nuclei	0.03 - 0.072	11 - 37	-0.97	8.19	0.216	16.8
Comet Dust	0.05	-1-12	-1.5	9.6	0.31	21.8
Centaurs	0.16	1	-1.37	1.5	?	? ~ 6.7
Large TNOs	0.23 - 0.96	7 - 48	?	?	?	?
Small TNOs	0.05 - 0.16	2 - 26	?	?	?	?
Trojans	0.04 - 0.1	2 - 15	-1.2	~ 10	?	?
C-Type asteroids	0.02 - 0.09	-3 - 20	-1.54	8.03	0.218	19.54
S-Type asteroids	0.085 - 0.33	-15 - 88	-0.78	7.47	0.09	20.30
E-Type asteroids	0.34 - 0.6	rather flat spectra	-0.32	6.01	0.038	17.64
M-Type asteroids	0.074 - 0.25	6 - 15	-1.00	9.12	0.133	21.71
F-Type asteroids	0.024 - 0.086	-24 (Interamnia)	-1.27	6.90	0.247	15.77

If we first compare the polarimetric properties of cometary nuclei to those of the cometary dust we can see that they differ. This is likely due to the difference in scattering mechanism i.e. by individual dust particles (single scattering) compared to the relatively dense surface of a cometary nucleus (multiple scattering).

The large and small TNOs are probably the group we would be most interested in comparing with the cometary nuclei since they were likely formed in a similar region of the Solar System. However due to their small observable phase angle range it is impossible to polarimetrically compare these objects.

Centaurs are another interesting group of objects to compare with cometary nuclei. To date there have been three centaurs polarimetrically observed in detail: Chiron, Chariklo, and Pholus (Belskaya et al., 2010). All three centaurs presented by Belskaya et al. (2010) exhibited different polarimetric behaviours. The values used in Table 7.3 are from Chiron as it was the centaur that has the most polarimetric measurements over its entire phase angle range. Both the photometric and polarimetric properties of Chiron differ considerably from the comet nuclei most notably in $\alpha_{\min}$ and α_{inv}.

Polarimetric properties of asteroids show a wide diversity. Unlike the previous groups compared to comet nuclei there is much more data available and over a much wider phase angle range. Using Equation 7.1 we can measure the best fit curve for each class of asteroid and directly compare them to the comet nuclei points. In Figure 7.5 we have constructed graphs showing the data points and best fit curve for each of the asteroid classes. The polarimetric properities of each of the best fits are presented in Table 7.3. Polarimetric data for the asteroids are taken from the asteroid polarimetric database (Lupishko, 2014). Since the asteroids have been observed over a comparable phase angle range we have plotted the best fits for each asteroid taxonomy presented in Figure 7.5 alongside our individual data points of the comet nuclei and this is presented in Figure 7.6. From Figure 7.6 we can see that the F-type asteroids are the closest in comparison to comet nuclei. C-type show a similar slope to through inversion as the comet nuclei but their polarisation minimum is too high in absolute terms.

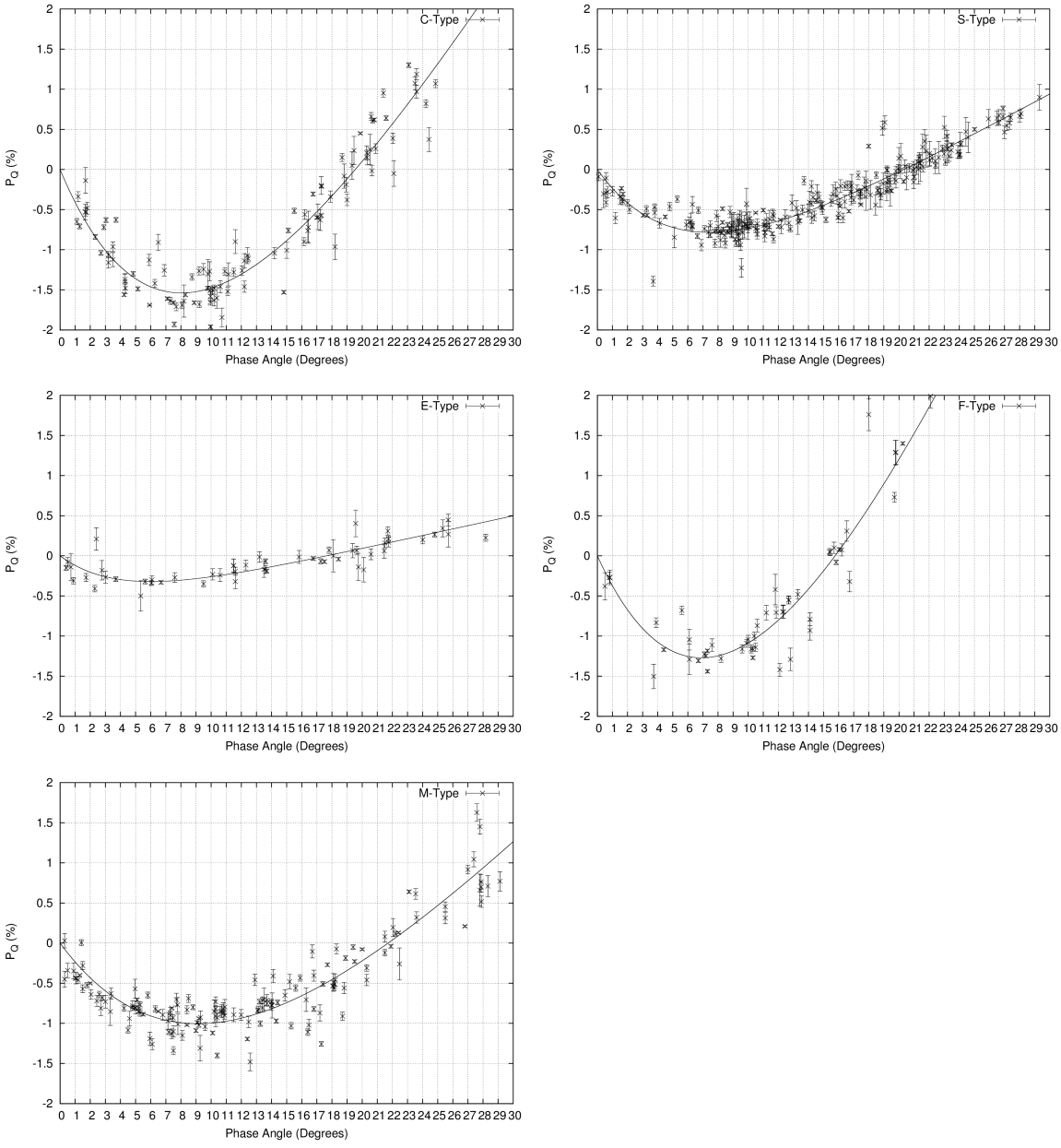

Figure 7.5: Polarimetric data for C-, S-, E-, M-, and F-type asteroids. The best fit lines are constructed using Equation 7.1.

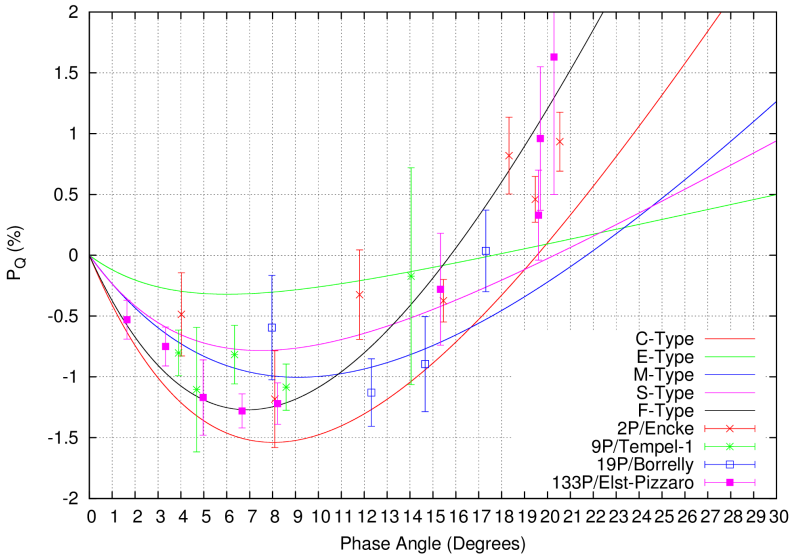

Figure 7.6: Polarimetric data for the cometary nuclei plotted with the best fits for various asteroid taxonomic classes.

Of the many asteroid observations there are a handful of asteroids that have been polarimetrically observed over the majority of their phase angle range and with enough points to be individually fitted by Equation 7.1. These asteroids should give us an idea of the parameter space each taxonomic class of asteroid occupies and compare it to our group of comet nuclei. These well observed asteroids populate every taxonomic type but mainly the S- and C-type. The majority of these observations have been taken from the asteroid polarimetric database but have been filtered by Cellino et al. (2015) to include only the most accurate observations. From this dataset we can use the polarimetric parameters P_{min}, α_{inv} and ψ and compare them to our group of comet nuclei. Again we must consider the comet nuclei as a group as individually we do not have enough data points. The parameter ψ is a newly introduced parameter by Cellino et al. (2015) which is defined as the polarisation (P_Q) at phase angle of 30° minus the polarisation (P_Q) at a phase angle of 10°. In Figure 7.7 we present the plots of P_{min} against α_{inv}, P_{min} against ψ, and α_{inv} against ψ. The point types used in Figure 7.7 represent the taxonomic class of the asteroid and the large black circle represents the data of the comet nuclei. In all three plots in Figure 7.7 similar taxonomic classes of asteroid tend to clump together to form

regions, this can be clearly seen for both C and S-Type which have the most observations. In all three panels in Figure 7.7 comet nuclei tend to stick out from the other asteroids, but tend to be always close to the F-type asteroids. However with so few F-type asteroids to compare to the comet nuclei it is unclear at what size the region F-type asteroids form and whether comet nuclei fall into it or form their own region.

7.5 Conclusion

From these new observations of comet nuclei 9P and 19P we have been able to constrain new estimates on the polarisation minimum and slope of the polarimetric phase as it passes through $\alpha_{\rm inv}$. As mentioned above these parameters for the comet nuclei best match those of F-type asteroids. However, with our limited number of observations of comet nuclei it is difficult to say that comet nuclei and F-type asteroids are similar but the current data do suggest it.

The empirical relationship between polarisation properties and albedo does not yield accurate results. Until this relationship can be calibrated to deal with low albedo sources of < 0.05 it is unlikely to yield robust results.

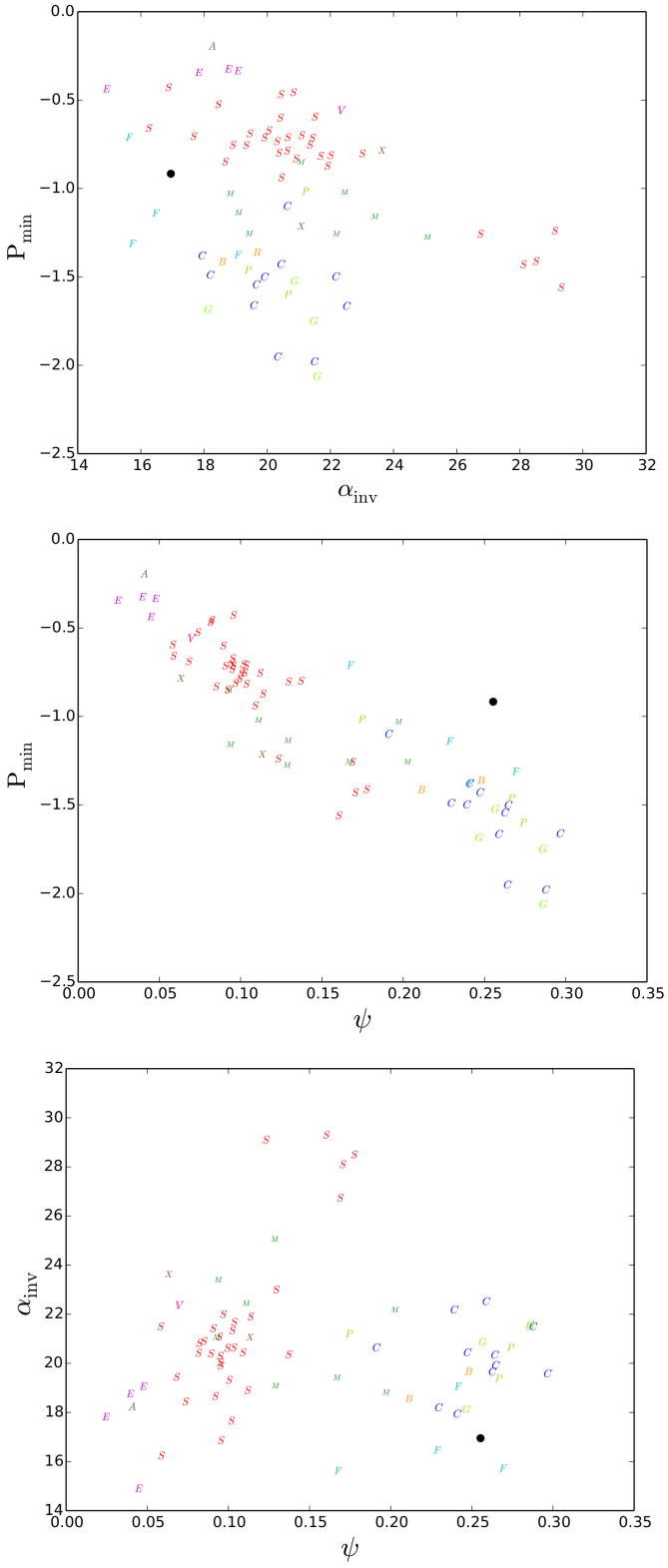

Figure 7.7: Polarisation parameters of asteroids of various taxonomic classes compared to comet nuclei

Chapter 8

Conclusions

In this thesis I have presented and discussed new polarimetric observations of many different small bodies of the Solar System and the careful considerations that have to be made when analysing them.

In Chapter 4 I presented the data reduction and analysis techniques used throughout this thesis. It is hoped that this will serve as a guide to others when observing small bodies of the Solar System.

In Chapter 5 I presented polarimetric observations of Barbarian asteroids, Trojan asteroids and the trans-neptunain objects. Although our results for the Barbarian asteroids turned out to be unusable the experienced gained by determining the reason why was very valuable. The polarimetric observations of the Trojan asteroids were the first ever carried out for this class of object. The polarimetric results showed at least two different types of Trojan in the L4 population and which is consistent with that already found by Emery et al. (2011) in an infra red survey. Additionally we found the polarisation minimum displayed by these Trojans is similar to that of the D-type asteroids. All the Trojans analysed using the deep imaging technique displayed no sign of coma activity even thought it has been postulated by Guilbert-Lepoutre (2014) that these bodies could contain small amounts of water ice below their surfaces.

In Chapter 6 I presented the first polarimetric observations of active comets at large heliocentric distances and polarimetric measurements during the Deep Impact event. In this chapter I showed that at large heliocentric distance the

comets 74P/Smirnova-Chernykh and 152P/Helin-Lawrence showed no trend of either colour or polarimetric properties throughout their comae. This suggests that there is no evidence of water ice sublimation, fragmentation or decomposition of the ejected dust particles from the nucleus. The lack of water ice absorption features on the near infra red spectrum of comet 152P/Helin-Lawrence also suggests the lack of water ice grains in the coma. The analysed polarimetric observations from the time of the Deep Impact mission showed no additional contribution from the dust excavated from the Deep Impact lander and showed polarimetric results consistent with those of other active comets.

Finally in Chapter 7 I presented two new observations of cometary nuclei. From these results I was able to better constrain the polarisation minimum ($P_{\min}$) and the slope of the polarimetric phase curve as polarisation switches from negative to positive h. Using the values of the $P_{\min}$ and h we determined that the polarisation albedo relationship that exists for asteroids does not yield accurate albedo estimates for comet nuclei. Additionally we compare the polarimetric properties of comet nuclei to many other Solar Systems bodies and found the best comparison to be F-type asteroids.

I believe that this work has made a significant contribution to the polarimetry of small Solar System objects by increasing our knowledge of cometary nuclei and presenting the first polarimetric results for Trojans and cometary dust at large heliocentric distances. The work described here on comets is presented in a manuscript to be submitted for publication in Astronomy and Astrophysics (Polarimetry of comets 67P/ChuryumovGerasimenko, 74P/SmirnovaChernykh, and 152P/HelinLawrence A. Stinson, S. Bagnulo, G.P. Tozzi, H. Boehnhardt, S. Protopapa, L. Kolokolova, K. Muinonen, and G.H.Jones).

8.1 Future work

In the future I would like to carry out further observations of cometary nuclei as the current understanding of the polarimetric properties of these object still needs to be enhanced. It should also help shed light on the connection between cometary

nuclei and the F-type asteroids. Additionally only a handful of Trojan asteroids have been polarimetrically observed and over a relatively small phase angle range. The addition of many more polarimetric observations of L4 Trojans may yield additional information on the two different populations currently found and perhaps lead to the discovery of additional populations.

In the future polarimetry could become a powerful tool in the detection and characterisation of exoplanets. As we wait for better instrumentation and larger telescopes to be constructed we can build up our knowledge of our own Solar System and perfect our data analysis techniques so we can be ready to apply our knowledge to the many planetary systems in our galaxy.

Bibliography

A'Hearn, M. F. 2008, Space Sci. Rev., 138, 237

A'hearn, M. F., Hoban, S., Birch, P. V., et al. 1986, Nature, 324, 649

A'Hearn, M. F., Schleicher, D. G., Millis, R. L., Feldman, P. D., & Thompson, D. T. 1984, AJ, 89, 579

A'Hearn, M. F., Belton, M. J. S., Delamere, W. A., et al. 2005, Science, 310, 258

A'Hearn, M. F., Belton, M. J. S., Delamere, W. A., et al. 2011, Science, 332, 1396

Appenzeller, I. 1967, PASP, 79, 136

Appenzeller, I., Fricke, K., Fürtig, W., et al. 1998, The Messenger, 94, 1

Avramchuk, V. V., Rosenbush, V. K., & Bul'Ba, T. P. 2007, Solar System Research, 41, 186

Bagnulo, S., Belskaya, I., Boehnhardt, H., et al. 2011, J. Quant. Spec. Radiat. Transf., 112, 2059

Bagnulo, S., Belskaya, I., Muinonen, K., et al. 2008, A&A, 491, L33

Bagnulo, S., Boehnhardt, H., Muinonen, K., et al. 2006, A&A, 450, 1239

Bagnulo, S., Landolfi, M., Landstreet, J. D., et al. 2009, PASP, 121, 993

Bagnulo, S., Tozzi, G. P., Boehnhardt, H., Vincent, J.-B., & Muinonen, K. 2010, A&A, 514, A99

Barkume, K. M., Brown, M. E., & Schaller, E. L. 2005, in Bulletin of the American Astronomical Society, Vol. 37, AAS/Division for Planetary Sciences Meeting Abstracts #37, 738

Barucci, M. A., Alvarez-Candal, A., Merlin, F., et al. 2011, Icarus, 214, 297

Beer, E. H., Podolak, M., & Prialnik, D. 2006, Icarus, 180, 473

Belskaya, I., Bagnulo, S., Muinonen, K., et al. 2008, A&A, 479, 265

Belskaya, I. N., Bagnulo, S., Barucci, M. A., et al. 2010, Icarus, 210, 472

Belskaya, I. N., Fornasier, S., & Krugly, Y. N. 2009a, Icarus, 201, 167

Belskaya, I. N., Levasseur-Regourd, A.-C., Cellino, A., et al. 2009b, Icarus, 199, 97

Belskaya, I. N., Shkuratov, Y. G., Efimov, Y. S., et al. 2005, Icarus, 178, 213

Belton, M. J. S., Meech, K. J., A'Hearn, M. F., et al. 2005, Space Sci. Rev., 117, 137

Belton, M. J. S., Thomas, P., Veverka, J., et al. 2007, Icarus, 191, 573

Belton, M. J. S., Meech, K. J., Chesley, S., et al. 2011, Icarus, 213, 345

Bertin, E., & Arnouts, S. 1996, A&AS, 117, 393

Beuzit, J.-L., Feldt, M., Dohlen, K., et al. 2008, in Society of Photo-Optical Instrumentation Engineers (SPIE) Conference Series, Vol. 7014, Society of Photo-Optical Instrumentation Engineers (SPIE) Conference Series, 18

Birkett, C. M. 1988, MNRAS, 235, 497

Boehnhardt, H., Bagnulo, S., Muinonen, K., et al. 2004, A&A, 415, L21

Boehnhardt, H., & Birkle, K. 1994, A&AS, 107, 101

Boehnhardt, H., Tozzi, G. P., Bagnulo, S., et al. 2008, A&A, 489, 1337

Boehnhardt, H., Pompei, E., Tozzi, G. P., et al. 2007, A&A, 470, 1175

Bohren, C. F., & Huffman, D. R. 1998, Absorption and Scattering of Light by Small Particles (Wiley)

Bonev, T., Ageorges, N., Bagnulo, S., et al. 2009, in Deep Impact as a World Observatory Event: Synergies in Space, Time, and Wavelength, ed. H. U. Käufl & C. Sterken (Springer), 177

Bonnet, H., Conzelmann, R., Delabre, B., et al. 2004, 130–138

Braga-Ribas, F., Sicardy, B., Ortiz, J. L., et al. 2014, Nature, 508, 72

Brasser, R., Morbidelli, A., Gomes, R., Tsiganis, K., & Levison, H. F. 2009, A&A, 507, 1053

Breger, M., & Cochran, W. D. 1982, Icarus, 49, 120

Brown, M. E. 2013, ApJ, 767, L7

Brown, M. E., Barkume, K. M., Blake, G. A., et al. 2007, AJ, 133, 284

Brown, M. E., Burgasser, A. J., & Fraser, W. C. 2011, ApJ, 738, L26

Brown, M. E., Ragozzine, D., Stansberry, J., & Fraser, W. C. 2010, AJ, 139, 2700

Buratti, B. J., Hicks, M. D., Soderblom, L. A., et al. 2004, Icarus, 167, 16

Bus, S. J., & Binzel, R. P. 2002, Icarus, 158, 146

Cañada-Assandri, M., Gil-Hutton, R., & Benavidez, P. 2012, A&A, 542, A11

Cellino, A., Bagnulo, S., Gil-Hutton, R., et al. 2015, MNRAS, 451, 3473

Cellino, A., Bagnulo, S., Tanga, P., Novaković, B., & Delbò, M. 2014, MNRAS, 439, L75

Cellino, A., Belskaya, I. N., Bendjoya, P., et al. 2006, Icarus, 180, 565

Cellino, A., Bus, S. J., Doressoundiram, A., & Lazzaro, D. 2002, Asteroids III, 633

Cellino, a., Gil-Hutton, R., Dell'Oro, a., et al. 2012, Journal of Quantitative Spectroscopy and Radiative Transfer, 113, 2552

Cellino, A., Gil Hutton, R., Tedesco, E. F., di Martino, M., & Brunini, A. 1999, Icarus, 138, 129

Chapman, C. R. 2004, Annual Review of Earth and Planetary Sciences, 32, 539

Clarke, D., & Neumayer, D. 2002, A&A, 383, 360

Comeron, F., Romaniello, M., & Breysacher, J. 2002, The Messenger, 113, 32

Connors, M., Wiegert, P., & Veillet, C. 2011, Nature, 475, 481

Davis, L. 1987, http://iraf.noao.edu/docs/photom.html

DeMeo, F. E., Binzel, R. P., Slivan, S. M., & Bus, S. J. 2009, Icarus, 202, 160

Dias-Oliveira, A., Sicardy, B., Lellouch, E., et al. 2015, ArXiv e-prints

Dlugach, J. M., & Mishchenko, M. I. 2004, J. Quant. Spec. Radiat. Transf., 88, 37

Dlugach, J. M., & Mishchenko, M. I. 2008, MNRAS, 384, 64

Dlugach, Z. M., & Mishchenko, M. I. 2005, Solar System Research, 39, 102

Dollfus, A. 1957, Supplements aux Annales d'Astrophysique, 4, 3

Dollfus, A. 1975, Icarus, 25, 416

Dollfus, A., Auriere, M., & Santer, R. 1979, AJ, 84, 1419

Dollfus, A., Bowell, E., & Ebisawa, S. 1984, A&A, 134, 343

Dollfus, A., Deschamps, M., & Ksanfomaliti, L. V. 1983, A&A, 123, 225

Dollfus, A., Ebisawa, S., & Crussaire, D. 1996, J. Geophys. Res., 101, 9207

Dollfus, A., & Focas, J. 1969, A&A, 2, 63

Doressoundiram, A., Boehnhardt, H., Tegler, S. C., & Trujillo, C. 2008, Color Properties and Trends of the Transneptunian Objects, ed. M. A. Barucci, H. Boehnhardt, D. P. Cruikshank, A. Morbidelli, & R. Dotson (The University of Arizona Press), 91–104

Draine, B. T., & Flatau, P. J. 2008, Journal of the Optical Society of America A, 25, 2693

Ebisawa, S., & Dollfus, A. 1993, A&A, 272, 671

Eisenhauer, F. 2003, A&A, 4841, 1548

Elliot, J. L., Kern, S. D., Clancy, K. B., et al. 2005, AJ, 129, 1117

Emery, J. P., & Brown, R. H. 2004, Icarus, 170, 131

Emery, J. P., Burr, D. M., & Cruikshank, D. P. 2011, AJ, 141, 25

Emery, J. P., Marzari, F., Morbidelli, A., French, L. M., & Grav, T. 2015, ArXiv e-prints

Farnham, T. L., & Cochran, A. L. 2002, Icarus, 160, 398

Feldman, P. D., Stern, S. A., Steffl, A. J., et al. 2007, Icarus, 187, 104

Fernández, Y. R., Lisse, C. M., Ulrich Käufl, H., et al. 2000, Icarus, 147, 145

Finson, M. J., & Probstein, R. F. 1968, ApJ, 154, 327

Fornasier, S., Belskaya, I. N., Shkuratov, Y. G., et al. 2006, A&A, 455, 371

Fornasier, S., Dotto, E., Hainaut, O., et al. 2007, Icarus, 190, 622

Furusho, R., Ikeda, Y., Kinoshita, D., et al. 2007, Icarus, 190, 454

Gehrels, T., Gradie, J. C., Howes, M. L., & Vrba, F. J. 1979, AJ, 84, 671

Gehrels, T., Herman, B. M., & Owen, T. 1969, AJ, 74, 190

Gil-Hutton, R., & Cañada-Assandri, M. 2011, A&A, 529, A86

Gil-Hutton, R., & Cañada-Assandri, M. 2012, VizieR Online Data Catalog, 353, 99115

Gil-Hutton, R., Mesa, V., Cellino, A., et al. 2008, A&A, 482, 309

Gradie, J., & Zellner, B. 1973, in Bulletin of the American Astronomical Society, Vol. 5, 404

Grav, T., Mainzer, A. K., Bauer, J. M., Masiero, J. R., & Nugent, C. R. 2012, ApJ, 759, 49

Guilbert-Lepoutre, A. 2014, Icarus, 231, 232

Hadamcik, E., Levasseur-Regourd, A. C., Leroi, V., & Bardin, D. 2007, Icarus, 190, 459

Hainaut, O. R., Boehnhardt, H., & Protopapa, S. 2012, A&A, 546, A115

Hall, J. S., & Riley, L. A. 1969, Journal of Atmospheric Sciences, 26, 920

Hansen, J. E., & Hovenier, J. W. 1974, Journal of Atmospheric Sciences, 31, 1137

Harrington, D. M., Meech, K., Kolokolova, L., Kuhn, J. R., & Whitman, K. 2007, Icarus, 187, 177

Heinze, A. N., & de Lahunta, D. 2009, AJ, 138, 428

Jackson, J. D. 1975, Classical electrodynamics (Wiley)

Jehin, E., Manfroid, J., Hutsemékers, D., et al. 2006, ApJ, 641, L145

Kaufl, H.-U., Ageorges, N., Bagnulo, S., et al. 2005, The Messenger, 121, 11

Keller, C. U. 2001, in Astrophysical Spectropolarimetry, ed. J. Trujillo-Bueno, F. Moreno-Insertis, & F. Sanchez (Cambridge University Press), 303–354, cambridge Books Online

Keller, H. U., Jorda, L., Küppers, M., et al. 2005, Science, 310, 281

Keller, H. U., Küppers, M., Fornasier, S., et al. 2007, Icarus, 187, 87

Kiselev, N., Rosenbush, V., Jockers, K., Velichko, S., & Kikuchi, S. 2006a, Earth, Moon, and Planets, 97, 365

Kiselev, N., Velichko, S., Jockers, K., Rosenbush, V., & Kikuchi, S., E. 2006, EAR-C-COMPIL-5-DB-COMET-POLARIMETRY-V1.0. NASA Planetary Data System

Kiselev, N. N., & Lupishko, D. F. 2004, Solar System Research, 38, 85

Kolokolova, L., Hough, J., & Levasseur-Regourd, A.-C., eds. 2015, Polarimetry of Stars and Planetary Systems (Cambridge University Press), cambridge Books Online

Kolokolova, L., Jockers, K., Gustafson, B. Å. S., & Lichtenberg, G. 2001, J. Geophys. Res., 106, 10113

Lakhtakia, A., & Mulholland, G. 1993, J Res Natl Inst Stand Technol, 98, 699

Lamy, P. L., Toth, I., Weaver, H. a., A'Hearn, M. F., & Jorda, L. 2011, MNRAS, 412, 1573

Lamy, P. L., & Weaver, H. A. 2004, in Comets II, 223–264

Landi Degl'Innocenti, E., Bagnulo, S., & Fossati, L. 2007, in Astronomical Society of the Pacific Conference Series, Vol. 364, The Future of Photometric, Spectrophotometric and Polarimetric Standardization, ed. C. Sterken, 495

Levasseur-Regourd, A. C., Hadamcik, E., & Renard, J. B. 1996, A&A, 313, 327

Levasseur-Regourd, A. C., Zolensky, M., & Lasue, J. 2008, Planet. Space Sci., 56, 1719

Levison, H. F., Bottke, W. F., Gounelle, M., et al. 2009, Nature, 460, 364

Li, J.-Y., A'Hearn, M. F., McFadden, L. A., & Belton, M. J. S. 2007a, Icarus, 188, 195

Li, J.-Y., A'Hearn, M. F., Belton, M. J. S., et al. 2007b, Icarus, 187, 41

Licandro, J., Pinilla-Alonso, N., Pedani, M., et al. 2006, A&A, 445, L35

Lim, T. L., Stansberry, J., Müller, T. G., et al. 2010a, A&A, 518, L148

Lim, T. L., Stansberry, J., Müller, T. G., et al. 2010b, A&A, 518, L148

Lowry, S. C., & Fitzsimmons, A. 2001, A&A, 365, 204

Lowry, S. C., Fitzsimmons, A., Cartwright, I. M., & Williams, I. P. 1999, A&A, 659, 649

Lowry, S. C., Fitzsimmons, A., & Collander-Brown, S. 2003, A&A, 397, 329

Lumme, K., & Muinonen, K. O. 1993, LPI Contributions, 810, 194

Lupishko, D. 2014, NASA Planetary Data System, 215

Lupishko, D. F., Bel'Skaia, I. N., Kvaratskheliia, O. I., Kiselev, N. N., & Morozhenko, A. V. 1988, Astronomicheskii Vestnik, 22, 142

Lupishko, D. F., Vasilyev, S. V., Efimov, J. S., & Shakhovskoj, N. M. 1995, Icarus, 113, 200

Lyot, B. 1929, Annales de l'Observatoire de Paris, Section de Meudon, 8, 1

Mallama, A., Wang, D., & Howard, R. A. 2002, Icarus, 155, 253

Masiero, J., & Cellino, A. 2009, Icarus, 199, 333

Meech, K. J., Ageorges, N., A'Hearn, M. F., et al. 2005, Science, 310, 265

Meech, K. J., Pittichová, J., Yang, B., et al. 2011, Icarus, 213, 323

Mishchenko, M. I., Travis, L. D., & Mackowski, D. W. 1996a, J. Quant. Spec. Radiat. Transf., 55, 535

Mishchenko, M. I., Travis, L. D., & Mackowski, D. W. 1996b, JQSRT, 55, 535

Mishchenko, M. I., Yatskiv, Y. S., Rosenbush, V. K., & Videen, G. 2011, Polarimetric Detection, Characterization and Remote Sensing (Springer)

Morbidelli, A., Brasser, R., Gomes, R., Levison, H. F., & Tsiganis, K. 2010, AJ, 140, 1391

Morbidelli, A., Levison, H. F., Tsiganis, K., & Gomes, R. 2005a, Nature, 435, 462

Morbidelli, A., Levison, H. F., Tsiganis, K., & Gomes, R. 2005b, Nature, 435, 462

Mottola, S., Di Martino, M., Erikson, A., et al. 2011, AJ, 141, 170

Mueller, B. E. A., Samarasinha, N. H., Rauer, H., & Helbert, J. 2010, Icarus, 209, 745

Muinonen, K. 2004, Waves in Random Media, 14, 365

Muinonen, K., Mishchenko, M. I., Dlugach, J. M., et al. 2012, ApJ, 760, 118

Muinonen, K., Piironen, J., Kaasalainen, S., & Cellino, A. 2002a, Mem. Soc. Astron. Italiana, 73, 716

Muinonen, K., Piironen, J., Shkuratov, Y. G., Ovcharenko, A., & Clark, B. E. 2002b, Asteroids III, 123

Muinonen, K., & Videen, G. 2012, JQSRT, 113, 2385

Murray, C. D., & Dermott, S. F. 1999, Solar system dynamics (Cambridge University Press)

Myers, R. 1985, Icarus, 216, 206

Myers, R., & Nordsieck, K. 1984, Icarus, 439

Nesvorný, D., & Morbidelli, A. 2012, AJ, 144, 117

Nesvorný, D., Vokrouhlický, D., & Morbidelli, A. 2013, ApJ, 768, 45

Ortiz, J. L., Sicardy, B., Braga-Ribas, F., et al. 2012, Nature, 491, 566

Penttilä, A., & Lumme, K. 2005, A&A, 1090, 1081

Penttilä, A., Zubko, E., Lumme, K., et al. 2007, JQSRT, 106, 417

Prialnik, D., & Rosenberg, E. D. 2009, MNRAS, 399, L79

Protopapa, S., Sunshine, J. M., Feaga, L. M., et al. 2014, Icarus, 238, 191

Psarev, V., Ovcharenko, A., Shkuratov, Y., Belskaya, I., & Videen, G. 2007, J. Quant. Spec. Radiat. Transf., 106, 455

Purcell, E. M., & Pennypacker, C. R. 1973, ApJ, 186, 705

Rauer, H., Weiler, M., Sterken, C., et al. 2006, A&A, 459, 257

Rosenbush, Vera., K., & Mishchenko, Michael., I. 2011, in Polarimetric Detection, Characterization and Remote Sensing, ed. M. I. Mishchenko, Y. S. Yatskiv, V. K. Rosenbush, & G. Videen, NATO Science for Peace and Security Series C: Environmental Security (Springer Netherlands), 409–436

Scarrott, S. M., Warren-Smith, R. F., Pallister, W. S., Axon, D. J., & Bingham, R. G. 1983, MNRAS, 204, 1163

Schaller, E. L., & Brown, M. E. 2008, ApJL, 684, L107

Schmid, H. M., Joos, F., & Tschan, D. 2006, A&A, 452, 657

Serkowski, K. 1974, in IAU Colloq. 23: Planets, Stars, and Nebulae: Studied with Photopolarimetry, ed. T. Gehrels, 135

Shevchenko, V. G., & Tedesco, E. F. 2006, Icarus, 184, 211

Shkuratov, I. G., Opanasenko, N. V., & Kreslavskii, M. A. 1992, Icarus, 95, 283

Shkuratov, Y., Ovcharenko, A., Zubko, E., et al. 2002, Icarus, 159, 396

Shkuratov, Y., Kreslavsky, M., Kaydash, V., et al. 2005, Icarus, 176, 1

Shkuratov, Y. G., Muinonen, K., Bowell, E., et al. 1994, Earth Moon and Planets, 65, 201

Sicardy, B., Ortiz, J. L., Assafin, M., et al. 2011, Nature, 478, 493

Smith, P. H., & Tomasko, M. G. 1984, Icarus, 58, 35

Stam, D. M. 2008, A&A, 482, 989

Sterzik, M. F., Bagnulo, S., & Palle, E. 2012, Nature, 483, 64

Tegler, S. C., Grundy, W. M., Olkin, C. B., et al. 2012, ApJ, 751, 76

Tegler, S. C., Grundy, W. M., Vilas, F., et al. 2007, in Bulletin of the American Astronomical Society, Vol. 39, AAS/Division for Planetary Sciences Meeting Abstracts #39, 509

Tegler, S. C., Grundy, W. M., Vilas, F., et al. 2008, Icarus, 195, 844

Tholen, D. J. 1989, in Asteroids II, ed. R. P. Binzel, T. Gehrels, & M. S. Matthews, 1139–1150

Thomas, P. C., Veverka, J., Belton, M. J. S., et al. 2007, Icarus, 187, 4

Tomasko, M. G., & Doose, L. R. 1984, Icarus, 58, 1

Tozzi, G. P., Lara, L. M., Kolokolova, L., et al. 2004, A&A, 424, 325

Tozzi, G. P., & Licandro, J. 2002, Icarus, 157, 187

Tozzi, G. P., Boehnhardt, H., Kolokolova, L., et al. 2007, A&A, 476, 979

Usui, F., Kuroda, D., Müller, T. G., et al. 2011, PASJ, 63, 1117

Veverka, J. 1971, Icarus, 14, 355

Waterman, P. C. 1971, Phys. Rev. D, 3, 825

Wiktorowicz, S. J., & Nofi, L. A. 2015, ApJ, 800, L1

Wolff, M. 1975, Appl. Opt., 14, 1395

Yang, B., & Sarid, G. 2010, IAU Circ., 9139, 2

Zellner, B., & Gradie, J. 1976, AJ, 81, 262

Zubko, E., Petrov, D., Shkuratov, Y., & Videen, G. 2005, Appl. Opt., 44, 6479